



저작자표시-비영리-변경금지 2.0 대한민국

이용자는 아래의 조건을 따르는 경우에 한하여 자유롭게

- 이 저작물을 복제, 배포, 전송, 전시, 공연 및 방송할 수 있습니다.

다음과 같은 조건을 따라야 합니다:



저작자표시. 귀하는 원저작자를 표시하여야 합니다.



비영리. 귀하는 이 저작물을 영리 목적으로 이용할 수 없습니다.



변경금지. 귀하는 이 저작물을 개작, 변형 또는 가공할 수 없습니다.

- 귀하는, 이 저작물의 재이용이나 배포의 경우, 이 저작물에 적용된 이용허락조건을 명확하게 나타내어야 합니다.
- 저작권자로부터 별도의 허가를 받으면 이러한 조건들은 적용되지 않습니다.

저작권법에 따른 이용자의 권리는 위의 내용에 의하여 영향을 받지 않습니다.

이것은 [이용허락규약\(Legal Code\)](#)을 이해하기 쉽게 요약한 것입니다.

[Disclaimer](#)

공학박사 학위논문

**A Study on the Solid Solution Anode with  
Hybrid Electrochemical Reaction for  
High Performance Secondary Ion Battery**

고성능 이차 전지용 하이브리드 전기화학 반응  
고용체 음극 소재 연구

2021 년 2 월

서울대학교 대학원  
재료공학부  
김 경 호

**A Study on the Solid Solution Anode with  
Hybrid Electrochemical Reaction for High  
Performance Secondary Ion Battery**

**A THESIS SUBMITTED TO  
DEPARTMENT OF MATERIALS SCIENCE AND  
ENGINEERING  
SEOUL NATIONAL UNIVERSITY**

**FOR THE DEGREE OF  
DOCTOR OF PHILOSOPHY**

**BY  
Kyeong-Ho Kim**

**FEBRUARY 2021**

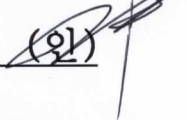
# A Study on the Solid Solution Anode with Hybrid Electrochemical Reaction for High Performance Secondary Ion Battery

지도교수 홍 성 현

이 논문을 공학박사 학위논문으로 제출함  
2021년 2월

서울대학교 대학원  
재료공학부  
김 경 호

김경호의 공학박사 학위논문을 인준함  
2020년 10월

위원장	박 병 우	(인) 
부위원장	홍 성 현	(인) 
위원	김 미 영	(인) 
위원	김 동 완	(인) 
위원	조 우 석	(인) 

## **Abstract**

# **A Study on the Solid Solution Anode with Hybrid Electrochemical Reaction for High Performance Secondary Ion Battery**

Kyeong-Ho Kim

Department of Materials Science and Engineering

The Graduate School

Seoul National University

Rechargeable lithium-ion battery (LIB) and sodium-ion battery (SIB) are emerging as next generation energy storage systems owing to their high energy and power densities to apply for large scale energy storage application such as electric vehicles (EVs), hybrid electric vehicles (HEVs), and energy storage system (ESS). The exploration of alternative electrode material for high energy density anode to replace the commercial graphite has been conducted on various electrochemical reaction mechanisms, such as alloying, conversion and insertion reactions. However, the intrinsic shortcomings of each reaction mechanism undermine the electrode performance.

In fact, the most desirable solution would be a combination between alloying or conversion reaction anodes with insertion reaction anode to overcome their own

distinct limitations of each electrochemical reaction mechanisms. So far, many researches have been conducted on high performance nanocomposite anodes to prevent electrode degradation by mixing or coating insertion reaction anode materials, which is mainly carbonaceous material and early transition metal (titanium and vanadium) oxide, with alloying or conversion reaction anode materials. This approach has improved cycle retention properties with the structural integrity of electrode obtained by mitigating the volume expansion, pulverization, and agglomeration of alloying or conversion reaction anodes by providing buffer spaces with negligible volume change of insertion reaction material. However, this approach requires complex optimization of nano-fabrication process for nanocomposites consisting of homogeneously distributed each reaction anodes in nanoscale. In addition, each reaction anode in nanocomposite would react individually in nanoscale and their interaction and synergistic effect are limited to effectively mitigate the electrode degradation factors occurred in few nanoscales of each material.

The objective of this thesis is to develop the novel solid solution anode with hybrid electrochemical reaction for high performance secondary-ion battery. This new strategy to overcome intrinsic shortcomings of each electrochemical reaction mechanism is to find out the material systems to form a single compound with different types of electrochemical reaction mechanism anodes and to allow the simultaneous hybrid electrochemical reaction of two different mechanisms in a single phase. This could lead to the excellent synergistic effect due to their atomically homogeneous and finer distribution than that of physically mixed nanocomposite between two different materials. In addition, electrode performance can be tailored

by varying the ratio of different reaction materials in solid solution compound.

First of all, complete solid solution compounds of  $\text{Mn}_{1-x}\text{Fe}_x\text{P}$  ( $0 \leq x \leq 1$ ) as a conversion/alloying hybrid electrochemical reaction anode was introduced for LIBs by using the iso-structural character of MnP and FeP compounds. The systematic studies on electrochemical properties of  $\text{Mn}_{1-x}\text{Fe}_x\text{P}$  ( $0 \leq x \leq 1$ ) compounds as anodes for LIBs were investigated, particularly focusing on the electrochemical reaction mechanism and the tunability of working voltage, specific capacity, and cycle performance and compared with those of MnP/FeP nanocomposite anode. As-prepared  $\text{Mn}_{1-x}\text{Fe}_x\text{P}$  ( $0 \leq x \leq 1$ ) electrode showed the hybrid reaction with alloying reaction of MnP and conversion reaction of FeP electrodes, and it was investigated that the contribution rate of conversion and alloying reactions to total electrochemical reaction can be controlled by varying the composition in  $\text{Mn}_{1-x}\text{Fe}_x\text{P}$  solid solution. Through this novel strategy, the intrinsic shortcomings of fast capacity fading for MnP electrode and capacity activation behavior at high current density for FeP electrode were improved by hybrid conversion/alloying reaction of  $\text{Mn}_{1-x}\text{Fe}_x\text{P}$  ( $x=0.75$ ) electrode, which delivered a reversible capacity of  $360 \text{ mA h g}^{-1}$  after 100 cycles at high current density at  $2 \text{ A g}^{-1}$ . This improved electrochemical performance of  $\text{Mn}_{1-x}\text{Fe}_x\text{P}$  electrode can be attributed to the *in situ* generated nanocomposite nature of the Li–Mn–P alloying element and the Fe nano-network in combination with the surrounding amorphous lithium phosphide, which effectively buffers the accompanying volume variation, hinders the aggregation of the alloying element, and ensures electron and ion transport.

In the second part, alloying/insertion hybrid electrochemical reaction anode as

$Mn_{1-x}V_xP$  was introduced to further obtain highly stable cycle retention properties with intermediate specific capacity. The series of  $Mn_{1-x}V_xP$  compounds ( $x = 0, 0.25, 0.5, 0.75,$  and  $1.0$ ) between alloying reaction-type of orthorhombic  $MnP$  and insertion reaction-type of hexagonal  $VP$  are synthesized based on their similar crystal structure relation. The homogeneously substituted vanadium ions in the  $Mn_{1-x}V_xP$  compounds enable the alloying/insertion hybrid electrochemical reactions in a solid solution phase by expanding the volume of prismatic site in  $Mn_{1-x}V_xP$  close to the that of insertion-reaction type  $VP$ . The optimized  $Mn_{1-x}V_xP$  ( $x=0.25$ ) electrode showed reversible capacity of  $352 \text{ mA h g}^{-1}$  after 1500 cycles even at high current density of  $1 \text{ A g}^{-1}$ . Such a superior electrochemical performance of  $Mn_{1-x}V_xP$  was attributed to the synergistic effect of hybrid alloying/insertion electrochemical reaction occurred close to a few-nanometer scale in a single compound  $Mn_{1-x}V_xP$  phase, which effectively reduce the rate of volume change and hinder pulverization and agglomeration of alloying reaction elements and ensure fast electron and ion transport.

Finally, solid solution compound of  $Mn_{1-x}TM_xP_4$  ( $TM = V$  and  $Fe$ ) anode was introduced as a hybrid conversion reaction anode for SIBs. The electrochemical reaction mechanism and performance of  $MnP_4$  phase in SIB application were firstly investigated and enhanced electrochemical performance by forming the solid solution phase was examined. By encapsulating as-synthesized  $MnP_4$  nanoparticles with commercial graphene nanosheets, superior electrochemical performance for both LIBs and SIBs could be achieved, which delivered reversible capacities of  $856 \text{ mA h g}^{-1}$  after 100 cycles at  $2 \text{ A g}^{-1}$  for LIBs and  $446 \text{ mA h g}^{-1}$  after 250 cycles at  $0.5 \text{ A g}^{-1}$  for SIBs, respectively. Further, different cation substituted  $Mn_{1-x}V_xP_4$

( $x=0.25$ ) solid solution exhibits improved rate capabilities for both LIBs and SIBs, which could be derived from the structural and electronic structure change. The  $\text{Mn}_{1-x}\text{V}_x\text{P}_4$  ( $x=0.25$ ) electrode showed improved high rate capability, which delivers reversible capacity of  $790 \text{ mA h g}^{-1}$  for 50 cycles at high current density of  $0.5 \text{ A g}^{-1}$ .

Overall, this thesis focuses on the synthesis and investigate on hybrid electrochemical reaction anode with their structural and chemical relationship to overcome intrinsic shortcomings of each electrochemical reaction mechanism. The obtained results through this thesis show the promising potential with dramatic changes in performance of hybrid electrochemical reaction materials designed with multi-component substitution by considering chemical and structural relation and suggests that there are many other candidates in transition metal compounds to explore in high performance both lithium-ion and sodium-ion battery application.

**Keywords:** Hybrid electrochemical reaction, Solid solution, Metal phosphide, Anode material, Lithium-ion battery, Sodium-ion battery

**Student Number:** 2015-20800

# Table of Contents

<b>Abstract</b> .....	<b>I</b>
<b>Table of Contents</b> .....	<b>VI</b>
<b>List of Tables</b> .....	<b>IX</b>
<b>List of Figures</b> .....	<b>X</b>
<b>Chapter 1. Introduction</b> .....	<b>1</b>
1.1. Overview: Rechargeable Batteries for Energy Storage .....	1
1.2. Thesis Motivation and Scopes.....	12
1.3. Bibliography.....	14
<b>Chapter 2. Background and Literature Review</b> .....	<b>18</b>
2.1. Li-ion and Na-ion Batteries .....	18
2.2. Electrochemical Reaction Mechanism for Anode Materials .....	25
2.2.1. Intercalation/Insertion Reaction Type Anode.....	26
2.2.2. Alloying Reaction Type Anode .....	29
2.2.3. Conversion Reaction Type Anode .....	31
2.3. Conventional Approach for High Performance Anode.....	39
2.3.1. Nanostructured Material and Nanocomposite with Different Electrochemical Reaction .....	40
2.3.2 Ternary Compound of Conversion/Alloying Materials .....	45

2.4. Bibliography.....	49
------------------------	----

**Chapter 3. Complete Solid Solution  $Mn_{1-x}Fe_xP$  as a Conversion/Alloying Hybrid Reaction Anode for Lithium-Ion Batteries .....56**

3.1. Introduction.....	56
3.2. Experimental Procedure .....	62
3.3. Results and Discussions	
3.3.1. Synthesis and Physicochemical Characterization .....	64
3.3.2. Electrochemical Properties and Reaction Mechanism.....	73
3.3.3. Electrochemical Performance .....	83
3.4. Conclusion.....	103
3.5. Bibliography.....	104

**Chapter 4. A Novel Solid Solution  $Mn_{1-x}V_xP$  Anode with Alloying/Insertion Hybrid Electrochemical Reaction for High Performance Lithium-Ion Batteries .....108**

4.1. Introduction.....	108
4.2. Experimental Procedure .....	112
4.3. Results and Discussions	
4.3.1. Synthesis and Physicochemical Characterization .....	115
4.3.2. Electrochemical Properties and Reaction Mechanism.....	129
4.3.3. Electrochemical Performance .....	144

4.3.4. Synergistic Effect of Hybrid Alloying/Insertion Reaction....	150
4.3.5 Discussion on Hybrid Alloying/Insertion Reaction Anodes..	160
4.3.6. Practical Application with Full-Cell Configuration .....	165
4.4. Conclusion.....	167
4.5. Bibliography.....	168
<b>Chapter 5. Solid Solution <math>Mn_{1-x}TM_xP_4</math> (TM = V and Fe) Anode with High Performance Conversion Reaction for Sodium-Ion Batteries .....</b>	<b>171</b>
5.1. Introduction .....	171
5.2. Experimental Procedure .....	175
5.3. Results and Discussions	
5.3.1. Synthesis and Physicochemical Characterization .....	178
5.3.2. Electrochemical Reaction Mechanism and Performance .....	185
5.3.3. Improvement of Rate Capability by Forming Solid Solution .....	202
5.4. Conclusion.....	216
5.5. Bibliography.....	217
<b>Chapter 6. Conclusions.....</b>	<b>221</b>
<b>Abstract in Korean .....</b>	<b>224</b>
<b>Research Achievement.....</b>	<b>229</b>
<b>Acknowledgement .....</b>	<b>233</b>

## List of Tables

**Table 3.3.1** The refined lattice parameters for  $\text{Mn}_{1-x}\text{Fe}_x\text{P}$  ( $x = 0, 0.5, 0.75, \text{ and } 1$ ) NPs.

**Table 3.3.2** Elemental analysis results of  $\text{Mn}_{1-x}\text{Fe}_x\text{P}$  ( $x = 0, 0.5, 0.75, \text{ and } 1$ ) NPs by ICP-AES.

**Table 3.3.3** Lithium storage performance comparison of  $\text{Mn}_{0.25}\text{Fe}_{0.75}\text{P}$  solid solution electrode with the previously reported FeP and MnP-based electrodes.

**Table 4.3.1** XRD Rietveld refinement parameters for as-synthesized  $\text{Mn}_{1-x}\text{V}_x\text{P}$  ( $x =$  (a) 0, (b) 0.25, (c) 0.5, (d) 0.75, and (e) 1.0) compounds.

**Table 4.3.2** Elemental analysis results of  $\text{Mn}_{1-x}\text{V}_x\text{P}$  ( $x = 0, 0.25, 0.5, 0.75, \text{ and } 1.0$ ) compounds by ICP-AES.

**Table 4.3.3** State-of-the-art intrinsic electrochemical performance of nanostructured LIB anode materials such as nanocomposite, ternary compound, and binary oxide based on insertion reaction type material.

**Table 4.3.4** Space group and structure type of transition metal monophosphide compounds.

**Table 5.3.1** Le Bail fitting results of as-synthesized  $\text{MnP}_4$  nanoparticles.

**Table 5.3.2** ICDD database of Li-Mn-P and Na-Mn-P ternary compounds.

**Table 5.3.3** Le Bail fitting results of as-synthesized  $\text{Mn}_{1-x}\text{TM}_x\text{P}_4$  (TM = V and Fe,  $x = 0.25$ ) nanoparticles.

## List of Figures

**Figure 1.1.1** Comparison of the different battery technologies in terms of volumetric and gravimetric energy density.[1.3]

**Figure 1.1.2** Approximate range of average discharge potentials and specific capacity of some of the most common intercalation-type cathode materials for LIBs (experimental).[1.13]

**Figure 1.1.3** Approximate range of reaction potentials and specific capacities of various electrochemical reaction-type anode materials for LIBs.[1.19]

**Figure 1.1.4** Average voltage (discharge) versus capacity plot of anode materials for SIBs.[1.29]

**Figure 2.1.1** Schematic illustration of a lithium ion battery showing charge/discharge processes.[2.1]

**Figure 2.1.2** Charge-discharge process of a lithium-ion cell using graphite and  $\text{LiCoO}_2$  electrodes.[2.2]

**Figure 2.1.3** Ragone diagram of specific energy versus specific power for major rechargeable battery systems.[2.6]

**Figure 2.2.1** Schematic representation of three typical reaction mechanisms between  $\text{Li}^+$ -ion and electrode materials.[2.8]

**Figure 2.2.2** Schematic illustration of reversible electrochemical insertion / extraction reaction of  $\text{MX}_2$  anode materials.[2.9]

**Figure 2.2.3** Schematic illustration of reversible electrochemical alloying/dealloying reaction of elemental M anode materials.[2.9]

**Figure 2.2.4** Schematic illustration of the local chemistry transformation of transition-metal compounds during the conversion reaction.[2.10]

**Figure 2.2.5** Comparison of density of states (DOS) for oxides, nitrides, and phosphides.[2.35]

**Figure 2.3.1** Schematic illustration of the basic four approaches to enhance the electrochemical performance LIBs and SIBs: (a) porous micro-sized secondary particle, (b) introduction of carbonaceous secondary nanostructures, (c) carbonaceous coating, and (d) transition metal doping.[2.50]

**Figure 2.3.2** Schematic of the volume expansion of mesocarbon microbeads (MCMB) graphite, silicon, and silicon-MCMB graphite composite electrodes.[2.73]

**Figure 2.3.3** Illustrative summary of the beneficial combination of conversion- and alloying-type lithium storage in conversion/alloying materials (CAMs).[2.50]

**Figure 2.3.4** Schematic illustration of the impact of introducing a TM dopant into ZnO on the lithiation mechanism and LiZn (Zn<sup>0</sup>) crystallite growth.[2.50]

**Figure 3.1.1** Crystal structure and electrochemical reaction mechanism for various 1st row transition metal monophosphides.

**Figure 3.1.2** (a) Cycle performance, (b) corresponding voltage profiles tested at current density of 50 mA g<sup>-1</sup>, and ex-situ XRD patterns for MnP/Li cell during (c) lithiation and (d) delithiation process.[3.34]

**Figure 3.1.3** (a) Voltage profiles, (b) corresponding differential capacity plots, (c) in-situ XRD patterns for FeP/Li cell during lithiation and (d) TEM image of as lithiated FeP nanoparticles.[3.35]

**Figure. 3.3.1** (a) XRD patterns for the as-synthesized Mn<sub>1-x</sub>Fe<sub>x</sub>P (x = 0, 0.5, 0.75, and 1.0) NPs and (b) corresponding refined lattice parameters.

**Figure. 3.3.2** XRD Rietveld refinement results for as-synthesized Mn<sub>1-x</sub>Fe<sub>x</sub>P (x = 0,

0.5, 0.75, and 1.0) NPs.

**Figure. 3.3.3** XRD patterns of as-synthesized MnP, MnP/FeP mixture, and FeP NPs.

**Figure. 3.3.4** SEM images and dynamic light scattering (DLS) particle size distributions of the as-synthesized  $\text{Mn}_{1-x}\text{Fe}_x\text{P}$  ( $x =$  (a) 0, (b) 0.5, (c) 0.75, and (d) 1.0) NPs, respectively.

**Figure. 3.3.5** (a,d) High resolution TEM images, (b,e) selected-area electron diffraction (SAED) patterns, and (c,f) STEM images and elemental mapping images (Mn K, Fe K, and P K) of  $\text{Mn}_{1-x}\text{Fe}_x\text{P}$  ( $x =$  0.5 and 0.75) NPs, respectively.

**Figure. 3.3.6** (a) Galvanostatic discharge/charge profiles, (b) corresponding differential capacity plots (DCPs), and (c) voltage variation of lithiation and delithiation plateaus as a function of Fe content in  $\text{Mn}_{1-x}\text{Fe}_x\text{P}$  electrodes.

**Figure. 3.3.7** (a) Galvanostatic discharge/charge profiles, and (b) corresponding differential capacity plots (DCPs) of MnP, MnP/FeP, and FeP electrodes.

**Figure. 3.3.8** Ex-situ XRD patterns for (a) fully lithiated (0.0 V vs.  $\text{Li/Li}^+$ ) and (b) delithiated (2.0 V vs.  $\text{Li/Li}^+$ ) states for  $\text{Mn}_{1-x}\text{Fe}_x\text{P}$  electrodes ( $x =$  0, 0.5, and 1.0), respectively.

**Figure. 3.3.9** Ex-situ TEM images and SAED patterns of fully discharged states of (a,d) MnP, (b,e)  $\text{Mn}_{0.5}\text{Fe}_{0.5}\text{P}$ , (c,f) FeP electrodes, and (g) STEM image and (h-j) EDS mapping (Mn K, Fe K, and P K) of (b)  $\text{Mn}_{0.5}\text{Fe}_{0.5}\text{P}$  electrode.

**Figure. 3.3.10** (a) High-magnification HAADF STEM image of fully discharged state of  $\text{Mn}_{0.5}\text{Fe}_{0.5}\text{P}$  electrode and (b) reduced FFT pattern of the marked area in (a). (c) HAADF STEM image and EDS mapping images of (d) Mn K, (e) Fe K, and (f) P K, respectively.

**Figure. 3.3.11** (a) TEM image of nano-sized transmission beam and (b) nano-beam electron diffraction pattern of fully discharged state of  $\text{Mn}_{0.5}\text{Fe}_{0.5}\text{P}$  electrode.

**Figure. 3.3.12** Cycle performance and corresponding Coulombic efficiency of (a,b)  $\text{Mn}_{1-x}\text{Fe}_x\text{P}$  ( $x = 0, 0.5, 0.75,$  and  $1.0$ ) electrodes and (c,d)  $\text{Mn}_{0.5}\text{Fe}_{0.5}\text{P}$  and  $\text{MnP/FeP}$  electrodes, respectively. (e) Comparison of experimentally determined and expected 2nd discharge capacity in  $\text{Mn}_{0.5}\text{Fe}_{0.5}\text{P}$  solid solution and  $\text{MnP/FeP}$  mixture electrodes. The expected values were estimated from the reversible capacities of both  $\text{MnP}$  and  $\text{FeP}$  electrodes.

**Figure. 3.3.13** Differential capacity plots (DCPs) for  $\text{MnP}$ ,  $\text{FeP}$ ,  $\text{Mn}_{0.5}\text{Fe}_{0.5}\text{P}$ , and  $\text{MnP/FeP}$  electrodes for 2nd, 10th, 20th, and 40th cycles at the current density of  $100 \text{ mA g}^{-1}$ .

**Figure. 3.3.14** Cycling performance at current density of  $1 \text{ A g}^{-1}$  for  $\text{Mn}_{1-x}\text{Fe}_x\text{P}$  ( $x = 0, 0.5, 0.75,$  and  $1.0$ ) electrodes, respectively.

**Figure. 3.3.15** (a) Cycling performance at current density of  $2 \text{ A g}^{-1}$  for  $\text{Mn}_{1-x}\text{Fe}_x\text{P}$  ( $x = 0, 0.5, 0.75,$  and  $1.0$ ) and  $\text{CoP}$  electrodes and the corresponding (b) galvanostatic discharge/charge voltage profiles and (c) differential capacity plots (DCPs).

**Figure. 3.3.16** Rate capabilities of the  $\text{Mn}_{1-x}\text{Fe}_x\text{P}$  ( $x = 0, 0.5, 0.75,$  and  $1.0$ ) electrodes.

**Figure. 3.3.17** Galvanostatic discharge voltage profiles of  $\text{Mn}_{1-x}\text{Fe}_x\text{P}$  ( $x = 0, 0.5, 0.75,$  and  $1.0$ ) electrodes for each 1st cycle at  $0.1, 1.0,$  and  $2.0 \text{ A g}^{-1}$ , respectively.

**Figure. 3.3.18** (a) Ex-situ XRD pattern, (b) TEM image, and (c) selected area electron diffraction (SAED) pattern of  $\text{FeP}$  electrode for 1st fully discharged state at  $2 \text{ A g}^{-1}$ .

**Figure. 3.3.19** (a) Cycling performance of  $\text{MnP/FeP}$  electrode at  $2 \text{ A g}^{-1}$  and corresponding (b) galvanostatic voltage profiles and (c) differential

capacity plots (DCPs).

**Figure. 3.3.20** STEM images and EDS mapping images (Mn K, Fe K, and P K) of after 1st and 100th cycled electrodes tested at  $2 \text{ A g}^{-1}$  for (a,b)  $\text{Mn}_{0.5}\text{Fe}_{0.5}\text{P}$  and (c,d) MnP/FeP electrodes.

**Figure. 3.3.21** Electrochemical impedance spectroscopy (EIS) data for  $\text{Mn}_{1-x}\text{Fe}_x\text{P}$  ( $x = 0, 0.5, 0.75, \text{ and } 1.0$ ) electrodes (a) before cycle, (b) after the 1st, (c) 20th, and (d) 100th cycles at a current density of  $2 \text{ A g}^{-1}$ .

**Figure. 3.3.22** SEM images of the pristine and cycled (100 cycles at  $2 \text{ A g}^{-1}$ )  $\text{Mn}_{1-x}\text{Fe}_x\text{P}$  electrodes (a,e)  $x = 0$ , (b,f)  $x = 0.5$ , (c,g)  $x = 0.75$ , and (d,h)  $x = 1.0$ , (i) STEM image of the cycled (100 cycles at  $2 \text{ A g}^{-1}$ )  $\text{Mn}_{0.25}\text{Fe}_{0.75}\text{P}$  electrode and EDS elemental mapping images (j) Mn K, (k) Fe K, and (l) P K) of (i).

**Figure. 3.3.23** Schematic illustration for the discharged state of MnP, FeP, and  $\text{Mn}_{1-x}\text{Fe}_x\text{P}$  electrodes.

**Figure. 4.3.1** (a) XRD patterns and (b) enlargement of the patterns in  $2\theta$  range of  $40\sim 50^\circ$  of  $\text{Mn}_{1-x}\text{V}_x\text{P}$  ( $x = 0, 0.25, 0.5, 0.75, \text{ and } 1.0$ ) compounds.

**Figure. 4.3.2** Crystal structure and local structure of  $\text{MP}_6$  octahedron of hexagonal VP and orthorhombic MnP.

**Figure. 4.3.3** XRD Rietveld refinement results for as-synthesized  $\text{Mn}_{1-x}\text{V}_x\text{P}$  ( $x = 0, 0.25, 0.5, 0.75, \text{ and } 1.0$ ) compounds.

**Figure. 4.3.4** XRD Rietveld refined lattice parameters and volumes of  $\text{Mn}_{1-x}\text{V}_x\text{P}$  ( $x = 0, 0.25, 0.5, 0.75, \text{ and } 1.0$ ) compounds.

**Figure. 4.3.5** XRD pattern for as-synthesized  $\text{Mn}_{0.75}\text{V}_{0.25}\text{P}$  solid solution and MnP/VP (3:1) mixture composite.

**Figure. 4.3.6** SEM images and dynamic light scattering (DLS) particle size

distributions of the as-synthesized  $\text{Mn}_{1-x}\text{V}_x\text{P}$  ( $x =$  (a,d) 0, (b,e) 0.25, and (c,f) 1.0) NPs, respectively.

**Figure. 4.3.7** (a) Low magnification TEM image, (b) SAED pattern of  $\text{Mn}_{0.75}\text{V}_{0.25}\text{P}$  nanoparticles, (c) atomic resolution HAADF STEM image of nanocrystallite aligned along the [001] direction, and elemental mapping images ((d) Mn K, (e) V K, and (f) P K) of (c).

**Figure. 4.3.8** Low magnification HAADF STEM image and elemental mapping images (Mn K, V K, and P K) of  $\text{Mn}_{1-x}\text{V}_x\text{P}$  ( $x=0.25$ ) nanoparticles.

**Figure. 4.3.9** Low magnification TEM image, SAED pattern, high-resolution TEM images, corresponding FFT pattern, STEM image, and EDS mapping images (Mn K, V K, and P K) of  $\text{Mn}_{1-x}\text{V}_x\text{P}$  ((a)  $x=0.5$  and (b)  $x=0.75$ ) nanoparticles.

**Figure. 4.3.10** (a) Galvanostatic discharge/charge voltage profiles and (b) corresponding differential capacity plots for  $\text{Mn}_{1-x}\text{V}_x\text{P}$  compounds ( $x = 0.0, 0.25, 0.5, 0.75,$  and  $1.0$ ).

**Figure. 4.3.11** (a) Galvanostatic discharge/charge voltage profiles of MnP/VP electrode. Differential capacity plots (DCPs) of (b) MnP/VP (3:1) composite and  $\text{Mn}_{1-x}\text{V}_x\text{P}$  ( $x =$  (c) 0.25, (d) 0.5, and (e) 0.75) electrodes, respectively.

**Figure. 4.3.12** (a) Bond lengths and (b) prismatic site parameters of  $\text{Mn}_{1-x}\text{V}_x\text{P}$  ( $x = 0, 0.25, 0.50, 0.75,$  and  $1.0$ ), respectively.

**Figure. 4.3.13** Lithiation/delithiation voltage profiles and ex-situ XRD patterns for pristine, fully lithiated (0.01 V), and delithiated (2.0 V) states for  $\text{Mn}_{1-x}\text{V}_x\text{P}$  ( $x = 0, 0.25, 0.50, 0.75,$  and  $1.0$ ) electrodes, respectively.

**Figure. 4.3.14** ICDD database of ternary Li-Mn-P phases ( $\text{Li}_{8-x}\text{Mn}_x\text{P}_4$ ), ex-situ XRD pattern of fully lithiated MnP electrode, and their crystal structure.

**Figure. 4.3.15** (a) HAADF STEM image, (b) corresponding FFT pattern for fully lithiated  $\text{Mn}_{0.75}\text{V}_{0.25}\text{P}$  electrode. High magnification HAADF STEM image with line profile along [001] direction of  $\text{Mn}_{0.75}\text{V}_{0.25}\text{P}$  nanoparticle for (c) pristine and (d) fully lithiated states, respectively.

**Figure. 4.3.16** Crystal structure illustration and diffraction pattern of aligned along the [100] direction for Li-inserted  $\text{Mn}_{0.75}\text{V}_{0.25}\text{P}$ ,  $\text{Li}_3\text{MnP}_2$ , and hybrid alloying/insertion phases, respectively.

**Figure. 4.3.17** HAADF STEM image and EDS mapping images (Mn K, V K, and P K) of fully lithiated  $\text{Mn}_{0.75}\text{V}_{0.25}\text{P}$  electrode.

**Figure. 4.3.18** TEM image of nano-beam and nano-beam electron diffraction (NBED) pattern for fully lithiated  $\text{Mn}_{0.75}\text{V}_{0.25}\text{P}$  electrode.

**Figure. 4.3.19** (a) Lithiation/delithiation voltage profiles and ex-situ XRD patterns for pristine, fully lithiated (0.01 V), and delithiated (2.0 V) states for MnP/VP (3:1) composite electrode, (b) HAADF STEM image and EDS mapping images (P K, Mn K, and V K) of fully lithiated state for MnP/VP electrode.

**Figure. 4.3.20** Cycle performance of  $\text{Mn}_{1-x}\text{V}_x\text{P}$  ( $x = 0, 0.25, 0.5, \text{ and } 1.0$ ) and MnP/VP(3:1) electrodes at  $0.1 \text{ A g}^{-1}$ . (b) Rate capability test and (c) Coulombic efficiency of  $\text{Mn}_{1-x}\text{V}_x\text{P}$  ( $x = 0, 0.25, 0.5, \text{ and } 1.0$ ) electrodes.

**Figure. 4.3.21** Cycle performance of  $\text{Mn}_{1-x}\text{V}_x\text{P}$  ( $x = 0, 0.25, 0.5, \text{ and } 1.0$ ) and MnP/VP(3:1) electrodes at (a)  $1 \text{ A g}^{-1}$  and (b)  $2 \text{ A g}^{-1}$ . (c) Comparison of high-rate long-term cycle performance between  $\text{Mn}_{1-x}\text{V}_x\text{P}$  ( $x = 0.25$ ) and MnP/VP(3:1) electrodes at  $1 \text{ A g}^{-1}$ .

**Figure. 4.3.22** Comparison of electrochemical performance of  $\text{Mn}_{0.75}\text{V}_{0.25}\text{P}$  with state of-the-art of nanostructured LIB anode materials such as nanocomposite, ternary compound, and binary oxide based on insertion reaction type material.

**Figure. 4.3.23** DCPs of  $\text{Mn}_{1-x}\text{V}_x\text{P}$  ( $x = 0, 0.25, 0.5,$  and  $1.0$ ) and  $\text{MnP/VP}(3:1)$  electrodes at  $1 \text{ A g}^{-1}$ .

**Figure. 4.3.24** SEM images of (a) pristine, (b) cycled (200 cycle at  $1 \text{ A g}^{-1}$ ) including SEI layer, and (c) cycled removing SEI layer for  $\text{MnP}$ ,  $\text{VP}$ ,  $\text{Mn}_{0.75}\text{V}_{0.25}\text{P}$ , and  $\text{MnP/VP}$  electrodes, respectively. (d) HAADF STEM image and EDS mapping images for  $\text{Mn K}$ ,  $\text{V K}$ , and  $\text{P K}$  for  $\text{Mn}_{0.75}\text{V}_{0.25}\text{P}$  electrode after 200 cycles at  $1 \text{ A g}^{-1}$ .

**Figure. 4.3.25** Nyquist plots of  $\text{Mn}_{1-x}\text{V}_x\text{P}$  ( $x = 0, 0.25, 1.0$ ) and  $\text{MnP/VP}$  electrodes for (a) pristine and (b) after 200 cycles at  $1 \text{ A g}^{-1}$ ; (c) the linear relationship between the Warburg impedance ( $Z_{\text{re}}$ ) and the inverse square root of angular frequency in low frequency region in (b).

**Figure. 4.3.26** (a) GITT profiles of the state of the lithiation/delithiation process for 2<sup>nd</sup> cycle; Reaction resistance derived from GITT measurement during (b) lithiation and (c) delithiation for  $\text{Mn}_{1-x}\text{V}_x\text{P}$  ( $x = 0.0, 0.25,$  and  $1.0$ ) and  $\text{MnP/VP}$  electrodes, respectively.

**Figure. 4.3.27** (a) GITT profiles of the state of the lithiation/delithiation process for 20<sup>th</sup> cycle; Reaction resistance derived from GITT measurement during (b) lithiation and (c) delithiation for  $\text{Mn}_{1-x}\text{V}_x\text{P}$  ( $x = 0.0, 0.25,$  and  $1.0$ ) and  $\text{MnP/VP}$  electrodes, respectively.

**Figure. 4.3.28** Schematic illustration for the cycling behavior of  $\text{MnP/VP}$  nanocomposite and  $\text{Mn}_{0.75}\text{V}_{0.25}\text{P}$  electrodes, respectively.

**Figure. 4.3.29** Illustration of crystal structure and prismatic site for  $\text{MnP}$ ,  $\text{VP}$ , and  $\text{MoP}$ , respectively.

**Figure. 4.3.30** (a) XRD patterns, (b) voltage profiles and DCPs of  $\text{MnP}$  and  $\text{Mn}_{1-x}\text{TM}_x\text{P}$  ( $\text{TM} = \text{V}$  and  $\text{Mo}$ ,  $x = 0.25$  and  $0.5$ ). (c) *Ex-situ* XRD pattern of  $\text{Mn}_{1-x}\text{Mo}_x\text{P}$  ( $x = 0.25$  and  $0.5$ ) electrodes for pristine and lithiated state. (d) Cycle performance of  $\text{MnP}$  and  $\text{Mn}_{1-x}\text{TM}_x\text{P}$  ( $\text{TM} = \text{V}$  and  $\text{Mo}$ ,  $x =$

0.25 and 0.5) electrodes at current density of 1 A g<sup>-1</sup>.

**Figure. 4.3.31** Galvanostatic charge/discharge voltage profiles and cycle performance of Mn<sub>0.75</sub>V<sub>0.25</sub>P/LiCoO<sub>2</sub> full cell tested at current density of (a,c) 0.1 C and (b,d) 1 C.

**Figure. 5.3.1** (a) XRD pattern and refined results, (b) crystal structure, (c) SEM image, (d) TEM image in low magnification, (e) SAED pattern, (f) HR-TEM image, (g) HAADF STEM image, and EDS mapping images of (h) Mn K and (i) P K of as-synthesized MnP<sub>4</sub> nanoparticles.

**Figure. 5.3.2** XRD pattern for as-fabricated MnP<sub>4</sub>/G20 composite.

**Figure. 5.3.3** (a) SEM image, TEM images in (b) low magnification and (c) high magnification, (g) HAADF STEM image, and EDS mapping images of (e) Mn K, (f) P K, and (g) C K of as-synthesized MnP<sub>4</sub>/G20 nanocomposite.

**Figure. 5.3.4** (a) Galvanostatic discharge/charge voltage profiles, (b) corresponding differential capacity plots (DCPs), (c) *ex-situ* XRD patterns, and (d) X-ray absorption near-edge structure (XANES) spectra of MnP<sub>4</sub>/Li cell for fully discharged and charged states.

**Figure. 5.3.5** Cycle performance of MnP<sub>4</sub> and MnP<sub>4</sub>/G-20 electrodes for LIBs at current density of (a) 100 mA g<sup>-1</sup>, and (b) 2 A g<sup>-1</sup> with activation of each initial 3 cycles at 100 mA g<sup>-1</sup>, 500 mA g<sup>-1</sup>, and 1 A g<sup>-1</sup>. Galvanostatic discharge/charge voltage profiles of (c) MnP<sub>4</sub> and (d) MnP<sub>4</sub>/G20 electrodes for (b).

**Figure. 5.3.6** State-of-the-art high-rate capability of transition metal-based P-rich phosphides (TMP<sub>x</sub>, x > ~2) as anodes for LIBs.

**Figure. 5.3.7** (a) Galvanostatic discharge/charge voltage profiles, (b) corresponding DCPs, (c) *ex-situ* XRD patterns, and (d) XANES spectra of MnP<sub>4</sub>/Na cell for fully discharged and charged states.

**Figure. 5.3.8** (a) HAADF STEM image and EDS mapping images of Na K, Mn K, and P K, respectively, for fully sodiated  $\text{MnP}_4$  electrode (0.01 V vs.  $\text{Na}/\text{Na}^+$ ), and (b) TEM image of marked area in (a).

**Figure. 5.3.9** (a) Cycle performance of  $\text{MnP}_4$  and  $\text{MnP}_4/\text{G}$  electrodes for SIBs at current density of  $50 \text{ mA g}^{-1}$  and (b) rate capability. Galvanostatic discharge/charge voltage profiles of (c)  $\text{MnP}_4$  and (d)  $\text{MnP}_4/\text{G}20$  electrodes for each 10<sup>th</sup> cycle at various current densities for (b).

**Figure. 5.3.10** (a) Cycle performance of  $\text{MnP}_4$  and  $\text{MnP}_4/\text{G}$  electrodes for SIBs at current density of  $500 \text{ mA g}^{-1}$  with activation initial 3 cycles at  $50 \text{ mA g}^{-1}$ . (b) State-of-the-art electrochemical performance of P-rich phosphides ( $\text{TMP}_x$ ,  $x > \sim 2$ ) synthesized by a high energy milling as anodes for SIBs.

**Figure. 5.3.11** (a) Schematic image, SEM image, EDS mapping images of Cu K, Mn K, P K, and C K for cross section of  $\text{MnP}_4$  electrode before cycle. Cross sectional SEM image of  $\text{MnP}_4$  and  $\text{MnP}_4/\text{G}20$  electrodes of (b,d) before cycle and (c,e) after fully sodiated state (0.01 vs.  $\text{Na}/\text{Na}^+$ ) at  $50 \text{ mA g}^{-1}$ , respectively.

**Figure. 5.3.12** (a) SEM image of before cycle, and (b,f) SEM, (c,g) TEM, (d,h) HAADF STEM, and EDS mapping images of C K, Mn K, and P K for after 100 cycles at  $500 \text{ mA g}^{-1}$  for  $\text{MnP}_4$  and  $\text{MnP}_4/\text{G}20$  electrodes, respectively.

**Figure. 5.3.13** Nyquist plots of  $\text{MnP}$  and  $\text{MnP}_4/\text{G}20$  electrodes (a) before cycle and (b) after 100 cycles tested at current density of  $500 \text{ mA g}^{-1}$ .

**Figure. 5.3.14** XRD patterns for  $\text{MnP}_4$  and  $\text{Mn}_{1-x}\text{TM}_x\text{P}_4$  (TM = V and Fe,  $x=0.25$ ), respectively.

**Figure. 5.3.15** Crystal structures of triclinic (*P-1*)  $\text{MnP}_4$  and monoclinic (*C2/c*) of  $\text{FeP}_4$  and  $\text{VP}_4$  phases.

**Figure. 5.3.16** XRD pattern and refined results of (a)  $\text{Mn}_{0.75}\text{V}_{0.25}\text{P}_4$  and (b)

$\text{Mn}_{0.75}\text{Fe}_{0.25}\text{P}_4$  compounds, respectively. (c) XRD pattern of  $\text{Mn}_{1-x}\text{V}_x\text{P}_4$  ( $x=0.5$ ) with the reference peak for  $\text{VP}_2$ .

**Figure. 5.3.17** HAADF STEM image, EDS mapping images for Mn K, V K, and P K, EDS spectrum and detected composition table for as-synthesized  $\text{Mn}_{0.75}\text{TM}_{0.25}\text{P}_4$  (TM = (a) V and (b) Fe) compounds, respectively.

**Figure. 5.3.18** (a) Cycle performances of  $\text{Mn}_{1-x}\text{TM}_x\text{P}_4$  (TM = V and Fe,  $x = 0.0$  and  $0.25$ ) electrodes as anodes for LIBs tested at current density of  $100 \text{ mA g}^{-1}$ . Galvanostatic discharge/charge voltage profiles and corresponding DCPs for 1<sup>st</sup> and 2<sup>nd</sup> cycles for  $\text{Mn}_{1-x}\text{TM}_x\text{P}_4$  (TM = (b) V and (c) Fe,  $x = 0.25$ ) electrodes.

**Figure. 5.3.19** (a) Cycle performances of  $\text{Mn}_{1-x}\text{TM}_x\text{P}_4$  (TM = V and Fe,  $x = 0.0$  and  $0.25$ ) electrodes as anodes for LIBs at current density of  $1 \text{ A g}^{-1}$  with initial activation 5 cycles at  $100 \text{ mA g}^{-1}$ . (b) Galvanostatic discharge/charge voltage profiles for 5<sup>th</sup>, 6<sup>th</sup>, and 40<sup>th</sup> cycles for  $\text{Mn}_{1-x}\text{TM}_x\text{P}_4$  (TM = V and Fe,  $x = 0.0$  and  $0.25$ ) electrodes.

**Figure. 5.3.20** Rate capability of  $\text{Mn}_{1-x}\text{TM}_x\text{P}_4$  (TM = V and Fe,  $x = 0.0$  and  $0.25$ ) electrodes as anodes for SIBs at various current densities.

**Figure. 5.3.21** High rate cyclability of  $\text{Mn}_{1-x}\text{TM}_x\text{P}_4$  (TM = V and Fe,  $x = 0.0$  and  $0.25$ ) electrodes as anodes for SIBs at current density of  $500 \text{ mA g}^{-1}$  with initial activation 3 cycles at  $50 \text{ mA g}^{-1}$ .

**Figure. 5.3.22** Nyquist plots after 50 cycles (inset figure for pristine state) for  $\text{MnP}_4$  and  $\text{Mn}_{1-x}\text{TM}_x\text{P}_4$  (TM = V and Fe,  $x=0.25$ ) electrodes, respectively.

# Chapter 1. Introduction

## 1.1. Overview: Rechargeable Batteries for Energy Storage

Increasing global energy demand and the rapid depletion of conventional fossil fuels have encouraged intensive research into clean, abundant, and sustainable energy sources and more efficient energy storage systems. The solar energy, wave power, and wind energy, which we use as primary renewable energy, show many advantages in terms of environment-friendly, but most of them have disadvantages such as daily and seasonal intermittence and regional variability.[1.1] To compensate for the shortcomings of these primary energy resources, extensive efforts have been made to convert from renewable energy sources into ideal chemical energy. In addition to the above issue of eco-friendly energy conversion, the development of high-performance energy storage systems (ESSs) that store renewable energy in various forms for convenient use in our daily lives is also absolutely necessary to make the best use of these energy sources.

Electrochemical ESSs, especially rechargeable batteries, have been widely employed for decades as an energy source for various portable electronic devices (PEDs), promoting the thriving growth of electric vehicles (EVs), hybrid electric vehicles (HEVs), and grid-scale ESS. To satisfy the ever-increasing requirements of ESSs, significant improvements have been attained in the electrochemical performance of rechargeable batteries. Since the 19<sup>th</sup> century, many researches have

been conducted on rechargeable batteries, including lead-acid, nickel-cadmium, nickel-metal hydride, and lithium-ion batteries (LIBs) (Figure 1.1.1).[1.2-1.4]

Among various types of rechargeable batteries, LIB, which consists of the C/LiCoO<sub>2</sub> rocking-chair cell, was commercialized by Sony Corp. in June 1991 and has dominated the entire electronics market for more than 30 years and is still popular.[1.5] The success of LIB as an energy storage system was attributed to the fascinating features of Li-ion chemistry, for example, lithium (Li) is not only the most electropositive element (-3.04 V vs. standard hydrogen electrode) capable of operating high working potential, but also has a high theoretical capacity (~3862 mA h g<sup>-1</sup>) because it is the lightest metal (molar weight of 6.94 g mol<sup>-1</sup> and specific gravity of 0.534 g cm<sup>-3</sup>).[1.3] In addition, LIBs have additional advantages over other secondary batteries with no memory effect and less self-discharge.[1.6-1.8] Another attraction of LIB technology is its ability to cover a wide range of applications from PEDs (dozens of watt-hours) to EVs (dozens of kilowatt-hours) and grid-scale applications (tens of megawatt-hours) by using its design capabilities to meet autonomy and power requirements.[1.9] However, developing LIBs for the ever-increasing requirements of next generation energy storage application is a formidable challenge, especially in terms of a materials perspective. Typically, two strategies have been widely performed to increase of energy density of LIBs either by using high-voltage cathode materials or by developing high-capacity anode and cathode materials.

In case of cathode material for commercial LIBs, LiNi<sub>x</sub>Co<sub>y</sub>Mn<sub>1-x-y</sub>O<sub>2</sub> (NCM) and LiNi<sub>x</sub>Co<sub>y</sub>Al<sub>1-x-y</sub>O<sub>2</sub> (NCA) layered oxides have received great attention as the

most competitive candidates for practical utilization of LIBs due to their enhanced specific capacity, rate capability, cost effectiveness, and thermal stability.[1.10-1.12] NCM- and NCA-based cathodes show the combined merits of three metals in which nickel can offer high specific capacities by the  $\text{Ni}^{2+/3+/4+}$  redox-active couples, whereas Co, Mn, and Al can provide layered structures and enhanced structural integrity.[1.12] Presently, the Ni-rich cathodes with nickel content less than 60% have been successfully commercialized in LIBs. An increase of more than 60% of Ni content in NCM and NCA cathodes results in a high specific capacity of 200-220  $\text{mA h g}^{-1}$ , which represents a greater increase in energy density ( $\sim 800 \text{ W h kg}^{-1}$ ) as compared with conventional  $\text{LiCoO}_2$  ( $\sim 570 \text{ W h kg}^{-1}$ ) and  $\text{LiMn}_2\text{O}_4$  spinel ( $\sim 440 \text{ W h kg}^{-1}$ ) materials (Figure 1.1.2),[1.13] but capacity fading of cathodes is severe for various reasons related with structural instability and electrolyte decomposition upon cycling.[1.10,1.14,1.15] To overcome these challenges of nickel-rich NCM and NCA cathodes, many researches have been conducted to mitigate surface/interface degradation, including microstructure control of active materials, bulk and surface-graded doping with other elements, and surface coating strategies.

Apart from the cathode materials for LIBs, graphite is the most common anode material in commercial LIBs showing a theoretical capacity of  $372 \text{ mA h g}^{-1}$  with highly reversible cycle retention properties. However, limited reversible capacity and its poor rate capability hamper its widespread implementation in large scale energy storage applications. To replace the conventional graphite anode, extensive research studies have been performed on materials which react with Li-ion either by alloying reaction such as Si, Ge, and Sn (group 14 elements) or by insertion reaction such as  $\text{TiO}_2$  and  $\text{Li}_4\text{Ti}_5\text{O}_{12}$  (LTO) materials due to their high electrochemical

performance and cost effectiveness.[1.16-1.18]

The group 14 elements of Si, Ge, and Sn have high theoretical specific capacities as 3579 mA h g<sup>-1</sup>, 1600 mA h g<sup>-1</sup>, and 994 mA h g<sup>-1</sup>, respectively, by forming the Li-rich alloying compounds as Li<sub>4.4</sub>M (M = Si, Ge, and Sn) phase during lithiation process at a low lower working potentials of < 0.5 V vs. Li/Li<sup>+</sup>. [1.16] In this regard, the alloying reaction anodes are one of the promising candidates to apply high energy density application, but their extensive volume expansion, electrode pulverization, and aggregation of active materials during cycles hamper their widespread implementation in practical LIBs. On the other hand, insertion reaction type TiO<sub>2</sub> and LTO materials undergo negligible volume change during Li-ion insertion/extraction reactions, which ensures an extremely long cycling life. However, the high-rate capability of these materials is hampered by their low intrinsic electronic conductivity and moderate Li-ion diffusion coefficient. In addition, relatively high reaction potentials and limited Li-ion insertion sites (limited capacity) of TiO<sub>2</sub> and LTO materials derive relatively low energy density of these materials compared to that of other anode materials (Figure 1.1.3).[1.19]

To address these shortcomings of each reaction mechanism materials, a number of strategies have been presented such as (1) reducing particle size from micron to nanoscale to mitigate mechanical strain and improve lithium-ion diffusivity due to its short diffusion pathways; (2) forming nanostructure or hierarchical porous structure to serve a stable solid-electrolyte interface (SEI) layer and mesopore providing sufficient space for volume change upon cycling; (3) fabricating nanocomposite structure that contains high capacity alloying or conversion reaction

anodes and stable insertion reaction anodes such as conductive carbon-based materials and early transition metal (titanium and vanadium) oxides.[1.20-1.27] Fabricating nanocomposite structure between two materials with different electrochemical reaction mechanism has improved cycle retention properties with the structural integrity of electrode obtained by mitigating the volume expansion, pulverization, and agglomeration of alloying or conversion reaction anodes by providing buffer spaces with negligible volume change of insertion reaction material. However, this approach requires complex optimization of nano-fabrication process for nanocomposites consisting of homogeneously distributed each reaction anodes in nanoscale. In addition, each reaction anode in nanocomposite would react individually in nanoscale and their interaction and synergistic effect are limited to effectively mitigate the electrode degradation factors occurred in few nanoscales of each material. In this regard, a new strategy should be introduced to overcome the intrinsic shortcomings of each reaction materials for LIBs with a deep consideration of the relation between intrinsic physicochemical properties of materials and electrochemical reaction mechanism and performance.

In addition to the enormous effort to increase the energy density of the conventional LIBs, the research on sodium-ion batteries (SIBs) has been intensively conducted as one of the potential candidates for large-scale grid storage system as a post LIBs owing to the natural abundance and low cost of sodium-containing resources (Figure 1.1.4).[1.28-1.30] The battery components and energy storage mechanisms of SIBs are basically similar with those of LIBs, but many of the challenging issues caused by thermodynamics and kinetic aspects should be overcome. The size of the  $\text{Na}^+$ -ion ( $2.04 \text{ \AA}$ ) is larger than the  $\text{Li}^+$ -ion ( $1.52 \text{ \AA}$ ), which

affects the mass transport and storage during the electrochemical reaction, leads to sluggish kinetics of Na<sup>+</sup>-ion transport during cycling, and falls short in terms of energy density.[1.28]

The commercial graphite anode used in LIBs is electrochemically less active in Na cells, presumably due to the large ionic size of the Na-ion (2.04 Å) as compared with the channel size of the graphene layer (1.86 Å).[1.31] Recent research has demonstrated that graphite can be used as an electrode material for SIBs with a reversible capacity close to 150 mA h g<sup>-1</sup> by forming ternary graphite intercalation compounds through the reduction of graphite.[1.32] However, the reversible specific capacity of graphite for SIBs is still relatively lower than that used for LIBs. In addition, another promising anode silicon, which shows the highest theoretical capacity among LIB anodes with alloying reaction by forming the Li-rich alloy phase of Li<sub>15</sub>Si<sub>4</sub> (Theoretical capacity of 3590 mA h g<sup>-1</sup>), cannot form Na-rich alloy phase. According to the theoretical calculation, silicon can react with Na-ion as forming Na<sub>0.76</sub>Si phase (Theoretical capacity of 725 mA h g<sup>-1</sup>), and experimentally confirmed reversible capacity was only about 500 mA h g<sup>-1</sup> due to the reaction kinetic limit.[1.33-1.35] Some alloying reaction based anode materials such as Sn, Sb, and P are electrochemically active toward both LIBs and SIBs, but their volume changes during sodiation/desodiation are much larger than that of lithiation/delithiation because of the larger ionic radius of Na-ion.[1.36] Besides, the larger size of Na-ion can make its sluggish ionic diffusion during sodiation/desodiation process.

Therefore, the major scientific challenge for SIBs still resides in developing new anode materials with high capacity and a low redox potential with considering

the thermodynamic and kinetic issues. This requires in-depth study of the correlation between the physicochemical properties and electrochemical properties of SIB anodes to clarify the design factors for high performance SIB anodes.

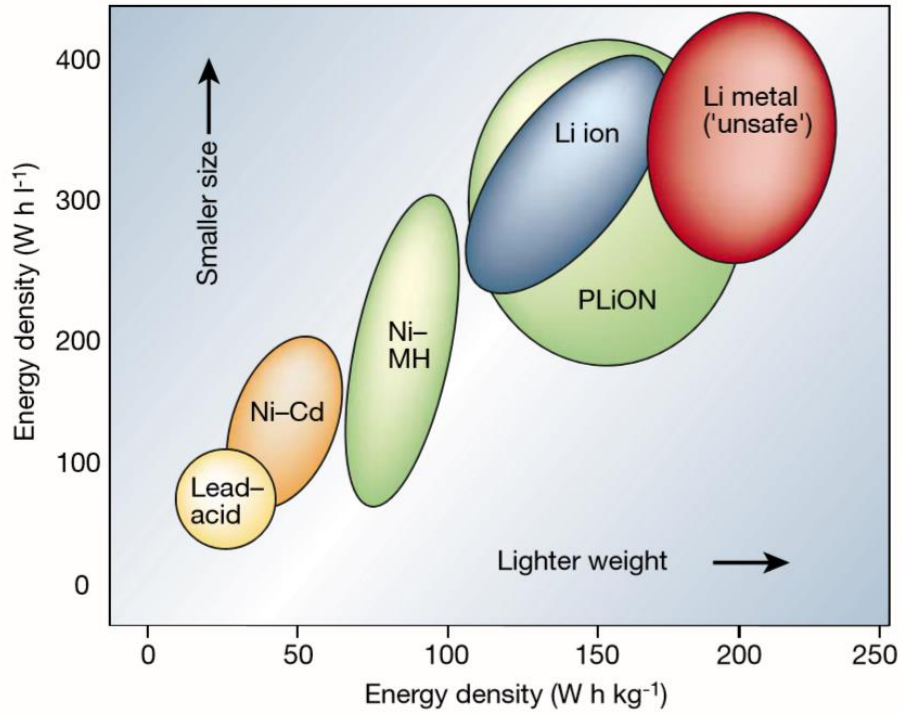


**Figure 1.1.1** Comparison of the different battery technologies in terms of volumetric and gravimetric energy density.[1.3]

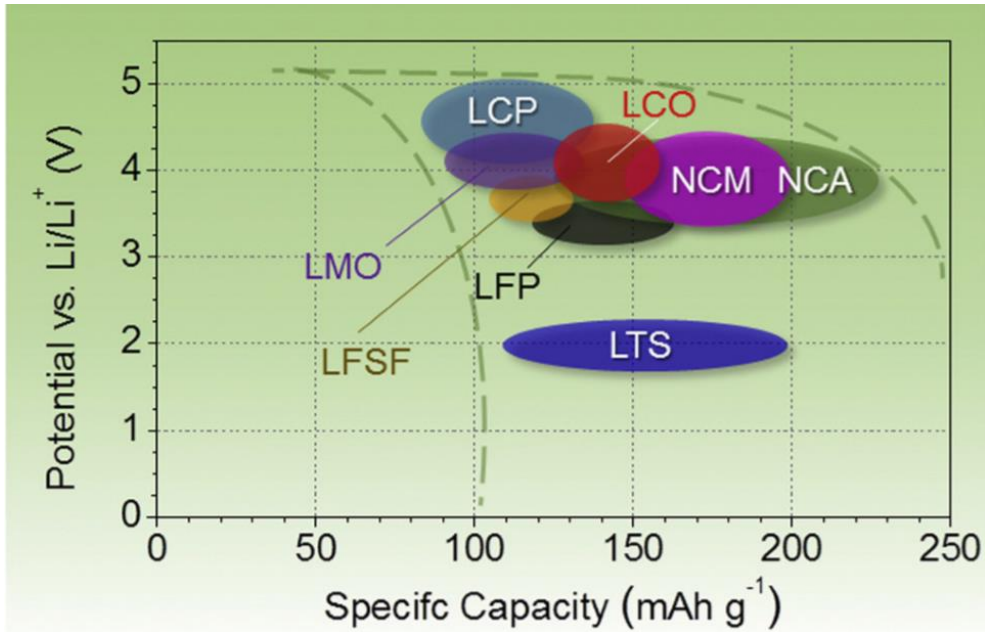


**Figure 1.1.2** Approximate range of average discharge potentials and specific capacity of some of the most common intercalation-type cathode materials for LIBs (experimental).[1.13]

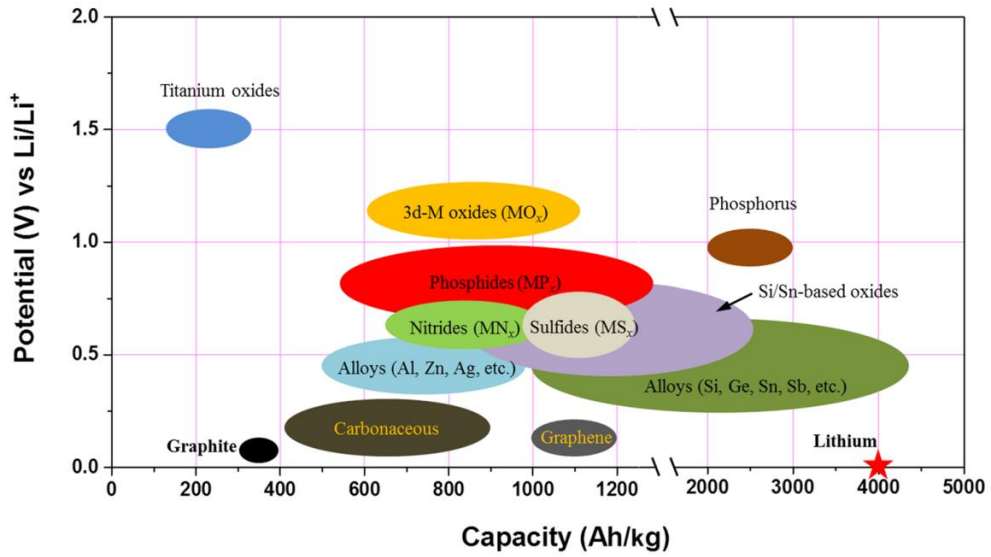


**Figure 1.1.3** Approximate range of reaction potentials and specific capacities of various electrochemical reaction-type anode materials for LIBs.[1.19]



## 1.2. Thesis Motivation and Scopes

The objective of this thesis is to develop the novel solid solution anode with hybrid electrochemical reaction for high performance secondary-ion battery. This new strategy to overcome intrinsic shortcomings of each electrochemical reaction mechanism is to find out the material systems to form a single compound with different types of electrochemical reaction mechanism anodes and to allow the simultaneous hybrid electrochemical reaction of two different mechanisms in a single phase. This could lead to the excellent synergistic effect due to their atomically homogeneous and finer distribution than that of physically mixed nanocomposite between two different materials. In addition, electrode performance can be tailored by varying the ratio of different reaction materials in solid solution compound.

To find out the novel solid solution anode showing hybrid electrochemical reaction, the monophosphides of 3d transition metals (Ti-Ni) were introduced as candidates for solid solution compound because they adopt the NiAs-type crystal structures and form the solid solutions with a high solubility limit,[1.37-1.39] but they exhibit the different types of electrochemical reaction (insertion, alloying, and conversion) depending on the nature of the metals.[1.40-1.45] In addition, metal phosphide group shows improved energy density compared with metal oxide group by lowering the Li-ion reaction potential and voltage hysteresis.

In chapter 2, the general background of LIBs and SIBs were introduced with different electrochemical reaction mechanism anodes such as intercalation/insertion, alloying, and conversion reaction type materials and conventional approach for high

performance anode with their literature review.

In chapter 3, complete solid solution compounds of  $Mn_{1-x}Fe_xP$  ( $0 \leq x \leq 1$ ) as a conversion/alloying hybrid electrochemical reaction anode was introduced for LIBs by using the iso-structural character of MnP and FeP compounds. The systematic studies on electrochemical properties of  $Mn_{1-x}Fe_xP$  ( $0 \leq x \leq 1$ ) compounds as anodes for LIBs were investigated, particularly focusing on the electrochemical reaction mechanism and the tunability of working voltage, specific capacity, and cycle performance and compared with those of MnP/FeP nanocomposite anode.

In chapter 4, solid solution compounds of  $Mn_{1-x}V_xP$  ( $x = 0.25$  and  $0.5$ ) as alloying/insertion hybrid electrochemical anodes were introduced to obtain the electrode performance with highly reversible cycle retention properties. The systematic studies on their structural relation and electrochemical performance were carried out and compared with those of MnP/VP nanocomposite anode.

In chapter 5, solid solution compound of  $Mn_{1-x}TM_xP_4$  ( $TM = V$  and  $Fe$ ) anode was introduced as a hybrid conversion reaction anode for SIBs. The electrochemical reaction mechanism and performance of  $MnP_4$  phase in SIB application were firstly investigated and enhanced electrochemical performance by forming the solid solution phase was examined.

### 1.3. Bibliography

- [1.1] H. Ibrahim, A. Ilinca and J. Perron, *Renew. Sustain. Energy Rev.*, **2008**, 12, 1221–1250.
- [1.2] Y. Ding, Z. P. Cano, A. Yu, J. Lu, Z. Chen, *Electrochem. Energy Rev.*, **2019**, 2, 1-28.
- [1.3] J.-M. Tarascon, M. Armand, *Nature*, **2001**, 414, 359-367.
- [1.4] M. A. Hannan, M. M. Hoque, A. Mohamed, A. Ayob, *Renew. Sustain. Energy Rev.*, **2017**, 69, 771-789.
- [1.5] T. Nagaura, K. Tozawa, *Prog. Batt. Solar Cells*, **1990**, 9, 209.
- [1.6] T. Sasaki, Y. Ukyo, P. Novak, *Nat. Mater.*, **2013**, 12, 569-575.
- [1.7] G. Nagasubramanian, D. Doughty, *J. Power Sources*, **2001**, 96, 29-32.
- [1.8] L. Lu, X. Han, J. Li, J. Hua, M. Ouyang, *J. Power Sources*, **2013**, 226, 272-288.
- [1.9] D. Larcher, J.-M. Tarascon, *Nat. Chem.*, **2014**, 7, 19-29.
- [1.10] L. Liang, W. Zhang, F. Zhao, D. K. Denis, F. U. Zaman, L. Hou, C. Yuan, *Adv. Mater. Inter.*, **2020**, 7, 1901749.
- [1.11] S. S. Zhang, *Energy Storage Materials*, **2020**, 24, 247-254.
- [1.12] J. Xu, F. Lin, M. M. Doeff, W. Tong, *J. Mater. Chem. A*, **2017**, 5, 874-901.
- [1.13] N. Nitta, F. Wu, J. T. Lee, G. Yushin, *Mater. Today*, **2015**, 18, 252-264.
- [1.14] T. Li, X.-Z. Yuan, L. Zhang, D. Song, K. Shi, C. Bock, *Electrochem. Energy*

*Rev.*, **2020**, 3, 43-80.

[1.15] J. Zheng, P. Yan, J. Zhang, M. H. Engelhard, Z. Zhu, B. J. Polzin, S. Trask, J. Xiao, C. Wang, J. Zhang, *Nano Res.*, **2017**, 10, 4221-4231.

[1.16] H. Tian, F. Xin, X. Wang, W. He, W. Han, *J. Materiomics*, **2015**, 1, 153-169.

[1.17] V. Aravindan, Y.-S. Lee, S. Madhavi, *Adv. Energy Mater.*, **2015**, 5, 1402225.

[1.18] N. Nitta, G. Yushin, *Part. Part. Syst. Charact.*, **2014**, 31, 317-336.

[1.19] J. Lu, Z. Chen, F. Pan, Y. Cui, K. Amine, *Electrochem. Energy Rev.*, **2018**, 1, 35-53.

[1.20] Y. Sun, N. Liu, Y. Cui, *Nat. Energy*, **2016**, 1, 16071.

[1.21] P. G. Bruce, B. Scrosati, J.-M. Tarascon, *Angew. Chem. Int. Ed.* **2008**, 47, 2930-2946.

[1.22] A. B. Yaroslavtsev, T. L. Kulova, A. M. Skundin, *Russ. Chem. Rev.*, **2015**, 84, 826-852.

[1.23] M. Ge, X. Fang, J. Rong, C. Zhou, *Nanotech.*, **2013**, 24, 422001.

[1.24] L. Hu, Q. Chen, *Nanoscale*, **2014**, 6, 1236-1257.

[1.25] P. Roy, S. K. Srivastava, *J. Mater. Chem. A*, **2015**, 3, 2454-2484.

[1.26] H. B. Wu, J. S. Chen, H. H. Hng, X. W. Lou, *Nanoscale*, **2012**, 4, 2526-2542.

[1.27] Y. Deng, C. Fang, G. Chen, *J. Power Sources*, **2016**, 304, 81-101.

[1.28] J.-Y. Hwang, S.-T. Myung, Y.-K. Sun, *Chem. Soc. Rev.*, **2017**, 46, 3529-3614.

- [1.29] H. Kang, Y. Liu, K. Cao, Y. Zhao, L. Jiao, Y. Wang, H. Yuan, *J. Mater. Chem. A*, **2015**, 3, 17899-17913.
- [1.30] T. Liu, Y. Zhang, Z. Jiang, X. Zeng, J. Ji, Z. Li, X. Gao, M. Sun, Z. Lin, M. Ling, J. Zheng, C. Liang, *Energy Environ. Sci.*, **2019**, 12, 1512-1533.
- [1.31] D. P. Divincenzo, E. J. Mele, *Phys. Rev. B: Condens. Matter Mater. Phys.*, **1985**, 32, 2538.
- [1.32] H. Kim, J. Hong, Y.-U. Park, J. Kim, I. Hwang, K. Kang, *Adv. Funct. Mater.*, **2015**, 25, 534-541.
- [1.33] S. C. Jung, D. S. Jung, J. W. Choi, Y. K. Han, *J. Phys. Chem. Lett.*, **2014**, 5, 1283-1288.
- [1.34] Y. Xu, E. Swaans, S. Basak, H. W. Zandbergen, D. M. Borsa, F. M. Mulder, *Adv. Energy Mater.*, **2016**, 6, 1501436.
- [1.35] C. H. Lim, T. Y. Huang, P. S. Shao, J. H. Chien, Y. T. Weng, H. F. Huang, B. J. Hwang, N. L. Wu, *Electrochim. Acta*, **2016**, 211, 265-272.
- [1.36] E. Edison, S. Sreejith, C. T. Lim, S. Madhavi, *Sustain. Energy & Fuels*, **2018**, 2, 2567-2582.
- [1.37] H. Fjellvag, A. Kjekshus, *J. Phys. Chem. Solids*, **1984**, 45, 709-718.
- [1.38] H. Fjellvag, A. Kjekshus, *Acta Chemi. Scan. A*, **1986**, 40, 8-16.
- [1.39] H. Fjellvag, A. Kjekshus, *Acta Chemi. Scan. A*, **1984**, 38, 703-710.
- [1.40] S.-G. Woo, J.-H. Jung, H. Kim, M. G. Kim, C. K. Lee, H.-J. Sohn, B. W. Cho,

*J. Electrochem. Soc.*, **2006**, 153, A1979-A1983.

[1.41] C.-M. Park, Y.-U. Kim, H.-J. Sohn, *Chem. Mater.*, **2009**, 21, 5566-5568.

[1.42] L. Li, Y. Peng, H. Yang, *Electrochim. Acta*, **2013**, 95, 230-236.

[1.43] K.-H. Kim, W.-S. Kim, S.-H. Hong, *Nanoscale*, **2019**, 11, 13494-13501.

[1.44] F. Han, C. Zhang, J. Yang, G. Ma, K. He, X. Li, *J. Mater. Chem. A*, **2016**, 4, 12781-12789.

[1.45] D. Yang, J. Zhu, X. Rui, H. Tan, R. Cai, H. E. Hoster, D. Y. W. Yu, H. H. Hng, Q. Yan, *ACS Appl. Mater. Interfaces*, **2013**, 5, 1093-1099.

## Chapter 2. Background and Literature Review

### 2.1. Li-ion and Na-ion Batteries

Lithium-ion and Na-ion batteries are most promising rechargeable energy storage devices that convert chemical energy into electrical energy through the charge storage at the electrodes. These rechargeable batteries consist of four main components such as a positive electrode (cathode material), a negative electrode (anode material), electrolyte, and separator (Figure 2.1.1).[2.1] The definition of anode (or negative electrode) is the electrode in which oxidation reaction occurs during the discharge cycle; the other electrode is the cathode (or positive electrode) (Figure 2.1.2).[2.2] The theoretical voltage of the cell is defined in the electrochemical potential difference of cathode and anode materials. When charging the cell, the positive electrode becomes the anode and the negative electrode becomes the cathode. The two electrodes, cathode and anode are separated by a porous electrically insulated membrane, which prevents short circuits between the two electrodes, and the exchange of alkaline metal (AM) ions (Li- or Na-ion) occurs between the two electrodes by electrolytes during discharging and charging reactions under ionically conducted but electronically insulated conditions. The common electrolyte used in LIBs is a non-aqueous electrolyte consisting of lithium hexafluorophosphate ( $\text{LiPF}_6$ ) dissolved in organic solvents, typically ethylene carbonate (EC) or dimethyl carbonate (DMC).[2.3]

The essential parameters for evaluating battery performance include charge storage capacity, cycle retention, cell voltage, power density, and energy density. The capacity of battery is typically determined by the ability of the electrode material to accommodate alkaline metal ions. Capacity is typically used in specific capacity, areal capacity, and volumetric capacity depending on the application with units of mA h g<sup>-1</sup>, mA h cm<sup>-2</sup>, and mA h cm<sup>-3</sup>, respectively. The theoretical specific capacity of active materials can be calculated by Faraday's law:  $Q_{theoretical} = (nF)/M_w$  in an unit of mA h g<sup>-1</sup>, where  $n$  is the number of electrons per mole involved in the oxidation or reduction of active material,  $F$  is the Faraday constant and  $M_w$  is the molecular weight of the active material used in the electrode.[2.4] This equation indicates that when we design high-capacity electrode materials for battery, it is important to find materials that are light in weight but can react with many alkaline metal ions. By using this equation, the theoretical areal and volumetric capacities can be also calculated by converting the molecular weight of active materials in the equation to the area or volume of active materials.

An important parameter related to the capacity storage is the capacity retention, which indicates how well the battery can maintain its accumulated energy during cycling. The coulombic efficiency (CE) is the ratio of the total charge injected into the battery to the total charge extracted from the battery, indicating the charge efficiency of electrons transferred to the battery. Since alkaline metals in cathode materials are transferred to and stored in anode materials when charging the battery, and then returned to cathode materials when discharging the battery, the high cycle retention property of the cell requires a high CE of each discharge/charge reaction that occurs in both cathode and anode materials.

The theoretical cell voltage of battery is determined by the electrochemical potential difference between cathode and anode. In order to maintain electrical neutrality, the injection and ejection of ions and electrons from electrodes are occurred with the difference in chemical potentials as the driving force of the conversion from chemical energy to electrical energy, which can be deduced from the relative Gibbs free energy of reactants and products. The maximum electrical work generated by the reaction in the cell under isothermal-isobaric process is equal to non-volume work generated by the change of the reaction system, namely the change of molar Gibbs free energy ( $\Delta_r G$ ).[2.5]



This Gibbs free energy change of pure chemical reaction of reactants A and B is the same as in the case of electrochemical reactions in which electrons and ions are transported across the cell. As these reactants A and B are electrically charged, the electrostatic energy transported across by a mole of such species is given by  $zFE$ , where  $z$  is the charge number of the transporting species,  $F$  is Faraday's constant, and  $E$  is the cell voltage. The cell voltage is determined to the Gibbs free energy change by,  $\Delta_r G = -zFE$  under open circuit conditions.[2.3]

After obtaining the capacity and cell voltage of the electrode, the energy density and power density of the cell can be calculated. The physical meaning of energy density is the amount of energy that can be stored in a given mass or volume of cells, and in the automotive industry generally means that how far an electric car can go on a single charge. The energy density of the cell can be calculated by multiplying

voltage and capacity of the cell in units of  $\text{W h kg}^{-1}$  (specific energy density) and  $\text{W h L}^{-1}$  (volumetric energy density), respectively. On the other hand, power density describes how quickly the cell can deliver energy in a given mass or volume. In the automotive industry, power density means how fast the same car can go. The power density of the cell can be obtained from the product between the capacity and the current and expressed in units of  $\text{W kg}^{-1}$  (specific power density) and  $\text{W L}^{-1}$  (volumetric power density), respectively. These two quantities of energy and power densities are typically plotted together in the so called Ragone plot (Figure 2.1.3).[2.6]

Due to its contribution to energy density, the voltage of the cell is one of the important parameters that determines battery performance. In a full cell application, a lower anode potential vs.  $\text{AM/AM}^+$  ( $\text{AM} = \text{Li}$  or  $\text{Na}$ ) and a higher cathode potential vs.  $\text{AM/AM}^+$  result in a high full cell voltage, and hence a higher energy density. In order to design secondary-ion batteries with high energy density, it is necessary to develop anode material that has large capacity and moderately low reaction voltage. It is also important to develop anode materials suitable for high rate capability, as demand for EVs applications has recently emphasized the importance of high power density needed for rapid charging abilities.[2.7]

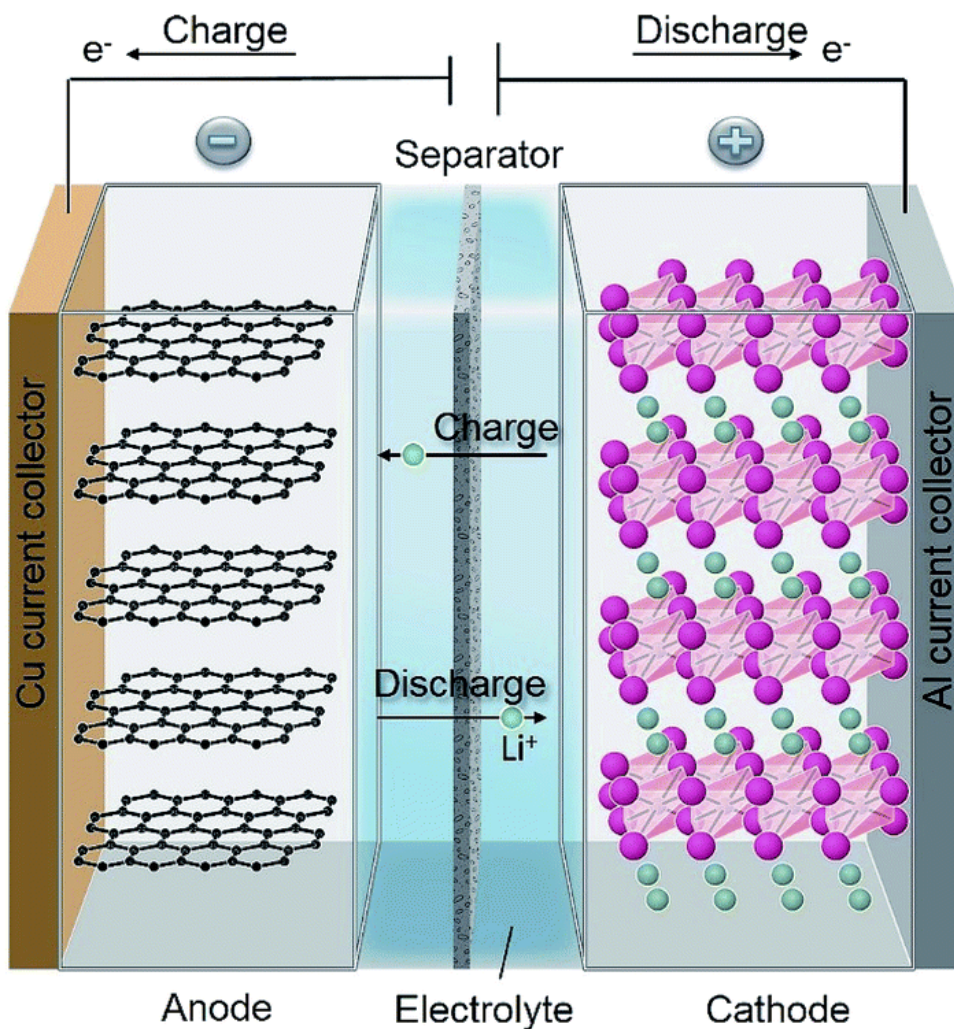


**Figure 2.1.1** Schematic illustration of a lithium ion battery showing charge/discharge processes.[2.1]

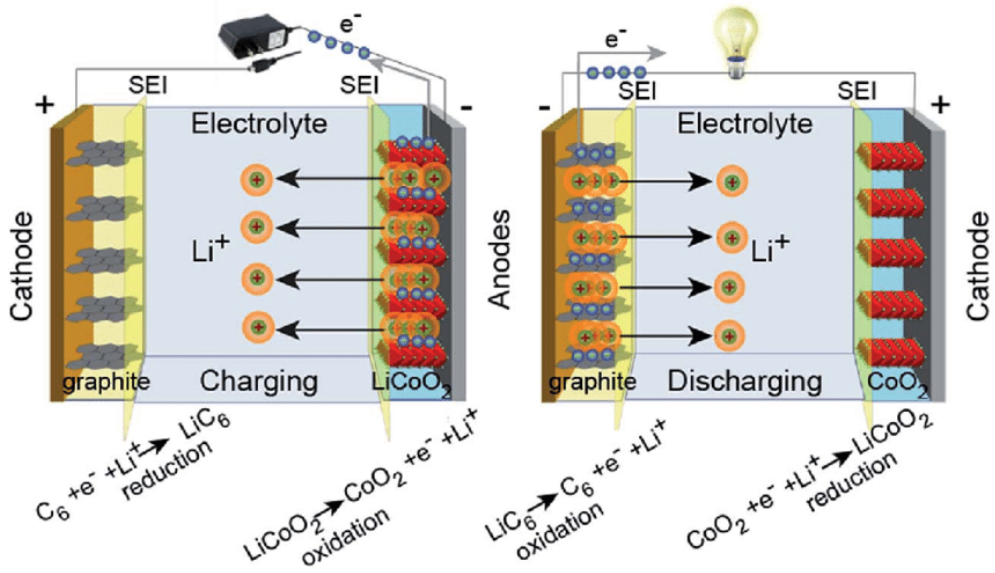


**Figure 2.1.2** Charge-discharge process of a lithium-ion cell using graphite and  $\text{LiCoO}_2$  electrodes.[2.2]

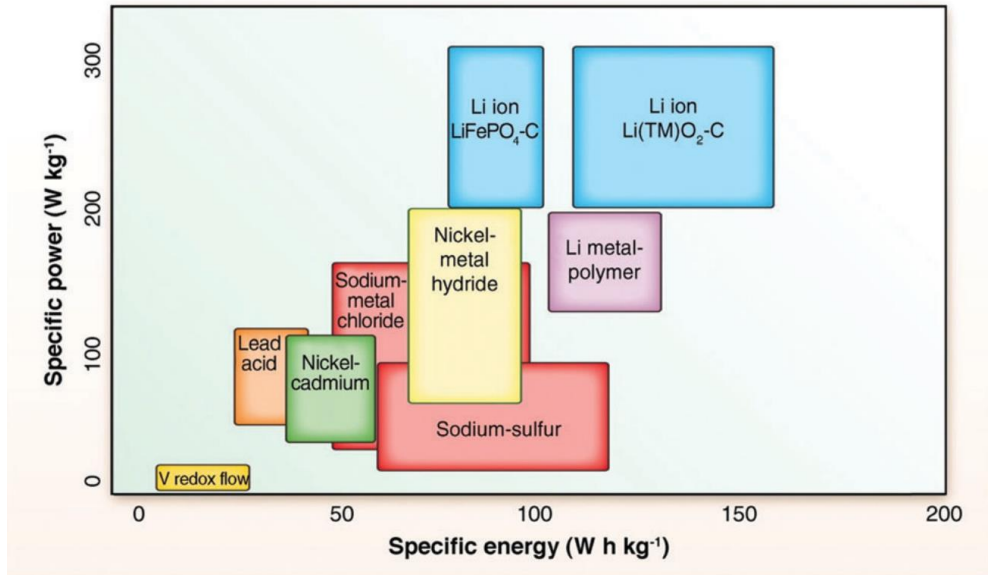


**Figure 2.1.3** Ragone diagram of specific energy versus specific power for major rechargeable battery systems.[2.6]

## 2.2. Electrochemical Reaction Mechanism for Anode Materials

The charge carriers in LIBs and SIBs are Li-ion and Na-ion, respectively, which react with active materials through three different electrochemical reaction mechanisms: (i) intercalation/insertion, (ii) alloying, and (iii) conversion reactions (Figure 2.2.1).[2.8]

The intercalation/insertion reaction materials accompany the insertion of Li-ions (or, e.g., Na-ion) into interstitial sites of active materials and capture electrons through the subsequent process ( $\text{Li}^+ + \text{e}^- + \text{MX} \leftrightarrow \text{LiMX}$ , where M and X are cation and anion, respectively, and MX and LiMX are typically isostructural) (Figure 2.2.2).[2.9] This reversible insertion/extraction of Li-ion occurred without significant phase transformation, and stable crystal structure of these materials can be retained during long-term cycling. However, the limited interstitial sites of these materials limit their reversible capacities to less than  $400 \text{ mA h g}^{-1}$ .

The alloying reaction elements or compounds typically form the alkaline metal-rich compounds during lithiation process and dealloying reaction occurs during delithiation process ( $y\text{Li}^+ + y\text{e}^- + \text{MX} \leftrightarrow \text{Li}_y\text{MX}$ , where MX and  $\text{Li}_y\text{MX}$  are not isostructural) (Figure 2.2.3).[2.9] Since the alloying reaction accompanies multiple charge carriers and electrons during electrochemical reaction, their theoretical capacity is relatively higher ( $1000 \sim 4200 \text{ mA h g}^{-1}$ ) than that of other reaction-type materials. However, their considerable large volume changes upon cycling cause serious degradation of cycle life for practical application.

The conversion reaction compounds convert to nanocomposite morphology

consisting of metal nanoclusters (~1-10 nm size) dispersed in  $\text{Li}_y\text{X}$  amorphous matrix upon lithiation and then reversibly return to their initial state upon delithiation ( $y\text{Li}^+ + ye^- + \text{MX} \leftrightarrow \text{M} + \text{Li}_y\text{X}$ ) (Figure 2.2.4).[2.10] The conversion reaction compounds commonly exhibit the multiple  $e^-$  reaction per M with high specific capacities ( $500 \sim 2000 \text{ mA h g}^{-1}$ ). However, their substantial volume variation, large voltage hysteresis, and poor reaction kinetics still limit them for next generation secondary-ion battery applications.

### **2.2.1. Intercalation/Insertion Reaction Type Anode**

Intercalation/Insertion reaction is primarily used in commercial electrode materials, including layered transition metal oxide cathodes and graphite anodes. In addition, various types of insertion reaction materials have been investigated as an anode for LIBs and SIBs including carbon allotropes, early transition metal (Ti and V) compounds, orthorhombic  $\text{Nb}_2\text{O}_5$ , and etc.[2.11-2.13] These materials can provide fast Li- and Na-ion reaction kinetics (with ion conductive 1D path or 2D plane in their crystal structure), and can retain structural integrity during cycles due to a robust open framework with less volume change, which is desirable for high-rate capability and cyclability of LIBs and SIBs. However, most intercalation/insertion reaction materials have a relatively low theoretical capacity (typically store one  $e^-$  per metal ion) due to the limited accommodation sites in their crystal structure.

Intercalation/Insertion reaction type anode materials have been mainly studied

on early transition metal compounds (Ti and V), since their strong M (metal)-X (anion) bond character is appropriate for maintaining their crystal structure during reversible alkaline metal-ion insertion and extraction. Titanium-based compounds, especially polymorphs of titanium dioxides ( $\text{TiO}_2$ ) and spinel structure of lithium titanium oxide ( $\text{Li}_4\text{Ti}_5\text{O}_{12}$ ), have been widely introduced as potential anodes for both LIBs and SIBs because of their excellent cycling stability, high discharge voltage plateau, and low economic cost.[2.14, 2.15] Several polymorphs of  $\text{TiO}_2$  such as anatase,  $\text{TiO}_2(\text{B})$ , brookite, and rutile structures have been extensively explored as intercalation-based materials .[2.16] Among them, anatase phase of  $\text{TiO}_2$  has been intensively studied as an anode for both LIBs and SIBs, which can only accommodate  $0.5 \text{ Li}^+/\text{Na}^+$  per  $\text{TiO}_2$  formula unit, delivering a reversible capacity of  $167.5 \text{ mA h g}^{-1}$  in a potential of  $\sim 1.6 \text{ V vs. Li/Li}^+$ .[2.17-2.19] A monoclinic structure of  $\text{TiO}_2(\text{B})$  with a space group of  $C/2m$  contains corrugated sheets of edge-and corner-sharing  $\text{TiO}_6$  polygons.[2.20] This monoclinic  $\text{TiO}_2(\text{B})$  can accommodate the volume change during Li-ion insertion/extraction without lattice deformation due to its 1D infinite channels.[2.21] The thermodynamically most stable phase of rutile  $\text{TiO}_2$  allows negligible amounts of Li-ion insertion ( $0.1 \text{ Li-ion per Ti atom}$ ) at room temperature owing to its Li-ion diffusion path, which is thermodynamically favorable only along the  $c$ -axis channels instead of the  $ab$ -planes.[2.22, 2.23] Another titanium-based promising anode material is the spinel structure of lithium titanium oxide ( $\text{Li}_4\text{Ti}_5\text{O}_{12}$ ) as “zero-strain structure” with its negligible volume variation of 0.2-0.3%, a flat reaction plateau ( $\sim 1.55 \text{ V vs. Li/Li}^+$ ), and cycling stability. This anode shows a theoretical capacity of  $175 \text{ mA h g}^{-1}$  by inserting 3 Li-ions to form  $\text{Li}_7\text{Ti}_5\text{O}_{12}$ .[2.24]

Another early transition metal oxide, vanadium oxide, also has been introduced as an attractive anode for secondary-ion battery due to its high specific capacity resulting from the multiple oxidation states of vanadium, ease of synthesis, and low cost. In particular, monoclinic structure of VO<sub>2</sub>(B) phase has been attracted as a promising anode due to its unique bilayer structure formed by edge-sharing VO<sub>6</sub> octahedra with tunnels for fast ionic diffusion, superior electronic conductivity, and higher capacity than other vanadium dioxide structures.[2.25-2.29] Thus, various nanostructured VO<sub>2</sub>(B) have been intensively investigated as high performance anode material for LIBs, and are now gradually being transferred to the application in SIBs.[2.30, 2.31]

Among the several polymorphs of niobium oxide (Nb<sub>2</sub>O<sub>5</sub>), the orthorhombic crystal structure with a space group of *Pbam* has been intensively studied as an attractive anode due to its rapid intercalation-pseudocapacitance behavior, since the most empty octahedral sites between (001) planes provide a 2-dimensional intercalation pathway and a negligible structural change during Li-ion intercalation/deintercalation.[2.32, 2.33]

The suggested transition metal oxide-based insertion reaction anodes exhibit a relatively lower specific capacity and a higher reaction potential (> 1.5 V vs. Li/Li<sup>+</sup>) than graphite anodes resulting in lower energy density. Typically, transition metal phosphide-based anode material exhibits a relatively lower Li-ion reaction potential compared to that of transition metal oxide because of their high covalent character between metal and phosphorus bond.[2.34] In common is the fact that the high-lying mixed anion-metal bands and a high degree of electron delocalization lead to a low

formal oxidation state of the metal, and a strong covalent character of the metal-pnictogen bond (Figure 2.2.5).[2.35-2.37] There are two insertion reaction type anode materials for LIBs have been reported in metal monophosphides as vanadium monophosphide (VP)[2.38] and molybdenum monophosphide (MoP)[2.39]. These two materials (VP and MoP) have similar hexagonal crystal structure with space groups of  $P6_3/mmc$  and  $P-62m$ , respectively, which crystal structures are suitable for accommodating Li-ion in their prismatic sites. Previous study of these materials indicated that highly reversible Li-ion insertion/extraction occurred with a relatively lower reaction potential compared to that of metal oxide, thus exhibiting high energy density of phosphide-based materials.

### **2.2.2. Alloying Reaction Type Anode**

Alloying reaction type anode is a typical candidate for high-power LIB and SIB applications by delivering high volumetric and gravimetric energy densities based on reactions with multiple Li- or Na-ions at low potentials. In addition, alloying reaction anodes are essentially mixed electronic-ionic conductors of both  $\text{Li}^+$ -ions and electrons, which are desirable for reversible electrochemical reaction. Previously reported alloying reaction anodes for LIBs and SIBs are group 14 and 15 elements, including metals (Sn, Pb, and Bi), metalloids (Si, Ge, As, and Sb), polyatomic non-metal (P), and other binary compound (Ti-P, V-P, Mn-P, and Si-O) materials.[2.40-2.46] Those materials are known to form binary or ternary compounds with multiple Li- or Na-ions. Silicon (Si) anode material has the highest theoretical capacity in

LIBs around  $4000 \text{ mA h g}^{-1}$ , and volumetric energy densities in the range  $700\text{--}972 \text{ W h L}^{-1}$ , which are 1.5-1.8 times higher than those of commercial cells.[2.47, 2.48] However, Si anode is suffered from severe volume variation about 400% upon cycling, which can result in rapid electrode structure degradation and capacity fading. In this regard, the main degradation factor of alloying reaction anode is caused by large volume change during cycling, which can lead delamination, pulverization, and aggregation of alloying reaction elements.

Not as well as the group 14 & 15 elements, there is another type of alloying reaction compounds, which can react with Li-ion to form lithium alloying phases. The typical example of another alloying reaction type anode includes binary and ternary compounds such as early and middle of transition metal phosphides (MnP,  $\text{V}_4\text{P}_7$ ,  $\text{VP}_2$ ,  $\text{TiP}_2$ , and  $\text{TiP}_4$ ), silicon oxide ( $\text{SiO}_x$ ), and silicon oxycarbide ( $\text{SiOC}$ ).[2.40-2.46] This type of compound can react with a large number of Li-ions as alloying reaction by accompanying phase transformation or amorphization, however, the conversion reaction was not occurred even at lower potential about 0.01 V vs.  $\text{Li/Li}^+$ . The lithium storage mechanism of these materials, known as alloying reactions, is complicated, and some of them are still controversial because they transformed to an amorphous state when lithiated, making it difficult to identify the phase. Similar to the alloying reaction type of group 14 & 15 elements, these compounds are also suffered from the severe capacity fading derived from the large volume change and agglomeration of active materials during discharge/charge reactions.

### 2.2.3. Conversion Reaction Type Anode

In 2000s, Tarascon et al. first reported a new Li-ion storage mechanism anode of later transition metal (Fe, Co, Ni, and Cu) oxides that shows conversion reaction as follows:  $TM_aX_b + (b \cdot n) AM \leftrightarrow aTM + bAM_nX$ , where TM is a transition metal, AM is an alkaline metal (e.g., Li, Na), X is an anion (such as H, N, P, O, S, Se, and F), and n is the formal oxidation state of X.[2.49]

Figure 2.2.4 is a schematic illustration of the local chemistry transformation of metal compounds ( $M_aX_b$ ) during conversion reaction for LIB anodes.[2.10] From the above equation for conversion reaction, Li-ions can react with anions through a conversion reaction, causing a reconstructive structure change and amorphization of  $M_aX_b$ . Through this lithiation process,  $M_aX_b$  are being transformed by conversion reaction into an interconnected nanocomposite morphology consisting of metal nanoclusters embedded in lithiated compounds ( $Li_nX$ ). This metallic nano-networks can serve as electronic conduction pathways throughout the initial primary particle, thus ensuring the reversible reaction forming a quasi-amorphous/nano-crystalline  $Li_nX$ . As a result, the diffusion of metal cation is the critical factor determining the size of metal nanocluster, and thus, a continuous electron-conductive network is formed. During delithiation, these metallic nanoclusters are oxidized to form metal compound in amorphous state.

Previously, various kinds of conversion reaction materials have been investigated including oxides, sulfides, nitrides, phosphides, and fluorides for both LIBs and SIBs. Those compounds show much higher theoretical capacity than

commercial graphite anode ( $372 \text{ mA h g}^{-1}$ ), and some can exceed  $2000 \text{ mA h g}^{-1}$ . Despite the high theoretical capacity, electrochemical properties of conversion reaction type compounds should be further improved to overcome other unsatisfactory drawbacks including voltage hysteresis. A voltage gap between the lithiation and delithiation profiles is originated from the substantial structural rearrangement during conversion reaction and this leads internal heat evolution and a low energy efficiency.[2.50] This voltage hysteresis is highly dependent on the nature of the anionic species, followed by fluorides > oxides > sulfides > nitrides > phosphides.[2.50, 2.51] In addition, there are other shortcomings to improve such as large volume changes during cycling, a low initial Coulombic efficiency (ICE), and capacity activation at high current density.

Capacity activation behavior is an example of poor rate capability of conversion reaction anodes in which reversible capacity is not fully delivered in initial cycles at high current density and is gradually increased with activation behavior in subsequent cycles. This capacity activation behavior of conversion reaction anodes has not been addressed in the past, but it is emerged as an important issue in fast charging performance for future battery application. The Li-ion diffusion is very fast along the particle surface and/or along the interface between metal nanoclusters and  $\text{Li}_n\text{X}$  matrix, while its penetration into the bulk particle is relatively much slower in the first lithiation due to its layer-by-layer propagation reaction, which can cause a heterogeneous reaction in larger particles. Previous study on capacity activation issue of iron oxide nanoparticles showed that despite the relatively slow bulk penetration of Li-ion in initial cycles, there is no significant capacity loss at a particle size of about 10 nm at discharge rate of 20 C.[2.52, 2.53] However, since the

complete conversion reaction of  $M_aX_b$  at high current density may not be allowed according to the nature of component metal cation and anion, and different stoichiometric composition ratio of  $M_aX_b$ , it still remains as an intrinsic shortcomings of conversion reaction anodes. To address these shortcomings of conversion reaction anodes, various nanostructured metal compounds have been investigated as high performance anodes.[2.54, 2.55]

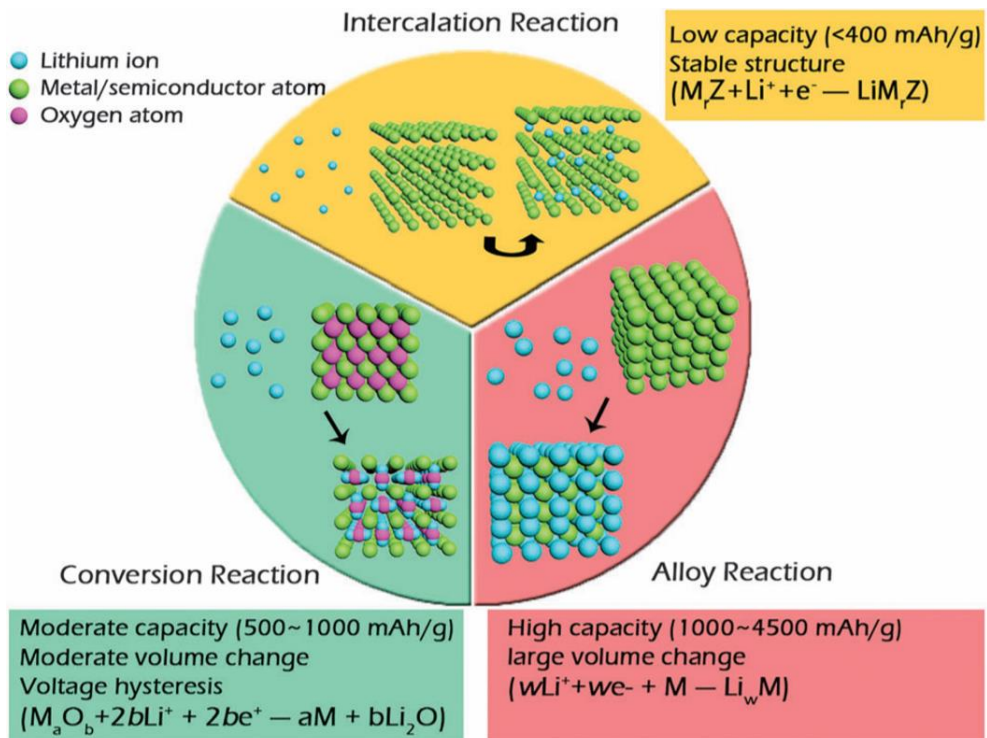


**Figure 2.2.1** Schematic representation of three typical reaction mechanisms between Li-ion and electrode materials.[2.8]

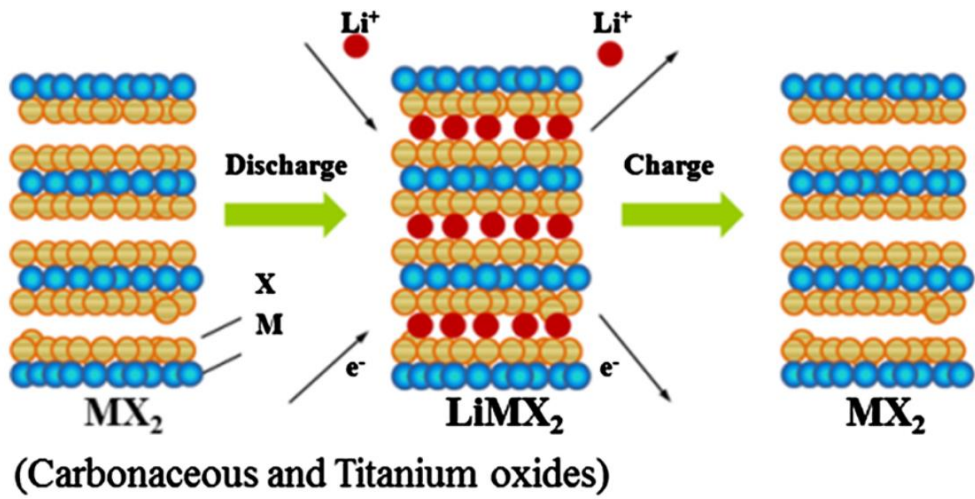
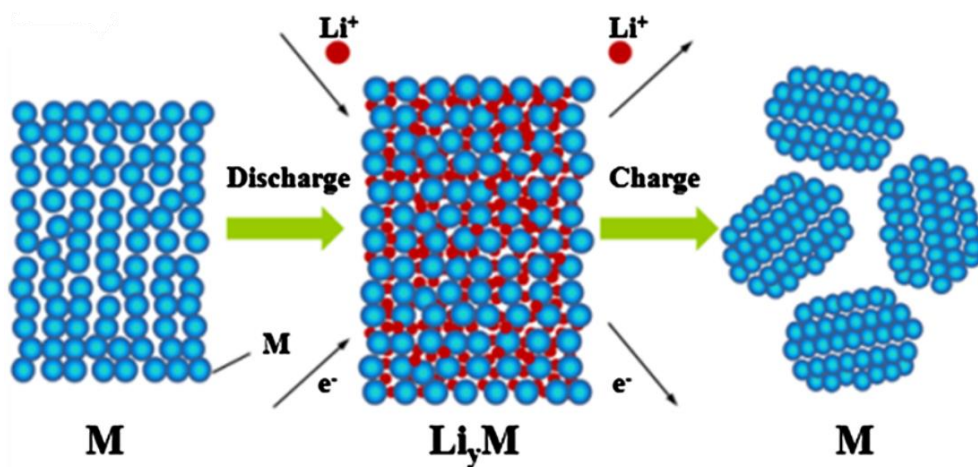


**Figure 2.2.2** Schematic illustration of reversible electrochemical insertion/extraction reaction of  $\text{MX}_2$  anode materials.[2,9]



(M = Si, Ge, Sn, Sb, etc., and Si/Sn-based oxides)

**Figure 2.2.3** Schematic illustration of reversible electrochemical alloying/dealloying reaction of elemental M anode materials.[2.9]

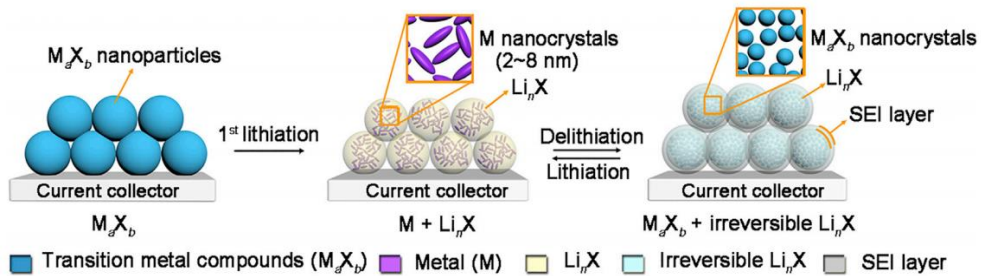


**Figure 2.2.4** Schematic illustration of the local chemistry transformation of transition-metal compounds during the conversion reaction.[2.10]

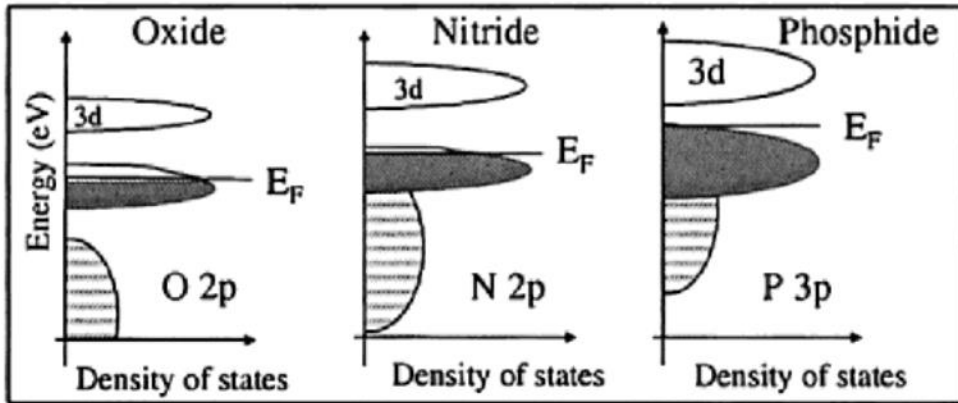


**Figure 2.2.5** Comparison of density of states (DOS) for oxides, nitrides, and phosphides.[2.35]

### **2.3. Conventional Approach for High Performance Anode**

To meet the electrochemical performance demands for next-generation secondary-ion batteries, alloying and conversion reaction anodes are of great significance due to their high theoretical capacity, moderate reaction voltage, and the diversity of candidates with various chemical compositions. However, many shortcomings, including particle pulverization and aggregation, mainly caused by severe volume change during cycling, need to be addressed before they are widely implemented in practical applications. In this regard, great attempts have been made to find efficient strategies to overcome these issues (Figure 2.3.1).[2.50] Since the solid-state charge diffusion accompanied by electrochemical reactions in batteries is the kinetically limited stage, high performance requires a nano-sizing approach to reduce ion/electron diffusion length as well as the rational design of an anode material with high ion/electron diffusion constants in its bulk or surface. In addition to the fabricating nanostructure morphology, hybrid nanocomposite fabrication with different electrochemical reaction mechanism materials, and introduction of ternary compound as conversion/alloying materials (CAMs) can additionally increase the ionic and electronic conductivity of anode materials in the bulk and the surface, respectively.

### **2.3.1. Nanostructured Material and Nanocomposite with Different Electrochemical Reaction Materials**

The development of nanotechnology has led to a paradigm shift in material design and provided a new path to high performance secondary-ion battery anodes.[2.56] Nano-sizing of electrode materials has been widely conducted on various nanostructured materials from 0-dimensional (0D) to 3-dimensional structures (3D) (e.g. 0D for nanoparticles, 1D for nanowires and nanotubes, 2D for nanosheets and films, and 3D for porous hollow structures) to give a short diffusion lengths and a high electrochemical active surface area.[2.57-2.63]

Beyond nano-structural engineering, hybrid nanocomposite fabrication with different electrochemical reaction materials is another effective route for improving electrochemical performance of high capacity materials. In particular, in case of alloying reaction- and conversion reaction-type materials accompanied by large volume changes and structural deformation during cycling due to their high theoretical capacity, fabricating nanocomposite strategy such as carbon nano-coating and embedding in carbonaceous matrix has been proposed. The high elasticity of carbon layers can effectively relieve the volumetric change of active materials upon cycling.[2.64] In addition, uniform nano-carbon layer on active materials can act as a physical barrier to prevent agglomeration of active materials and direct contact between active materials and electrolytes. This can retain a stable solid-electrolyte interface (SEI) layer to suppress the increase in electrochemical resistance during cycling.[2.65] In general, conformal carbon nano-coating is achieved through a

chemical coating process of a polymer layer by using glucose or sucrose as a carbon source, and a subsequent carbonization process under an inert gas atmosphere.[2.59]

Recently, various nano-coating strategies have been proposed with some other organic monomers to generate carbon layers.[2.55] Dopamine hydrochloride has been reported as a fascinating carbon precursor to form a polydopamine (PDA) layer, which is known to be a biomimetic adhesive polymer, that can self-polymerize to form the conformal coatings on various substrates and can be converted into nitrogen-doped graphitic carbon through carbonization.[2.66-2.68] As an example, alloying reaction type transition metal phosphide,  $V_4P_7$  nanoparticles were encapsulated with the conformal carbon layer with a thickness of 30 nm, which is achieved through polymerization of dopamine and subsequent carbonization. As-fabricated  $V_4P_7@C$  nanocomposite showed improved electrochemical properties, which is attributed to high electrical conductivity, high Li-ion mobility, and structural stability to restrict the aggregation and pulverization of active materials.

Graphene is another promising conductive material with a carbon monolayer packed into a 2D honeycomb lattice, which shows outstanding properties, such as excellent electron conductivity, high mechanical flexibility, large surface area, and chemical stability. For these reasons, a large number of publications have discussed application of graphene in LIBs and SIBs in recent years.[2.69-2.72]

Another heterogeneous hybrid nanocomposite structure has been introduced with other materials group as by mixing or coating insertion reaction anode materials, which is mainly carbonaceous material and early transition metal (titanium and vanadium) oxide, with alloying or conversion reaction anode materials (Figure

2.3.2).[2.73] This approach has improved cycle retention properties with the structural integrity of electrode obtained by mitigating the volume expansion, pulverization, and agglomeration of alloying or conversion reaction anodes by providing buffer spaces with negligible volume change of insertion reaction material. The typical example of these nanocomposites are  $\text{TiO}_2/\text{Co}_3\text{O}_4$  porous nanoparticles,  $\text{TiO}_2/\text{SnO}_2$  mesoporous bead,  $\text{TiO}_2/\text{MoS}_2$  nanowires,  $\text{TiO}_2@\text{Fe}_2\text{O}_3$  nanotube materials, which nanocomposite was composed with stable insertion reaction of  $\text{TiO}_2$  and high capacity alloying or conversion reaction materials.[2.74-2.77]

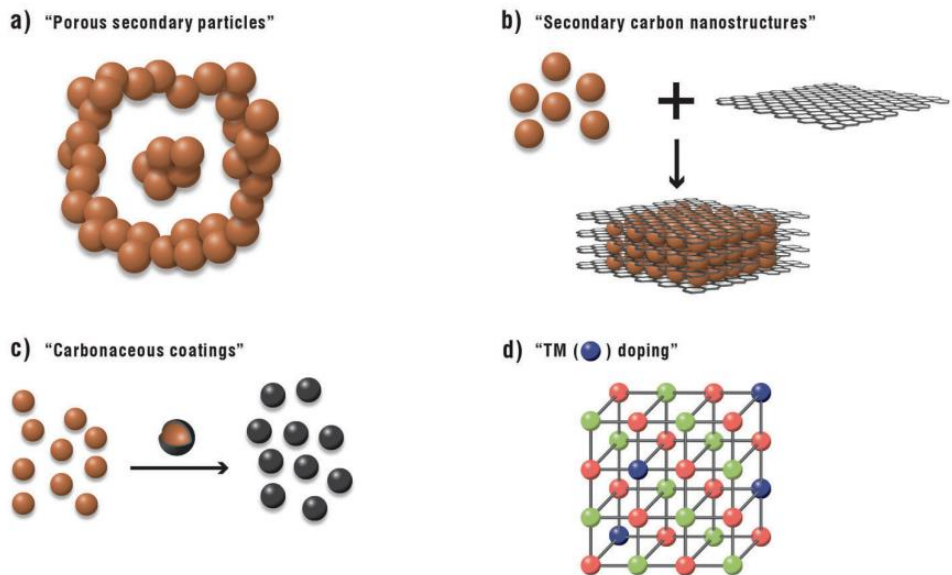


**Figure 2.3.1** Schematic illustration of the basic four approaches to enhance the electrochemical performance LIBs and SIBs: (a) porous micro-sized secondary particle, (b) introduction of carbonaceous secondary nanostructures, (c) carbonaceous coating, and (d) transition metal doping.[2.50]

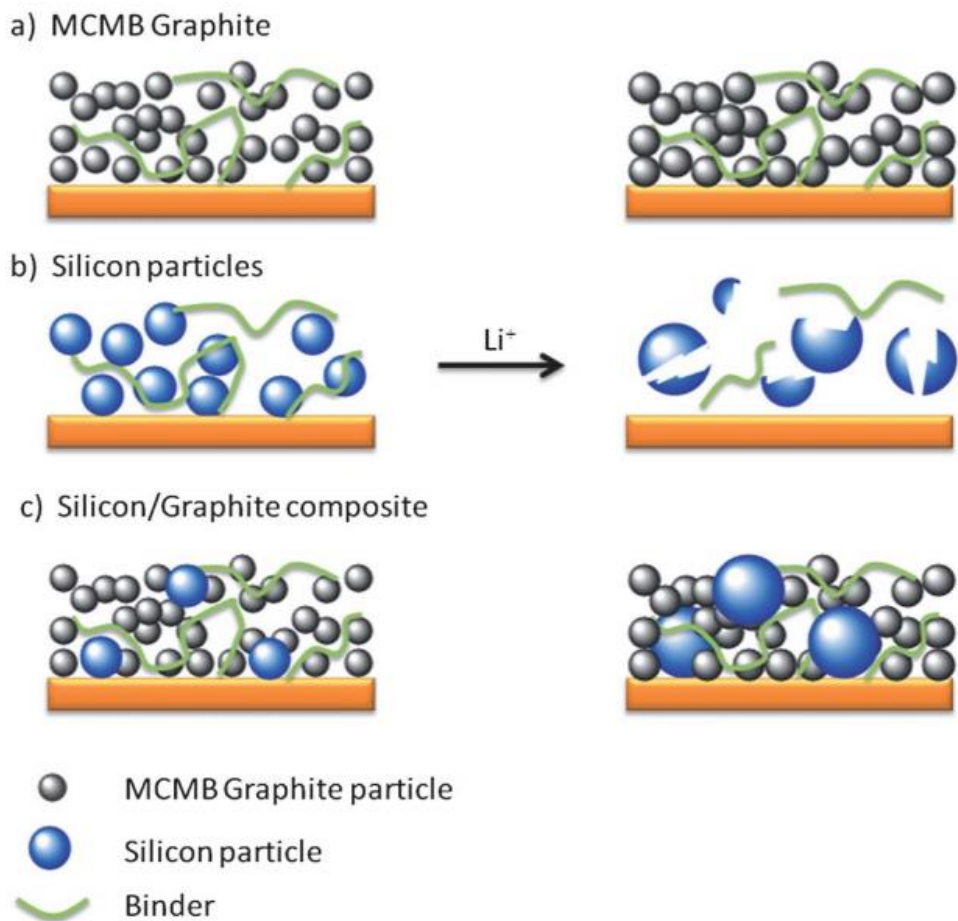


**Figure 2.3.2** Schematic of the volume expansion of mesocarbon microbeads (MCMB) graphite, silicon, and silicon-MCMB graphite composite electrodes.[2.73]

### 2.3.2. Ternary Compound of CAMs (Conversion/Alloying Materials)

Recently, conversion/alloying materials (CAMs), a material system that forms a single compound with a beneficial combination of conversion and alloying reaction materials, has been introduced as a new strategy to overcome intrinsic shortcomings of alloying and conversion reaction mechanisms.[2.50] In general, alloying reaction anodes exhibit low reaction potential and react with a large number of Li-ions per formula unit, resulting in a high energy density. However, large volume expansion during cycling leads pulverization, delamination, and agglomeration of active materials, resulting in poor cycle retention. To overcome this issue, it might be an effective approach to embed alloying reaction elements into a buffering matrix consisting of ideally good ionic and electronic conductors.

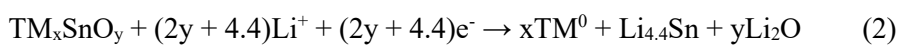
The combination of conversion and alloying reaction in CAMs can relieve capacity degradation factors of alloying reaction anodes by using the *in-situ* generated nanocomposite morphology of conversion reaction during lithiation. When CAMs were lithiated during discharge process, simultaneous hybrid conversion/alloying reaction can occur in very fine nanoscale based on their atomically homogeneous distribution in initial state (Figure 2.3.3 and 2.3.4).[2.50] The initially formed  $\text{Li}_2\text{O}$  matrix and conductive nano-network of metallic nano grains ( $\text{TM}^0$ ) can serve as a buffer matrix for volume expansion of alloying reaction phase ( $\text{Li}_n\text{M}$ ) as well as a physical barrier for hindering agglomeration. Vice and versa, CAMs can improve the shortcomings of conversion reaction anodes by

increased specific capacities, decreased reaction voltages, and reduced voltage hysteresis, which can lead to improved energy density and efficiency. Thus, the beneficial combination of conversion and alloying reactions of CAMs shows an excellent synergistic effect that enhances the advantages of each reaction mechanism while complementing their shortcomings. The synergistic effects derived from the simultaneous hybrid electrochemical reaction of CAMs can be much more effective than that of nanocomposites physically mixed with conversion and alloying materials due to their atomically homogeneous and fine distribution. However, as both conversion and alloying reaction mechanisms involve substantial volumetric changes and structural rearrangement during lithiation, reversible electrochemical performance can be highly dependent on the composition of CAMs.

Conventionally known CAMs for LIBs are especially focused on the ternary metal oxide compounds, for which one transition metal (TM) is replaced by zinc (Zn) or tin (Sn),  $ZnTM_2O_4$  (TM = Fe, Co, or Mn) or  $TM_2SnO_4$  (TM = Co, Ni, or Mn) and  $TMSnO_3$  (TM = Co or Ni), as Zn and Sn can themselves reversibly form an alloy phase with  $Li^+$ -ion.[2.79-2.83] Those CAMs can react with much increased the number of  $Li^+$ -ions per unit formula than pure conversion reaction type TM oxides. Typical lithiation process with hybrid conversion/alloying reaction is given below.[2.50]



In case of the CAMs including Sn, a specific capacity can be improved further based on high lithium content in the alloy phase ( $Li_{4.4}Sn$ ).



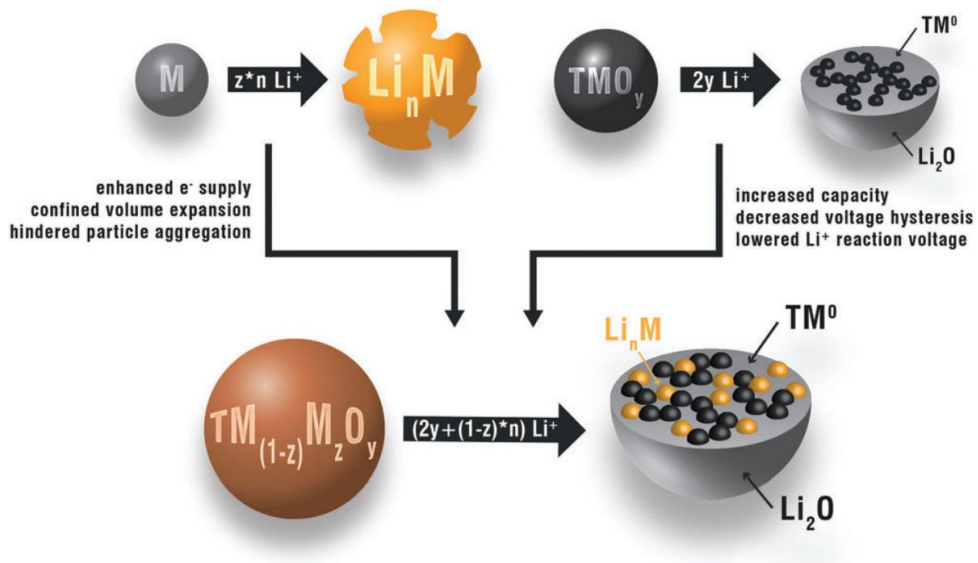


**Figure 2.3.3** Illustrative summary of the beneficial combination of conversion- and alloying-type lithium storage in conversion/alloying materials (CAMs).[2.50]

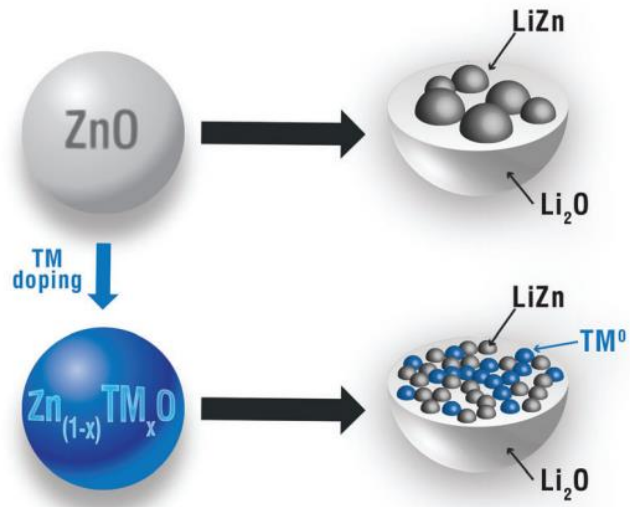


**Figure 2.3.4** Schematic illustration of the impact of introducing a TM dopant into ZnO on the lithiation mechanism and LiZn crystallite growth.[2.50]

## 2.4. Bibliography

- [2.1] S. Nowak, M. Winter, *J. Anal. At. Spectrom.*, **2017**, 32, 1833-1847.
- [2.2] U. Gulzar, S. Goriparti, E. Miele, T. Li, G. Maidecchi, A. Toma, F. D. Angelis, C. Capiglia, R. P. Zaccaria, *J. Mater. Chem. A*, **2016**, 4, 16771-16800.
- [2.3] T. M. Gur, *Energy Environ. Sci.*, **2018**, 11, 2696-2767.
- [2.4] C. Julien, A. Mauger, A. K. Vijh, K. Zaghbi, Lithium batteries: science and technology, Springer, Cham, **2016**.
- [2.5] G. Jian, S. S. Qi, L. Hong, *Chinese Physics B*, **2016**, 25, 018210.
- [2.6] B. Dunn, H. Kamath, J. M. Tarascon, *Science*, **2011**, 334, 928-935.
- [2.7] J. Li, Z. Du, R. E. Ruther, S. J. An, L. A. David, K. Hays, M. Wood, N. D. Phillip, Y. Sheng, C. Mao, S. Kalnaus, C. Daniel, D. L. Wood, *The journal of the Minerals*, **2017**, 69, 1484-1496.
- [2.8] Y. Tang, Y. Zhang, W. Li, B. Ma, X. Chen, *Chem. Soc. Rev.*, **2015**, 44, 5926-5940.
- [2.9] J. Lu, Z. Chen, F. Pan, Y. Cui, K. Amine, *Electrochem. Energy Rev.*, **2018**, 1, 35-53
- [2.10] Y. Lu, L. Yu, X. W. Lou, *Chem*, **2018**, 4, 972-996.
- [2.11] S. Wang, Y. Yang, Y. Dong, Z. Zhang, Z. Tang, *J. Adv. Ceram.*, **2019**, 8, 1-18.
- [2.12] S. Goriparti, E. Miele, F. D. Angelis, E. D. Fabrizio, R. P. Zaccaria, C. Capiglia, *J. Power Sources*, **2014**, 257, 421-443.

- [2.13] Z. Liu, W. Dong, J. Wang, C. Dong, Y. Lin, I.-W. Chen, F. Huang, *iScience*, **2020**, 23, 100767.
- [2.14] X. Li, Y. Zhang, T. Li, Q. Zhong, H. Li, J. Huang, *J. Power Sources*, **2014**, 268, 372-378.
- [2.15] J. Jin, S.-Z. Huang, J. Liu et al., *J. Mater. Chem. A*, **2014**, 2, 9699-9708.
- [2.16] V. Aravindan, Y. Lee, R. Yazami, S. Madhavi, *Materials Today*, **2015**, 18, 345-351.
- [2.17] J. S. Chen, X. W. Lou, *Electrochem. Commun.*, **2009**, 11, 2332-2335.
- [2.18] S. S. E. Deen, A. M. Hashem, A. E. A. Ghany, S. Indris, H. Ehrenberg, A. Mauger, C. M. Julien, *Ionics*, **2018**, 2925-2934.
- [2.19] M. Madian, A. Eychmuller, L. Giebeler, *Batteries*, **2018**, 4, 7.
- [2.20] A. Vittadini, A., M. Casarin, A. Selloni, *J. Phys. Chem. C*, **2009**, 113, 18973-18977.
- [2.21] Z. Yang, D. Choi, S. Kerisit, K. M. Rosso, D. Wang, J. Zhang, G. Graff, J. Liu, *J. Power Sources*, **2009**, 192, 588-598.
- [2.22] M. V. Koudriachova, N. M. Harrison, S. W. De Leeuw, *Solid State Ion.*, **2003**, 157, 35-38.
- [2.23] M. Koudriachova, N. Harrison, S. de Leeuw, *Phys. Rev. Lett.*, **2001**, 86, 1275-1278.
- [2.24] K. Amine, I. Belharouak, Z. Chen, et al., *Adv. Mater.*, **2010**, 22, 3052-3057.

- [2.25] Y. Wang, K. Takahashi, K. H. Lee, G. Z. Cao, *Adv. Funct. Mater.*, **2006**, 16, 1133-1144.
- [2.26] C. Leroux, G. Nihoul, *Phys. Rev. B: Condens. Matter Mater. Phys.*, **1998**, 57, 5111-5121.
- [2.27] S. Li, J. Liu, Q. Wan, J. Xu, B.-X. Liu, *Chem. Mater.*, **2017**, 29, 10075-10087.
- [2.28] C. Niu, J. Meng, C. Han, K. Zhao, M. Yan, L. Mai, *Nano Lett.*, **2014**, 14, 2873-2878.
- [2.29] L. Mai, Q. Wei, Q. An, X. Tian, Y. Zhao, X. Xu, L. Xu, L. Chang, Q. Zhang, *Adv. Mater.*, **2013**, 25, 2969-2973.
- [2.30] B. Yan, X. Li, Z. Bai, L. Lin, G. Chen, X. Song, D. Xiong, D. Li, X. Sun, *J. Mater. Chem. A*, **2017**, 5, 4850-4860.
- [2.31] G. He, L. Li and A. Manthiram, *J. Mater. Chem. A*, **2015**, 3, 14750-14758.
- [2.32] S. Li, Q. Xu, E. Uchaker, X. Cao, G. Cao, *CrystEngComm.*, **2016**, 18, 2532-2540.
- [2.33] V. Augustyn et al., *Nat. Mater.*, **2013**, 12, 518-522.
- [2.34] M. G. Kim, J. Cho, *Adv Funct. Mater.*, **2009**, 19, 1497-1514.
- [2.35] G.-A. Nazri, G. Pistoia, *Lithium Batteries: Science and Technology*, Springer, **2008**.
- [2.36] L. Monconduit, M. T. Charbonnel, C. Belin, *J. Solid State Chem.*, **2001**, 156, 37.

- [2.37] I. L. Devos, M. Lassalle, X. Wallart, J. O. Fourcade, L. Monconduit, J. C. Jumas, *Phys. Rev. B*, **2001**, 63, 125110.
- [2.38] C.-M. Park, Y.-U. Kim, H.-J. Sohn, *Chem. Mater.*, **2009**, 21, 5566-5568.
- [2.39] X. Wang, P. Sun, J. Qin, J. Wang, Y. Xiao, M. Cao, *Nanoscale*, **2016**, 8, 10330-10338.
- [2.40] R. Chen, R. Luo, Y. Huang, F. Wu, L. Li, *Adv. Sci.*, **2016**, 3, 1600051.
- [2.41] S.-O. Kim, A. Manthiram, *Chem. Mater.*, **2016**, 28, 5935-5942.
- [2.42] S.-G. Woo, J.-H. Jung, H. Kim, M. G. Kim, C. K. Lee, H.-J. Sohn, B. W. Cho, *J. Electrochem. Soc.*, **2006**, 153, A1979-A1983.
- [2.43] K.-H. Kim, C.-H. Jung, W.-S. Kim, S.-H. Hong, *J. Power Sources*, **2018**, 400, 204-211.
- [2.44] F. Gillot, M. Menetrier, E. Bekaert, L. Dupont, M. Morcrette, L. Monconduit, J. M. Tarascon, *J. Power Sources*, **2007**, 172, 877-885.
- [2.45] L. Li, Y. Peng, H. Yang, *Electrochim. Acta*, **2013**, 95, 230-236.
- [2.46] M. S. Tahir, M. Weinberger, P. Balasubramanian, T. Diemant, R. J. Behm, M. Linden, M. Wohlfahrt-Mehrens, *J. Mater. Chem. A*, **2017**, 5, 10190-10199.
- [2.47] C.-M. Park, J.-H. Kim, H. Kim, H.-J. Sohn, *Chem. Soc. Rev.*, **2010**, 39, 3115-3141.
- [2.48] I. H. Son et al., *Nat. Commun.*, **2015**, 6, 7393.
- [2.49] S. Fang, D. Bresser, S. Passerini, *Adv. Energy Mater.*, **2020**, 10, 1902485.

- [2.50] D. Bresser, S. Passerini, B. Scrosati, *Energy Environ. Sci.*, **2016**, 9, 3348-3367.
- [2.51] J. Cabana, L. Monconduit, D. Larcher, M. R. Palacin, *Adv. Mater.*, **2010**, 22, E170-E192.
- [2.52] F. Wang, H.-C. Yu, M.-H. Chen, L. Wu, N. Pereira, K. Thornton, A. van der Ven, Y. Zhu, G. G. Amatucci, J. Graetz, *Nat. Commun.*, **2012**, 3, 1201.
- [2.53] P. L. Taberna, S. Mitra, P. Poizot, P. Simon, J.-M. Tarascon, *Nat. Mater.*, **2006**, 5, 567-573.
- [2.54] W. Zhao, W. Choi, W.-S. Yoon, *J. Electrochem. Sci. Technol.*, **2020**, 11(3), 195-219.
- [2.55] Y. Lu, L. Yu, X. W. Lou, *Chem*, **2018**, 4, 972-996.
- [2.56] N. Mahmood, T. Y. Tang, Y. L. Hou, *Adv. Energy Mater.*, **2016**, 6, 1600374.
- [2.57] N. N. Wang, Z. C. Bai, Y. T. Qian, J. Yang, *Adv. Mater.*, **2016**, 28, 4126-4133.
- [2.58] L. N. Cong, H. M. Xie, J. H. Li, *Adv. Energy Mater.*, **2017**, 7, 1601906.
- [2.59] H. B. Wu, G. Q. Zhang, L. Yu, X. W. Lou, *Nanoscale Horiz.*, **2016**, 1, 27-40.
- [2.60] N. N. Wang, H. Y. Xu, L. Chen, X. Gu, J. Yang, Y. T. Qian, *J. Power Sources*, **2014**, 247, 163-169.
- [2.61] G.-A. Li, C.-Y. Wang, W.-C. Chang, H.-Y. Tuan, *ACS Nano*, **2016**, 10, 8632-8644.
- [2.62] B. Liu, J. G. Zhang, G. Z. Shen, *Nano Today*, **2016**, 11, 82-97.
- [2.63] Z. Y. Wang, L. Zhou, X. W. Lou, *Adv. Mater.*, **2012**, 24, 1903-1911.

- [2.64] C.-H. Jung, J. Choi, W.-S. Kim, S.-H. Hong, *J. Mater. Chem. A*, **2018**, 6, 8013-8020.
- [2.65] K.-H. Kim, C.-H. Jung, W.-S. Kim, S.-H. Hong, *J. Power Sources*, **2018**, 400, 204-211.
- [2.66] C. Lei, F. Han, D. Li, W.-C. Li, Q. Sun, X.-Q. Zhang, A.-H. Lu, *Nanoscale*, **2013**, 5, 1168-1175.
- [2.67] H. Lee, S. M. Dellatore, W. M. Miller, P. B. Messersmith, *Science*, **2007**, 19, 426-430.
- [2.68] A. Postma, Y. Yan, Y. Wang, A. N. Zelikin, E. Tjipto, F. Caruso, *Chem. Mater.*, **2009**, 21, 3042-3044.
- [2.69] U. Farooq, F. Ahmed, S. A. Pervez, S. Rehman, M. A. Pope, M. Fichtner, E. P. L. Roberts, *RSC Adv.*, **2020**, 10, 29975.
- [2.70] K. C. Wasalathilake, H. Li, L. Xu, C. Yan, *J. Energy Chem.*, **2020**, 42, 91-107.
- [2.71] M. R. Al Hassan, A. Sen, T. Zaman, M. S. Mostari, *Materials Today Chem.*, **2019**, 11, 225-243.
- [2.72] J.-I. Lee, J. Song, Y. Cha, S. Fu, C. Zhu, X. Li, Y. Lin, M.-K. Song, *Nano Research*, **2017**, 10, 4398-4414.
- [2.73] C.-H. Yim, F. M. Courtel, Y. A. Lebdeh, *J. Mater. Chem. A*, **2013**, 1, 8234-8243.
- [2.74] D. Zhao, Q. Hao, C. Xu, *Electrochim. Acta*, **2016**, 211, 83-91.

- [2.75] S. Liu, K. Zhu, J. Tian, W. Zhang, S. Bai, Z. Shan, *J. Alloys and Comp.*, **2015**, 639, 60-67.
- [2.76] J.-Y. Liao, B. D. Luna, A. Manthiram, *J. Mater. Chem. A*, **2016**, 4, 801.
- [2.77] Y. Zhong, Y. Ma, Q. Guo, J. Liu, Y. Wang, M. Yang, H. Xia, *Sci. Rep.*, **2017**, 7, 40927.
- [2.78] K.-H. Kim, W.-S. Kim, S.-H. Hong, *Nanoscale*, **2019**, 11, 13494-13501.
- [2.79] Y. Sharma, N. Sharma, G. V. S. Rao, B. V. R. Chowdari, *Electrochim. Acta*, **2008**, 53, 2380-2385.
- [2.80] X. Guo, X. Lu, X. Fang, Y. Mao, Z. Wang, L. Chen, X. Xu, H. Yang, Y. Liu, *Electrochem. Commun.* **2010**, 12, 847-850.
- [2.81] Z. Xing, Z. Ju, J. Yang, H. Xu, Y. Qian, *Nano Res.*, **2012**, 5, 477-485.
- [2.82] P. A. Connor, J. T. S. Irvine, *Journal of Power Sources* **2001**, 97-98, 223-225.
- [2.83] C. Hua, X. Fang, Z. Wang, L. Chen, *Chem. –Eur. J.*, **2014**, 20, 5487-5491.

# **Chapter 3. Complete Solid Solution $Mn_{1-x}Fe_xP$ as a Conversion/Alloying Hybrid Reaction Anode for Lithium-Ion Batteries**

## **3.1. Introduction**

Rechargeable Li-ion batteries (LIBs) are currently being explored for next generation energy storage systems such as electric vehicles and hybrid electric vehicles.[3.1-3.3] Such applications require electrode materials with high energy density, high power density, lower cost, light weight, and improved safety.[3.4] Graphite is the most common anode material in commercial LIBs because it shows a highly stable cycle retention with an intercalation reaction mechanism, but its specific capacity is relatively low ( $372 \text{ mA h g}^{-1}$ ) with a poor rate capability.[3.4-3.8] To develop high performance anode materials for next generation LIBs, extensive research studies have been performed on materials which react with lithium either by alloying reaction such as Si, Ge, and Sn or by conversion reaction such as transition metal oxides.[3.9-3.15] The alloying reaction anodes offer high specific capacities, but the extensive volume expansion, electrode pulverization, and aggregation of active materials during cycles hamper their widespread implementation in practical LIBs.[3.16,3.17] The conversion materials are also alternative high capacity anodes, but accompany the bond cleavage and reforming between metals and anions, resulting in a wide operational voltage range, a large

voltage hysteresis, and a relatively low energy storage efficiency.[3.16,3.18] Recently, the beneficial combination of these two lithium storage mechanisms in a single compound, referred to as conversion and alloying materials (CAMs), has been noticed to complement the shortcomings of the conversion and alloying mechanisms.[3.16,3.19] One approach is the partial substitution of the electrochemically inactive transition metal in conversion type compounds such as  $\text{ZnFe}_2\text{O}_4$  and  $\text{Co}_2\text{SnO}_4$  with an element which can reversibly form an alloy with lithium.[3.20-3.23] The other alternative is starting from an alloying compound and enhancing the reversibility of the  $\text{Li}_2\text{O}$  formation by incorporating a transition metal, as realized in Fe-doped ZnO and  $\text{SnO}_2$ . [3.24-3.26] The known CAMs exhibited an enhanced electrochemical performance over pure conversion or alloying materials due to the synergistic effects of both mechanisms, which can effectively buffer the large volume expansion and ensure electron and ion transport.

A new strategy to extend the concept of the present CAMs is to find out material systems to form a complete solid solution whose end members have different types of reaction mechanisms with  $\text{Li}^+$ -ions, which can additionally control the ratio of alloying and conversion materials. A representative example is a  $\text{SnO}_2$ (alloying type)– $\text{TiO}_2$ (intercalation type) solid solution, which showed superior cycling stability and rate capability due to the synergistic effects contributed from individual components.[3.27] Since most of the current studies about CAMs are limited to oxides, it is required to switch from oxides to phosphides, which leads to an improved energy density by lowering the  $\text{Li}^+$  reaction potential and voltage hysteresis.[3.28-3.30] However, no such study has been performed on metal phosphides, to the best of our knowledge. Transition metal monophosphides exhibit

three types of reaction mechanisms (intercalation, alloying, and conversion) and form solid solutions depending on the nature of the metals (Figure 3.1.1).[3.31-3.36] Among them, MnP and FeP are iso-structural with a space group of *Pnma* and form the complete solid solution of  $Mn_{1-x}Fe_xP$  ( $0 \leq x \leq 1$ ). MnP shows an alloying reaction with lithium by forming the  $Li_xMn_yP_z$  ternary phase and delivers a high initial lithiation and delithiation capacity of 1104 and 870 mA h  $g^{-1}$ , respectively, but suffers a rapid capacity fading (Figure 3.1.2).[3.34] On the other hand, FeP reacts with lithium through a conversion reaction by forming the percolating network of Fe nanograins embedded in the  $Li_3P$  matrix and delivers an initial discharge and charge capacity of  $\sim 860$  and 720 mA h  $g^{-1}$ , respectively (Figure 3.1.3).[3.35] The combination of conversion and alloying in a single phase  $Mn_{1-x}Fe_xP$  is expected to generate the in situ nanocomposite where nanocrystalline  $Li_xMn_yP_z$  and the Fe nano-network are embedded in the amorphous  $Li_3P$  matrix, which can effectively buffer the accompanying volume variation and ensure electron and ion transport resulting in improved capacity retention and high rate stability.

In this study, we suggest a new concept to tailor the electrochemical performance using solid solution compounds of alloying type MnP and conversion type FeP.[3.34–3.37] The solid solution series  $Mn_{1-x}Fe_xP$  ( $0 \leq x \leq 1$ ) were synthesized using a high energy mechanical milling (HEMM), which is widely used for the synthesis of metal phosphides and solid solutions of oxides or carbides,[3.27,3.38-3.41] and their electrochemical properties as an anode for LIBs were investigated.

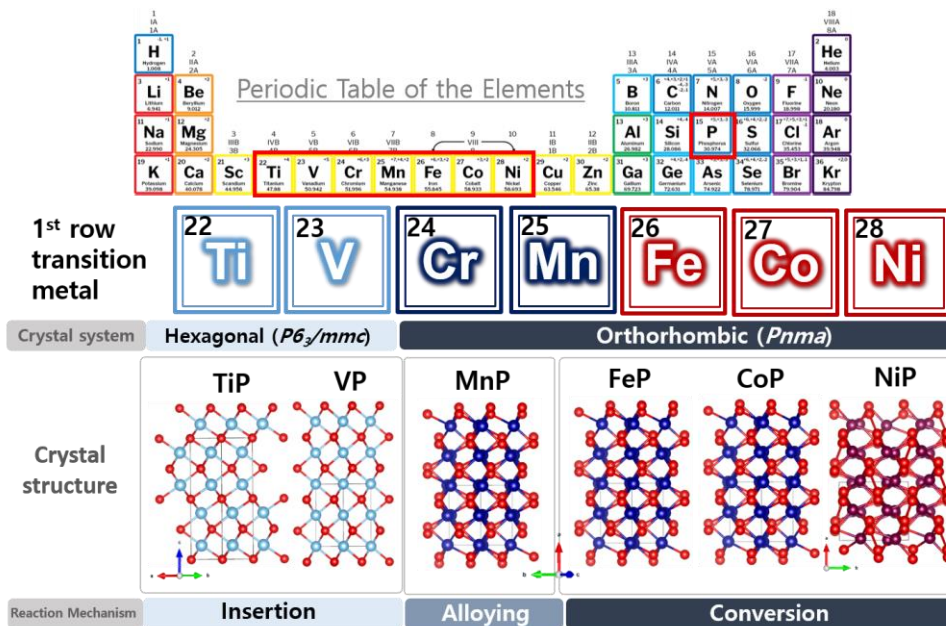


**Figure 3.1.1** Crystal structure and electrochemical reaction mechanism for various 1<sup>st</sup> row transition metal monophosphides.

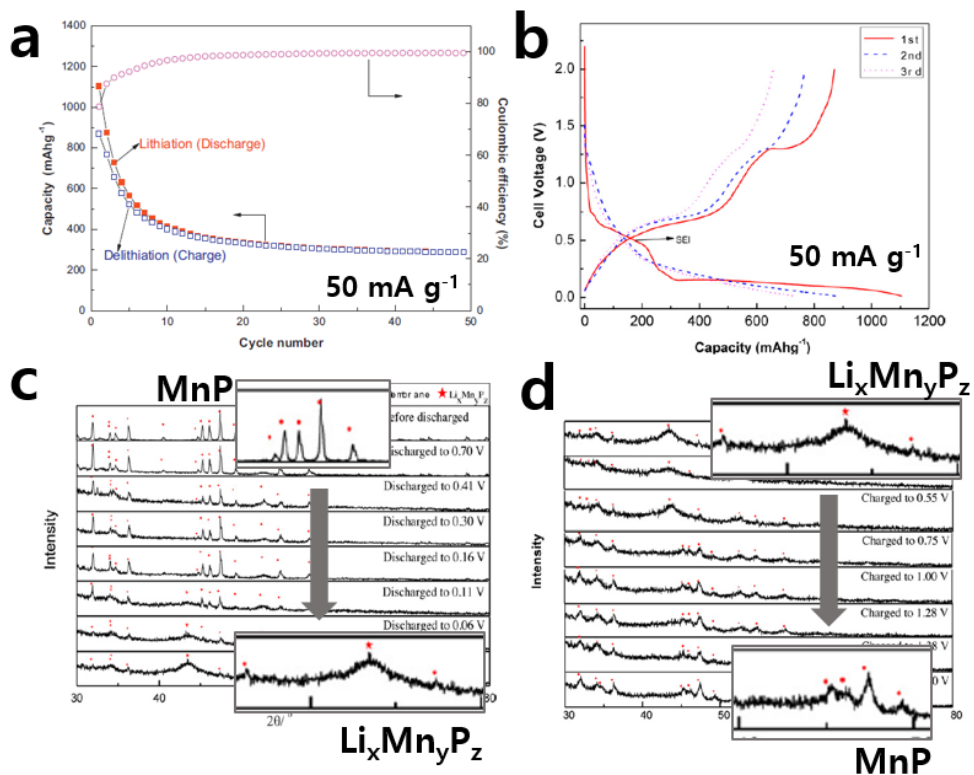


**Figure 3.1.2** (a) Cycle performance, (b) corresponding voltage profiles tested at current density of  $50 \text{ mA g}^{-1}$ , and ex-situ XRD patterns for MnP/Li cell during (c) lithiation and (d) delithiation process.[3.34]

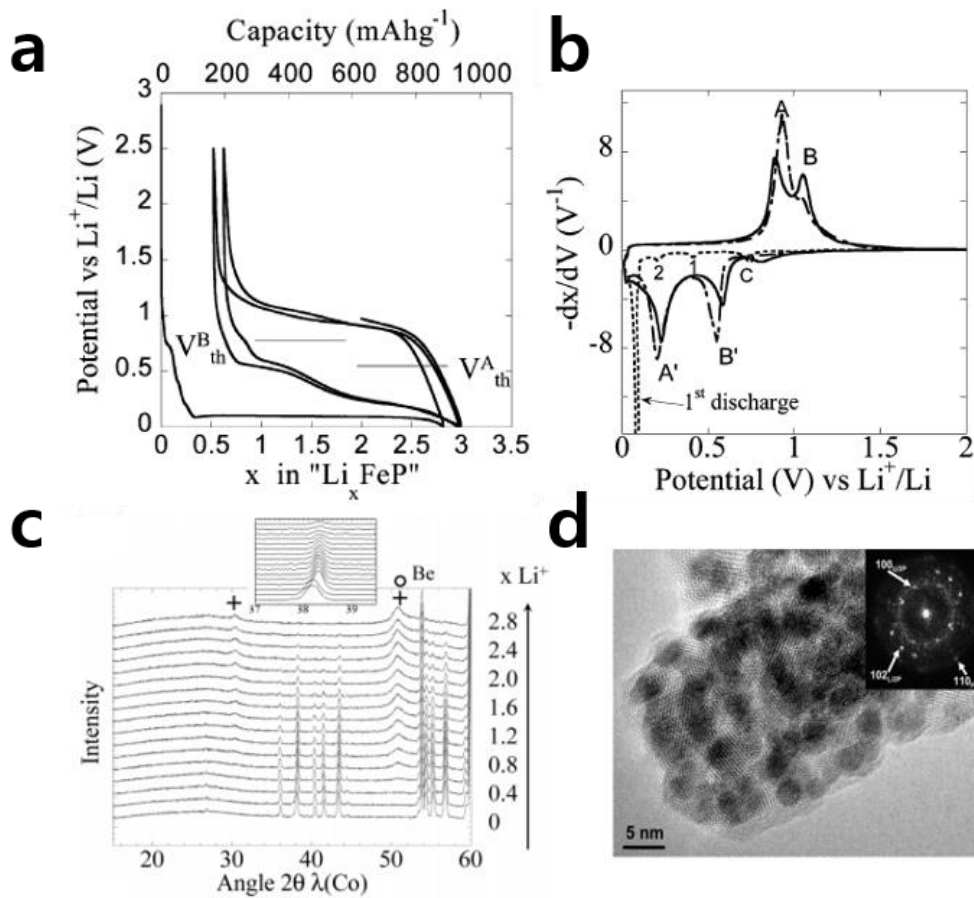


**Figure 3.1.3** (a) Voltage profiles, (b) corresponding differential capacity plots, (c) in-situ XRD patterns for FeP/Li cell during lithiation and (d) TEM image of as lithiated FeP nanoparticles.[3.35]

## 3.2. Experimental Procedure

### *Synthesis of the $Mn_{1-x}Fe_xP$ ( $x = 0, 0.5, 0.75, \text{ and } 1$ ) nanoparticles*

$Mn_{1-x}Fe_xP$  ( $x = 0, 0.5, 0.75, \text{ and } 1.0$ ) nanoparticles (NPs) were synthesized via a high energy mechanical milling (HEMM) method using a planetary ball mill (Pulverisette 6, Fritsch). The starting materials used were commercial manganese (Mn, 99.95%, Alfa Aesar), iron (Fe, 99.5%, Alfa Aesar), and red phosphorus (98.9%, Alfa Aesar) without further purification. The stoichiometric amount of the starting materials was placed into a hardened steel vial (80 cm<sup>3</sup>) with hardened steel balls (a diameter of 3/8 in.) at a ball-to-powder weight ratio of 20:1 and the vial was sealed inside an argon-filled glove box. HEMM was carried out at room temperature with a rotation speed of 300 rpm for 20 h. The as-synthesized powder was collected, softly ground, and stored in a glove box to minimize surface oxidation.

### *Materials characterization*

The high resolution powder diffraction (HRPD) patterns of the as-synthesized NPs were obtained using synchrotron X-rays at the 9B HRPD beamline of the Pohang Accelerator Laboratory (PAL). The diffraction data were collected at room temperature with  $2\theta$  ranging from 10° to 130° with a step size of 0.02° at a wavelength of  $\lambda = 1.5167 \text{ \AA}$ . The lattice parameters were determined using Rigaku PDXL commercial software.[3.37] The chemical composition of the as-synthesized NPs was analyzed by inductively coupled plasma atomic emission spectrometry (ICP-AES, OPTIMA 8300, PerkinElmer). The morphology of the as-synthesized NPs and the as-fabricated electrodes was observed by field emission scanning

electron microscopy (FE-SEM, SU70, Hitachi) and transmission electron microscopy (TEM, JEM-2100F, JEOL).

#### *Electrochemical measurements*

The electrode was prepared by mixing 70% active material, 15% Super P carbon black, and 15% carboxymethyl cellulose (CMC) binder by weight to form a slurry, which was coated on the copper foil, followed by drying in a vacuum oven at 65 °C overnight. The electrode was punched into a round disk with 1.0–1.5 mg cm<sup>-2</sup> loading of active material and then kept in the vacuum oven at 70 °C for 12 h. The CR2032 coin cell was fabricated inside an argon-filled glove box by employing a polypropylene (Welcose, Korea) separator and a lithium foil counter/reference electrode. The electrolyte used was 1.0 M LiPF<sub>6</sub> in a mixture of ethylene carbonate (EC) and dimethyl carbonate (DMC) (1:1 v/v) with the addition of 5 vol% of fluoroethylene carbonate (FEC). A galvanostatic cycling test was performed with a battery testing system (Wonatech, Korea) within the voltage range of 0.01–2 V (vs. Li/Li<sup>+</sup>). Electrochemical impedance spectroscopy (EIS) experiment was carried out in the frequency range of 100 kHz to 0.1 Hz with an AC amplitude of 5 mV using an impedance analyzer (Zive, SP1).

### 3.3. Results and Discussions

#### 3.3.1. Synthesis and Physicochemical Characterization

Figure 3.3.1a shows the XRD patterns of the as-synthesized  $\text{Mn}_{1-x}\text{Fe}_x\text{P}$  ( $x = 0, 0.5, 0.75, \text{ and } 1.0$ ) nanoparticles (NPs), and the patterns were replotted based on the wavelength of Cu  $\text{K}_\alpha$  ( $\lambda = 1.5406 \text{ \AA}$ ) instead of the measured wavelength ( $\lambda = 1.5167 \text{ \AA}$ ) to compare with the reference ICDD database (MnP: #00-051-0942,  $\text{Mn}_{0.5}\text{Fe}_{0.5}\text{P}$ : #01-079-3948, and FeP: #01-0781443). All of the synthesized  $\text{Mn}_{1-x}\text{Fe}_x\text{P}$  NPs were a single phase, and the obtained diffraction peaks were completely indexed based on the orthorhombic crystal structure with a space group  $Pnma$ . The main XRD peaks ((121), (220), and (211)) shifted to a higher  $2\theta$  with increasing Fe content, due to the smaller ionic radius of  $\text{Fe}^{3+}$  ( $0.55 \text{ \AA}$ , CN = 6) than  $\text{Mn}^{3+}$  ( $0.58 \text{ \AA}$ , CN = 6).[3.36] The lattice constants ( $a$ ,  $b$ , and  $c$ ), extracted from Rietveld refinements,[3.42] were consistent with the reference ICDD database and linearly decreased with increasing Fe content obeying Vegard's law (Table 3.3.1, and Figure 3.3.1b and 3.3.2). Thus, the substitutional solid solution  $\text{Mn}_{1-x}\text{Fe}_x\text{P}$  compounds were successfully synthesized by HEMM between two end members (MnP and FeP). To compare the electrochemical properties, a MnP/FeP NP mixture was also prepared by mixing the as-synthesized MnP and FeP NPs with a 1:1 mole ratio. The XRD pattern of the MnP/FeP mixture was different from that of the  $\text{Mn}_{0.5}\text{Fe}_{0.5}\text{P}$  ( $x = 0.5$ ) compound and both MnP and FeP peaks simultaneously appeared in the diffraction pattern (Figure 3.3.3). The chemical composition of the as-synthesized NPs was analyzed by ICP-AES and the actual atomic ratios of Mn, Fe, and P in all of the solid solutions are

very close to the expected values, as shown in Table 3.3.2.

The morphology of the as-synthesized  $\text{Mn}_{1-x}\text{Fe}_x\text{P}$  NPs observed by SEM and it was very similar and the particle size was a few hundred nanometers irrespective of chemical compositions (Figure 3.3.4). The as-prepared solid solution  $\text{Mn}_{1-x}\text{Fe}_x\text{P}$  ( $x = 0.5$  and  $0.75$ ) NPs were further investigated by TEM (Figure 3.3.5). The high resolution (HR) TEM image of the as-prepared  $\text{Mn}_{0.5}\text{Fe}_{0.5}\text{P}$  NPs (Figure 3.3.5a) showed lattice fringes with lattice spacings of 1.9, 2.44, and 2.77 Å corresponding to the (211), (111), and (011) planes of the  $\text{Mn}_{0.5}\text{Fe}_{0.5}\text{P}$  phase (ICDD #01-079-3948). In addition, the selected-area electron diffraction (SAED) pattern (Figure 3.3.5b) was completely indexed to the  $\text{Mn}_{0.5}\text{Fe}_{0.5}\text{P}$  phase, and the ring-like pattern indicates the randomly oriented polycrystalline nature. The scanning transmission electron microscopy (STEM) image and elemental mapping images by energy dispersive spectroscopy (EDS) revealed that Mn, Fe, and P elements were homogeneously distributed throughout the  $\text{Mn}_{0.5}\text{Fe}_{0.5}\text{P}$  NPs (Figure 3.3.5c). The  $\text{Mn}_{0.25}\text{Fe}_{0.75}\text{P}$  NPs showed a similar HRTEM image and SAED pattern with slightly smaller interplanar spacings of 1.89, 2.43, and 2.76 Å corresponding to the (211), (111), and (011) planes consistent with the Rietveld results (Figure 3.3.5d and e). In addition, composed elements of Mn, Fe, and P in  $\text{Mn}_{0.25}\text{Fe}_{0.75}\text{P}$  compound were also homogenous throughout the  $\text{Mn}_{0.25}\text{Fe}_{0.75}\text{P}$  NPs (Figure 3.3.5f). Consequently, the substitutional solid solution  $\text{Mn}_{1-x}\text{Fe}_x\text{P}$  ( $x = 0.5$  and  $0.75$ ) compounds between MnP and FeP were successfully synthesized via a facile high energy mechanical milling process.

**Table 3.3.1** The refined lattice parameters for  $\text{Mn}_{1-x}\text{Fe}_x\text{P}$  ( $x = 0, 0.5, 0.75, \text{ and } 1$ ) NPs.

Material	a (Å)	b (Å)	c (Å)	V (Å <sup>3</sup> )	$R_{\text{wp}}^{\text{a}}$ (%)	$R_{\text{p}}^{\text{b}}$ (%)
MnP	5.2671(5)	3.1680(4)	5.9238(6)	98.844(2)	4.91	4.13
$\text{Mn}_{0.5}\text{Fe}_{0.5}\text{P}$	5.2412(4)	3.1514(2)	5.8616(3)	96.817(2)	6.18	4.51
$\text{Mn}_{0.25}\text{Fe}_{0.75}\text{P}$	5.2180(3)	3.1350(1)	5.8180(4)	95.173(1)	5.94	4.33
FeP	5.2076(6)	3.1229(3)	5.7999(5)	94.323(7)	6.16	4.74

<sup>a</sup>Weighted profile  $R$ -factor.

<sup>b</sup>Unweighted profile  $R$ -factor.

**Table 3.3.2** Elemental analysis results of  $\text{Mn}_{1-x}\text{Fe}_x\text{P}$  ( $x = 0, 0.5, 0.75, \text{ and } 1$ ) NPs by ICP-AES.

Compound	Element	Mass %	Atomic ratio (actual)	Atomic ratio (expected)
MnP	Mn	63.6	0.5	0.5
	P	36.4	0.5	0.5
$\text{Mn}_{0.5}\text{Fe}_{0.5}\text{P}$	Mn	34.0	0.27	0.25
	Fe	32.5	0.26	0.25
	P	33.5	0.47	0.5
$\text{Mn}_{0.25}\text{Fe}_{0.75}\text{P}$	Mn	50.7	0.13	0.125
	Fe	15.8	0.39	0.375
	P	33.5	0.48	0.5
FeP	Fe	67.0	0.53	0.5
	P	33.0	0.47	0.5

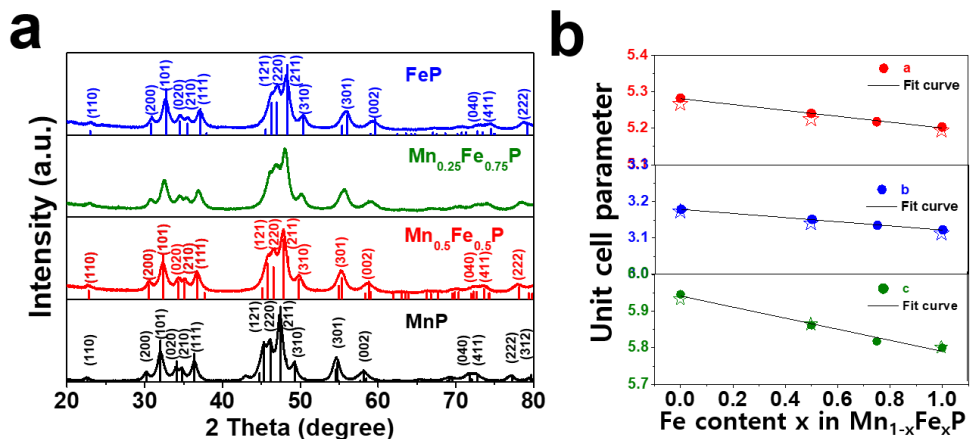


**Figure. 3.3.1** (a) XRD patterns for the as-synthesized  $\text{Mn}_{1-x}\text{Fe}_x\text{P}$  ( $x = 0, 0.5, 0.75,$  and  $1.0$ ) NPs and (b) corresponding refined lattice parameters. The reference peaks for MnP (ICDD #00-051-0942, black color),  $\text{Mn}_{0.5}\text{Fe}_{0.5}\text{P}$  (ICDD #01-079-3948, red color), and FeP (ICDD #01-078-1443, blue color) are included. ☆ in (b) is the lattice parameter from ICDD.

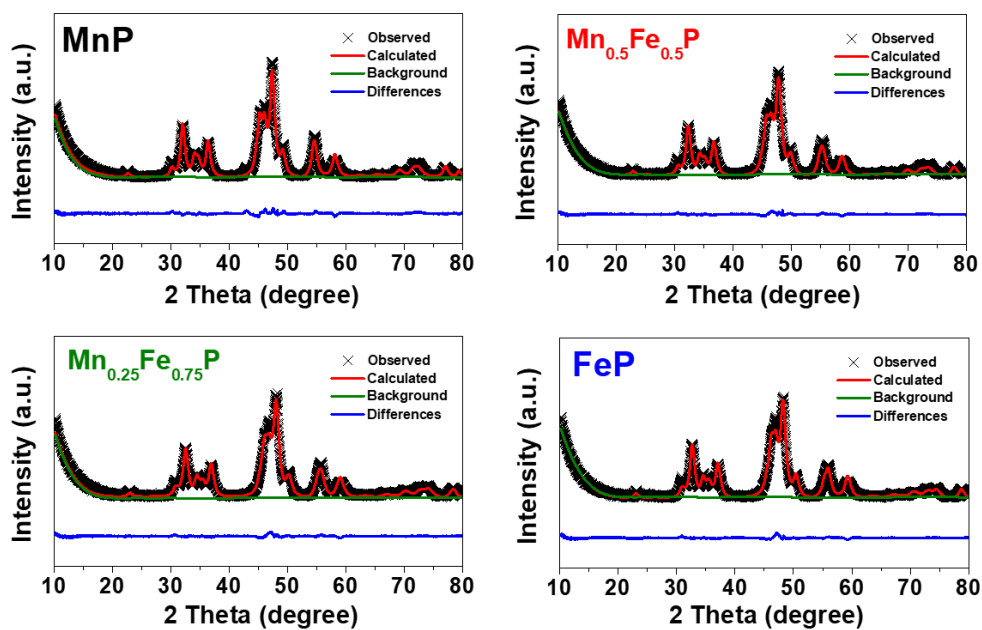


**Figure. 3.3.2** XRD Rietveld refinement results for as-synthesized  $\text{Mn}_{1-x}\text{Fe}_x\text{P}$  ( $x = 0, 0.5, 0.75, \text{ and } 1.0$ ) NPs.

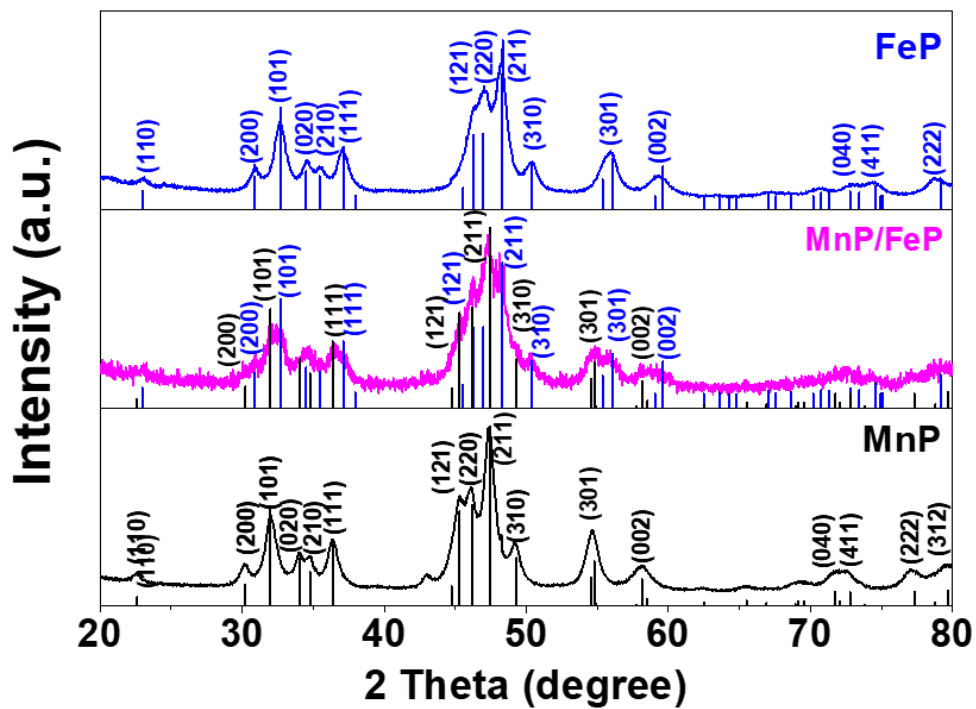


**Figure. 3.3.3** XRD patterns of as-synthesized MnP, MnP/FeP mixture, and FeP NPs.

The reference peaks for MnP (ICDD # 00-051-0942, black color) and FeP (ICDD # 01-078-1443, blue color) are included.

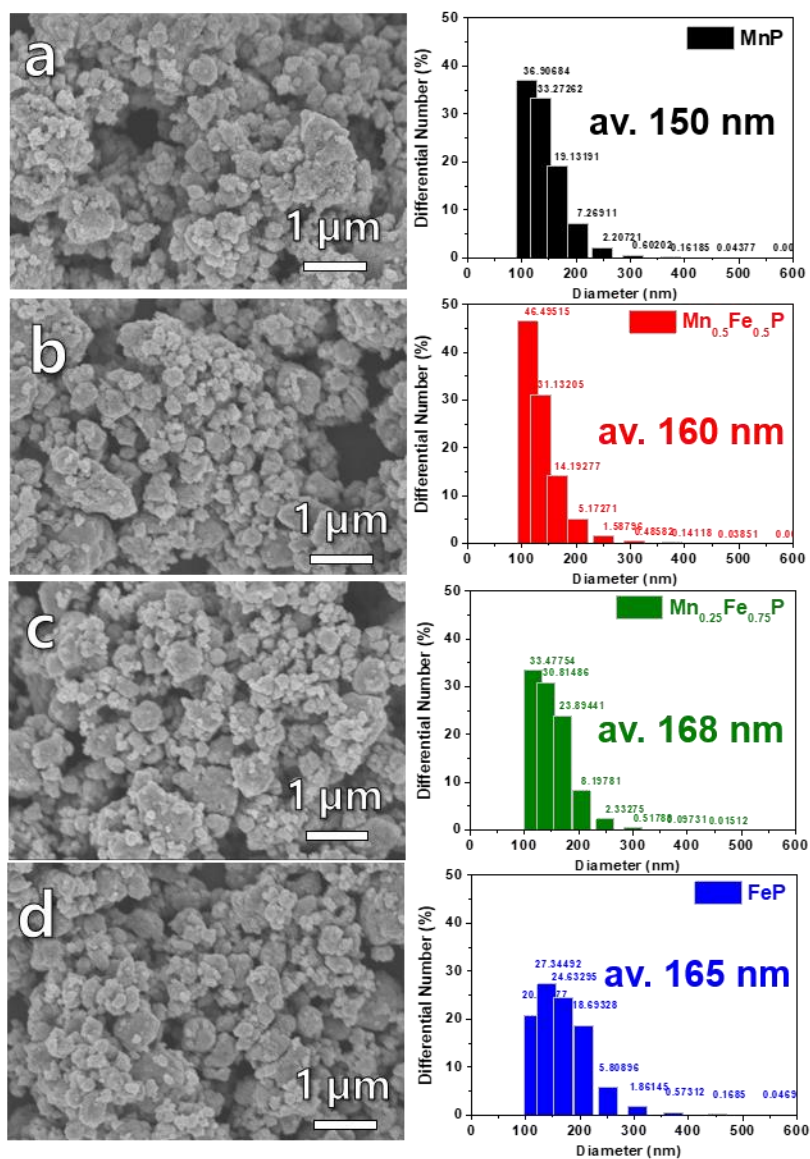


**Figure. 3.3.4** SEM images and dynamic light scattering (DLS) particle size distributions of the as-synthesized  $Mn_{1-x}Fe_xP$  ( $x =$  (a) 0, (b) 0.5, (c) 0.75, and (d) 1.0) NPs, respectively.

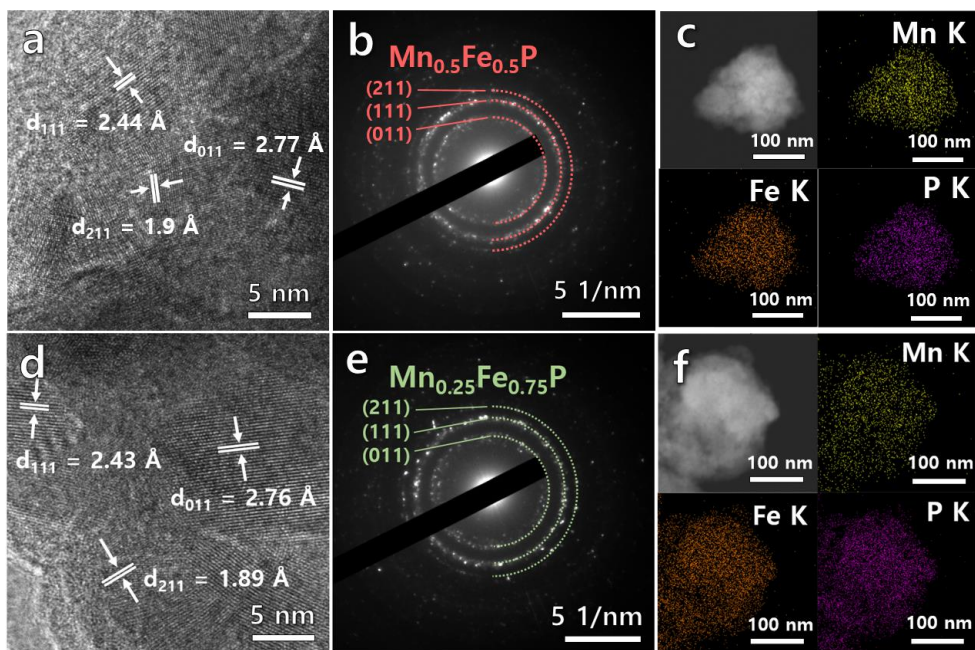


**Figure. 3.3.5** (a,d) High resolution TEM images, (b,e) selected-area electron diffraction (SAED) patterns, and (c,f) STEM images and elemental mapping images (Mn K, Fe K, and P K) of  $\text{Mn}_{1-x}\text{Fe}_x\text{P}$  ( $x = 0.5$  and  $0.75$ ) NPs, respectively.

### 3.3.2. Electrochemical Properties and Reaction Mechanism

Figure 3.3.6a and b show the galvanostatic discharge (lithiation) and charge (delithiation) voltage profiles and the corresponding differential capacity ( $dQ/dV$ ) plots obtained from the  $Mn_{1-x}Fe_xP$  electrodes at a current density of  $100 \text{ mA g}^{-1}$ , respectively. The 1<sup>st</sup> and 2<sup>nd</sup> voltage profiles of the alloying type MnP electrode exhibited a sloping voltage plateau below  $0.25 \text{ V vs. Li/Li}^+$  to form a ternary  $Li_xMn_yP_z$  alloy phase in the lithiation and two flat delithiation voltage plateaus at  $0.7$  and  $1.23 \text{ V vs. Li/Li}^+$  for the de-alloying reaction, which are in good agreement with the previous report.[3.34] The conversion-type FeP electrode showed two lithiation peaks at  $0.2$  and  $0.68 \text{ V vs. Li/Li}^+$  and two delithiation peaks at  $0.95$  and  $1.05 \text{ V vs. Li/Li}^+$  in the  $dQ/dV$  plot which are consistent with the previous report.[3.35] In the  $dQ/dV$  plot of the  $Mn_{0.5}Fe_{0.5}P$  ( $x = 0.5$ ) solid solution electrode, three lithiation peaks at  $0.66$ ,  $0.15$ , and  $<0.1 \text{ V vs. Li/Li}^+$  and three delithiation peaks at  $0.77$ ,  $1.05$ , and  $1.28 \text{ V vs. Li/Li}^+$  were observed. All of the voltage plateaus (or peaks in the  $dQ/dV$  plot) corresponding to the MnP and FeP electrodes appeared in the profiles of the  $Mn_{0.5}Fe_{0.5}P$  electrode indicating that both the alloying/dealloying reaction of MnP and the conversion reaction of FeP simultaneously occurred during the discharge/charge process. However, two delithiation peaks of MnP shifted to higher voltages and two lithiation peaks of FeP slightly shifted to lower voltages (Figure 3.3.6c). On the other hand, these peak shifts were not observed in the MnP/ FeP mixture electrode and all of the lithiation and delithiation peaks of MnP and FeP were found at the same voltages (Figure 3.3.7). The simultaneous reactions in the

$\text{Mn}_{0.5}\text{Fe}_{0.5}\text{P}$  solid solution electrode were further confirmed using the *ex situ* XRD pattern, the high magnification TEM image, and the selected area electron diffraction (SAED) pattern of the 1<sup>st</sup> fully discharged (0 V vs.  $\text{Li}/\text{Li}^+$ ) and charged (2.0 V vs.  $\text{Li}/\text{Li}^+$ ) states. The XRD peaks were broad and weak and thus, the phases were not well identified, but the ternary  $\text{Li}_x\text{Mn}_y\text{P}_z$  and  $\text{Li}_3\text{MnP}_2$  phases were formed during the alloying reaction in  $\text{MnP}$  and  $\text{Mn}_{0.5}\text{Fe}_{0.5}\text{P}$  electrodes (Figure 3.3.8a).[3.33] The conversion reacted Fe was observed in the XRD patterns of the  $\text{Mn}_{0.5}\text{Fe}_{0.5}\text{P}$  and  $\text{FeP}$  electrodes (Figure 3.3.8a). The *ex situ* XRD pattern of the 1<sup>st</sup> fully charged  $\text{Mn}_{0.5}\text{Fe}_{0.5}\text{P}$  electrode showed an original solid solution phase (Figure 3.3.8b), implying the reversible discharge/charge reaction of the solid solution electrode.

The SAED pattern analysis using TEM was further performed to clarify the phase identification and the SAED pattern for the fully discharged  $\text{Mn}_{0.5}\text{Fe}_{0.5}\text{P}$  electrode (Figure 3.3.9e) showed the fully discharged states of both  $\text{MnP}$  and  $\text{FeP}$  electrodes, which formed the ternary  $\text{Li}_x\text{Mn}_y\text{P}_z$  and  $\text{Li}_3\text{MnP}_2$  phases by alloying reaction (Figure 3.3.9d) and the Fe nano-grain and  $\text{Li}_3\text{P}$  amorphous matrix by conversion reaction (Figure 3.3.9f), respectively. The chemical composition and crystal structure of the ternary  $\text{Li}_x\text{Mn}_y\text{P}_z$  phase are not available up to this point.[3.34] The STEM and EDS mapping images (Mn K, Fe K, and P K, Figure 3.3.9g-j) indicated that Mn, Fe, and P elements were homogeneously distributed throughout the fully discharged  $\text{Mn}_{0.5}\text{Fe}_{0.5}\text{P}$  NPs. The high-magnification HAADF STEM image of fully discharged  $\text{Mn}_{0.5}\text{Fe}_{0.5}\text{P}$  electrode shows that lithiated  $\text{Mn}_{0.5}\text{Fe}_{0.5}\text{P}$  NPs are composed with crystallites smaller than 5 nm (Figure 3.3.10a). Further inspection of the reduced fast Fourier transform (FFT) pattern of marked area in STEM image exhibits that observed planes in the FFT pattern are well matched with both  $\text{Li}_3\text{MnP}_2$

and  $\text{Li}_3\text{P}$  phases as zone axis of  $[111]$  and  $[212]$ , respectively, indicating simultaneous alloying and conversion hybrid reactions in few nanometer scale (Figure 3.3.10b). This was further corroborated with high magnification EDS mapping images (Figure 3.3.10c-f) and nano-beam electron diffraction patterns of lithiated  $\text{Mn}_{0.5}\text{Fe}_{0.5}\text{P}$  electrode obtained with a  $\sim 4$  nm size transmission beam, which is also matched with both  $\text{Li}_3\text{MnP}_2$  and  $\text{Li}_3\text{P}$  phases with zone axis of  $[302]$  and  $[452]$ , respectively (Figure 3.3.11).

The voltage profiles of the  $\text{Mn}_{0.25}\text{Fe}_{0.75}\text{P}$  ( $x = 0.75$ ) electrode were very similar to those of the FeP electrode with a slight shift of lithiation peaks to lower voltages, but still contained those of MnP with a slight shift of delithiation peaks to higher voltages. Thus, the discharge/charge voltage profiles of  $\text{Mn}_{1-x}\text{Fe}_x\text{P}$  solid solution compounds were not a simple linear combination of the voltage profiles of two end members (MnP and FeP), which was observed in the MnP/FeP mixture electrode. Instead, the solid solution affected the redox reactions of each end member and shifted the reaction potentials during discharge/ charge processes.[3.16,3.20,3.21] In particular, Mn substitution into FeP resulted in a gradual shift of working potentials to lower voltages, which improved the energy density in the negative electrodes. In the  $\text{Zn}_{1-x}\text{Mn}_x\text{Fe}_2\text{O}_4$  nanofibers,[3.21] Mn substitution brought down the working voltage, which was derived from the lower Gibbs free energy of formation for MnO ( $\Delta G^\circ = -363 \text{ kJ mol}^{-1}$ ) than ZnO ( $\Delta G^\circ = -320 \text{ kJ mol}^{-1}$ ). In addition,  $\text{Mn}_{3-x}\text{Fe}_x\text{O}_4$  showed that the ratio of the plateau at the upper potential gradually increased with the Fe content of the compound.[3.43] In the  $\text{Mn}_{1-x}\text{Fe}_x\text{P}$  solid solution compounds, it was not accurate to compare the working voltage with only the Gibbs free energy of formation for each end member because the electrochemical reaction mechanisms

of MnP and FeP are different. The Gibbs free energy of formation for MnP ( $\Delta G^\circ = -117.916 \text{ kJ mol}^{-1}$ ) was lower than that for FeP ( $\Delta G^\circ = -97.281 \text{ kJ mol}^{-1}$ ), which can be related to a relatively low standard redox potential of Mn than that of Fe[3.21] and could affect the down-shifting of working potentials. Our obtained results suggest that the working potentials of multicomponent transition metal monophosphides can be tuned by varying the component and composition in transition metals.

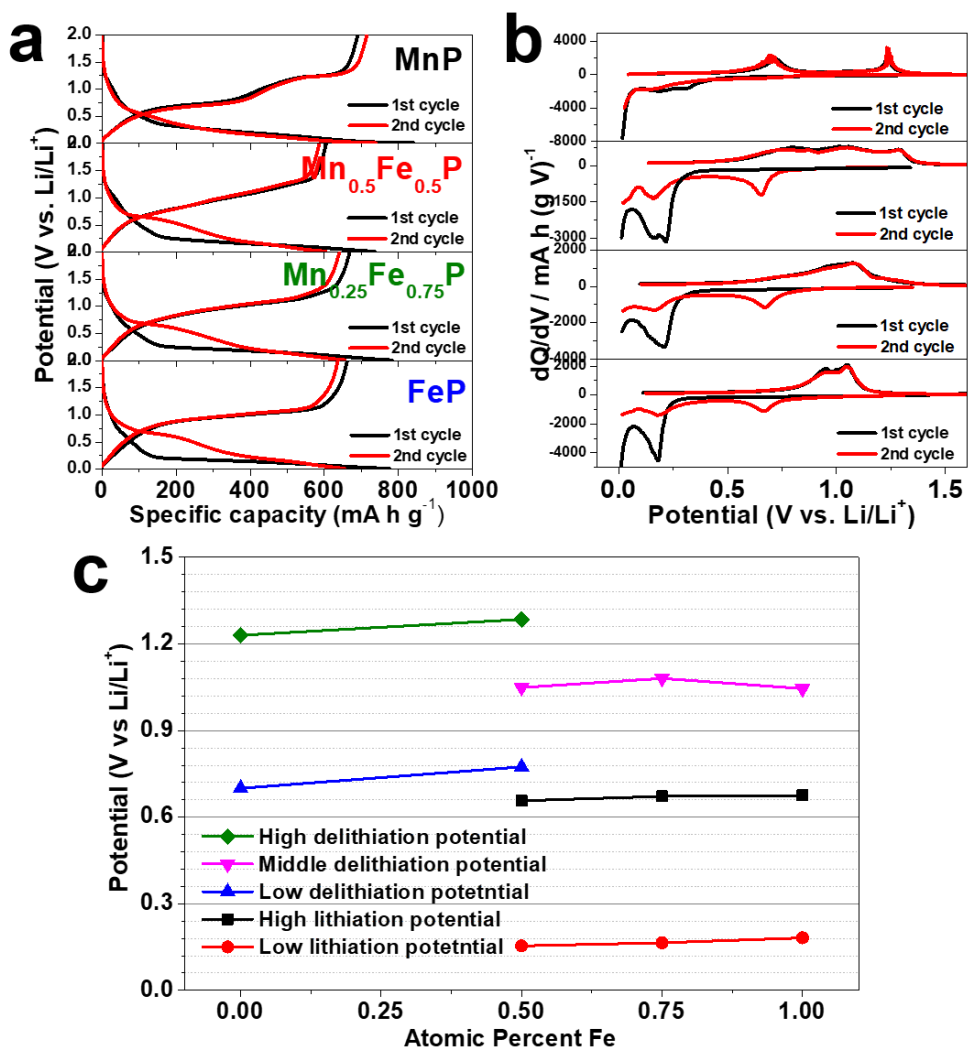


**Figure. 3.3.6** (a) Galvanostatic discharge/charge profiles, (b) corresponding differential capacity plots (DCPs), and (c) voltage variation of lithiation and delithiation plateaus as a function of Fe content in Mn<sub>1-x</sub>Fe<sub>x</sub>P electrodes.

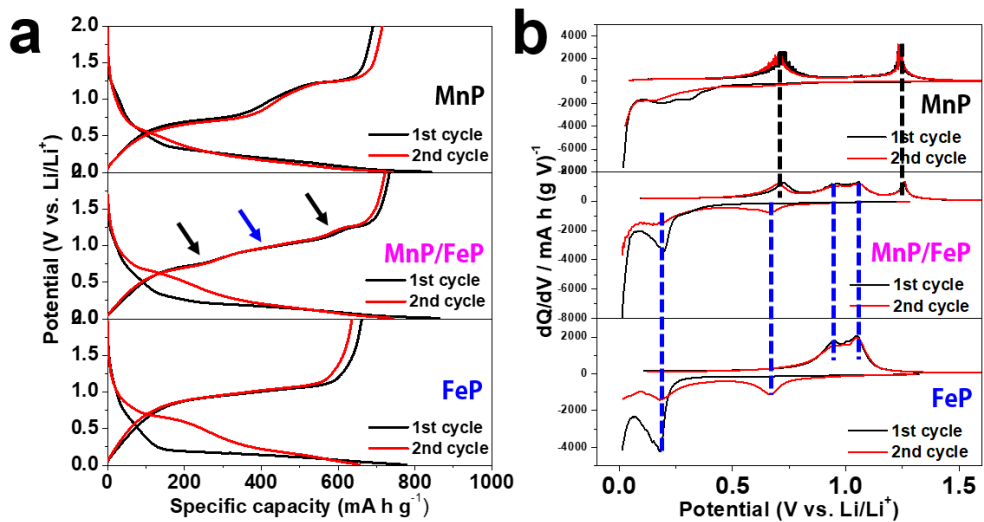


**Figure. 3.3.7** (a) Galvanostatic discharge/charge profiles, and (b) corresponding differential capacity plots (DCPs) of MnP, MnP/FeP, and FeP electrodes.

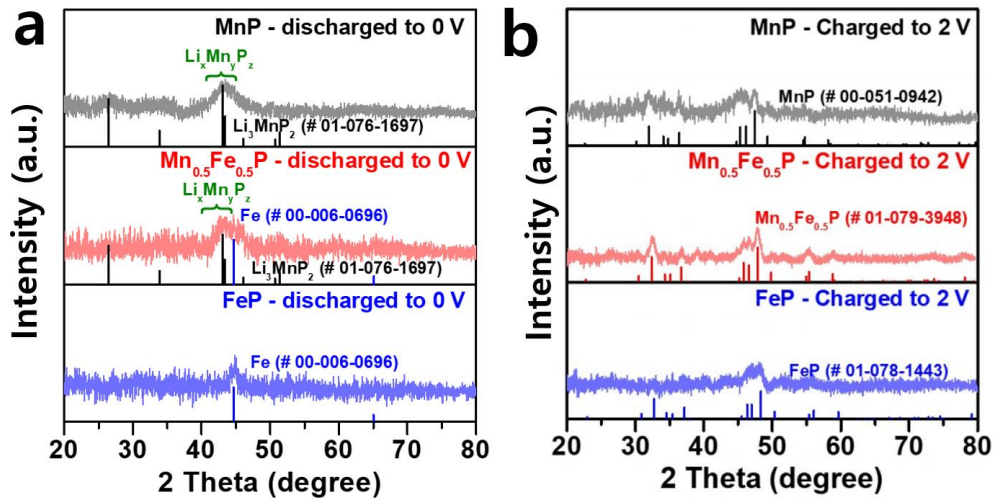


**Figure. 3.3.8** Ex-situ XRD patterns for (a) fully lithiated (0.0 V vs. Li/Li<sup>+</sup>) and (b) delithiated (2.0 V vs. Li/Li<sup>+</sup>) states for Mn<sub>1-x</sub>Fe<sub>x</sub>P electrodes (x = 0, 0.5, and 1.0), respectively.

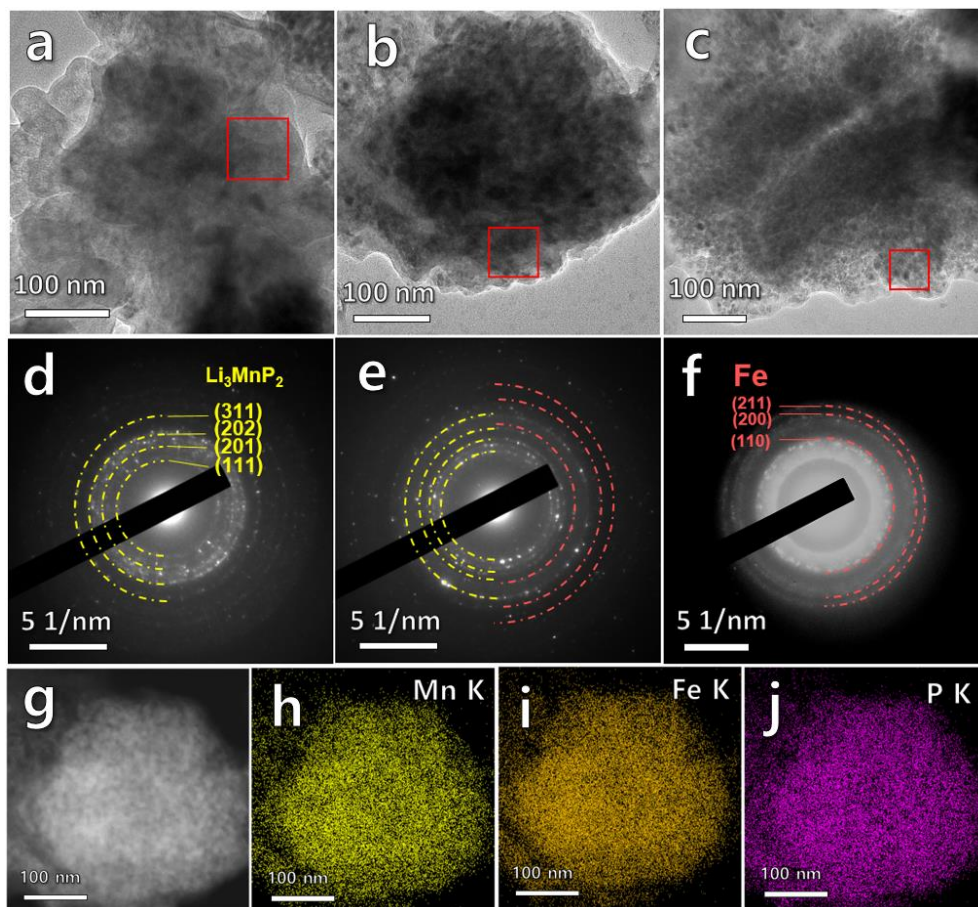


**Figure. 3.3.9** Ex-situ TEM images and SAED patterns of fully discharged states of (a,d) MnP, (b,e) Mn<sub>0.5</sub>Fe<sub>0.5</sub>P, (c,f) FeP electrodes, and (g) STEM image and (h-j) EDS mapping (Mn K, Fe K, and P K) of (b) Mn<sub>0.5</sub>Fe<sub>0.5</sub>P electrode.

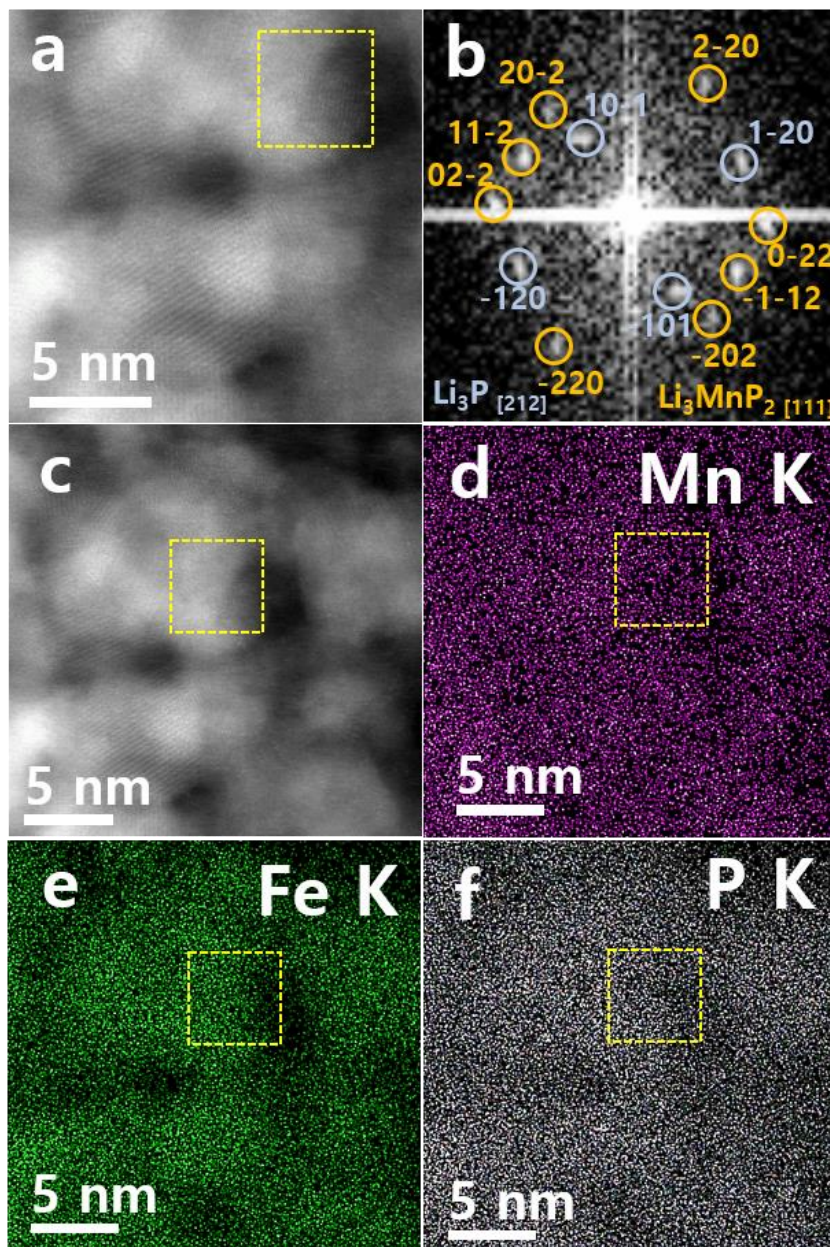


**Figure. 3.3.10** (a) High-magnification HAADF STEM image of fully discharged state of  $\text{Mn}_{0.5}\text{Fe}_{0.5}\text{P}$  electrode and (b) reduced FFT pattern of the marked area in (a). (c) HAADF STEM image and EDS mapping images of (d) Mn K, (e) Fe K, and (f) P K, respectively.

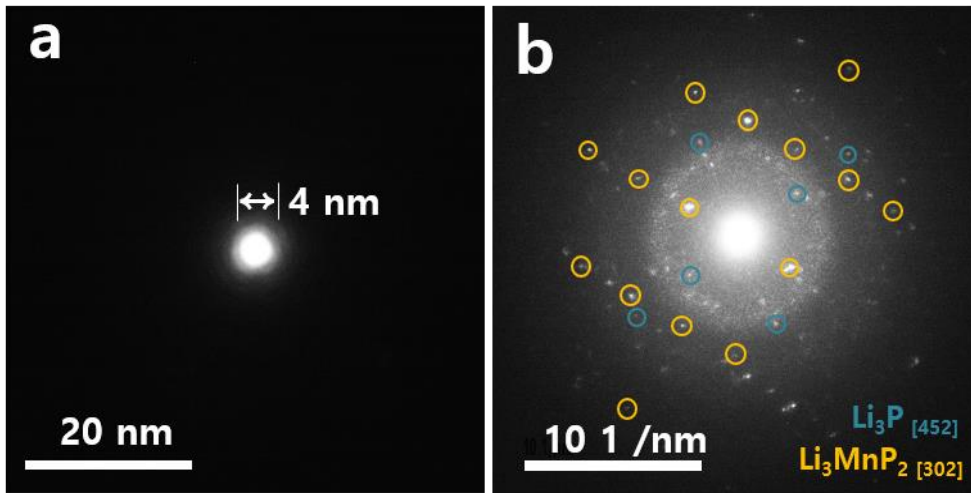


**Figure. 3.3.11** (a) TEM image of nano-sized transmission beam and (b) nano-beam electron diffraction pattern of fully discharged state of  $\text{Mn}_{0.5}\text{Fe}_{0.5}\text{P}$  electrode.

### 3.3.3. Electrochemical Performance

The cycle performance of the  $\text{Mn}_{1-x}\text{Fe}_x\text{P}$  electrodes was investigated in the voltage range of 0.01–2 V vs.  $\text{Li}/\text{Li}^+$  at a current density of  $100 \text{ mA g}^{-1}$  (Figure 3.3.12a and b). All the  $\text{Mn}_{1-x}\text{Fe}_x\text{P}$  electrodes exhibited a relatively high initial coulombic efficiency, and it was 82, 82, 85, and 85% for the electrodes with  $x = 0, 0.5, 0.75,$  and  $1.0,$  respectively. The MnP electrode showed the 1<sup>st</sup> discharge and charge capacities of  $842$  and  $692 \text{ mA h g}^{-1}$ , respectively, but the capacity gradually decreased and only  $229 \text{ mA h g}^{-1}$  was retained after 40 cycles with a 33% cycle retention. The initial discharge and charge capacities of the FeP electrode were  $777$  and  $662 \text{ mA h g}^{-1}$ , respectively. The reversible capacity was relatively well maintained and reduced to  $495 \text{ mA h g}^{-1}$  after 40 cycles, which was 74% of the initial discharge capacity. For the  $\text{Mn}_{0.5}\text{Fe}_{0.5}\text{P}$  solid solution electrode, the 1<sup>st</sup> discharge and charge capacities were  $737.6$  and  $605.3 \text{ mA h g}^{-1}$ , respectively and the reversible capacity was  $463 \text{ mA h g}^{-1}$  after 40 cycles with a cycle retention of 72%. The  $\text{Mn}_{0.25}\text{Fe}_{0.75}\text{P}$  electrode showed initial discharge and charge capacities of  $783.4$  and  $668.5 \text{ mA h g}^{-1}$ , respectively and the discharge capacity of  $506 \text{ mA h g}^{-1}$  was well maintained after 40 cycles with a cycle retention of 76%. Compared to the MnP electrode, the  $\text{Mn}_{0.5}\text{Fe}_{0.5}\text{P}$  and  $\text{Mn}_{0.25}\text{Fe}_{0.75}\text{P}$  solid solution electrodes showed stable cycle retention at the current density of  $100 \text{ mA g}^{-1}$ . One thing to note is that the  $\text{Mn}_{0.5}\text{Fe}_{0.5}\text{P}$  solid solution electrode showed slightly lower initial capacities, but stable cycle retention compared with that of the MnP/FeP mixture electrode (Figure 3.3.12c and d). The reversible 2<sup>nd</sup> discharge capacity of the MnP/FeP mixture electrode was close to the expected value estimated from the reversible capacities of

both the MnP and FeP electrodes whereas the  $\text{Mn}_{0.5}\text{Fe}_{0.5}\text{P}$  solid solution electrode showed a slightly lower capacity (Figure 3.3.12e). Based on the comparison of the reaction peak intensity in the DCPs (Figure 3.3.13), it was found that the contribution of the alloying reaction of MnP to the total capacity was smaller in the 2<sup>nd</sup> cycle of the  $\text{Mn}_{0.5}\text{Fe}_{0.5}\text{P}$  solid solution electrode compared to the MnP/FeP mixture electrode. However, the reversible discharge/charge peaks for MnP continuously decreased with the cycles in the MnP/FeP mixture electrode, indicating that MnP is responsible for the capacity decay in the MnP/FeP mixture electrode (Figure 3.3.12c and 3.3.13d).

When the current density increased to  $1 \text{ A g}^{-1}$ , the initial coulombic efficiency was 76, 83, 82, and 82% and the initial discharge capacity was 517.8, 616.6, 545.8, and 469.6  $\text{mA h g}^{-1}$  for the  $\text{Mn}_{1-x}\text{Fe}_x\text{P}$  electrodes with  $x = 0, 0.5, 0.75,$  and  $1.0,$  respectively (Figure 3.3.14). The reversible specific capacity after 60 cycles was 260, 400, 464, and 370  $\text{mA h g}^{-1}$  with the cycle retention of 59, 80, 97, and 95% for the  $\text{Mn}_{1-x}\text{Fe}_x\text{P}$  electrodes with  $x = 0, 0.5, 0.75,$  and  $1.0,$  respectively. Thus, the  $\text{Mn}_{0.25}\text{Fe}_{0.75}\text{P}$  solid solution electrode showed excellent capacity retention at a high current density of  $1 \text{ A g}^{-1}$ . The good cycling behavior of solid solution electrodes was further corroborated by testing the electrodes at an even higher current density of  $2 \text{ A g}^{-1}$  (Figure 3.3.15). The reversible capacity of the MnP electrode rapidly decreased after 20 cycles, but a relatively high reversible capacity of 370  $\text{mA h g}^{-1}$  was well maintained up to 100 cycles in the  $\text{Mn}_{0.25}\text{Fe}_{0.75}\text{P}$  solid solution electrode. The high electrode kinetics of solid solution electrodes was further confirmed by the rate capability test (Figure 3.3.16). The  $\text{Mn}_{0.25}\text{Fe}_{0.75}\text{P}$  electrode delivered a high capacity of 364  $\text{mA h g}^{-1}$  at a high current density of  $2 \text{ A g}^{-1}$ , and the reversible capacity fully recovered to its original capacity when the current density returned to

100 mA g<sup>-1</sup>. The obtained specific capacity and cycle retention in the Mn<sub>0.25</sub>Fe<sub>0.75</sub>P solid solution electrode were superior to those of the previously reported MnP and FeP-based anodes (Table 3.3.3).

Unexpectedly, the FeP electrode exhibited quite different cycling behavior at the current density of 2 A g<sup>-1</sup>. Initially, the capacity of FeP electrode was negligible, but it gradually increased with cycles and reached 382 mA h g<sup>-1</sup> after 50 cycles (Figure 3.3.15a). The galvanostatic discharge voltage profiles for the 1<sup>st</sup> cycle at various current densities showed that the discharge voltage plateau of the FeP electrode became lower with increasing current density due to a large polarization and reached the cut-off voltage at the current density of 2 A g<sup>-1</sup> before the conversion reaction occurred, which resulted in a negligible capacity (Figure 3.3.17). Meanwhile, in case of solid solution compounds (Mn<sub>1-x</sub>Fe<sub>x</sub>P, x = 0.5 and 0.75), the polarization resulting from increased current density is relatively less than that of FeP electrode, indicating that the overall alloying and conversion reactions occurred at the current density of 2 A g<sup>-1</sup>. Similar capacity activation behavior was observed in the CoP electrode, which was prepared by HEMM under the same synthesis conditions (Figure 3.3.15). Both FeP and CoP are conversion-type materials, which could suffer from the kinetic problems with solid state lithium diffusion in the pristine state by breaking the bond between metal and phosphorus when discharged and reforming the bonding when charged. Indeed, unreacted FeP was detected in the XRD and selected area electron diffraction (SAED) patterns for the 1<sup>st</sup> fully discharged state obtained at the current density of 2 A g<sup>-1</sup> (Figure 3.3.18) indicating that the conversion reaction was not completed and a few hundred nanometersized powder was not fully lithiated at such a high rate. This was possibly due to the slow

layer-by-layer propagation process in the conversion reaction.[3.44,3.45] By repeating the cycles, the reversible capacity gradually increased and the corresponding DCPs (Figure 3.3.15) also showed a continuous increase of the reaction peaks implying that the conversion reaction progressively propagated into larger particles by forming an interconnected, percolating network of metallic nanograins (Fe or Co) and an amorphous  $\text{Li}_3\text{P}$  matrix.[3.44,3.46] The CoP electrode showed much slower capacity activation than that of the FeP electrode (Figure 3.3.15). The difference appears to be related to the diffusivity of the transition metal cations, which determines the size of metallic nanograins, but further study is required to find out the reason for this difference.

The capacity activation behavior was also clearly observed in the cycle data for the MnP/FeP mixture electrode tested at the current density of  $2 \text{ A g}^{-1}$  (Figure 3.3.19). In DCPs, the redox peaks for MnP were present from the first cycle and the peak intensity corresponding to the lithiation/delithiation for FeP gradually increased with cycles, resulting in a continuous increase of the reversible capacity. In contrast, the solid solution  $\text{Mn}_{1-x}\text{Fe}_x\text{P}$  ( $x = 0.5$  and  $0.75$ ) electrodes were fully lithiated from the first discharge and retained their capacity up to 100 cycles without the capacity activation behavior (Figure 3.3.15). Thus, the occurrence of capacity activation in the MnP/FeP electrode can be attributed to the fact that MnP/FeP is a physically mixed composite, whereas  $\text{Mn}_{0.5}\text{Fe}_{0.5}\text{P}$  is chemically mixed and has a much more homogenous distribution of Mn, Fe, and P at the atomic level. This was corroborated with TEM observation (Figure 3.3.20). The STEM and EDS mapping images of the  $\text{Mn}_{0.5}\text{Fe}_{0.5}\text{P}$  electrode showed that Mn, Fe, and P were homogeneously distributed throughout the nanoparticles after the 1<sup>st</sup> cycle (Figure 3.3.20a) and this uniform

distribution was well maintained after 100 cycles (Figure 3.3.20b). On the other hand, the MnP/FeP mixture electrode exhibited a few hundred nanometer-sized MnP and FeP nanoparticles after the 1<sup>st</sup> and 100<sup>th</sup> cycles (Figure 3.3.20c and d), implying that a few hundred nanometer-sized FeP nanoparticles require capacity activation for the full lithiation at such a high rate. However, the capacity activation behavior was not observed in the rate capability test of the FeP electrode (Figure 3.3.16) because the FeP electrode was fully activated at lower current densities.

The fast kinetics in  $Mn_{1-x}Fe_xP$  solid solution compounds ( $x = 0.5$  and  $0.75$ ) were supported by the Nyquist plots obtained by electrochemical impedance spectroscopy (EIS) where the semicircle at high and middle frequencies represented the SEI and charge transfer resistance and the straight sloping line at low frequency corresponded to lithium ion diffusion within the bulk electrode (Figure 3.3.21).[3.47] Before the cycle, all the electrodes exhibited similar EIS spectra indicating that the charge transfer resistance and lithium ion diffusion kinetics were similar (Figure 3.3.21a). For the MnP electrode, the semicircle became smaller with the number of cycles up to 20, but it was the largest after 100 cycles (Figure 3.3.21b–d). The sloping line at low frequency was relatively less steep. This observation (large charge transfer resistance and slow lithium ion diffusion) was consistent with the rapid decrease of reversible capacity after 20 cycles at the current density of  $2 \text{ A g}^{-1}$  (Figure 3.3.15a) and might be related to the agglomeration of the active material typical of alloying reaction materials.[3.48] In the FeP electrode, the semicircle became smaller and the sloping line became steeper with cycles consistent with the capacity activation behavior observed at  $2 \text{ A g}^{-1}$  (Figure 3.3.15a). The solid solution  $Mn_{1-x}Fe_xP$  ( $x = 0.5$  and  $0.75$ ) electrodes exhibited a smaller semicircle and a steeper sloping line during

cycling, which indicate that fast electron transfer and facile lithium ion diffusion have been achieved in the solid solution electrodes. The fast kinetics in  $\text{Mn}_{1-x}\text{Fe}_x\text{P}$  solid solution compounds can be attributed to the in situ generated nanocomposite microstructure where nanocrystalline  $\text{Li}_x\text{Mn}_y\text{P}_z$  and the Fe nano-network are embedded in the amorphous  $\text{Li}_3\text{P}$  matrix, which facilitates the electron and lithium ion transport.[3.44]

To further corroborate the enhanced electrochemical performance of solid solution  $\text{Mn}_{1-x}\text{Fe}_x\text{P}$  electrodes, the morphology of the cycled electrodes (100 cycles at  $2 \text{ A g}^{-1}$ ) was examined by SEM (Figure 3.3.22a–h), which were disassembled in an argon-filled glove box. The as-prepared pristine electrodes showed similar morphologies, and the average particle size was 150–200 nm, irrespective of chemical composition (Figure 3.3.22a–d). To demonstrate the structural stability, the dissembled electrodes were rinsed with dimethyl carbonate (DMC), acetic acid, and D.I. water to remove the SEI layer.[3.47] A severe agglomeration was observed and the original morphology was not retained in the MnP electrode resulting in an increased particle size of  $\sim 500 \text{ nm}$  after 100 cycles at  $2 \text{ A g}^{-1}$  (Figure 3.3.22e). On the other hand, the agglomeration and structural deformation were less severe in  $\text{Mn}_{1-x}\text{Fe}_x\text{P}$  ( $x = 0.5, 0.75$  and  $1.0$ ) electrodes (Figure 3.3.22f–h) and the average particle size was 230, 270, and 290 nm, respectively, indicating that the agglomeration of active materials was significantly inhibited. The cycled  $\text{Mn}_{0.25}\text{Fe}_{0.75}\text{P}$  solid solution electrode (Figure 3.3.22g) was further investigated by TEM (Figure 3.3.22i–l). The STEM image showed the nanostructured morphology (Figure 3.3.22i) and the EDS mapping images (Mn K, Fe K, and P K, Figure 3.3.22j–

l) indicated that Mn, Fe, and P elements were homogenously distributed throughout the  $\text{Mn}_{0.25}\text{Fe}_{0.75}\text{P}$  NPs. From these observations, it can be concluded that the solid solution compound electrodes generate an in situ nanocomposite of the Fe nano-network, the  $\text{Li}_3\text{P}$  matrix, and the ternary  $\text{Li}_x\text{Mn}_y\text{P}_z$  phase, which effectively buffers the accompanying volume variation, hinders the aggregation of the alloying element, and ensures fast electron and ion transport resulting in excellent capacity retention and high rate capability (Figure 3.3.23).[3.16,3.46] At this stage, the scale of homogeneous distribution, the atomic or nano range, is not clearly identified and thus, further study is highly required.

**Table 3.3.3** Lithium storage performance comparison of  $\text{Mn}_{0.25}\text{Fe}_{0.75}\text{P}$  solid solution electrode with the previously reported FeP and MnP-based electrodes.

Materials	Current density ( $\text{mA g}^{-1}$ )	Capacity ( $\text{mA h g}^{-1}$ )	Cycle number (cycle retention)	Ref.
MnP nanorod	144	350		<i>ACS Appl. Mater. Inter.</i> <b>2018</b> , 10, 19739-19745.
	1440	200		
	3600	150		
MnP powder	50	287	50 (33%)	<i>Electrochim. Acta.</i> <b>2013</b> , 95, 230-236.
MnP nanoparticle	120	289	10 (80%)	<i>J. Electrochem. Soc.</i> <b>2012</b> , 159(5), A669-A672.
FeP spheroidal particle	100	600		<i>RSC advance</i> , <b>2016</b> , 6, 87675-87679.
	1000	300		
FeP nanoplate	200	350	100 (60%)	<i>J. Mater. Chem. A</i> , <b>2016</b> , 4, 12781-12789.
FeP nanosphere	200	207	100 (23%)	<i>ACS Nano</i> , <b>2017</b> , 11, 11602-11616.
$\text{Mn}_{0.25}\text{Fe}_{0.75}\text{P}$ nanoparticle	100	506	40 (76%)	This work
	1000	464	60 (97%)	
	2000	370	100 (99%)	

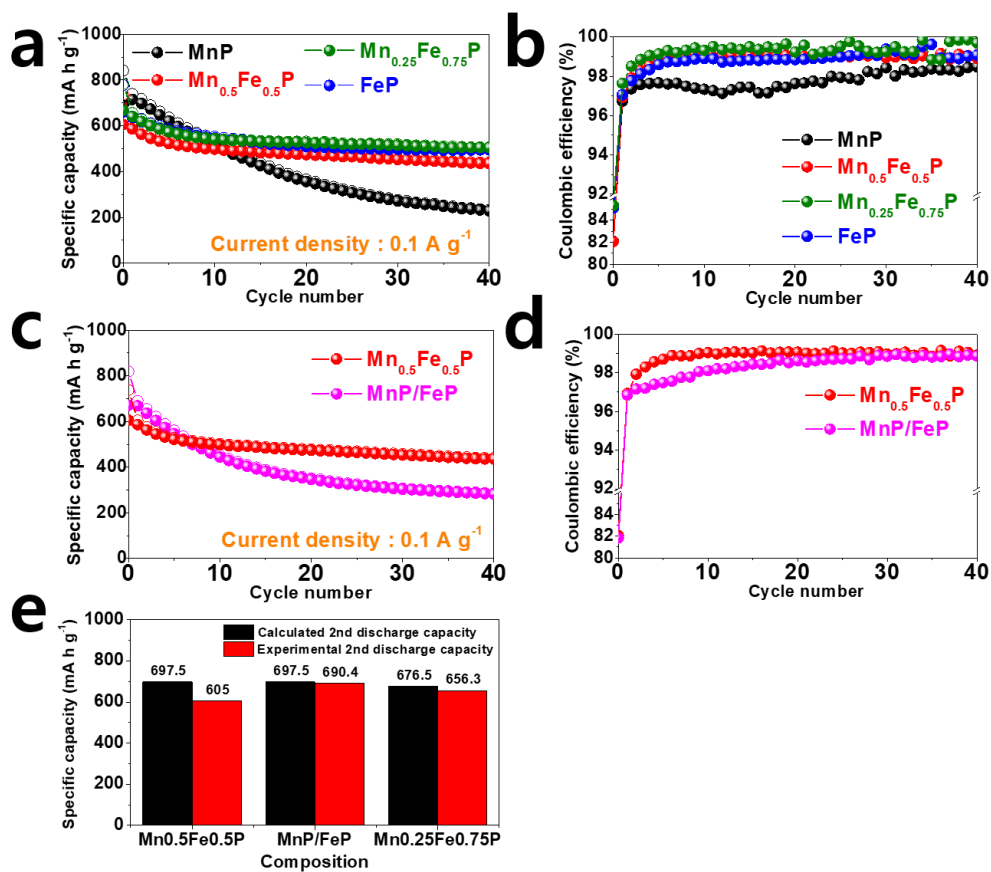


**Figure. 3.3.12** Cycle performance and corresponding Coulombic efficiency of (a,b)  $\text{Mn}_{1-x}\text{Fe}_x\text{P}$  ( $x = 0, 0.5, 0.75,$  and  $1.0$ ) electrodes and (c,d)  $\text{Mn}_{0.5}\text{Fe}_{0.5}\text{P}$  and MnP/FeP electrodes, respectively. (e) Comparison of experimentally determined and expected 2<sup>nd</sup> discharge capacity in  $\text{Mn}_{0.5}\text{Fe}_{0.5}\text{P}$  solid solution and MnP/FeP mixture electrodes. The expected values were estimated from the reversible capacities of both MnP and FeP electrodes.

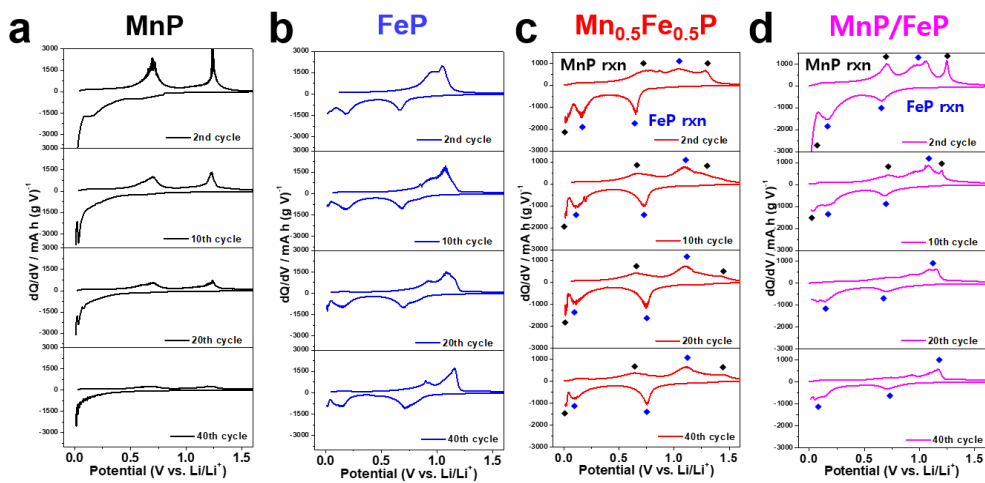


**Figure. 3.3.13** Differential capacity plots (DCPs) for MnP, FeP, Mn<sub>0.5</sub>Fe<sub>0.5</sub>P, and MnP/FeP electrodes for 2<sup>nd</sup>, 10<sup>th</sup>, 20<sup>th</sup>, and 40<sup>th</sup> cycles at the current density of 100 mA g<sup>-1</sup>.

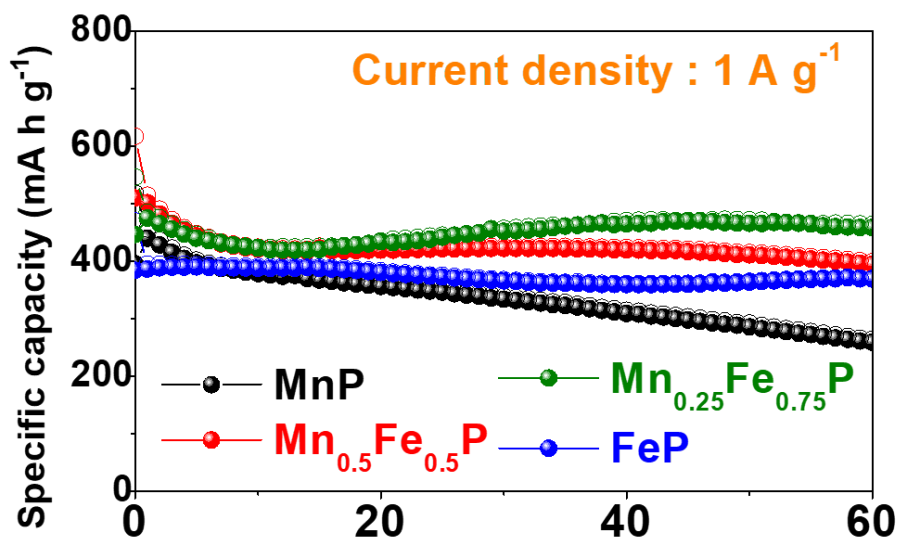


**Figure. 3.3.14** Cycling performance at current density of 1 A g<sup>-1</sup> for Mn<sub>1-x</sub>Fe<sub>x</sub>P (x = 0, 0.5, 0.75, and 1.0) electrodes, respectively.

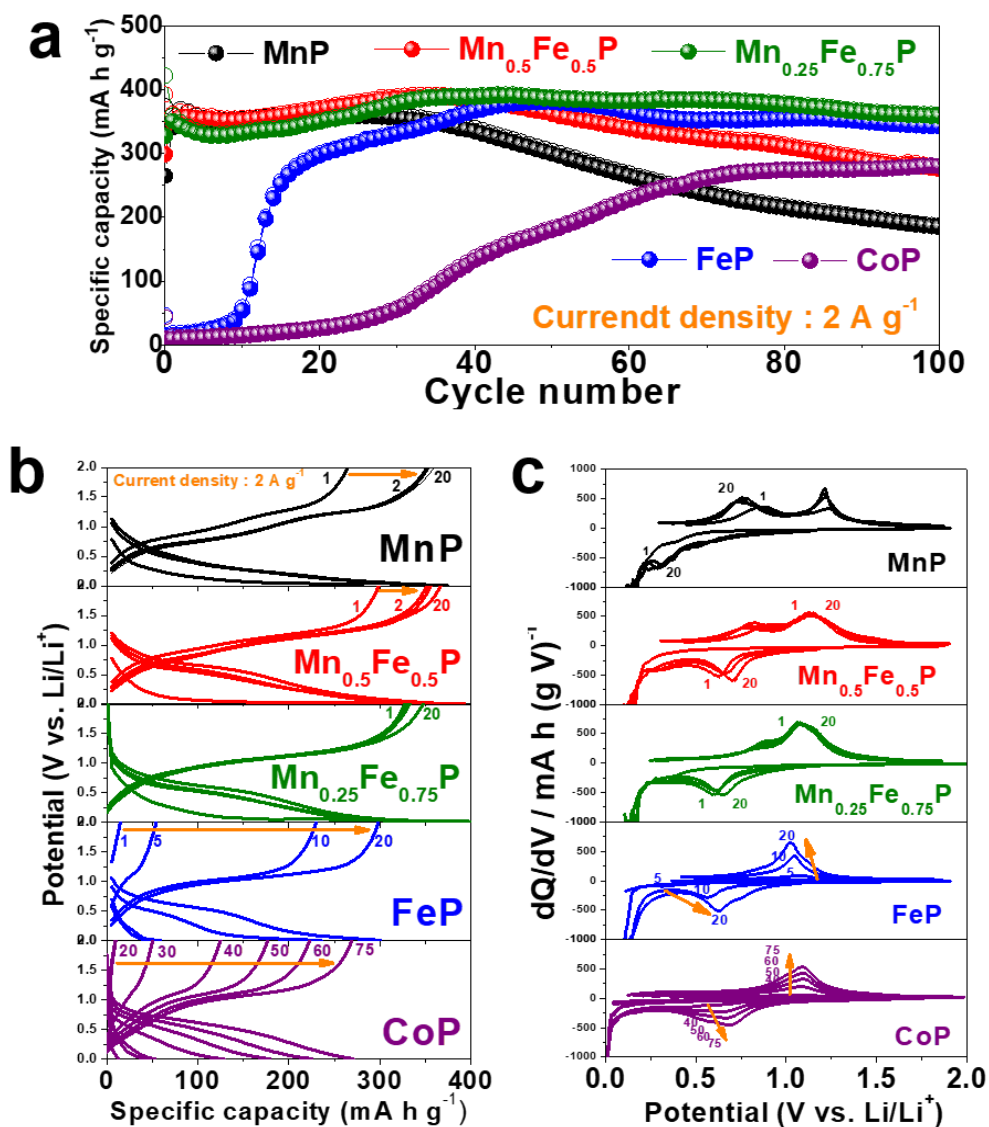


**Figure. 3.3.15** (a) Cycling performance at current density of  $2 \text{ A g}^{-1}$  for  $\text{Mn}_{1-x}\text{Fe}_x\text{P}$  ( $x = 0, 0.5, 0.75,$  and  $1.0$ ) and CoP electrodes and the corresponding (b) galvanostatic discharge/charge voltage profiles and (c) differential capacity plots (DCPs).

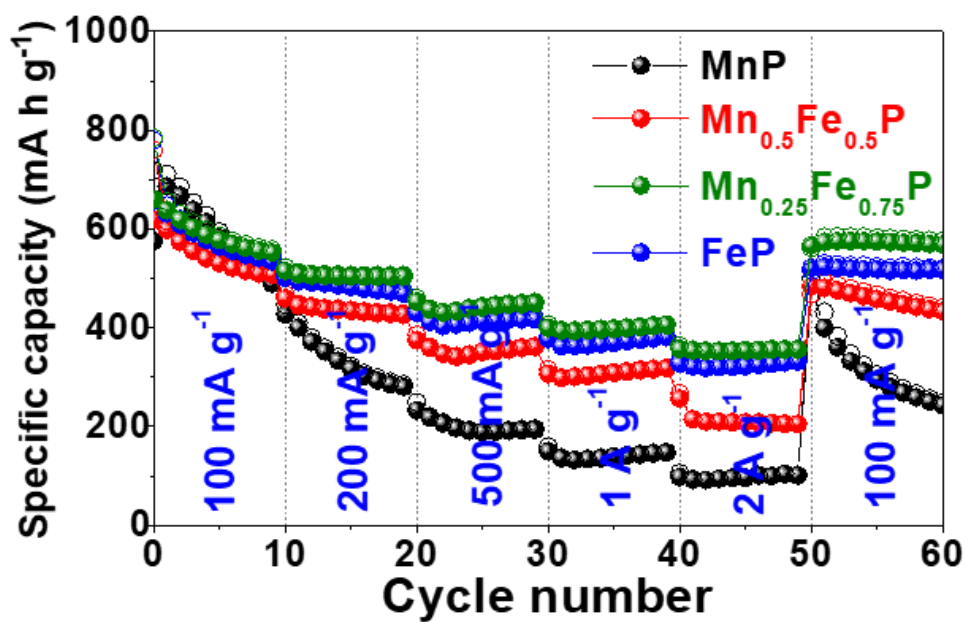


Figure 3.3.16 Rate capabilities of the  $Mn_{1-x}Fe_xP$  ( $x = 0, 0.5, 0.75, \text{ and } 1.0$ ) electrodes.

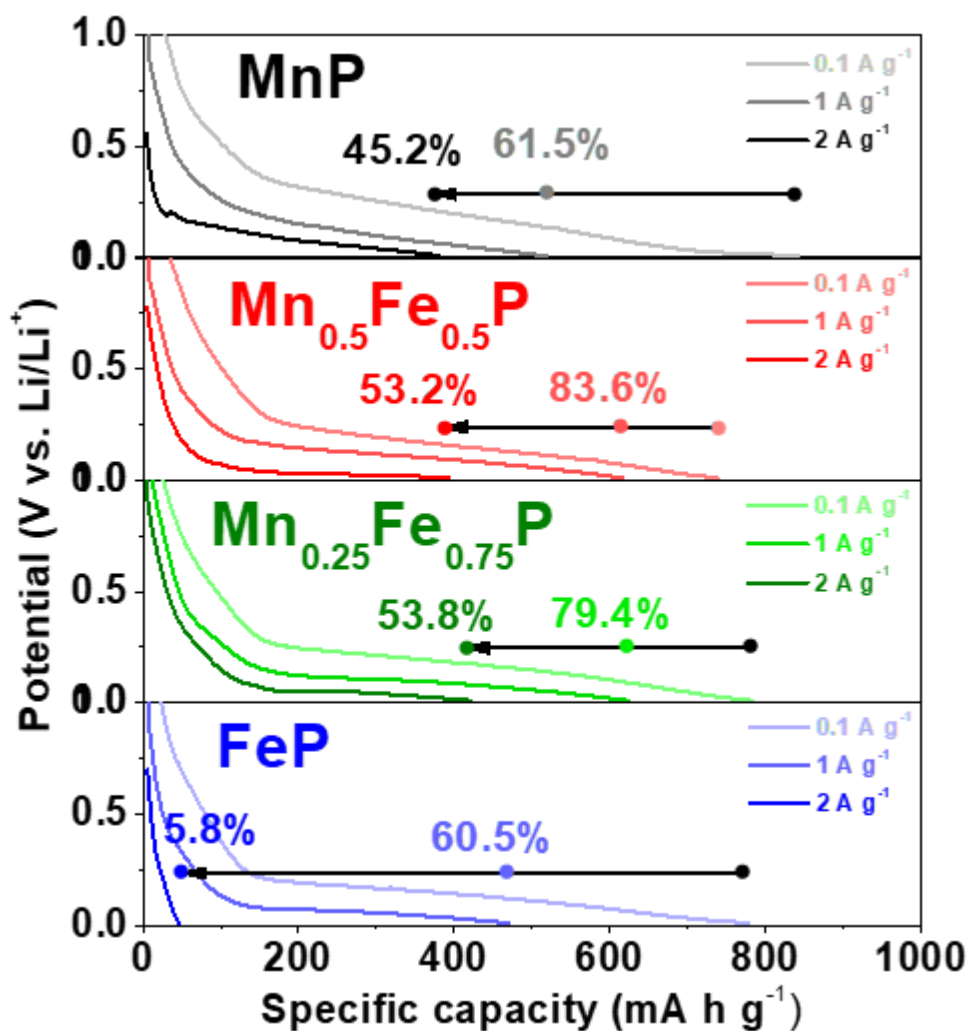
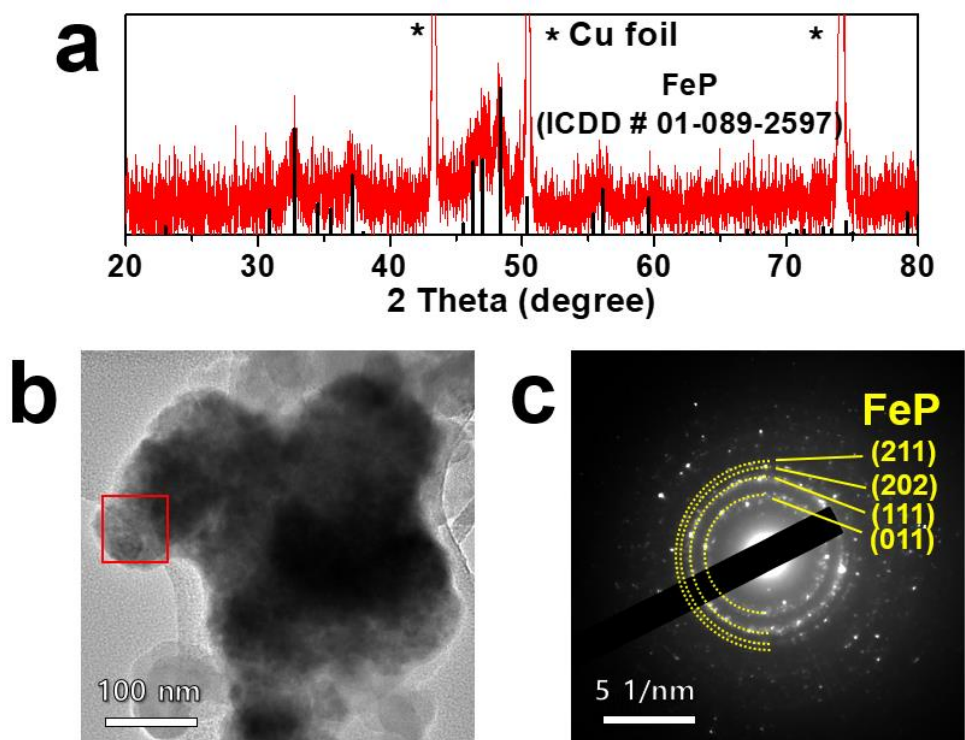
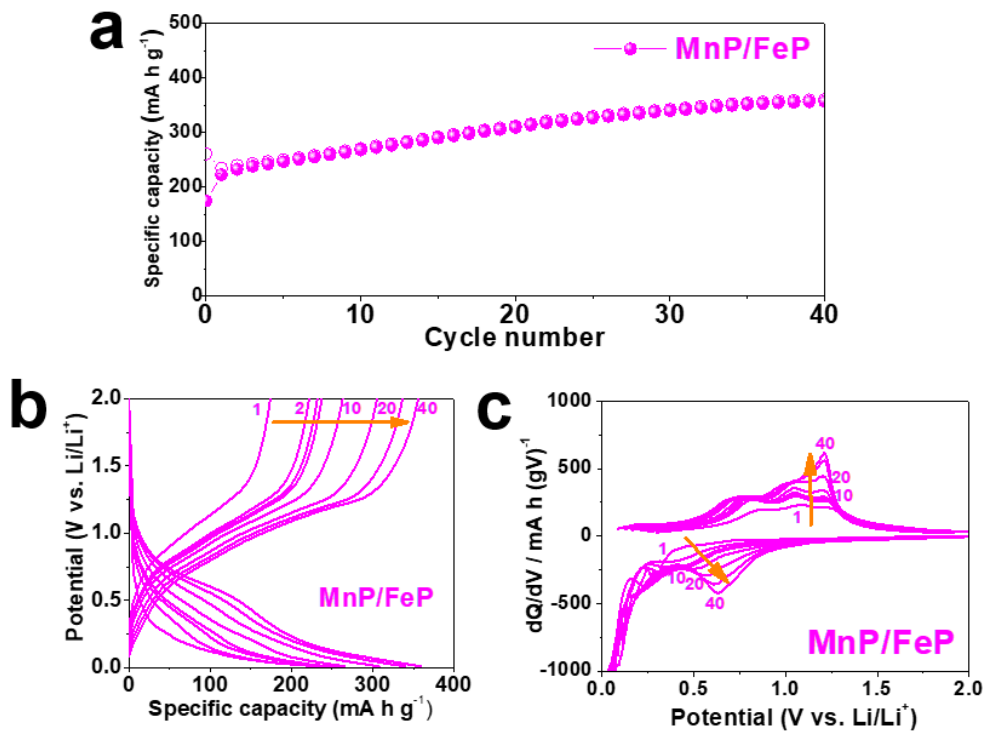


Figure. 3.3.17 Galvanostatic discharge voltage profiles of Mn<sub>1-x</sub>Fe<sub>x</sub>P (x = 0, 0.5, 0.75, and 1.0) electrodes for each 1<sup>st</sup> cycle at 0.1, 1.0, and 2.0 A g<sup>-1</sup>, respectively.



**Figure. 3.3.18** (a) Ex-situ XRD pattern, (b) TEM image, and (c) selected area electron diffraction (SAED) pattern of FeP electrode for 1<sup>st</sup> fully discharged state at 2 A g<sup>-1</sup>.



**Figure. 3.3.19** (a) Cycling performance of MnP/FeP electrode at 2 A g<sup>-1</sup> and corresponding (b) galvanostatic voltage profiles and (c) differential capacity plots (DCPs).

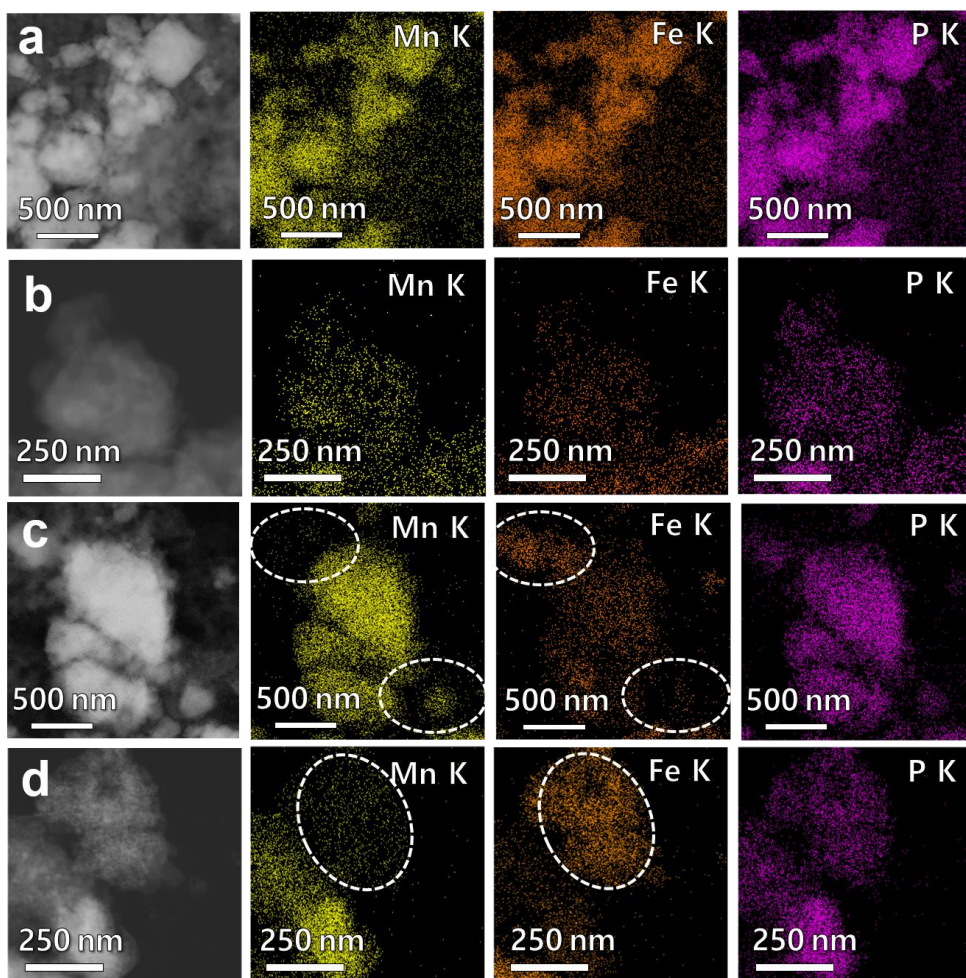


**Figure. 3.3.20** STEM images and EDS mapping images (Mn K, Fe K, and P K) of after 1<sup>st</sup> and 100<sup>th</sup> cycled electrodes tested at 2 A g<sup>-1</sup> for (a,b) Mn<sub>0.5</sub>Fe<sub>0.5</sub>P and (c,d) MnP/FeP electrodes.

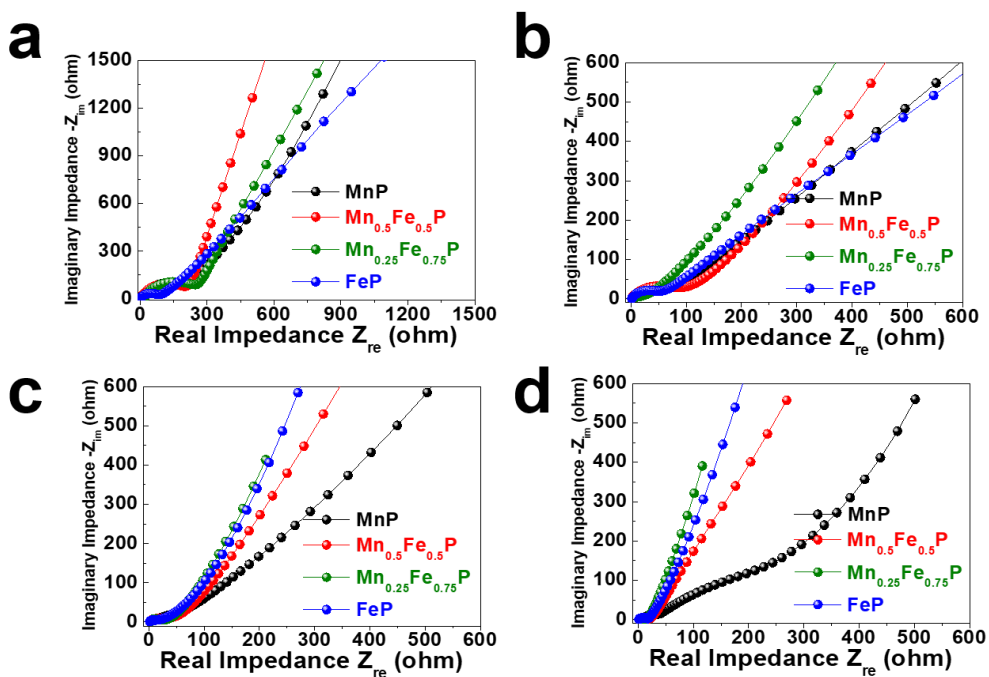


**Figure. 3.3.21** Electrochemical impedance spectroscopy (EIS) data for  $\text{Mn}_{1-x}\text{Fe}_x\text{P}$  ( $x = 0, 0.5, 0.75, \text{ and } 1.0$ ) electrodes (a) before cycle, (b) after the 1<sup>st</sup>, (c) 20<sup>th</sup>, and (d) 100<sup>th</sup> cycles at a current density of  $2 \text{ A g}^{-1}$ .

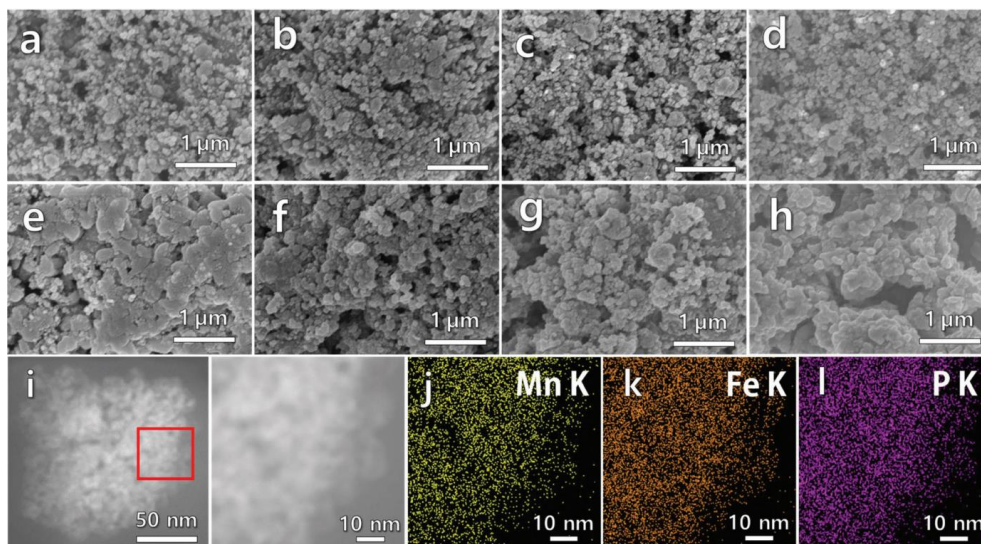


**Figure. 3.3.22** SEM images of the pristine and cycled (100 cycles at  $2 \text{ A g}^{-1}$ )  $\text{Mn}_{1-x}\text{Fe}_x\text{P}$  electrodes (a,e)  $x = 0$ , (b,f)  $x = 0.5$ , (c,g)  $x = 0.75$ , and (d,h)  $x = 1.0$ , (i) STEM image of the cycled (100 cycles at  $2 \text{ A g}^{-1}$ )  $\text{Mn}_{0.25}\text{Fe}_{0.75}\text{P}$  electrode and EDS elemental mapping images (j) Mn K, (k) Fe K, and (l) P K) of (i).

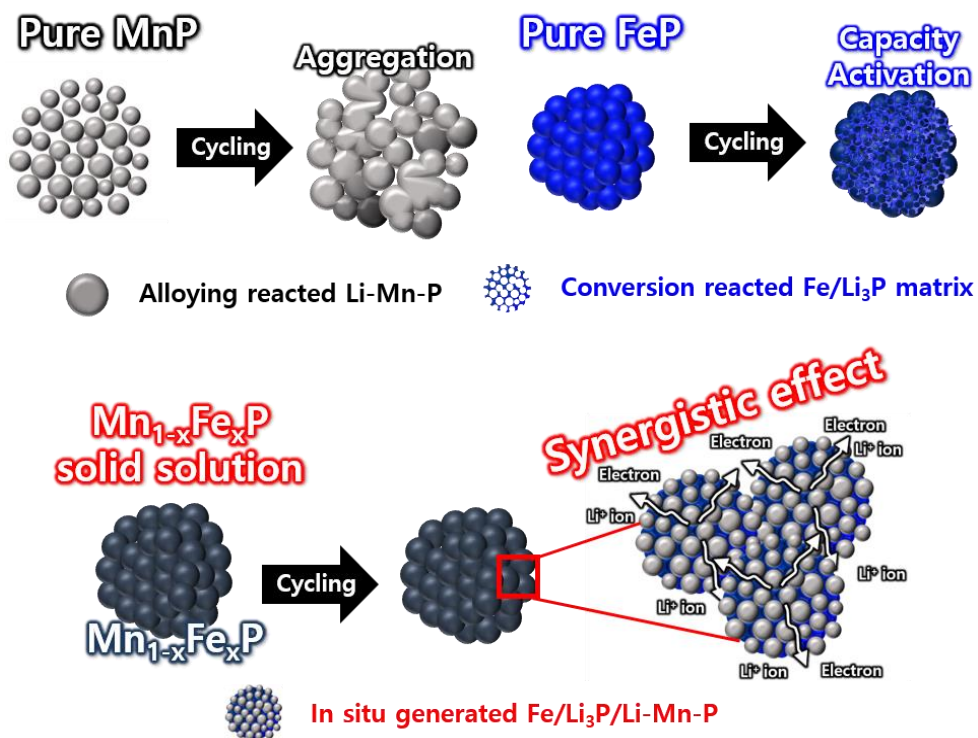


**Figure. 3.3.23** Schematic illustration for the discharged state of MnP, FeP, and Mn<sub>1-x</sub>Fe<sub>x</sub>P electrodes.

### 3.4. Conclusion

The substitutional solid solution  $Mn_{1-x}Fe_xP$  compounds between alloying reaction-type MnP and conversion reaction type FeP were successfully synthesized via a facile high energy mechanical milling process. The lattice parameters of the as prepared compounds determined by synchrotron X-ray diffraction followed Vegard's law confirming the complete solid solution behavior. The  $Mn_{1-x}Fe_xP$  solid solution electrodes showed the combined lithiation/delithiation voltage plateaus of MnP and FeP electrodes with a slight voltage shift indicating that the solid solution affected the redox reactions of each end member. The  $Mn_{1-x}Fe_xP$  solid solution electrodes showed an enhanced electrochemical performance in terms of initial coulombic efficiency, reversible specific capacities, cycle retention, and rate capability resulting from the beneficial combination of the advantages of two end members. These synergistic effects can be attributed to the in situ generated nanocomposite nature of the Li-Mn-P alloying element and the Fe nano-network in combination with the surrounding amorphous lithium phosphide, which effectively buffers the accompanying volume variation, hinders the aggregation of the alloying element, and ensures electron and ion transport. The obtained results suggest that the solid solution of different reaction type materials is one of the effective methods for developing new promising anode materials for lithium- and sodium-ion batteries.

### 3.5. Bibliography

- [3.1] N. Nitta, F. Wu, J. T. Lee, G. Yushin, *Mater. Today*, **2015**, 18, 252–264.
- [3.2] V. Aravindan, Y.-S. Lee, S. Madhavi, *Adv. Energy Mater.*, **2015**, 5, 1402225.
- [3.3] Y. Wang, H. Li, P. He, E. Hosono, H. Zhou, *Nanoscale*, **2010**, 2, 1294–1305.
- [3.4] L. Lu, X. Han, J. Li, J. Hua, M. Ouyang, *J. Power Sources*, **2013**, 226, 272–288.
- [3.5] I. R. M. Kottegoda, Y. Kadoma, H. Ikuta, Y. Uchimoto, M. Wakihara, *Electrochem. Solid-State Lett.*, **2002**, 5, A275–A278.
- [3.6] D. Aurbach, E. Zinigrad, Y. Cohen, H. Teller, *Solid State Ionics*, **2002**, 148, 405–416.
- [3.7] F. Ding, W. Xu, D. Choi, W. Wang, X. Li, M. H. Engelhard, X. Chen, Z. Yang, J.-G. Zhang, *J. Mater. Chem.*, **2012**, 22, 12745–12751.
- [3.8] Y. Zhang, X. Rui, Y. Tang, Y. Liu, J. Wei, S. Chen, W. R. Leow, W. Li, Y. Liu, J. Deng, B. Ma, Q. Yan, X. Chen, *Adv. Energy Mater.*, **2016**, 6, 1502409.
- [3.9] M. Ashuri, Q. He, L. L. Shaw, *Nanoscale*, **2016**, 8, 74 – 103.
- [3.10] W.-J. Zhang, *J. Power Sources*, **2011**, 196, 13 –24.
- [3.11] M. T. McDowell, S. W. Lee, W. D. Nix, Y. Cui, *Adv. Mater.*, **2013**, 25, 4966.
- [3.12] S.-H. Yu, S. H. Lee, D. J. Lee, Y.-E. Sung, T. Hyeon, *Small*, **2016**, 12, 2146–2172.
- [3.13] X. Xu, W. Liu, Y. Kim, J. Cho, *Nano Today*, **2014**, 9, 604– 630.

- [3.14] V. Etacheri, R. Marom, R. Elazari, G. Salitra, D. Aurbach, *Energy Environ. Sci.*, **2011**, 4, 3243–3262.
- [3.15] N. Nitta, G. Yushin, *Part. Part. Syst. Character.*, **2014**, 31, 317–336.
- [3.16] D. Bresser, S. Passerini, B. Scrosati, *Energy Environ. Sci.*, **2016**, 9, 3348–3367.
- [3.17] M. N. Obrovac, V. L. Chevrier, *Chem. Rev.*, **2014**, 114, 11444–11502.
- [3.18] N. Loeffler, D. Bresser, S. Passerini, *Johnson Matthey Technol. Rev.*, **2015**, 59, 34–44.
- [3.19] F. Wu, J. Bai, J. Feng, S. Xiong, *Nanoscale*, **2015**, 7, 17211–17230.
- [3.20] P. F. Teh, S. S. Pramana, C. Kim, C.-M. Chen, C.-H. Chuang, Y. Sharma, J. Cabana, S. Madhavi, *J. Phys. Chem. C*, **2013**, 117, 24213–24223.
- [3.21] P. F. Teh, S. S. Pramana, Y. Sharma, Y. W. Ko, S. Madhavi, *ACS Appl. Mater. Interfaces*, **2013**, 5, 5461–5467.
- [3.22] X. Guo, X. Lu, X. Fang, Y. Mao, Z. Wang, L. Chen, X. Xu, H. Yang, Y. Liu, *Electrochem. Commun.*, **2010**, 12, 847–850.
- [3.23] P. A. Connor, J. T. S. Irvine, *J. Power Sources*, **2001**, 97–98, 223–225.
- [3.24] D. Bresser, F. Mueller, M. Fiedler, S. Krueger, R. Kloepsch, D. Baither, M. Winter, E. Paillard, S. Passerini, *Chem. Mater.*, **2013**, 25, 4977.
- [3.25] G. Giuli, A. Trapananti, F. Mueller, D. Bresser, F. d’Acapito, S. Passerini, *Inorg. Chem.*, **2015**, 54, 9393.

- [3.26] F. Mueller, D. Bresser, V. S. K. Chakrayadhanula, S. Passerini, *J. Power Sources*, **2015**, 299, 398.
- [3.27] S. Li, M. Ling, J. Qiu, J. Han, S. Zhang, *J. Mater. Chem. A*, **2015**, 3, 9700.
- [3.28] Y. Oumellal, A. Rougier, G. A. Nazri, J.-M. Tarascon, L. Aymard, *Nat. Mater.*, **2008**, 7, 916–921.
- [3.29] D. H. Gregory, *Chem. Rec.*, **2008**, 8, 229–239.
- [3.30] W. Li, G. Wu, C. M. Araujo, R. H. Scheicher, A. Blomqvist, R. Ahuja, Z. Xiong, Y. Feng, P. Chen, *Energy Environ. Sci.*, **2010**, 3, 1524–1530.
- [3.31] X. Wang, P. Sun, J. Qin, J. Wang, Y. Xiao, M. Cao, *Nanoscale*, **2016**, 8, 10330–10338.
- [3.32] C.-M. Park, Y.-U. Kim, H.-J. Sohn, *Chem. Mater.*, **2009**, 21, 5566–5568.
- [3.33] D. Yang, J. Zhu, X. Rui, H. Tan, R. Cai, H. E. Hoster, D. Y. W. Yu, H. H. Hng, Q. Yan, *ACS Appl. Mater. Interfaces*, **2013**, 5, 1093–1099.
- [3.34] L. Li, Y. Peng, H. Yang, *Electrochim. Acta*, **2013**, 95, 230.
- [3.35] S. Boyanov, J. Bernardi, F. Gillot, L. Dupont, M. Womes, J.-M. Tarascon, L. Monconduit, M.-L. Doublet, *Chem. Mater.*, **2006**, 18, 3531–3538.
- [3.36] H. Fjellvag, A. Kjekshus, *Acta Chem. Scand., Ser. A*, **1986**, 40,8 –16.
- [3.37] S. Rundqvist, P. C. Nawapong, *Acta Chem. Scand.*, **1965**, 19, 1006–1008.
- [3.38] H.-T. Kwon, C. K. Lee, K.-J. Jeon, C.-M. Park, *ACS Nano*, **2016**, 10, 5701–5709.

- [3.39] W. Li, L. Ke, Y. Wei, S. Guo, L. Gan, H. Li, T. Zhai, H. Zhou, *J. Mater. Chem. A*, **2017**, 5, 4413–4420.
- [3.40] S.-O. Kim, A. Manthiram, *Chem. Commun.*, **2016**, 52, 4337–4340.
- [3.41] D. Ha, J. Kim, J. Han, S. Kang, *Ceram. Int.*, **2018**, 44, 19247–19253.
- [3.42] G. Schuck, A. Iwata, A. Sasaki, A. Himeda, H. Konaka, N. Muroyama, *Acta Crystallogr., Sect. A: Found. Crystallogr.*, **2010**, 66, S311.
- [3.43] M. H. Oh, T. Yu, S.-H. Yu, B. Lim, K.-T. Ko, M.-G. Willinger, D.-H. Seo, B. H. Kim, M. G. Cho, J.-H. Park, K. Kang, Y.-E. Sung, N. Pinna, T. Hyeon, *Science*, **2013**, 340, 964.
- [3.44] F. Wang, H.-C. Yu, M.-H. Chen, L. Wu, N. Pereira, K. Thornton, A. Van der Ven, Y. Zhu, G. G. Amatucci, J. Graetz, *Nat. Commun.*, **2012**, 3, 1201.
- [3.45] F. Lin, D. Nordlund, T.-C. Weng, Y. Zhu, C. Ban, R. M. Richards, H. L. Xin, *Nat. Commun.*, **2014**, 5, 3358.
- [3.46] F. Wang, R. Robert, N. A. Chernova, N. Pereira, F. Omenya, F. Badway, X. Hua, M. Ruotolo, R. Zhang, L. Wu, V. Volkov, D. Su, B. Key, M. S. Whittingham, C. P. Grey, G. G. Amatucci, Y. Zhu, J. Graetz, *J. Am. Chem. Soc.*, **2011**, 133, 18828–18836.
- [3.47] J. W. Choi, J. McDonough, S. J. Jeong, J. S. Yoo, C. K. Chan, Y. Cui, *Nano Lett.*, **2010**, 10, 1409–1413.
- [3.48] M. Fan, Y. Chen, Y. Xie, T. Yang, X. Shen, N. Xu, H. Yu, C. Yan, *Adv. Funct. Mater.*, **2016**, 26, 5019–5027.

# **Chapter 4. A Novel Solid Solution $Mn_{1-x}V_xP$ Anode with Alloying/Insertion Hybrid Electrochemical Reaction for High Performance Lithium-Ion Batteries**

## **4.1. Introduction**

Rechargeable Li-ion battery (LIB) is emerging as a next generation energy storage system owing to its attractive electrochemical properties such as high energy and power density, fast charge-discharge capability, and long service lifetime. With the emergence of large-scale energy storage applications, including electric vehicles (EVs), hybrid electric vehicles (HEVs), and energy storage system (ESS), the relatively low charge capacity of the commercial graphite anode limits its practical application.[4.1-4.3] Even though the exploration of alternative electrode materials for high energy density anode has been conducted on various electrochemical reaction mechanisms, such as alloying, conversion, and insertion reactions, the intrinsic shortcomings of each reaction mechanism undermine the electrode performance.[4.4-4.7] The alloying and conversion reaction anodes typically exhibit the high theoretical capacity than insertion reaction anode, but a rapid capacity fading occurs during cycles due to large volume change, pulverization, and agglomeration of active materials.[4.8-4.11] On the other hand, the insertion reaction anodes show an excellent cycle retention but a low theoretical capacity hampers its implementation in high energy density applications.[4.7,4.12]

The most desirable solution would be a combination between alloying or conversion reaction anode with insertion reaction anode to overcome their own distinct limitations. Many researches have been conducted on the high performance nanocomposite anodes to prevent the electrode degradation by mixing or coating the insertion reaction anode materials, which are mainly carbonaceous materials and early transition metal (titanium and vanadium) oxides, on the alloying or conversion reaction anode materials.[4.13-4.20] This approach has improved the cycle retention properties by mitigating the volume expansion, pulverization, and agglomeration of alloying or conversion reaction anodes by providing the buffer spaces with a negligible volume change of insertion reaction material.

A new strategy has been proposed to overcome these intrinsic shortcomings of each reaction mechanism by introducing the material systems to form a single compound with different types of reaction mechanisms and to allow the simultaneous hybrid electrochemical reaction of two different mechanisms in a single phase. The typical example of this material system is conversion and alloying materials (CAMs), which is the beneficial combination of alloying and conversion reactions in a single compound, that allow the hybrid conversion/alloying reactions in a single phase.[4.21,4.22] This leads to the excellent synergistic interactions due to their atomically homogeneous and finer distribution than that of physically mixed nanocomposite between two individual materials.[4.23-4.26] However, a single compound between alloying/conversion reaction and insertion reaction has been rarely investigated. Unlike the CAMs, since the realization of hybrid electrochemical reaction with the insertion reaction in a single compound requires sufficient spaces to Li-ion insertion/extraction in the crystal structure, the hybrid reaction anodes

should be designed with a similar crystal structure of insertion reaction anode, which can be mainly a solid solution phase.

A rutile structure  $\text{Sn}_{1-x}\text{Ti}_x\text{O}_2$  ( $0 \leq x \leq 1$ ) solid solution is the typical example of a single compound between alloying/conversion reaction and insertion reaction.[4.27-4.30] However, a dramatic improvement of the electrochemical performance has not been observed yet, and this can be attributed to large initial irreversibility and significant structural changes resulting from conversion and alloying reaction of  $\text{SnO}_2$ ,[4.31] where the lithiated phases ( $\text{Li}_{4.4}\text{Sn}$  and  $\text{Li}_2\text{O}$ ) have no structural relation with initial  $\text{Sn}_{1-x}\text{Ti}_x\text{O}_2$  solid solution. In this regard, the structural relation between lithiated phase and initial solid solution phase should be also considered when designing a highly reversible hybrid electrochemical reaction solid solution compounds.

The monophosphides of 3d transition metals (Ti-Ni) can be promising candidates for hybrid electrochemical reaction anodes because they adopt the NiAs-type crystal structures and form the solid solutions with a high solubility limit,[4.32-4.34] but they exhibit the different types of electrochemical reaction with Li-ions (insertion, alloying, and conversion) depending on the nature of the metals.[4.35-4.40] In addition, metal phosphide group shows the improved energy density compared with the metal oxide group by lowering the Li-ion reaction potential and voltage hysteresis.[4.41,4.42] Among the monophosphides, vanadium monophosphide (VP) with a hexagonal NiAs structure (space group  $P6_3/mmc$ ) shows an insertion reaction with Li-ions and delivers a reversible capacity of  $\sim 250 \text{ mA h g}^{-1}$  with an excellent cycle retention.[4.36] On the other hand, manganese monophosphide (MnP) with an orthorhombic distorted NiAs structure (space group

*Pnma*) shows an alloying reaction with Li-ions by forming the  $\text{Li}_x\text{Mn}_y\text{P}_z$  alloy phase in which spatial atomic arrangement is similar to the original MnP structure. MnP delivers high initial discharge and charge capacities of 1104 and 870 mA h g<sup>-1</sup>, respectively, but suffers a rapid capacity fading.[4.37] The crystal structures of VP and MnP are related to NiAs-type and thus, VP and MnP can form the solid solution to a certain extent. The solid solution  $\text{Mn}_{1-x}\text{V}_x\text{P}$  is highly feasible to exhibit both insertion and alloying hybrid electrochemical reactions in a few-nanometer scale and maintain its initial structure during cycling, which possibly results in a high capacity with an excellent cycle stability.

In this work,  $\text{Mn}_{1-x}\text{V}_x\text{P}$  solid solution compound is proposed as a high performance alloying/insertion hybrid electrochemical reaction anode for LIBs. The series of  $\text{Mn}_{1-x}\text{V}_x\text{P}$  compounds ( $x = 0, 0.25, 0.5, 0.75, \text{ and } 1.0$ ) between alloying reaction-type orthorhombic MnP and insertion reaction-type hexagonal VP are synthesized using a facile and mass productive high energy mechanical milling (HEMM). The systematic studies on their structural relation and electrochemical properties as an anode for LIBs are carried out and compared with those of MnP/VP mixture anode. The  $\text{Mn}_{1-x}\text{V}_x\text{P}$  ( $x = 0.25$ ) solid solution electrode shows the excellent high-rate cyclability delivering the reversible capacity of 352 mA h g<sup>-1</sup> after 1500 cycles at 1.0 A g<sup>-1</sup> by the synergistic effects of two different reaction mechanisms.

## 4.2. Experimental Procedure

### *Synthesis of the $Mn_{1-x}V_xP$ ( $x = 0, 0.25, 0.5, 0.75, \text{ and } 1.0$ ) nanoparticles*

$Mn_{1-x}V_xP$  ( $x = 0, 0.25, 0.5, 0.75, \text{ and } 1.0$ ) nanoparticles (NPs) were synthesized via a facile high-energy mechanical milling (HEMM) method with a planetary ball mill (Pulverisette 6, Fritsch). The starting materials used for synthesis are commercial manganese (99.95%, Alfa Aesar), vanadium (99.95%, Alfa Aesar), and red phosphorus (98.9%, Alfa Aesar) without a further purification. Stoichiometric amount of starting materials (Mn, V, and red P) were placed into a hardened steel vial ( $80 \text{ cm}^3$ ) with hardened steel balls (diameter of 3/8 in.) at a ball-to-powder weight of 20:1 and sealed inside an argon-filled glove box. The HEMM was conducted at room temperature with a rotation speed of 300 rpm for 20 h.

### *Materials Characterization*

Synchrotron X-ray powder diffraction (SXPD) patterns of as-prepared powders were examined at the 9B high-resolution powder X-ray diffraction (HRPD) beamline of the Pohang Accelerator Laboratory (PAL) in Korea. The incident beam was vertically collimated using a mirror and monochromatized to a wave length of 1.5167 Å using a double-crystal Si (111) monochromator. Diffraction patterns were collected in the 2 theta scan mode with a step size of  $0.02^\circ$ , step time of 15 s, from 10 to  $130^\circ$ . The lattice parameters of the synthesized samples were obtained with the FullProf software. The chemical composition of as-prepared powder was analyzed by inductively coupled plasma atomic emission spectrometer (ICP-AES, OPTIMA 8300, Perkin-Elmer). The morphology of the powder and electrodes were observed

by field emission scanning electron microscopy (FE-SEM, SU70, Hitachi), transmission electron microscopy (TEM, JEM-2100F, JEOL), and spherical-aberration ( $C_s$ )-corrected scanning transmission electron microscope (STEM, JEM-ARM200F, JEOL).

### *Electrochemical Measurements*

The electrode was prepared by mixing 70% active material, 15% Super P carbon black, and 15% carboxymethyl cellulose (CMC) binder by weight to form a slurry, which was coated on the copper foil and followed by drying in a vacuum oven at 65 °C overnight. The electrode was punched into a round disk with 1.0-1.5 mg cm<sup>-2</sup> loading of active material and then kept in the vacuum oven at 70 °C for 12 h. The CR2032 coin cell was fabricated inside an argon-filled glove box by employing polypropylene (Welcose, Korea) separator and lithium foil counter/reference electrode. The electrolyte used was 1.0 M LiPF<sub>6</sub> in a mixture of ethylene carbonate (EC) and dimethyl carbonate (DMC) (1:1 v/v) with the addition of 5 vol.% of fluoroethylene carbonate (FEC) additive. Galvanostatic cycling test was performed with a battery testing system (Wonatech, Korea) within a voltage range of 0.01–2 V (vs. Li/Li<sup>+</sup>). Electrochemical impedance spectroscopy (EIS) experiment was carried out at a frequency range of 100 kHz to 0.1 Hz with an AC amplitude of 5 mV using an impedance analyzer (Zive, SP1). The full-cell was assembled with as-fabricated Mn<sub>0.75</sub>V<sub>0.25</sub>P electrode as a negative (N) and commercial LiCoO<sub>2</sub> (LCO, Welcos Corporation, Korea) as positive (P). The preparation process of LCO electrode was similar to that of anode. The mass ratio of LCO: Super P: PVDF was 94:3:3. Before the full-cell assembly, negative electrode was pre-lithiated for the formation of stable

SEI layer. The areal capacity of anode was  $2.5 \text{ mA h cm}^{-2}$  while the areal capacity of  $\text{LiCoO}_2$  (LCO) cathode was  $2.5 \text{ mA h cm}^{-2}$ , giving the N/P (negative electrode capacity/positive electrode capacity) ratio of  $\sim 1$ . The full cell was cycled in voltage range between 2.0 and 4.2 V using the same separator and electrolyte condition used in the half-cell test at current density of 0.1 and 1 C ( $1 \text{ C} = 2.5 \text{ mA h cm}^{-2}$ ).

## 4.3. Results and Discussions

### 4.3.1. Synthesis and Physicochemical Characterization

The  $\text{Mn}_{1-x}\text{V}_x\text{P}$  ( $x = 0, 0.25, 0.5, 0.75, \text{ and } 1.0$ ) compounds were synthesized by a high energy mechanical milling (HEMM) using the micron-sized powders of manganese, vanadium, and red phosphorus as starting materials. Figure 4.3.1a shows the high resolution powder diffraction (HRPD) patterns of as-synthesized  $\text{Mn}_{1-x}\text{V}_x\text{P}$  compounds obtained by synchrotron radiation X-ray beam. The XRD patterns of as-prepared MnP ( $x=0$ ),  $\text{Mn}_{0.75}\text{V}_{0.25}\text{P}$  ( $x=0.25$ ), and VP ( $x=1.0$ ) were completely indexed based on the reported orthorhombic (ICDD #00-051-0942), orthorhombic (#01-078-0809), and hexagonal (#01-089-1907) crystal structures, respectively. The diffraction patterns of  $\text{Mn}_{0.5}\text{V}_{0.5}\text{P}$  ( $x=0.5$ ) and  $\text{Mn}_{0.25}\text{V}_{0.75}\text{P}$  ( $x=0.75$ ) were very similar to those of MnP and  $\text{Mn}_{0.75}\text{V}_{0.25}\text{P}$ . The main XRD peaks ((121), (220), and (211)) shifted to the lower  $2\theta$  with increasing the vanadium (V) substitution up to  $x=0.75$ , and the (121) and (220) peaks gradually became a single peak with the highest intensity (Figure 4.3.1b). As described earlier, the crystal structures of VP and MnP are related to NiAs-type structure (Figure 4.3.2) and they are reported to form the solid solution up to  $x=0.25$ . [4.34] Based on the XRD patterns, it can be inferred that the orthorhombic MnP crystal structure (i.e. solid solution) can be extended to  $x=0.75$ . The peak shift to the lower  $2\theta$  is attributed to the larger ionic radius of  $\text{V}^{3+}$  (0.64 Å, CN = 6) compared with that of  $\text{Mn}^{3+}$  (0.58 Å, CN = 6). [4.33,4.34] The Rietveld refinements were conducted on the obtained XRD patterns using FullProf software (Figure 4.3.3) and the refined lattice constants ( $a, b,$

and  $c$ ) and unit cell volume ( $V$ ) are shown in Figure 4.3.4 and Table 4.3.1. The diffraction patterns of  $\text{Mn}_{0.5}\text{V}_{0.5}\text{P}$  and  $\text{Mn}_{0.25}\text{V}_{0.75}\text{P}$  were successfully refined using the MnP crystal structure (space group  $Pnma$ ) confirming the solid solution up to  $x=0.75$ . Consistent with the peak shift to the lower  $2\theta$ , the lattice constants ( $a_{orth}$  and  $c_{orth}$ ) and unit cell volume ( $V_{orth}$ ) of  $\text{Mn}_{1-x}\text{V}_x\text{P}$  compounds linearly increased with increasing the V substitution up to  $x=0.75$ , obeying the Vegard's law. In addition, a MnP/VP mixture (3:1 molar ratio) was prepared by physically mixing the as-synthesized MnP and VP powders to compare the electrochemical properties. The resulting XRD pattern showed the diffraction peaks of both MnP and VP, which was different from that of  $\text{Mn}_{0.75}\text{V}_{0.25}\text{P}$  solid solution (Figure 4.3.5). The chemical composition of as-synthesized  $\text{Mn}_{1-x}\text{V}_x\text{P}$  compounds was analyzed by inductively coupled plasma-atomic emission spectroscopy (ICP-AES) and the actual chemical compositions (Mn, V, and P ratio) are very close to the nominal compositions in all  $\text{Mn}_{1-x}\text{V}_x\text{P}$  compounds (Table 4.3.2).

The powder morphology of as-synthesized  $\text{Mn}_{1-x}\text{V}_x\text{P}$  ( $x = 0, 0.25, \text{ and } 1.0$ ) compounds is shown in Figure 4.3.6a-c. All the powders were spherical and average secondary particle size determined by a dynamic light scattering was  $\sim 150$  nm (Figure 4.3.6d-f). Thus,  $\text{Mn}_{1-x}\text{V}_x\text{P}$  nanoparticles were successfully synthesized by HEMM and the V substitution did not affect the particle morphology and size. As-prepared  $\text{Mn}_{0.75}\text{V}_{0.25}\text{P}$  nanoparticles were further investigated by TEM. The low magnification TEM image shows that as-prepared  $\text{Mn}_{0.75}\text{V}_{0.25}\text{P}$  nanoparticles were aggregates of ca. 5-10 nm sized nanocrystallites (Figure 4.3.7a). The selected area electron diffraction (SAED) pattern was completely indexed to  $\text{Mn}_{0.75}\text{V}_{0.25}\text{P}$  and the ring-like SAED pattern indicates that  $\text{Mn}_{0.75}\text{V}_{0.25}\text{P}$  nanoparticles were randomly

oriented polycrystalline (Figure 4.3.7b). The atomic resolution high angle annular dark field (HAADF) scanning transmission electron microscopy (STEM) image and fast Fourier transform (FFT) pattern of nanocrystallite obtained with spherical aberration( $C_s$ )-corrected STEM confirmed an orthorhombic distorted NiAs structure (space group  $Pnma$ ) of  $Mn_{0.75}V_{0.25}P$  along the  $[001]$  direction (Figure 4.3.7c). The elemental mapping images by energy dispersive spectroscopy (EDS) showed the homogenous distribution of Mn, V, and P not only in tens of nanometer scale but even in a few-nanometer scale (Figure 4.3.7d-f and Figure 4.3.8). In addition, as-synthesized  $Mn_{0.5}V_{0.5}P$  and  $Mn_{0.25}V_{0.75}P$  nanoparticles showed the similar morphology and elemental distribution to those of  $Mn_{0.75}V_{0.25}P$  nanoparticles (Figure 4.3.9).

**Table 4.3.1** XRD Rietveld refinement parameters for as-synthesized  $\text{Mn}_{1-x}\text{V}_x\text{P}$  ( $x =$  (a) 0, (b) 0.25, (c) 0.5, (d) 0.75, and (e) 1.0) compounds.

	Composition				
	MnP	$\text{Mn}_{0.75}\text{V}_{0.25}\text{P}$	$\text{Mn}_{0.5}\text{V}_{0.5}\text{P}$	$\text{Mn}_{0.25}\text{V}_{0.75}\text{P}$	VP
a (Å)	5.2671(5)	5.3344(6)	5.4077(6)	5.5096(1)	3.1837(2)
b (Å)	3.1680(4)	3.1660(5)	3.1761(4)	3.1895(6)	-
c (Å)	5.9238(6)	5.9966(6)	6.0573(6)	6.1100(1)	6.184(4)
V (Å <sup>3</sup> )	98.844(2)	101.28(2)	104.04(2)	107.37(3)	54.28(8)
$R_{\text{wp}}^{\text{a}}$ (%)	4.91	4.30	4.03	7.43	9.15

<sup>a</sup> Weighted profile R-factor.

**Table 4.3.2** Elemental analysis results of  $\text{Mn}_{1-x}\text{V}_x\text{P}$  ( $x = 0, 0.25, 0.5, 0.75, \text{ and } 1.0$ ) compounds by ICP-AES.

<b>Compound</b>	<b>Element</b>	<b>Atomic ratio (actual)</b>	<b>Atomic ratio (expected)</b>
<b>MnP</b>	<b>Mn</b>	<b>0.5</b>	<b>0.5</b>
	<b>P</b>	<b>0.5</b>	<b>0.5</b>
<b>Mn<sub>0.75</sub>V<sub>0.25</sub>P</b>	<b>Mn</b>	<b>0.38</b>	<b>0.375</b>
	<b>V</b>	<b>0.12</b>	<b>0.125</b>
	<b>P</b>	<b>0.5</b>	<b>0.5</b>
<b>Mn<sub>0.5</sub>V<sub>0.5</sub>P</b>	<b>Mn</b>	<b>0.26</b>	<b>0.25</b>
	<b>V</b>	<b>0.24</b>	<b>0.25</b>
	<b>P</b>	<b>0.5</b>	<b>0.5</b>
<b>Mn<sub>0.25</sub>V<sub>0.75</sub>P</b>	<b>Mn</b>	<b>0.13</b>	<b>0.125</b>
	<b>V</b>	<b>0.37</b>	<b>0.375</b>
	<b>P</b>	<b>0.5</b>	<b>0.5</b>
<b>VP</b>	<b>V</b>	<b>0.51</b>	<b>0.5</b>
	<b>P</b>	<b>0.49</b>	<b>0.5</b>

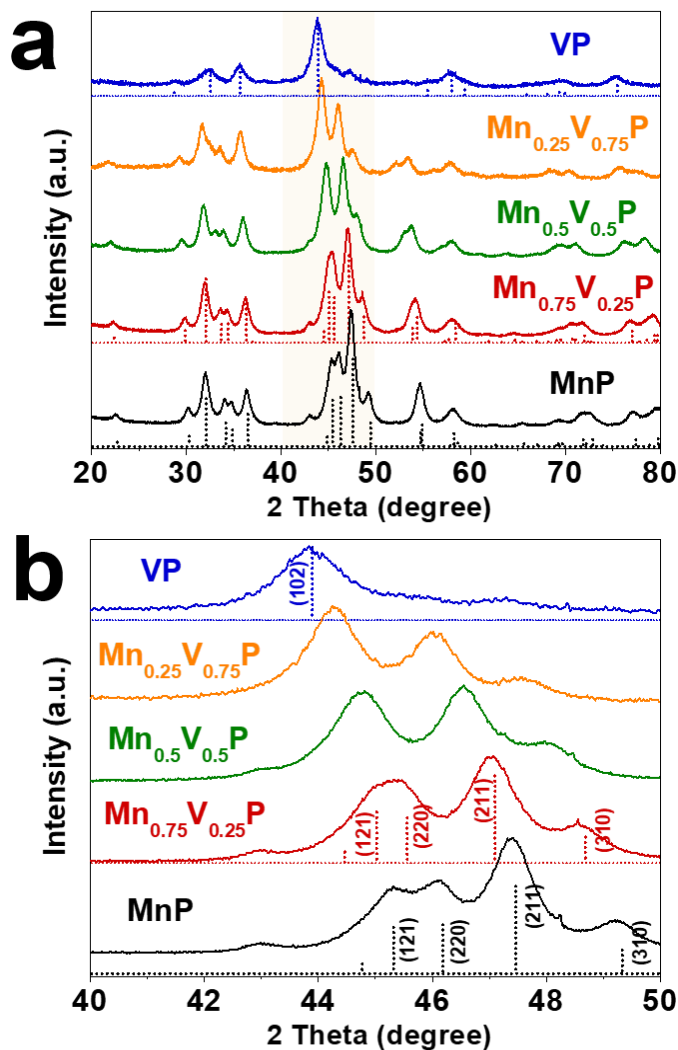


**Figure 4.3.1** (a) XRD patterns and (b) enlargement of the patterns in 2 theta range of 40~50° of  $Mn_{1-x}V_xP$  ( $x = 0, 0.25, 0.5, 0.75, \text{ and } 1.0$ ) compounds. The reference peaks for MnP (ICDD # 00-051-0942, black dash line),  $Mn_{0.75}V_{0.25}P$  (ICDD # 01-078-0809, red dash line), and VP (ICDD # 01-089-1907, blue dash line) are included.

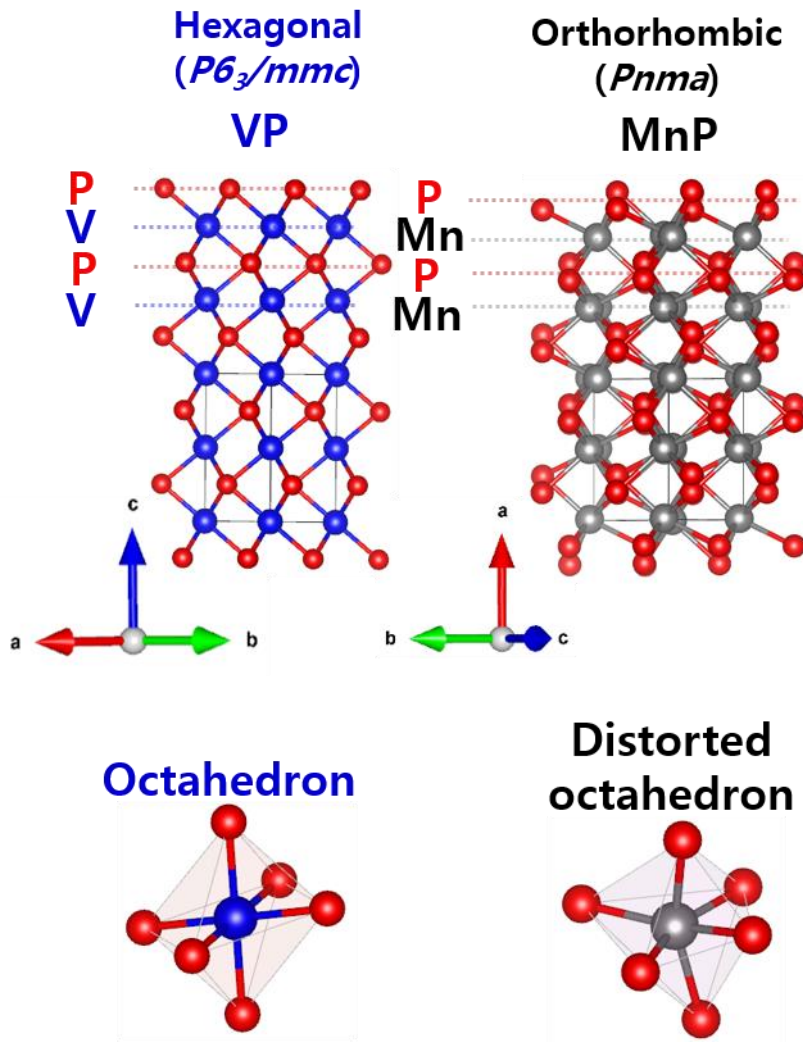


**Figure 4.3.2** Crystal structure and local structure of  $MP_6$  octahedron of hexagonal VP and orthorhombic MnP.

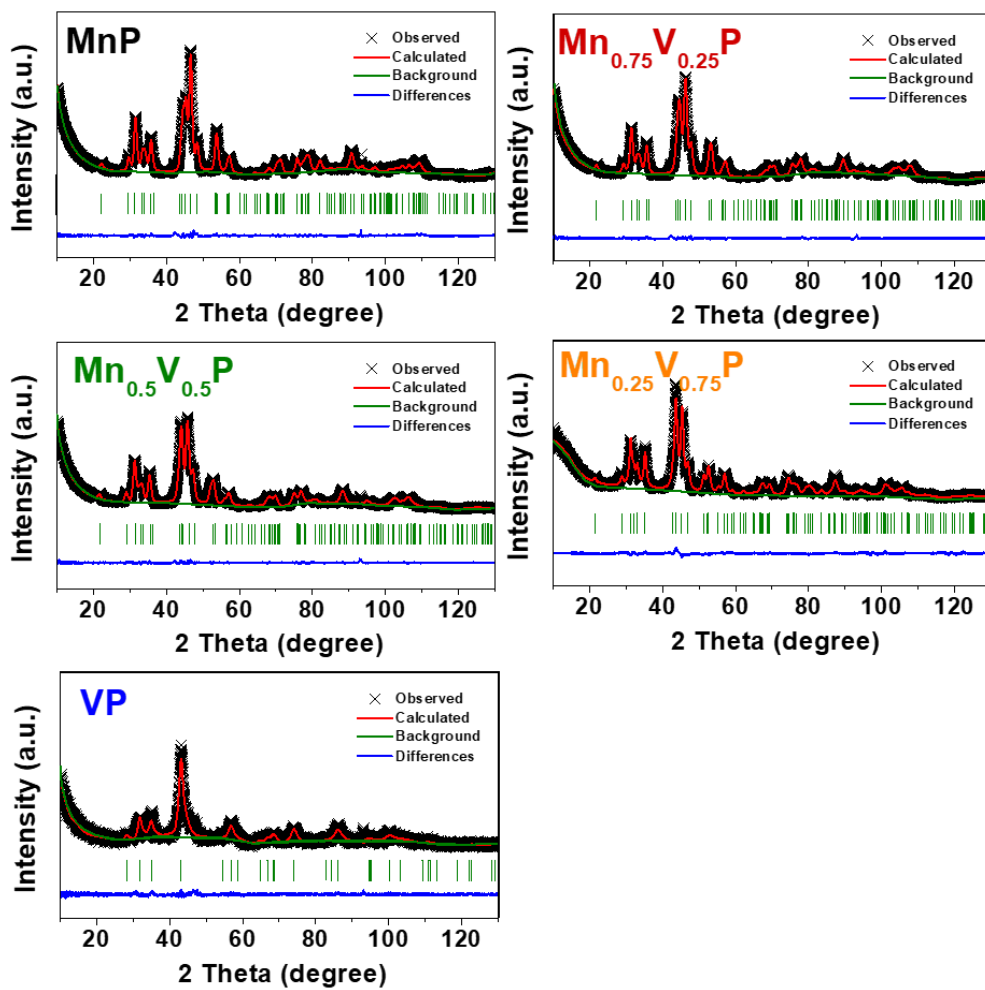


**Figure 4.3.3** XRD Rietveld refinement results for as-synthesized  $Mn_{1-x}V_xP$  ( $x = 0, 0.25, 0.5, 0.75,$  and  $1.0$ ) compounds.

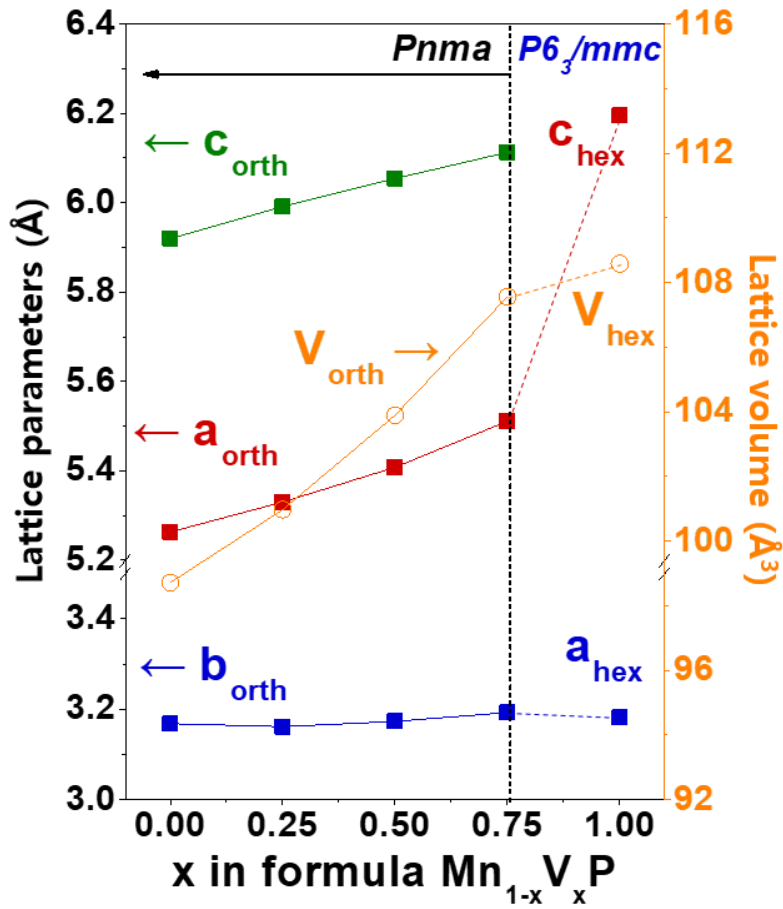
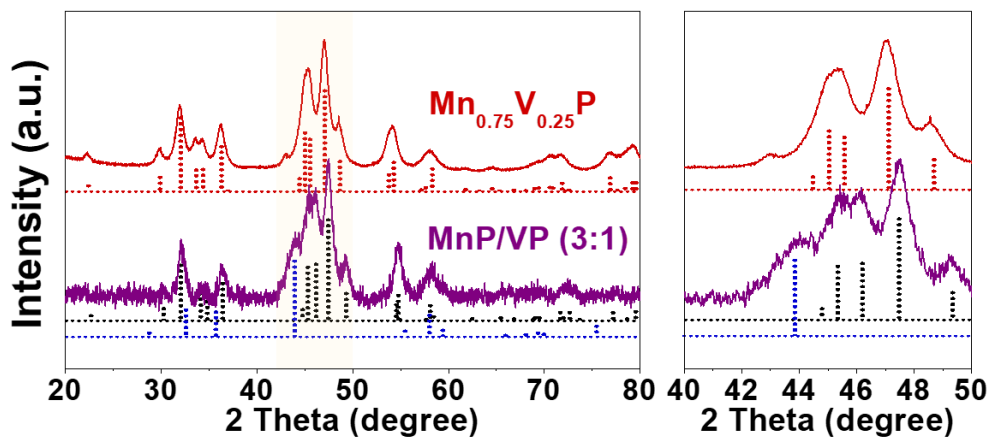
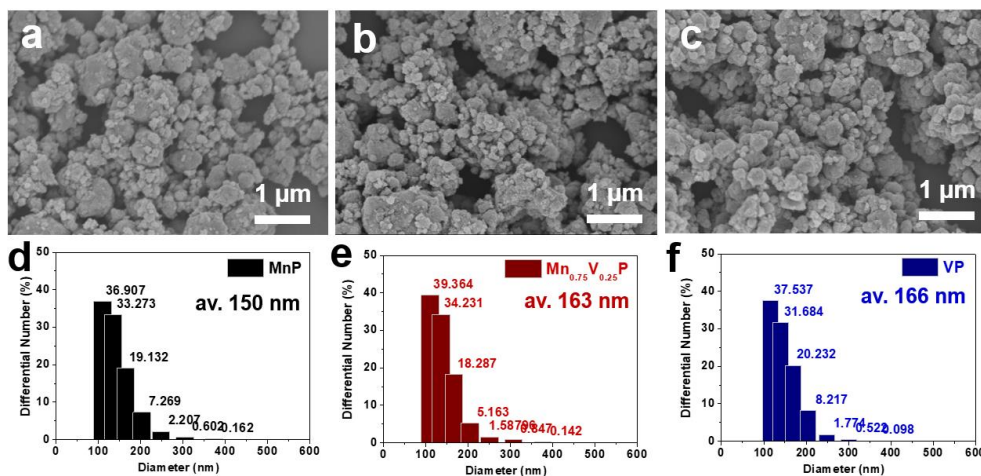


Figure 4.3.4 XRD Rietveld refined lattice parameters and volumes of  $\text{Mn}_{1-x}\text{V}_x\text{P}$  ( $x = 0, 0.25, 0.5, 0.75, \text{ and } 1.0$ ) compounds.



**Figure 4.3.5** XRD pattern for as-synthesized  $\text{Mn}_{0.75}\text{V}_{0.25}\text{P}$  solid solution and MnP/VP (3:1) mixture composite. The reference peaks for  $\text{Mn}_{0.75}\text{V}_{0.25}\text{P}$  (ICDD # 01-078-0809, red dash line), MnP (ICDD # 00-051-0942, black dash line), and VP (ICDD # 01-089-1907, blue dash line) are included.



**Figure 4.3.6** SEM images and dynamic light scattering (DLS) particle size distributions of the as-synthesized Mn<sub>1-x</sub>V<sub>x</sub>P (x = (a,d) 0, (b,e) 0.25, and (c,f) 1.0) NPs, respectively.

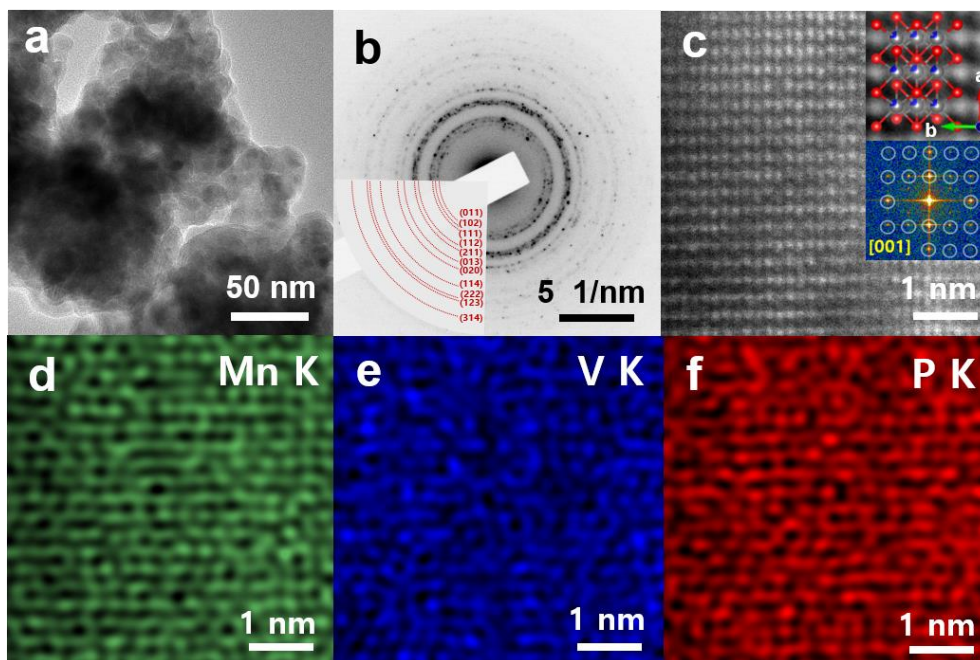


**Figure 4.3.7** (a) Low magnification TEM image, (b) SAED pattern of  $\text{Mn}_{0.75}\text{V}_{0.25}\text{P}$  nanoparticles, (c) atomic resolution HAADF STEM image of nanocrystallite aligned along the [001] direction, and elemental mapping images ((d) Mn K, (e) V K, and (f) P K) of (c).

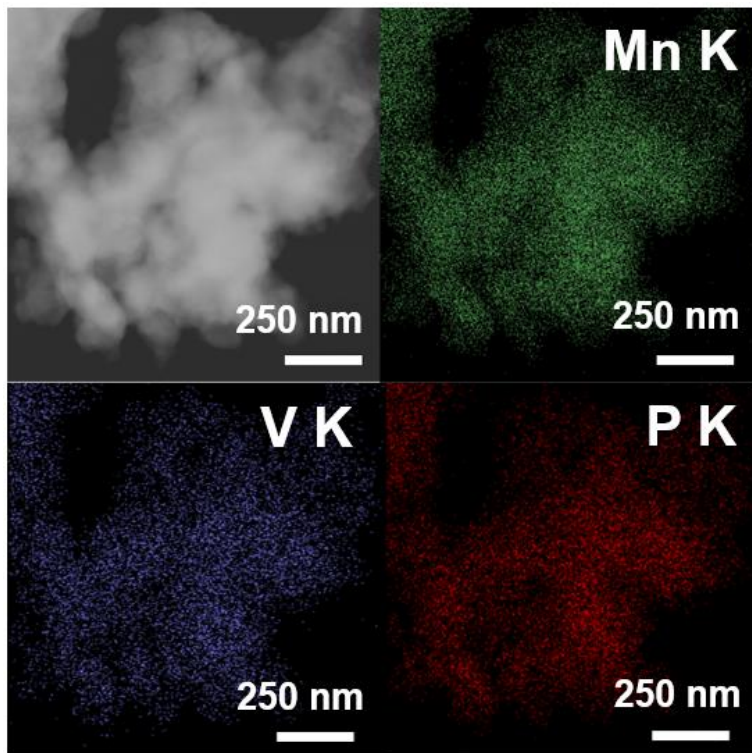


**Figure 4.3.8** Low magnification HAADF STEM image and elemental mapping images (Mn K, V K, and P K) of  $\text{Mn}_{1-x}\text{V}_x\text{P}$  ( $x=0.25$ ) nanoparticles.

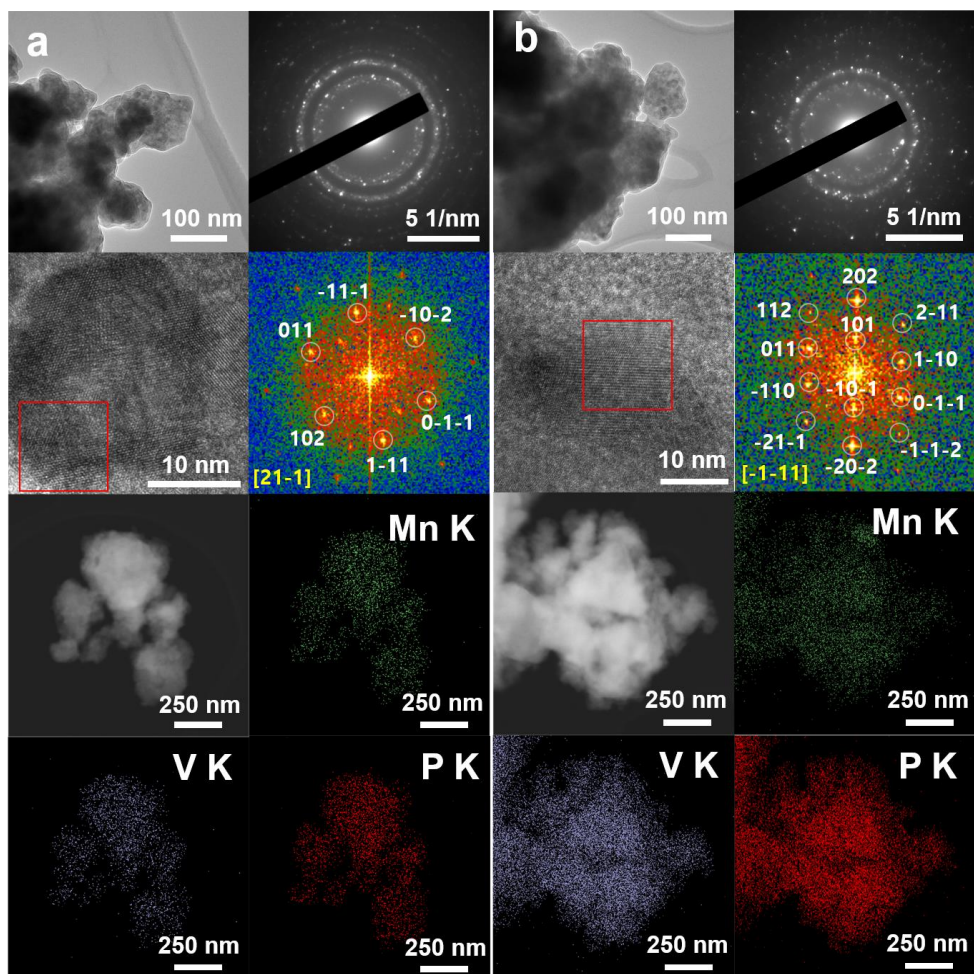


**Figure 4.3.9** Low magnification TEM image, SAED pattern, high-resolution TEM images, corresponding FFT pattern, STEM image, and EDS mapping images (Mn K, V K, and P K) of  $Mn_{1-x}V_xP$  ((a)  $x=0.5$  and (b)  $x=0.75$ ) nanoparticles.

### 4.3.2. Electrochemical Properties and Reaction Mechanism

The galvanostatic discharge (lithiation) and charge (delithiation) voltage profiles and corresponding differential capacity ( $dQ/dV$ ) plots (DCPs) of  $Mn_{1-x}V_xP$  ( $x = 0, 0.25, 0.5, 0.75$  and  $1.0$ ) electrodes obtained at the current density of  $100 \text{ mA g}^{-1}$  are shown in Figure 4.3.10. The discharge/charge voltage profile of MnP electrode is in a good agreement with the previous work: the sloping lithiation voltage plateau below  $0.50 \text{ V vs. Li/Li}^+$  for alloying reaction to form the amorphous ternary Li-Mn-P phase and two flat delithiation voltage plateaus at  $0.70$  and  $1.23 \text{ V vs. Li/Li}^+$  for de-alloying reaction.[4.37] The voltage profile and DCP of VP electrode are also consistent with the previous report as a topotactic insertion/extraction reaction, exhibiting the delithiation peak at  $0.95 \text{ V vs. Li/Li}^+$  in the  $dQ/dV$  plot.[4.36] The  $Mn_{0.75}V_{0.25}P$  electrode showed a sloping lithiation plateau below  $0.5 \text{ V vs. Li/Li}^+$  in the voltage profile and three delithiation peaks at  $0.63, 1.04,$  and  $1.18 \text{ V vs. Li/Li}^+$  in the  $dQ/dV$  plot. Thus, all of the voltage plateaus (or peaks in the  $dQ/dV$  plot) corresponding to the MnP and VP electrodes were observed with a slight peak shift, indicating that both alloying/de-alloying reaction and topotactic insertion/extraction reaction simultaneously occurred in the  $Mn_{0.75}V_{0.25}P$  electrode. The shift of reaction peaks in the  $Mn_{0.75}V_{0.25}P$  electrode indicates that the solid solution affected the redox reactions of each end member during discharge/charge processes.[4.21-4.23,4.38] On the other hand, the reaction peak shift was not observed in the MnP/VP (3:1) mixture electrode (Figure 4.3.11a and b). Its discharge/charge voltage profile was a simple linear combination of two end members delivering the sum reversible capacity of MnP (75%) and VP (25%)

electrodes, and all the reaction peaks for MnP and VP were found in the  $dQ/dV$  plot at the same voltages (Figure 4.3.11b). One thing to note is that the peak intensity at 0.95 V vs.  $\text{Li/Li}^+$  corresponding to the delithiation of VP was much higher in the solid solution electrode than the mixture electrode (Figure 4.3.11c), implying that the insertion/extraction reaction was more contributed to the total electrochemical reaction than the composition ratio in the solid solution electrode. Consequently, initial discharge/charge capacities of  $\text{Mn}_{0.75}\text{V}_{0.25}\text{P}$  electrode were slightly lower than those of MnP/VP (3:1) mixture electrode. The  $\text{Mn}_{0.5}\text{V}_{0.5}\text{P}$  electrode also exhibited the combined voltage profile of MnP and VP electrodes with a further shift to the lower voltage, and the contribution of insertion/extraction reaction to overall electrochemical reaction was more significant than that of  $\text{Mn}_{0.75}\text{V}_{0.25}\text{P}$  electrode (Figure 4.3.11d). On the other hand, the voltage profile and DCP of  $\text{Mn}_{0.25}\text{V}_{0.75}\text{P}$  electrode were very similar to those of VP electrode with a slight peak shift to higher voltage and the contribution of alloying/de-alloying reaction in total electrochemical reaction was negligible (Figure 4.3.11e). The Li-ion insertion/extraction occurs in the prismatic sites of solid solution phases and thus, the increase of insertion/extraction reaction contribution in the  $\text{Mn}_{1-x}\text{V}_x\text{P}$  solid solution electrodes can be attributed to the volume expansion and geometry change of prismatic sites with V substitution in the solid solution (Figure 4.3.12). In addition, it appeared that the partial substitution of V with Mn in the prismatic sites still allowed the Li-ion insertion/extraction and increased the contribution of insertion/extraction reaction to the overall electrochemical reaction than the composition ratio. These results suggest that the V ion substitution into  $\text{Mn}_{1-x}\text{V}_x\text{P}$  solid solution enables a hybrid alloying/insertion reaction and the contribution of each reaction to the overall

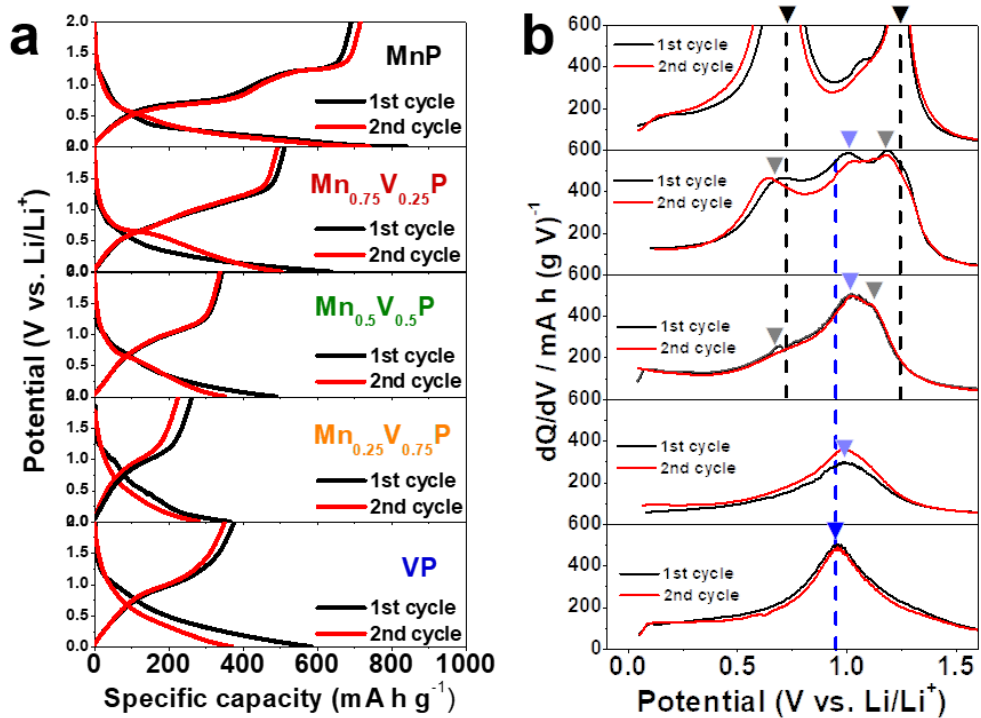
electrochemical reaction could be controlled by varying the composition ratio in  $\text{Mn}_{1-x}\text{V}_x\text{P}$ .

To further characterize the alloying/insertion hybrid electrochemical reactions in the  $\text{Mn}_{1-x}\text{V}_x\text{P}$  electrodes, *ex-situ* XRD analysis was conducted on the 1<sup>st</sup> fully discharged and charged states (Figure 4.3.13). The XRD pattern for the fully lithiated MnP showed the formation of amorphous-like ternary  $\text{Li}_x\text{Mn}_y\text{P}_z$  phase with the stoichiometry close to  $\text{Li}_3\text{MnP}_2$  phase during the alloying reaction although the diffraction peaks were weak and broad (Figure 4.3.14).[4.37] On the other hand, no phase change was observed in the VP electrode during 1<sup>st</sup> lithiation/delithiation confirming the topotactic insertion/extraction reaction with Li-ion.[4.36] When  $\text{Mn}_{0.75}\text{V}_{0.25}\text{P}$  and  $\text{Mn}_{0.5}\text{V}_{0.5}\text{P}$  electrodes were fully lithiated, ternary alloying  $\text{Li}_3\text{MnP}_2$  phase and pristine solid solution-like phase were observed. Indeed, this pristine solid solution-like phase was a topotactic lithium inserted solid solution phase, which was confirmed by  $\text{C}_s$ -corrected TEM and will be discussed in detail later. Upon the fully charging, ternary  $\text{Li}_3\text{MnP}_2$  phase disappeared and the original solid solution phase re-appeared in the XRD patterns. Thus, the simultaneous alloying/insertion hybrid reactions in  $\text{Mn}_{0.75}\text{V}_{0.25}\text{P}$  and  $\text{Mn}_{0.5}\text{V}_{0.5}\text{P}$  solid solution electrodes were further confirmed by *ex-situ* XRD. Consistent with the DCP result, the XRD patterns of the  $\text{Mn}_{0.25}\text{V}_{0.75}\text{P}$  electrode were unchanged during cycling and the alloying phase was not detected in the fully lithiated state indicating the only topotactic Li insertion/extraction reaction similar to the VP electrode.

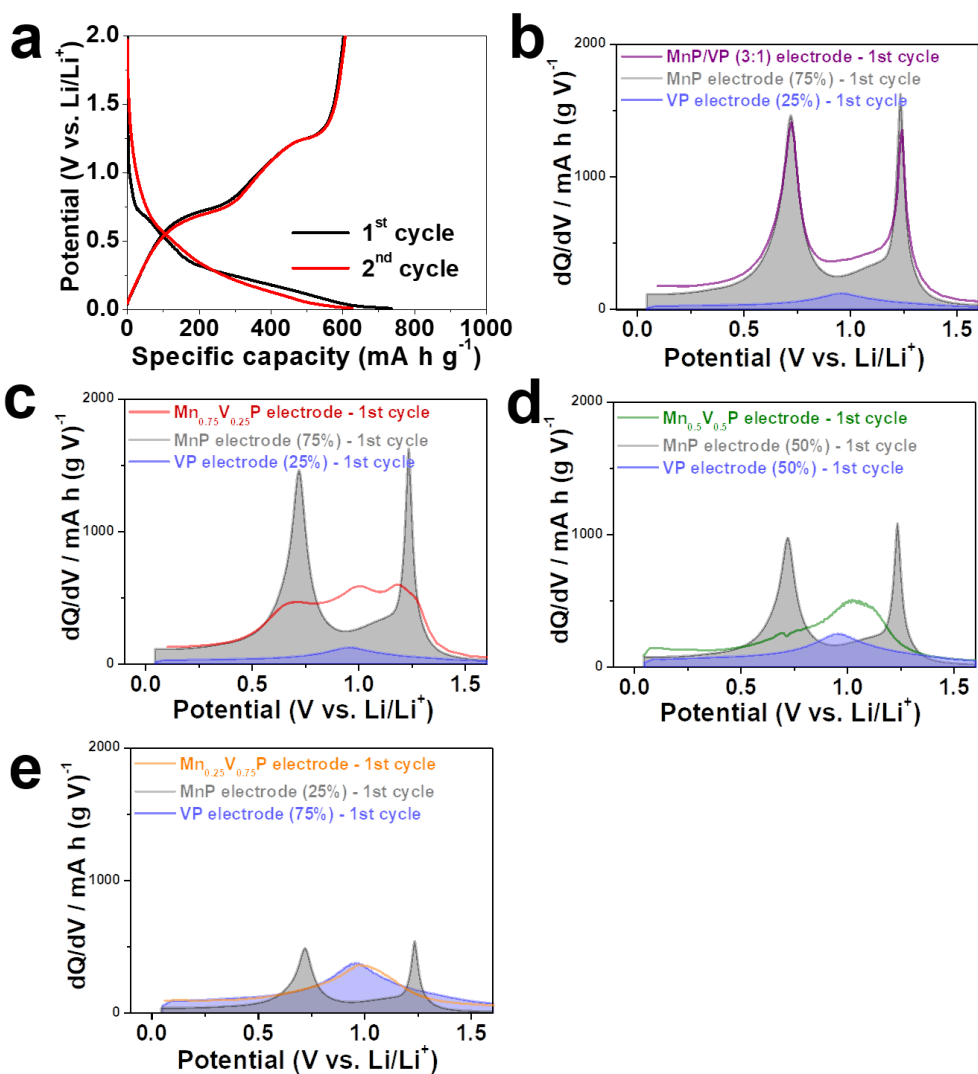
The alloying/insertion hybrid electrochemical reactions in the  $\text{Mn}_{0.75}\text{V}_{0.25}\text{P}$  electrode were further examined using the  $\text{C}_s$ -corrected TEM. The HAADF STEM

image and corresponding FFT pattern of lithiated  $\text{Mn}_{0.75}\text{V}_{0.25}\text{P}$  nanoparticles are matched with the orthorhombic structure of  $\text{Mn}_{0.75}\text{V}_{0.25}\text{P}$  with a [100] zone axis (Figure 4.3.15a and b). However, the interplanar spacing of (002) plane was slightly larger than that of pristine  $\text{Mn}_{0.75}\text{V}_{0.25}\text{P}$  solid solution (3.09 vs. 3.04 Å) due to the topotactic lithium insertion (Figure 4.3.15c and d). From now on, this phase will be referred as Li-inserted  $\text{Mn}_{0.75}\text{V}_{0.25}\text{P}$ . In addition, the forbidden {001}, {010}, and {012} reflections were observed in the FFT pattern (Figure 4.3.15b), which were not detected in the pristine state of  $\text{Mn}_{0.75}\text{V}_{0.25}\text{P}$  nanoparticles (Figure 4.3.15c). The forbidden reflections in the FFT pattern might be originated from the hybrid alloying/insertion reaction in  $\text{Mn}_{0.75}\text{V}_{0.25}\text{P}$  nanoparticles such that the diffraction patterns of Li-inserted  $\text{Mn}_{0.75}\text{V}_{0.25}\text{P}$  and  $\text{Li}_3\text{MnP}_2$  phases are overlapped with a [100] zone axis (Figure 4.3.16), but further *in-situ* TEM study with a spectroscopy in atomic resolution is required to address this issue. The EDS mapping images of lithiated  $\text{Mn}_{0.75}\text{V}_{0.25}\text{P}$  nanoparticles indicated that Mn and V were well retained and homogeneously distributed at an atomic scale as well as at tens of nanometer scale (Figure 4.3.17). The similar atomic arrangement between Li-inserted  $\text{Mn}_{0.75}\text{V}_{0.25}\text{P}$  and  $\text{Li}_3\text{MnP}_2$  phases can minimize the atomic migration and rearrangement required for alloying/de-alloying reaction in solid solution  $\text{Mn}_{1-x}\text{V}_x\text{P}$  and thus, allow the reversible hybrid alloying/insertion reaction within a few nanometer scale. In the nano-beam electron diffraction (NBED) pattern of fully lithiated  $\text{Mn}_{0.75}\text{V}_{0.25}\text{P}$  nanoparticles obtained with a beam size of ~5 nm, both ternary  $\text{Li}_3\text{MnP}_2$  and Li-inserted  $\text{Mn}_{0.75}\text{V}_{0.25}\text{P}$  phases were confirmed (Figure 4.3.18), but they could not be spatially resolved even using  $C_s$ -corrected STEM implying that the lithiation products had the similar crystal structure and were distributed in a few-nanometer

scale with low crystallinity. Unlike the solid solution  $\text{Mn}_{0.75}\text{V}_{0.25}\text{P}$ , the XRD pattern of MnP/VP mixture electrode showed that MnP and VP separately reacted with Li-ion as alloying and insertion reactions, respectively (Figure 4.3.19a). The EDS mapping images of fully lithiated MnP/VP electrode showed that Mn and V were separately distributed in tens of nanometer scale (Figure 4.3.19b).



**Figure 4.3.10** (a) Galvanostatic discharge/charge voltage profiles and (b) corresponding differential capacity plots for Mn<sub>1-x</sub>V<sub>x</sub>P compounds ( $x = 0.0, 0.25, 0.5, 0.75,$  and  $1.0$ ).



**Figure 4.3.11** (a) Galvanostatic discharge/charge voltage profiles of MnP/VP electrode. Differential capacity plots (DCPs) of (b) MnP/VP (3:1) composite and  $\text{Mn}_{1-x}\text{V}_x\text{P}$  ( $x =$  (c) 0.25, (d) 0.5, and (e) 0.75) electrodes, respectively.

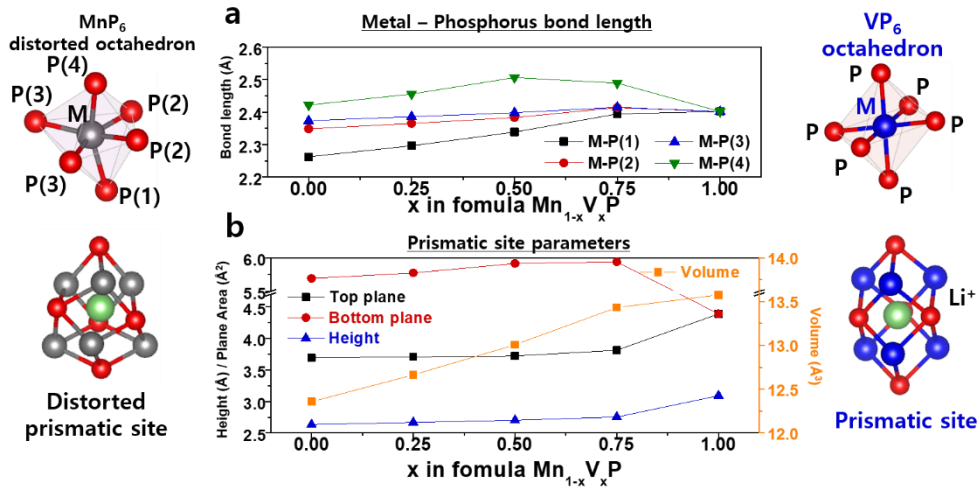


**Figure 4.3.12** (a) Bond lengths and (b) prismatic site parameters of  $Mn_{1-x}V_xP$  ( $x = 0, 0.25, 0.50, 0.75,$  and  $1.0$ ), respectively.

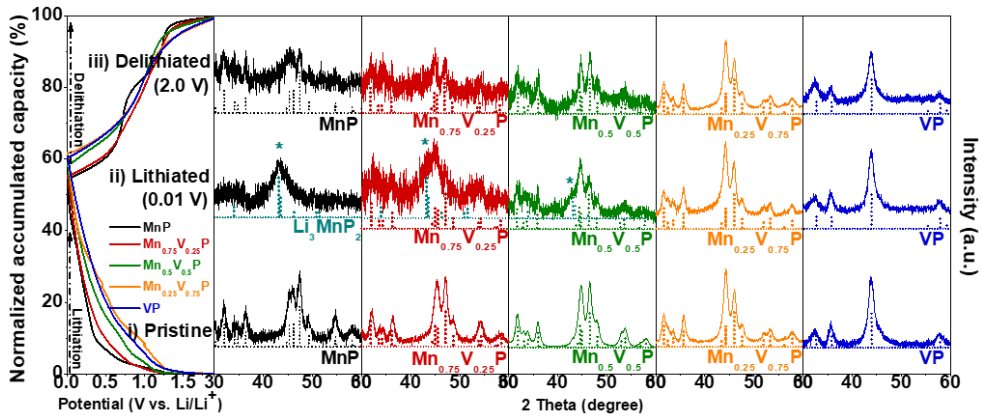


**Figure 4.3.13** Lithiation/delithiation voltage profiles and ex-situ XRD patterns for pristine, fully lithiated (0.01 V), and delithiated (2.0 V) states for  $\text{Mn}_{1-x}\text{V}_x\text{P}$  ( $x = 0, 0.25, 0.50, 0.75,$  and  $1.0$ ) electrodes, respectively.

### Li<sub>8-x</sub>Mn<sub>x</sub>P<sub>4</sub> compounds from ICDD database

Composition	Crystal system	Space group	ICDD number
Li <sub>7</sub> MnP <sub>4</sub>	Cubic	Fm-3m	00-014-0045
Li <sub>7</sub> MnP <sub>4</sub>	Cubic	Fm-3m	04-005-3949
Li <sub>6.67</sub> Mn <sub>1.33</sub> P <sub>4</sub>	Cubic	-	00-014-0047
Li <sub>1.67</sub> Mn <sub>0.33</sub> P	Tetragonal	P4/nmm	04-005-3951
Li <sub>3</sub> MnP <sub>2</sub>	Tetragonal	P-42m	04-009-9099
Li <sub>3</sub> MnP <sub>2</sub>	Tetragonal	P4/nmm	04-005-3954
Li <sub>1.37</sub> Mn <sub>0.63</sub> P	Tetragonal	P4/nmm	04-005-3955
LiMnP	Tetragonal	P4/nmm	04-004-0359

### Fully lithiated MnP electrode (0.01 V vs. Li/Li<sup>+</sup>)

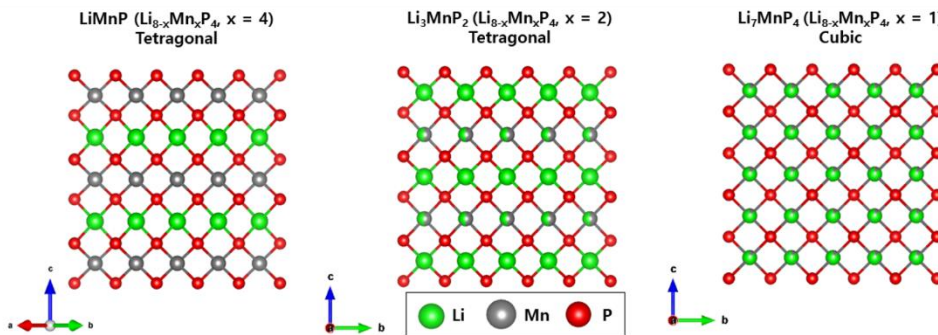
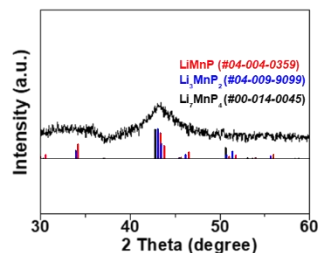


**Figure 4.3.14** ICDD database of ternary Li-Mn-P phases (Li<sub>8-x</sub>Mn<sub>x</sub>P<sub>4</sub>), *ex-situ* XRD pattern of fully lithiated MnP electrode with reference peaks with LiMnP (# 04-004-0359, red solid line), Li<sub>3</sub>MnP<sub>2</sub> (# 04-009-9099, blue solid line), and Li<sub>7</sub>MnP<sub>4</sub> (# 00-014-0045, black solid line), and their crystal structure.

(The chemical composition of amorphous-like ternary Li<sub>x</sub>Mn<sub>y</sub>P<sub>z</sub> phase is not accurately quantified because the observed diffraction peaks were weak and broad and there are many Li-Mn-P compounds with a similar crystal structure by varying occupancy and site between lithium and manganese<sup>[ref]</sup>, although it can be expected to be close to the Li<sub>3</sub>MnP<sub>2</sub> phase based on the observed 2 theta values in *ex-situ* XRD pattern.

[ref.] R. Juza, T. Bohmann, Z. anorg. Allg. Chem., 1961, 308, 159-178.)

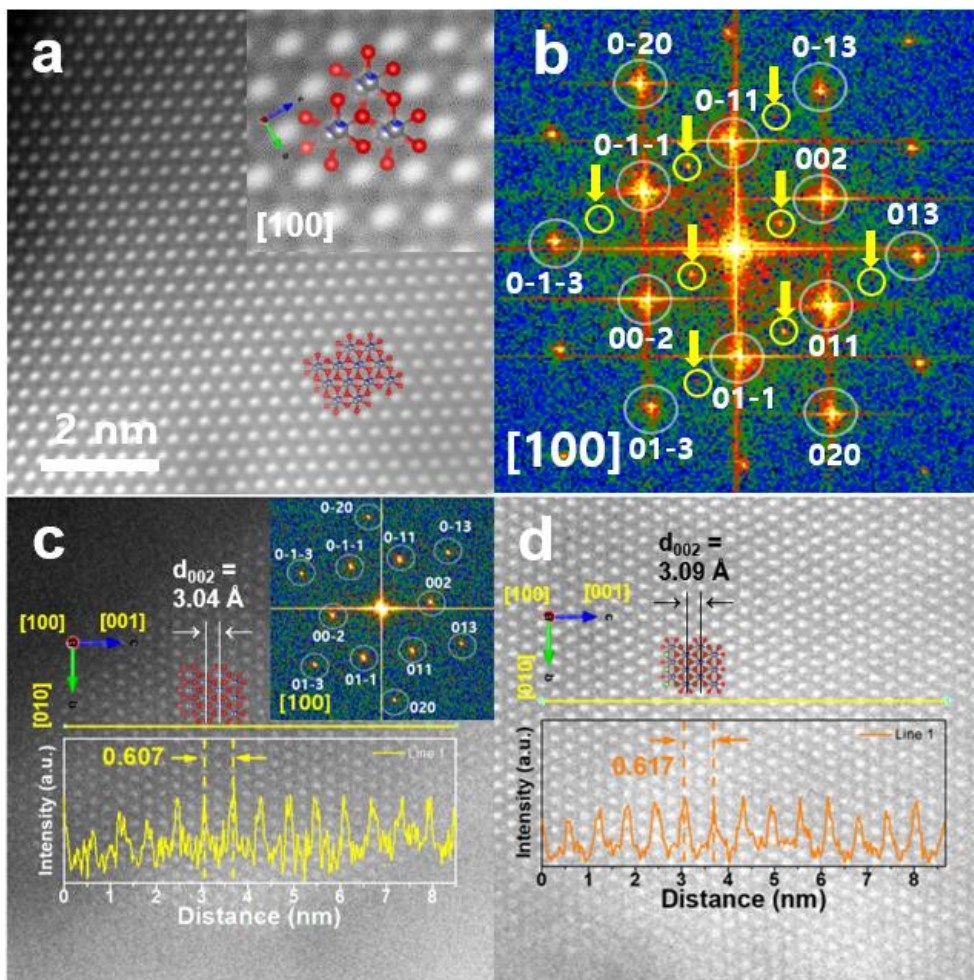


**Figure 4.3.15** (a) HAADF STEM image, (b) corresponding FFT pattern for fully lithiated  $\text{Mn}_{0.75}\text{V}_{0.25}\text{P}$  electrode. High magnification HAADF STEM image with line profile along  $[001]$  direction of  $\text{Mn}_{0.75}\text{V}_{0.25}\text{P}$  nanoparticle for (c) pristine and (d) fully lithiated states, respectively.

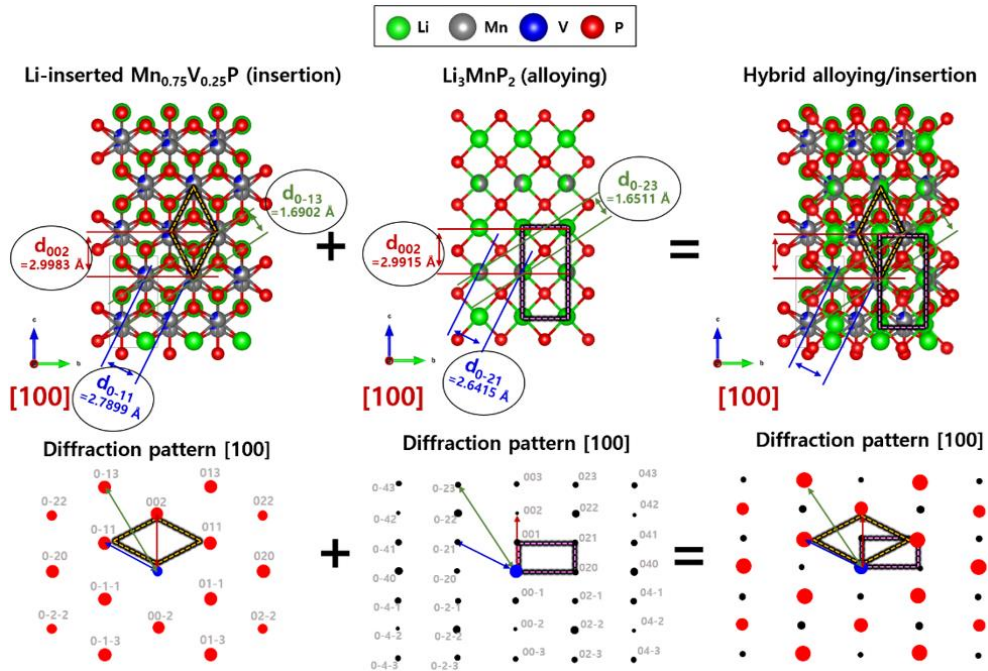


**Figure 4.3.16** Crystal structure illustration and diffraction pattern of aligned along the [100] direction for Li-inserted  $Mn_{0.75}V_{0.25}P$ ,  $Li_3MnP_2$ , and hybrid alloying/insertion phases, respectively.

(From the similar topological relationship between  $Mn_{0.75}V_{0.25}P$  and  $Li_3MnP_2$  phases, the mismatch of interplanar space and crystallographic angle between two phases are negligible, which results very similar periodic array of the supercell in the diffraction pattern along the same crystallographic direction. Along the [100] zone-axis, two structures may have the overlapping positions of Mn, V, and P as shown in the schematic image, in which case the diffraction pattern also overlaps as follows, which is similar to the observed FFT pattern in Figure 4.3.19b.)

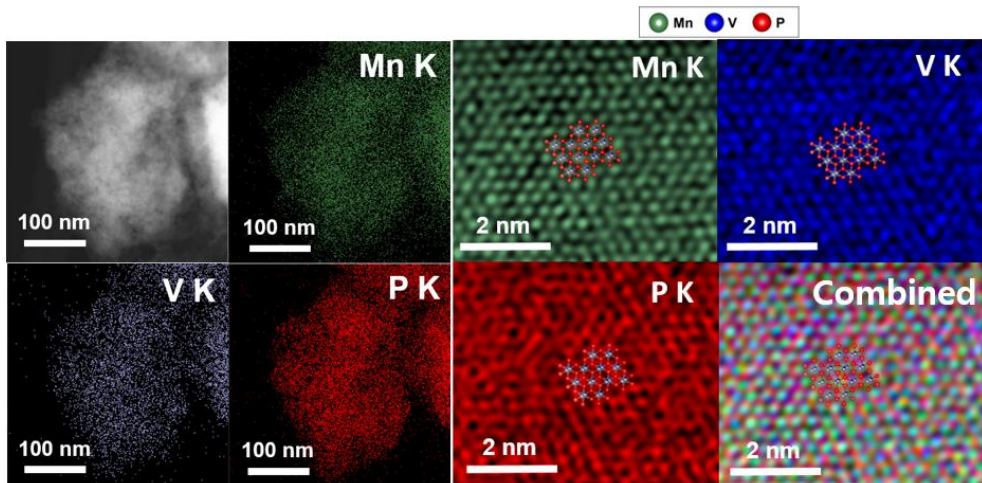


**Figure 4.3.17** HAADF STAM image and EDS mapping images (Mn K, V K, and P K) of fully lithiated  $\text{Mn}_{0.75}\text{V}_{0.25}\text{P}$  electrode.

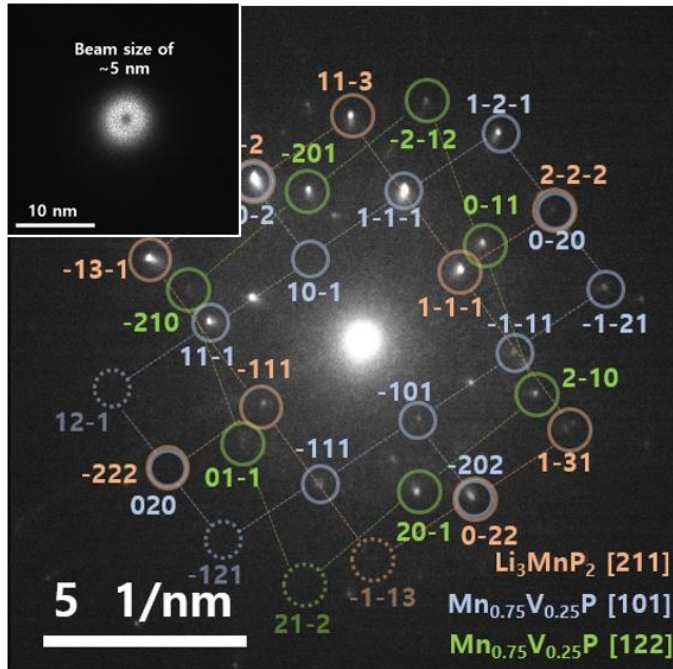


**Figure 4.3.18** TEM image of nano-beam and nano-beam electron diffraction (NBED) pattern for fully lithiated  $\text{Mn}_{0.75}\text{V}_{0.25}\text{P}$  electrode.

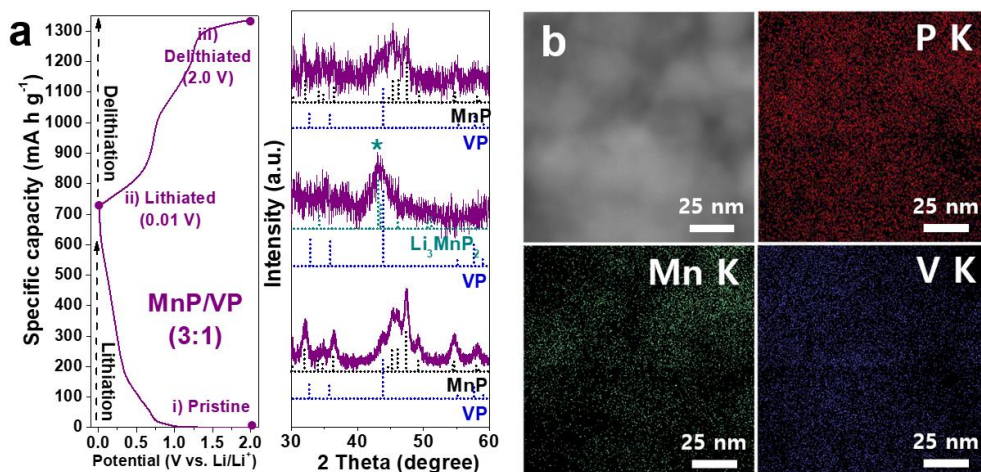


**Figure 4.3.19** (a) Lithiation/delithiation voltage profiles and ex-situ XRD patterns for pristine, fully lithiated (0.01 V), and delithiated (2.0 V) states for MnP/VP (3:1) composite electrode, (b) HAADF STEM image and EDS mapping images (P K, Mn K, and V K) of fully lithiated state for MnP/VP electrode.

### 4.3.3. Electrochemical Performance

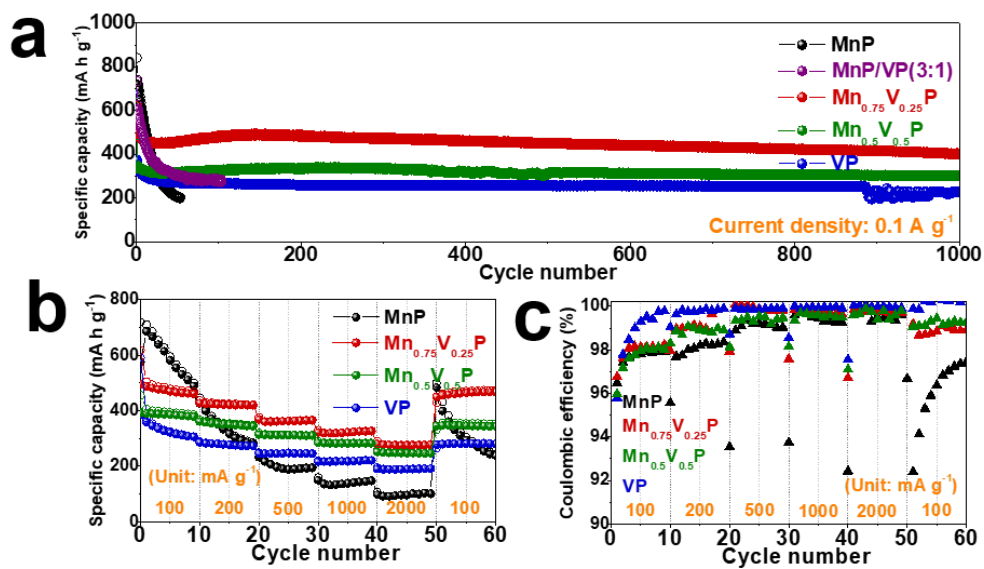
The cycle retention properties of the  $\text{Mn}_{1-x}\text{V}_x\text{P}$  ( $x = 0, 0.25, 0.5,$  and  $1.0$ ) and physically mixed MnP/VP (3:1) electrodes were compared at current density of  $100 \text{ mA g}^{-1}$  (Figure 4.3.20a). The initial Coulombic efficiencies of  $\text{Mn}_{1-x}\text{V}_x\text{P}$  ( $x = 0, 0.25, 0.5,$  and  $1.0$ ), and MnP/VP electrodes were 82%, 81%, 71%, 64%, and 82%, respectively. The MnP electrode showed the high initial discharge and charge capacities of 842 and  $692 \text{ mA h g}^{-1}$ , but it degraded rapidly. On the other hand, VP electrode showed the relatively low initial discharge and charge capacities of 583 and  $375 \text{ mA h g}^{-1}$ , respectively and the capacity of  $226 \text{ mA h g}^{-1}$  was well maintained after 1000 cycles with a cycle retention of 60%, which was derived from the stable Li-ion insertion/extraction reaction into VP phase. The physically mixed MnP/VP (3:1) composite electrode showed the initial discharge and charge capacities of 734 and  $602 \text{ mA h g}^{-1}$ , respectively and higher cycle retention than that of pure MnP electrode. However, it also showed a rapid capacity fading indicating that VP in the MnP/VP mixture composite was not effective to prevent the degradation of MnP electrode performance. On the other hand,  $\text{Mn}_{0.75}\text{V}_{0.25}\text{P}$  solid solution electrode showed the initial discharge and charge capacities of 619 and  $500 \text{ mA h g}^{-1}$ , respectively, and the reversible capacity of  $403 \text{ mA h g}^{-1}$  was well maintained during 1000 cycles with a cycle retention of 80% indicating highly stable cycle performance. In addition, the  $\text{Mn}_{0.5}\text{V}_{0.5}\text{P}$  electrode also showed excellent cycle performance with cycle retention of 88% after 1000 cycles, however, the retained reversible capacity was  $\sim 300 \text{ mA h g}^{-1}$ , relatively lower than that of  $\text{Mn}_{0.75}\text{V}_{0.25}\text{P}$  electrode.

Figure 4.3.20b and c show rate capability test and corresponding coulombic

efficiency of  $\text{Mn}_{1-x}\text{V}_x\text{P}$  compounds ( $x = 0, 0.25, 0.5, \text{ and } 1.0$ ) at various current densities ( $100, 200, 500, 1000, \text{ and } 2000 \text{ mA g}^{-1}$ ). The reversible capacities of  $\text{Mn}_{1-x}\text{V}_x\text{P}$  compounds steadily decreased with stepwise increase of current density (Figure 4.3.20b). In particular,  $\text{Mn}_{1-x}\text{V}_x\text{P}$  compounds ( $x = 0.25, 0.5, \text{ and } 1.0$ ) showed stable rate capabilities even at high current density of  $2 \text{ A g}^{-1}$ , and especially the higher the V substitution in  $\text{Mn}_{1-x}\text{V}_x\text{P}$  compound, the relatively higher coulombic efficiency compared to MnP at a step when changing at each current density 10<sup>th</sup> cycle (Figure 4.3.20c). The high-rate long-term cyclability was also compared in the  $\text{Mn}_{1-x}\text{V}_x\text{P}$  ( $x = 0, 0.25, 0.5, \text{ and } 1.0$ ) and physically mixed MnP/VP (3:1) electrodes at current densities of  $1 \text{ A g}^{-1}$  and  $2 \text{ A g}^{-1}$  (Figure 4.3.21a and b). Both MnP and MnP/VP composite electrodes showed reversible capacities were gradually decreased during cycles indicating poor high-rate cyclabilities. Although the VP electrode showed excellent cyclability with almost negligible capacity fading, the reversible capacity could not over than  $200 \text{ mA h g}^{-1}$ . Both the high reversible capacity and excellent high rate cyclability could be obtained in case of the  $\text{Mn}_{1-x}\text{V}_x\text{P}$  ( $x = 0.25 \text{ and } 0.5$ ) solid solution electrodes, especially for  $\text{Mn}_{0.75}\text{V}_{0.25}\text{P}$  electrode, which reversible capacity of  $352 \text{ mA h g}^{-1}$  was well maintained during 1500 cycles at a high current density of  $1 \text{ A g}^{-1}$ , with a capacity decay less than 0.0086% per cycle (Figure 4.3.21c). The achieved electrochemical performance of  $\text{Mn}_{0.75}\text{V}_{0.25}\text{P}$  electrode, obtained without conductive carbon-based composite material, showed better performance when comparing with state-of-the-art intrinsic electrochemical performance of nanostructured LIB anodes such as nanocomposite, ternary compound, and binary oxide based on insertion reaction type materials (Figure 4.3.22 and Table 4.3.3).

**Table 4.3.3** State-of-the-art intrinsic electrochemical performance of nanostructured LIB anode materials such as nanocomposite, ternary compound, and binary oxide based on insertion reaction type material.

Materials	Synthesis method	Cycle performance (Reversible capacity, @current density, cycle number)	Initial Coulombic efficiency	Reference
TiO <sub>2</sub> /Co <sub>3</sub> O <sub>4</sub> porous nanoparticle	Melt spinning & chemical etching	180 mAh g <sup>-1</sup> , @300 mA g <sup>-1</sup> , 500 cycles	50%	Electrochim. Acta 2016, 211, 83-91.
TiO <sub>2</sub> /SnO <sub>2</sub> mesoporous bead	Sol-gel & Solvothermal	225.7 mAh g <sup>-1</sup> , @850 mA g <sup>-1</sup> , 2000 cycles	45.7%	J. Alloys and Comp. 2015, 639, 60-67.
TiO <sub>2</sub> @Fe <sub>2</sub> O <sub>3</sub> nanotube	Atomic layer deposition	436 mAh g <sup>-1</sup> , @100 mA g <sup>-1</sup> , 600 cycles	67.2%	Sci. Rep. 2017, 7, 40927.
Cu <sub>3</sub> V <sub>2</sub> O <sub>8</sub> nanoflower	Solution synthesis	~420 mAh g <sup>-1</sup> , @1 A g <sup>-1</sup> , 70 cycles	-	Adv. Sci. 2015, 2, 1500154.
Ru <sub>0.01</sub> Ti <sub>0.99</sub> Nb <sub>2</sub> O <sub>7</sub> nanoparticle	Solid state reaction	162 mAh g <sup>-1</sup> , @1 A g <sup>-1</sup> , 100 cycles	86.4%	J. Mater. Chem. A 2015, 3, 8627-8635.
V <sub>2</sub> O <sub>5</sub> -TeO <sub>2</sub> glass powder	Melting & quenching	172 mAh g <sup>-1</sup> , @1 A g <sup>-1</sup> , 1000 cycles	40%	Nano Energy 2018, 49, 596-602.
ZnTiO <sub>3</sub> porous nanorod	Solution synthesis	202 mAh g <sup>-1</sup> , @500 mA g <sup>-1</sup> , 200 cycles	36.3%	Ceram. Internat. 2020, 46, 14030-14037.
Ti <sub>0.88</sub> Sn <sub>0.12</sub> O <sub>2</sub> nanoparticle	Hydrothermal	129 mAh g <sup>-1</sup> , @500 mA g <sup>-1</sup> , 150 cycles	-	Electrochim. Acta 2017, 231, 247-254.
V <sub>0.8</sub> Sn <sub>0.2</sub> O <sub>2</sub> nanoparticle	Hydrothermal	423 mAh g <sup>-1</sup> , @500 mA g <sup>-1</sup> , 150 cycles	-	Electrochim. Acta 2017, 231, 247-254.
Mn <sub>0.5</sub> V <sub>0.5</sub> O <sub>2</sub> nanoparticle	Hydrothermal	483 mAh g <sup>-1</sup> , @1 A g <sup>-1</sup> , 150 cycles	65%	Electrochim. Acta 2019, 322, 134695.
V <sub>2</sub> O <sub>5</sub> -P <sub>2</sub> O <sub>5</sub> glass powder	Melt & quenching	169 mAh g <sup>-1</sup> , @1 A g <sup>-1</sup> , 600 cycles	64.3%	J. Alloys and Comp. 2019, 810, 151938.
NaV <sub>2</sub> O <sub>5</sub> nanotube	Hydrothermal	162 mAh g <sup>-1</sup> , @200 mA g <sup>-1</sup> , 1000 cycles	~36%	ACS Appl. Energy Mater. 2019, 2, 822-832.
NiVO <sub>3</sub> nanoparticle	Hydrothermal	180 mAh g <sup>-1</sup> , @200 mA g <sup>-1</sup> , 500 cycles	41%	J. Mater. Chem. A 2018, 6, 18103.
TiO <sub>2</sub> hollow sphere	Solution synthesis	200 mAh g <sup>-1</sup> , @100 mA g <sup>-1</sup> , 500 cycles	~71%	J. Am. Chem. Soc. 2018, 140, 16676-16684.
TiO <sub>2</sub> hollow sphere	Solution synthesis	68 mAh g <sup>-1</sup> , @940 mA g <sup>-1</sup> , 200 cycles	~88%	J. Mater. Chem. A 2017, 5, 23853-23862.
TiO <sub>2</sub> nanoparticle	Hydrothermal	114 mAh g <sup>-1</sup> , @500 mA g <sup>-1</sup> , 2000 cycles	~47%	J. Alloys and Comp. 2017, 727, 998-1005.
Li <sub>4</sub> Ti <sub>5</sub> O <sub>12</sub> hollow sphere	Hydrothermal	235 mAh g <sup>-1</sup> , @750 mA g <sup>-1</sup> , 200 cycles	~88%	Electrochim. Acta 2017, 254, 287-298.
Li <sub>4</sub> Ti <sub>5</sub> O <sub>12</sub> particle	Solution synthesis	~125 mAh g <sup>-1</sup> , @175 mA g <sup>-1</sup> , 500 cycles	94.6%	Ionic 2019, 25, 2549-2561.
V <sub>2</sub> O <sub>5</sub> nanosheet	Solution synthesis & microwave	~500 mAh g <sup>-1</sup> , @1 A g <sup>-1</sup> , 200 cycles	74.6%	J. Mater. Chem. A 2016, 4, 13907-13915.
V <sub>2</sub> O <sub>5</sub> nanoparticle	Solution synthesis	~400 mAh g <sup>-1</sup> , @500 mA g <sup>-1</sup> , 100 cycles	-	Inorg. Chem. 2015, 54, 11799-11806.
Mn <sub>0.75</sub> V <sub>0.25</sub> P nanoparticle	High energy mechanical milling	352 mAh g <sup>-1</sup> , @1 A g <sup>-1</sup> , 1500 cycles	81%	This work



**Figure 4.3.20** Cycle performance of Mn<sub>1-x</sub>V<sub>x</sub>P ( $x = 0, 0.25, 0.5,$  and  $1.0$ ) and MnP/VP(3:1) electrodes at  $0.1 \text{ A g}^{-1}$ . (b) Rate capability test and (c) Coulombic efficiency of Mn<sub>1-x</sub>V<sub>x</sub>P ( $x = 0, 0.25, 0.5,$  and  $1.0$ ) electrodes.

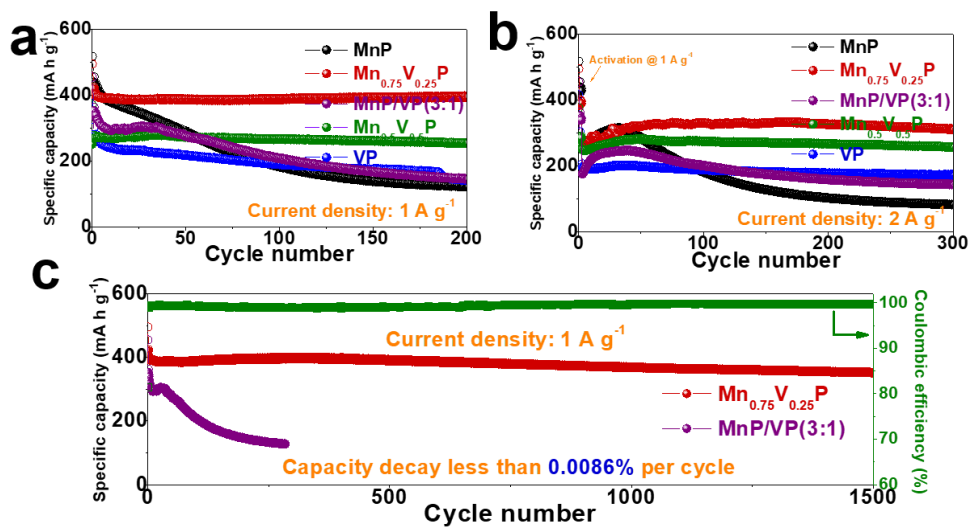


**Figure 4.3.21** Cycle performance of  $\text{Mn}_{1-x}\text{V}_x\text{P}$  ( $x = 0, 0.25, 0.5,$  and  $1.0$ ) and  $\text{MnP/VP}(3:1)$  electrodes at (a)  $1 \text{ A g}^{-1}$  and (b)  $2 \text{ A g}^{-1}$ . (c) Comparison of high-rate long-term cycle performance between  $\text{Mn}_{1-x}\text{V}_x\text{P}$  ( $x = 0.25$ ) and  $\text{MnP/VP}(3:1)$  electrodes at  $1 \text{ A g}^{-1}$ .

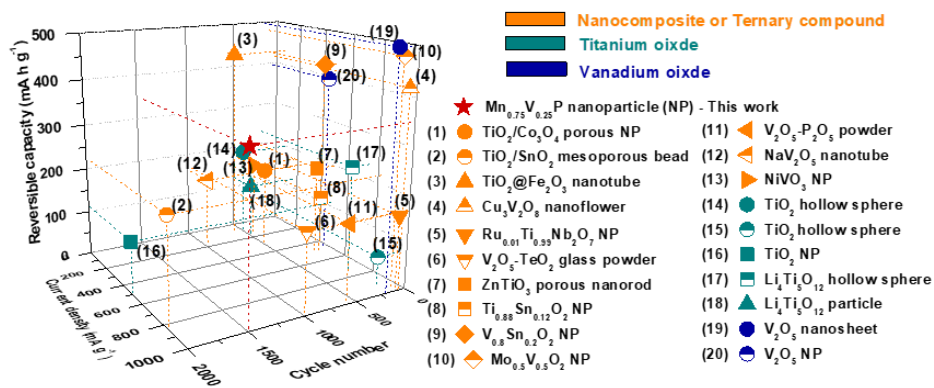


**Figure 4.3.22** Comparison of electrochemical performance of Mn<sub>0.75</sub>V<sub>0.25</sub>P with state-of-the-art of nanostructured LIB anode materials such as nanocomposite, ternary compound, and binary oxide based on insertion reaction type material.

#### 4.3.4. Synergistic Effects of Hybrid Alloying/Insertion Reaction

To understand the different cycling behavior between  $\text{Mn}_{1-x}\text{V}_x\text{P}$  ( $x = 0, 0.25, 0.5$  and  $1.0$ ) compounds and MnP/VP mixture composite electrodes, the differential capacity plots (DCPs) were compared at different cycles of 50<sup>th</sup>, 100<sup>th</sup>, and 200<sup>th</sup> tested at  $1 \text{ A g}^{-1}$  (Figure 4.3.23). Based on the comparison of the reaction peak intensity in the DCPs, it was found that the reversible lithiation/delithiation peaks for MnP continuously decreased with increasing the cycles in the MnP/VP mixture composite electrode, indicating that MnP is responsible for the capacity decay in the MnP/VP mixture composite electrode. On the other hand, the reversible lithiation/delithiation for both MnP and VP as alloying and insertion reactions were well maintained for solid solution  $\text{Mn}_{0.75}\text{V}_{0.25}\text{P}$  electrode during cycling.

To clarify the reason for superior cycle retention in the  $\text{Mn}_{0.75}\text{V}_{0.25}\text{P}$  solid solution electrode, the morphology of the cycled electrodes was examined by SEM. The disassembled electrodes were rinsed with dimethyl carbonate (DMC) for the electrodes with SEI layer and further rinsed with acetic acid and deionized water for the electrodes without SEI layer.[4.43] As-prepared pristine electrodes for solid solution  $\text{Mn}_{1-x}\text{V}_x\text{P}$  ( $x = 0, 0.25, \text{ and } 1.0$ ) and MnP/VP mixture composite had the similar morphology derived from the same synthesis conditions (Figure 4.3.24a). After 200 cycles at the current density of  $1.0 \text{ A g}^{-1}$ , a non-uniform and thick SEI layer was formed on the surface and a severe agglomeration of active material was observed in the MnP and MnP/VP mixture electrodes (Figure 4.3.24b and c). This

can be attributed to the accompanying large volume expansion of alloying reaction MnP, which caused the unstable SEI layer and particle pulverization and agglomeration. Thus, the physical mixing of VP in tens of nanometer scale was not effective to suppress the volume expansion and agglomeration of alloying element in case of MnP/VP mixture electrode. On the other hand, a uniform SEI layer was formed and agglomeration and structural deformation were not observed in the VP and  $\text{Mn}_{0.75}\text{V}_{0.25}\text{P}$  solid solution electrodes. The TEM-EDS mapping of the cycled electrodes further confirmed that Mn, V, and P were homogeneously distributed throughout the  $\text{Mn}_{0.75}\text{V}_{0.25}\text{P}$  nanoparticles at an atomic scale (Figure 4.3.24d) indicating that the solid solution phase was well maintained without an agglomeration even after 200 cycles at  $1.0 \text{ A g}^{-1}$ . Consequently, the solid solution electrode effectively buffered the accompanying volume variation and hindered the aggregation of the alloying element through the hybrid reaction at an atomic scale.

To determine the electrode resistances related to the morphological change, electrochemical impedance spectroscopy (EIS) measurements were conducted at 2.0 V vs.  $\text{Li/Li}^+$  for  $\text{Mn}_{1-x}\text{V}_x\text{P}$  ( $x = 0, 0.25, \text{ and } 1.0$ ) solid solution and MnP/VP mixture electrodes before cycle and after 200 cycles at the current density of  $1 \text{ A g}^{-1}$ . At the pristine state, all four electrodes exhibited similar EIS spectra indicating that the charge transfer resistance ( $R_{\text{ct}}$ ) and lithium ion diffusion kinetics were similar (Figure 4.3.25a).[4.43] After 200<sup>th</sup> cycles, the charge transfer resistance of MnP and MnP/VP mixture electrode became relatively larger (Figure 4.3.25b) and the sloping line at low frequency region in the Nyquist plot corresponding to the diffusivity of lithium ion decreased (Figure 4.3.25c), which can be related to the agglomeration of alloying elements during cycling (Figure 4.3.24c).[4.44] On the other hand, charge transfer

resistance and sloping line of the solid solution  $\text{Mn}_{0.75}\text{V}_{0.25}\text{P}$  electrode were well maintained during cycling similar to the VP electrode, which can be attributed to the structural stability of solid solution  $\text{Mn}_{0.75}\text{V}_{0.25}\text{P}$  electrode during cycling.

Galvanostatic intermittent titration technique (GITT) was used to further evaluate the reaction resistance of  $\text{Mn}_{1-x}\text{V}_x\text{P}$  ( $x = 0, 0.25, \text{ and } 1.0$ ) solid solution and MnP/VP mixture electrodes at each reaction potential during lithiation/delithiation for 2<sup>nd</sup> cycle (Figure 4.3.26a).[4.45,4.46] During the GITT measurements, a constant current of  $100 \text{ mA g}^{-1}$  was applied for 10 min and the cells were subsequently rested for 90 min at open circuit. Figure 4.3.26b shows the evaluated reaction resistances at each reaction potential during lithiation, which were obtained from the potential difference between end of the current step and end of the relaxation step. During the lithiation process, one and two volcano-shaped profiles were identified for VP and MnP electrodes, respectively. The two volcano-shaped profile was also identified in the MnP/VP mixture electrode, while two distinct volcano shapes were not observed in the  $\text{Mn}_{0.75}\text{V}_{0.25}\text{P}$  electrode and the reaction resistance was relatively lower than that of MnP and MnP/VP mixture electrodes, which indicates that the  $\text{Mn}_{0.75}\text{V}_{0.25}\text{P}$  electrode exhibited the improved lithiation kinetics compared to those of MnP and MnP/VP mixture electrodes. The reaction resistance of all four electrodes increased during delithiation process and the reaction resistance of  $\text{Mn}_{0.75}\text{V}_{0.25}\text{P}$  electrode was also slightly lower than that of MnP and MnP/VP mixture electrodes (Figure 4.3.26c). After 20 cycles, the reaction resistance of MnP and MnP/VP mixture electrodes was still higher than that of  $\text{Mn}_{0.75}\text{V}_{0.25}\text{P}$  and VP electrodes for both lithiation and delithiation processes (Figure 4.3.27). It can be inferred that the solid solution electrode not only hindered the agglomeration of the alloying element, but also

maintained the structural integrity (i.e. lithium diffusion path), which facilitated the electron and ion transport during the extended cycling.

From these observations, it can be concluded that the substitution of vanadium ion into the MnP crystal structure induces the expansion and geometric change of prismatic site similar to the VP crystal structure, which can accommodate more Li-ion and allows the alloying/insertion hybrid electrochemical reaction in a single phase. The solid solution electrode exhibits much improved electrochemical performance compared to that of mixture composite electrode due to its synergistic effects of alloying/insertion hybrid electrochemical reactions occurred in a few-nanometer scale, which effectively buffer the volume change, hinder the pulverization and agglomeration of alloying reaction elements during cycling, and ensure the fast electron and ion transport (Figure 4.3.28).

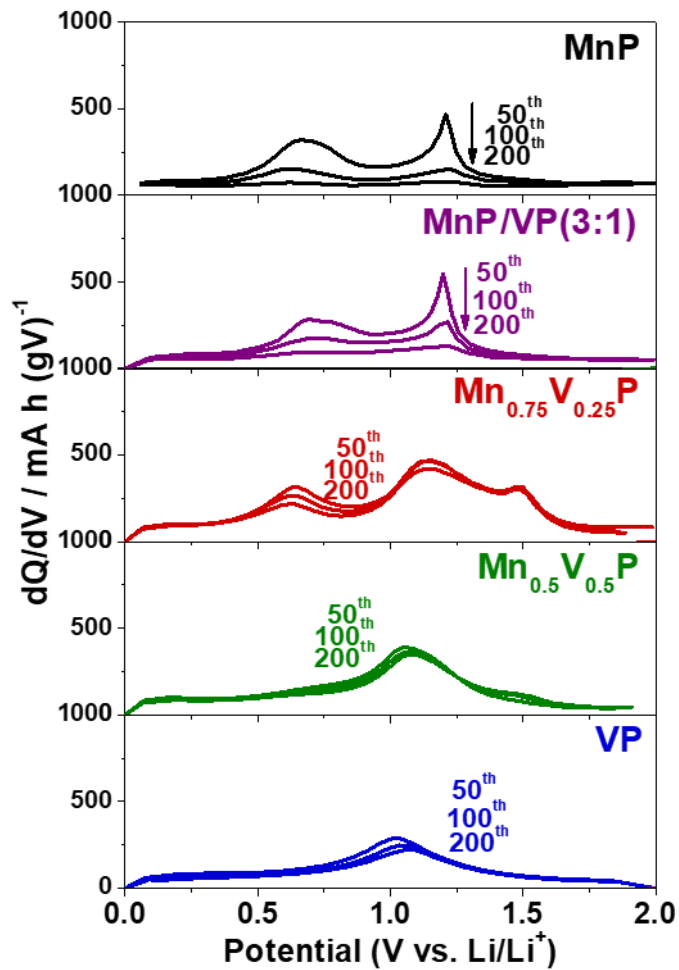


**Figure 4.3.23** DCPs of  $\text{Mn}_{1-x}\text{V}_x\text{P}$  ( $x = 0, 0.25, 0.5, \text{ and } 1.0$ ) and  $\text{MnP/VP}(3:1)$  electrodes at  $1 \text{ A g}^{-1}$ .

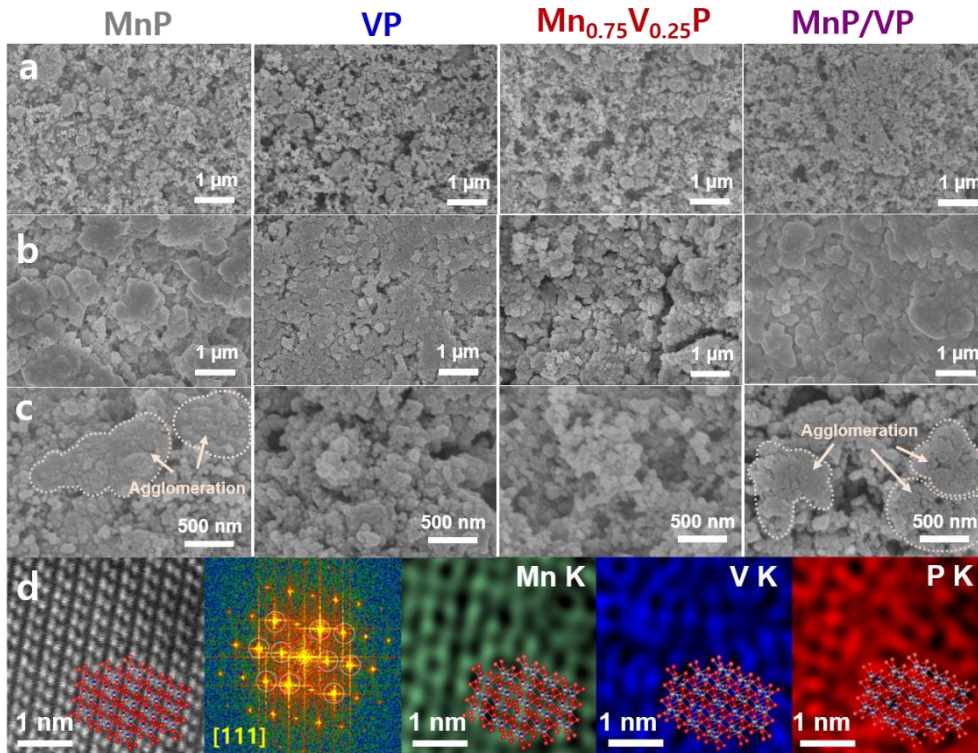


**Figure 4.3.24** SEM images of (a) pristine, (b) cycled (200 cycle at  $1 \text{ A g}^{-1}$ ) including SEI layer, and (c) cycled removing SEI layer for MnP, VP,  $Mn_{0.75}V_{0.25}P$ , and MnP/VP electrodes, respectively. (d) HAADF STEM image and EDS mapping images for Mn K, V K, and P K for  $Mn_{0.75}V_{0.25}P$  electrode after 200 cycles at  $1 \text{ A g}^{-1}$ .

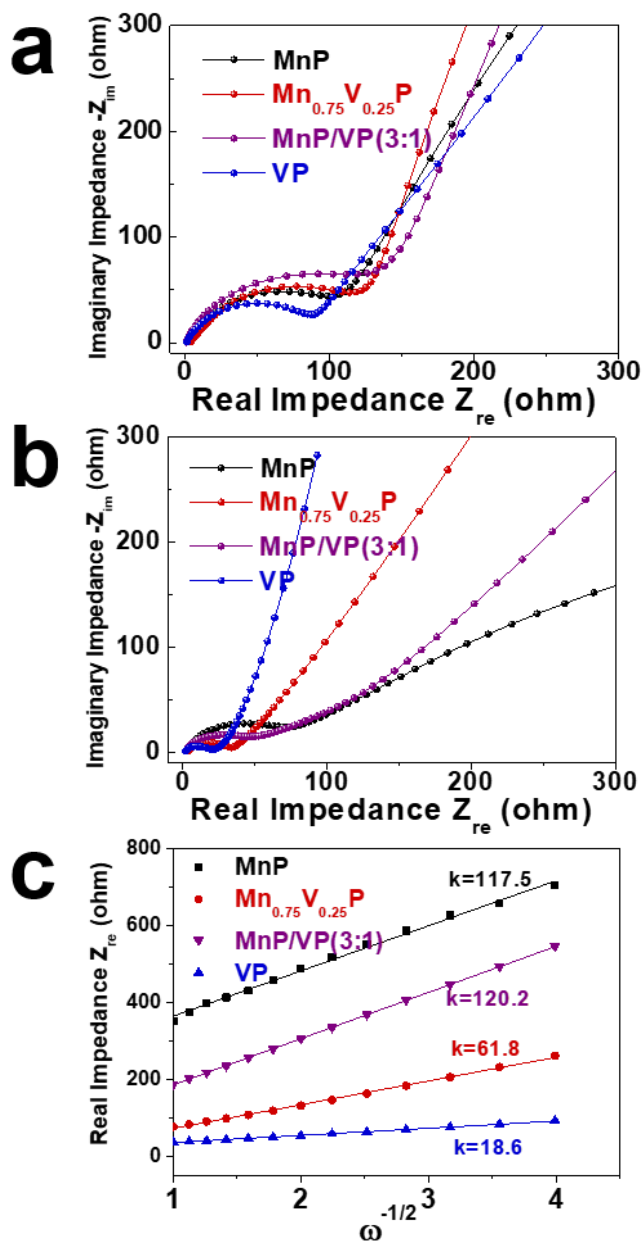


**Figure 4.3.25** Nyquist plots of  $Mn_{1-x}V_xP$  ( $x = 0, 0.25, 1.0$ ) and MnP/VP electrodes for (a) pristine and (b) after 200 cycles at  $1 \text{ A g}^{-1}$ ; (c) the linear relationship between the Warburg impedance ( $Z_{re}$ ) and the inverse square root of angular frequency in low frequency region in (b).

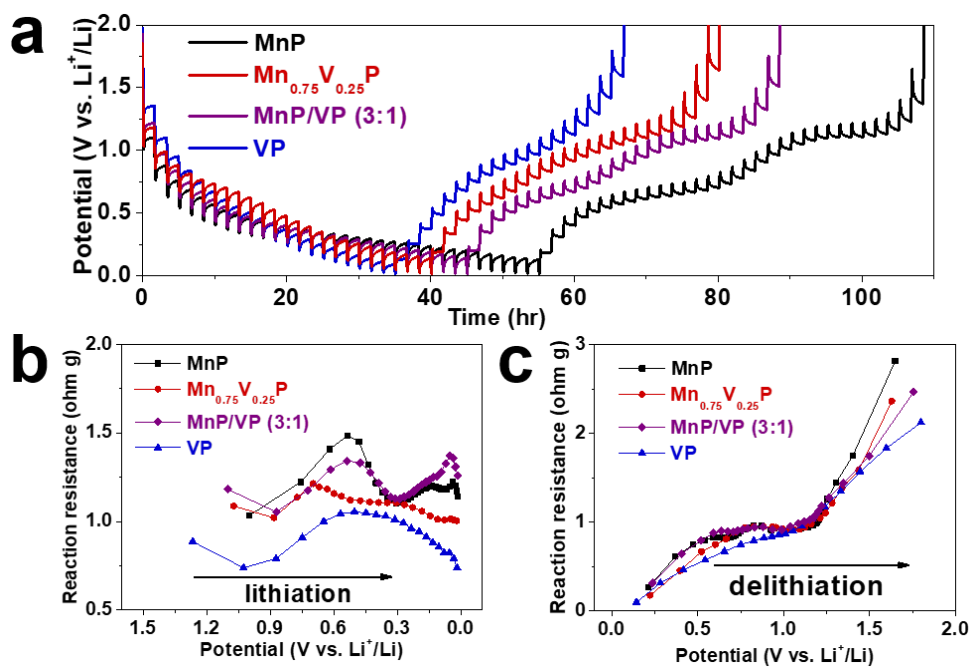


**Figure 4.3.26** (a) GITT profiles of the state of the lithiation/delithiation process for 2<sup>nd</sup> cycle; Reaction resistance derived from GITT measurement during (b) lithiation and (c) delithiation for  $\text{Mn}_{1-x}\text{V}_x\text{P}$  ( $x = 0.0, 0.25, \text{ and } 1.0$ ) and MnP/VP electrodes, respectively.

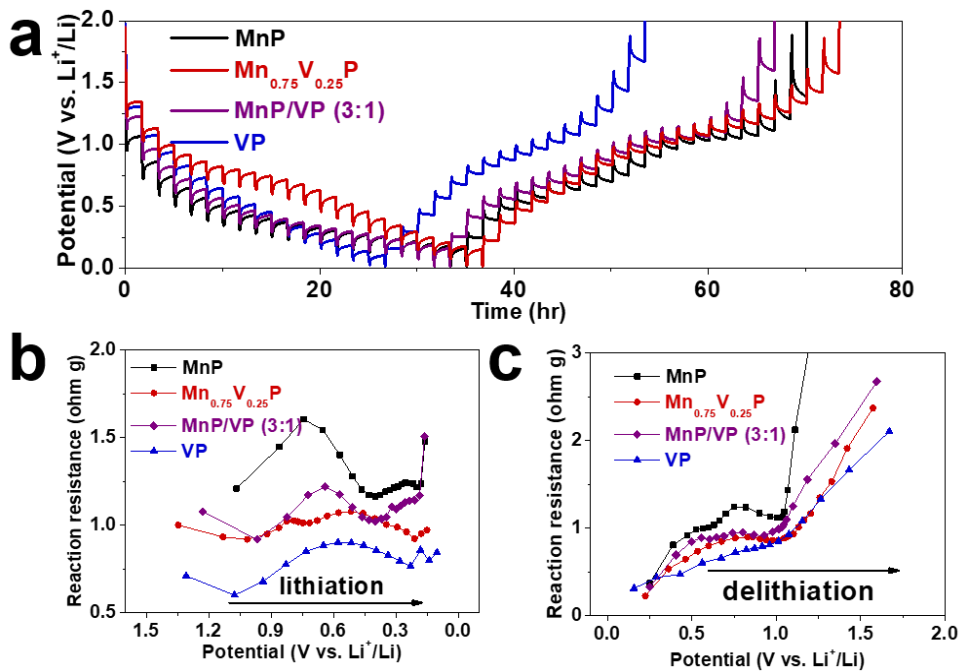


**Figure 4.3.27** (a) GITT profiles of the state of the lithiation/delithiation process for 20<sup>th</sup> cycle; Reaction resistance derived from GITT measurement during (b) lithiation and (c) delithiation for  $\text{Mn}_{1-x}\text{V}_x\text{P}$  ( $x = 0.0, 0.25, \text{ and } 1.0$ ) and MnP/VP electrodes, respectively.

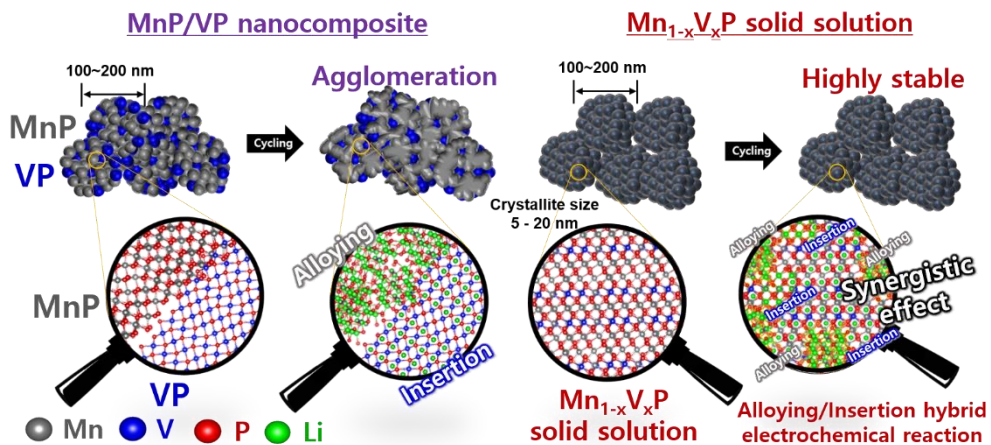


**Figure 4.3.28** Schematic illustration for the cycling behavior of MnP/VP nanocomposite and  $Mn_{0.75}V_{0.25}P$  electrodes, respectively.

### 4.3.5. Discussion on Hybrid Alloying/Insertion Reaction Anodes

Based on the findings in the  $Mn_{1-x}V_xP$  solid solution electrode, a local geometry of Li-ion insertion site in solid solution phase as well as a similar structural relationship between lithiated phase and initial solid solution phase could be the critical factors to exhibit the reversible hybrid alloying/insertion reaction. In this regard, two different electrochemical reaction-type materials with a similar space group or group-subgroup relation can form a hybrid reaction solid solution anode when the solid solution is composed of an insertion reaction-type material as a host structure and an alloying or conversion reaction-type material with a similar local geometry of lithium insertion site of this host structure. A case study was performed on  $Mn_{1-x}Mo_xP$  compounds to ascertain above correlation for hybrid alloying/insertion anode.

Among the various transition metal monophosphides (Table 4.3.4)[4.47], molybdenum monophosphide (MoP) with a hexagonal WC structure (space group  $P-6m2$ ) can be an insertion reaction alternative[4.48] to form the solid solution with alloying reaction MnP (space group  $Pnma$ ) for the alloying/insertion hybrid reaction based on the structural similarity and ionic radius ( $Mn^{3+} = 0.58 \text{ \AA}$ ,  $Mo^{3+} = 0.69 \text{ \AA}$ ,  $V^{3+} = 0.64 \text{ \AA}$ , CN = 6) (Figure 4.3.29). The  $Mn_{1-x}Mo_xP$  ( $x = 0.25$  and  $0.5$ ) compounds were also synthesized by HEMM and the formation of solid solution with orthorhombic MnP crystal structure was confirmed by XRD (Figure 4.3.30a). The  $Mn_{1-x}Mo_xP$  ( $x = 0.25$  and  $0.5$ ) compounds showed the similar structural change to

$\text{Mn}_{1-x}\text{V}_x\text{P}$  compounds and the diffraction peaks further shifted to the lower  $2\theta$  than those of  $\text{Mn}_{1-x}\text{V}_x\text{P}$  ( $x = 0.25$  and  $0.5$ ), which was resulted from the relatively large ionic radius of  $\text{Mo}^{3+}$  ( $0.69 \text{ \AA}$ ) than that of  $\text{V}^{3+}$  ( $0.64 \text{ \AA}$ ). The  $\text{Mn}_{0.75}\text{Mo}_{0.25}\text{P}$  electrode showed the alloying/insertion hybrid reaction similar to  $\text{Mn}_{0.75}\text{V}_{0.25}\text{P}$  electrode in the DCP plots (Figure 4.3.30b). The *ex-situ* XRD pattern of fully lithiated  $\text{Mn}_{0.75}\text{Mo}_{0.25}\text{P}$  electrode indicated the formation of  $\text{Li}_3\text{MnP}_2$  and Li-inserted  $\text{Mn}_{0.75}\text{Mo}_{0.25}\text{P}$  phases (Figure 4.3.30c). Thus, the  $\text{Mn}_{0.75}\text{Mo}_{0.25}\text{P}$  electrode showed the stable cycle performance similar to  $\text{Mn}_{0.75}\text{V}_{0.25}\text{P}$  electrode at high current density of  $1.0 \text{ A g}^{-1}$  (Figure 4.3.30d). On the other hand, the DCP of  $\text{Mn}_{0.5}\text{Mo}_{0.5}\text{P}$  electrode was very similar to that of VP electrode and the *ex-situ* XRD pattern was unchanged and the alloying phase was not detected after the full lithiation (Figure 4.3.30b-d). Consequently, the  $\text{Mn}_{0.5}\text{Mo}_{0.5}\text{P}$  electrode showed only topotactic Li-ion insertion/extraction reaction different from the  $\text{Mn}_{0.5}\text{V}_{0.5}\text{P}$  electrode, which can be attributed to the greater structural change and prismatic site expansion of  $\text{Mn}_{0.5}\text{Mo}_{0.5}\text{P}$  due to the larger radius of  $\text{Mo}^{3+}$  than that of  $\text{V}^{3+}$ .

This preliminary result shows the promising potential of the solid solution electrodes with hybrid electrochemical reactions achieved through the multi-component substitution by considering the local structural geometry for Li-ion insertion as well as structural similarity between lithiated phase and initial solid solution phase. Following these considerations, there would be many candidates in other transition metal compounds ( $\text{TM}_a\text{X}_y$ , TM = transition metal and X = O, P, S, N, As, and etc.) to form the solid solutions that enable the hybrid alloying/insertion reactions to develop high performance anodes for secondary-ion battery applications.

**Table 4.3.4** Space group and structure type of transition metal monophosphide compounds.

MP <sub>6</sub> Polyhedra	Space group / Structure type	Compounds
Octahedron	Fm-3m / NaCl	ScP, YP, ZrP
	P6 <sub>3</sub> /mmc / NiAs	VP
	P6 <sub>3</sub> /mmc / TiAs	TiP, ZrP, HfP
	Pbca / NiP	NiP
	Pnma / MnP	MnP, CrP, FeP, CoP, WP, RuP
	Cmc2 <sub>1</sub> / Na <sub>2</sub> SiO <sub>3</sub>	NiP
	Pnma / Nd <sub>3</sub> Br <sub>5</sub> S <sub>3</sub>	NiP
	P-6m2 / WC	MoP
Trigonal prism	I4 <sub>1</sub> md /	NbP, TaP

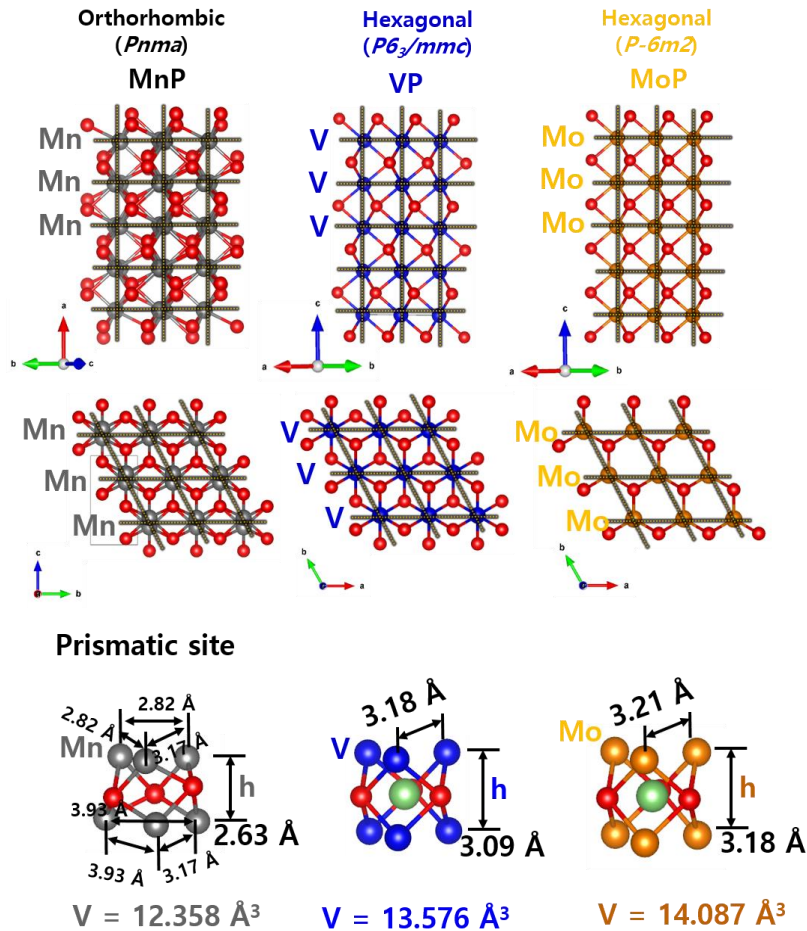


**Figure 4.3.29** Illustration of crystal structure and prismatic site for MnP, VP, and MoP, respectively.

(MoP structure has a relatively large volume of prismatic site compared to that of MnP and VP structures. The metal arrangement in MoP structure that consists prismatic site is almost identical to that of MnP and VP structures and the height of prismatic site is large, which can increase the height and volume of the distorted prismatic site in MnP structure when Mo ion is substituted into MnP structure.)

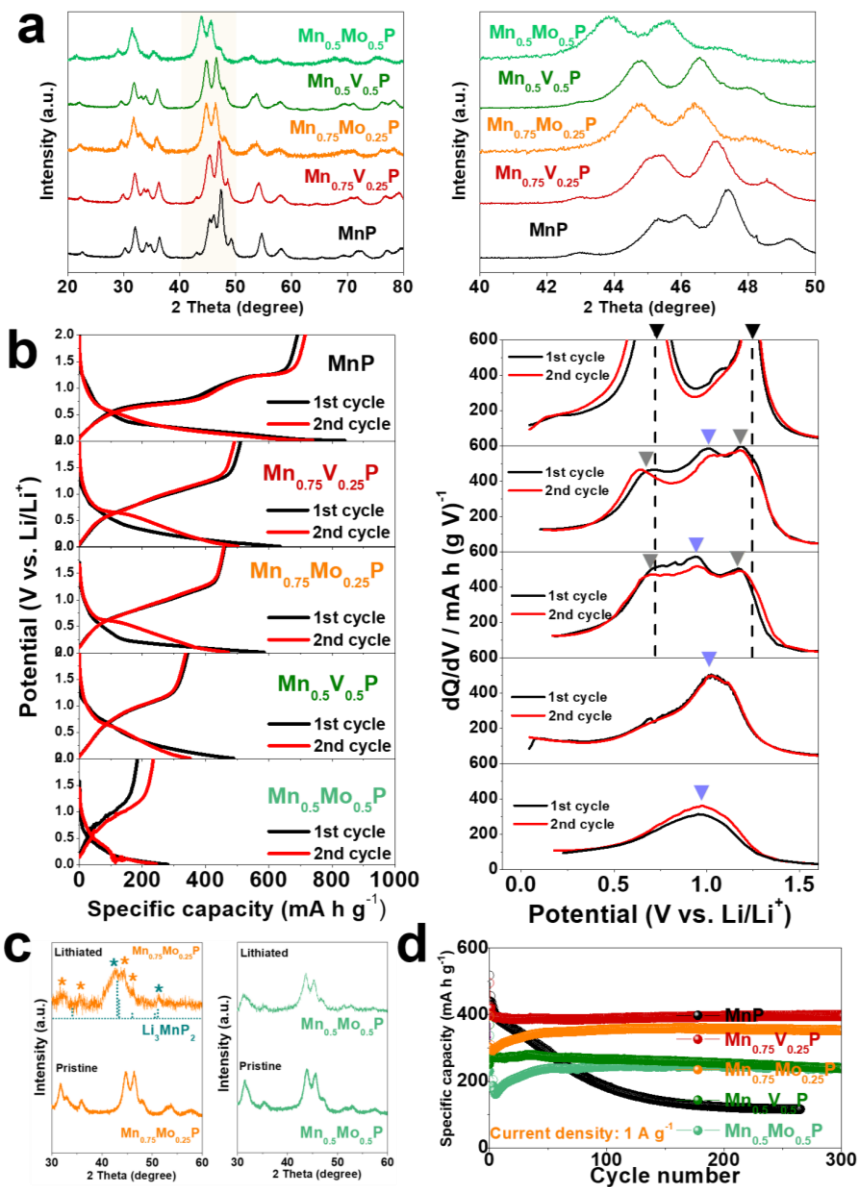


**Figure 4.3.30** (a) XRD patterns, (b) voltage profiles and DCPs of MnP and Mn<sub>1-x</sub>TM<sub>x</sub>P (TM = V and Mo, x = 0.25 and 0.5). (c) *Ex-situ* XRD pattern of Mn<sub>1-x</sub>Mo<sub>x</sub>P (x = 0.25 and 0.5) electrodes for pristine and lithiated state. (d) Cycle performance of MnP and Mn<sub>1-x</sub>TM<sub>x</sub>P (TM = V and Mo, x = 0.25 and 0.5) electrodes at current density of 1 A g<sup>-1</sup>.

### 4.3.6. Practical Application with Full-Cell Configuration

To evaluate the possibility of  $\text{Mn}_{0.75}\text{V}_{0.25}\text{P}$  solid solution for practical applications, a full-cell has been constructed with as-synthesized pure  $\text{Mn}_{0.75}\text{V}_{0.25}\text{P}$  electrode as negative (N) and commercially available  $\text{LiCoO}_2$  (LCO) electrode as positive (P) at a commercial level of mass loading (areal capacity  $> 2.5 \text{ mA h cm}^{-2}$ ). The negative electrode  $\text{Mn}_{0.75}\text{V}_{0.25}\text{P}$  was precycled at  $100 \text{ mA g}^{-1}$  to higher the initial Coulombic efficiency of  $\text{Mn}_{0.75}\text{V}_{0.25}\text{P/LCO}$  full cell. The  $\text{Mn}_{0.75}\text{V}_{0.25}\text{P/LCO}$  full cell was electrochemically tested at C-rate of 0.1 C and 1 C ( $1 \text{ C} = 2.5 \text{ mA h cm}^{-2}$ ) within the voltage range between 2.0 and 4.2 V (Figure 4.3.31). The  $\text{Mn}_{0.75}\text{V}_{0.25}\text{P/LCO}$  full cell showed initial charge and discharge capacities of 2.54 and  $2.26 \text{ mA h cm}^{-2}$  with high initial Coulombic efficiency of 89% at 0.1 C (Figure 4.3.31a). In addition, the Coulombic efficiency of  $\text{Mn}_{0.75}\text{V}_{0.25}\text{P/LCO}$  full cell continuously increased and reached 99.8% within 10 cycles indicating highly stable reversible charge/discharge reactions (Figure 4.3.31c). The  $\text{Mn}_{0.75}\text{V}_{0.25}\text{P/LCO}$  full-cell delivered the high areal capacity of  $1.57 \text{ mA h cm}^{-2}$  after 100 cycles with average Coulombic efficiency of 99.73%. In addition, the high-rate cycle performance of the  $\text{Mn}_{0.75}\text{V}_{0.25}\text{P/LCO}$  full-cell was tested at 1 C after two activation cycles at 0.1 C and 0.5 C, respectively, and it still exhibited an excellent performance with a high reversible capacity of  $1.48 \text{ mA h cm}^{-2}$  after 100 cycles with a coulombic efficiency of about 99.8%. (Figure 4.3.31b and d). This demonstrates the sustainable operation of the pure  $\text{Mn}_{0.75}\text{V}_{0.25}\text{P}$  electrode even at the full-cell configuration with commercial LCO electrode at the practical mass loading.

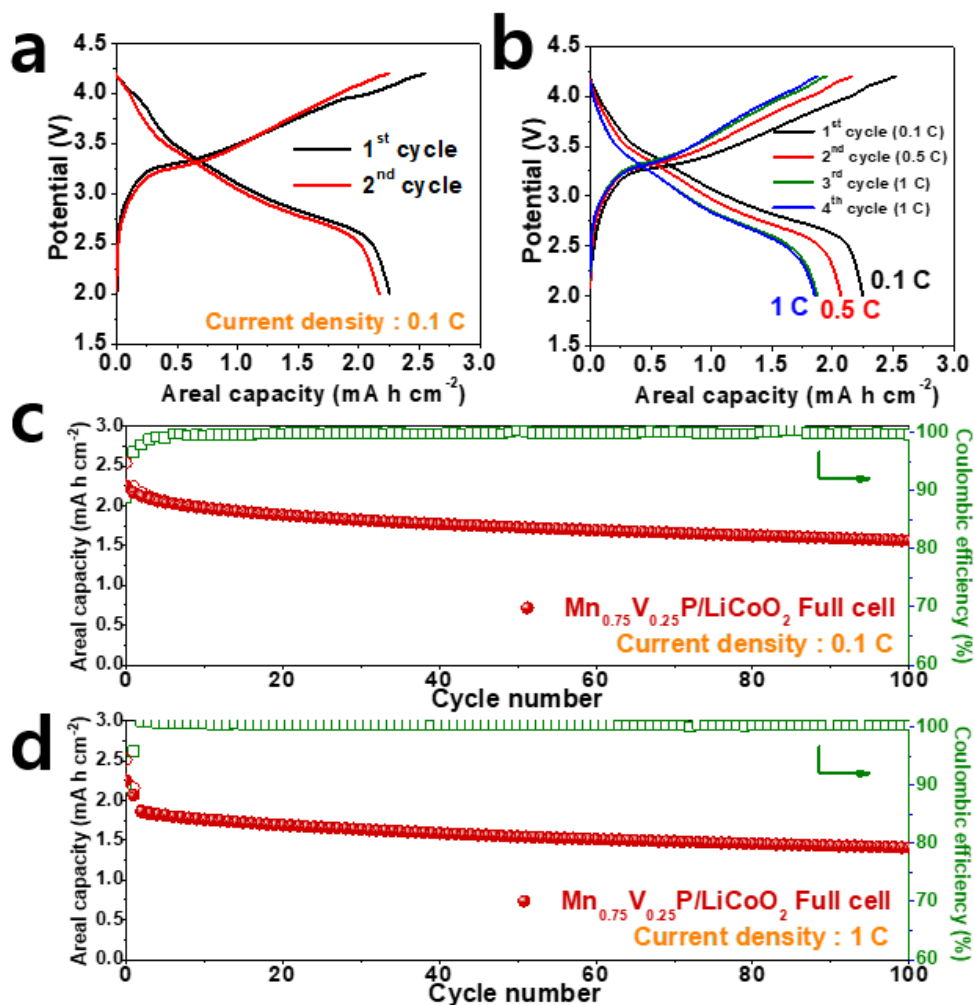


**Figure 4.3.31** Galvanostatic charge/discharge voltage profiles and cycle performance of  $\text{Mn}_{0.75}\text{V}_{0.25}\text{P}/\text{LiCoO}_2$  full cell tested at current density of (a,c) 0.1 C and (b,d) 1 C with two activation cycles at 0.1 C and 0.5 C, respectively.

## 4.4. Conclusion

The introduction of solid solution compound between two different materials with similar crystal structure and different electrochemical reaction mechanism is a very promising and novel approach that can strengthen the advantages of each reaction mechanism while mitigating the shortcomings as well. The solid solution compounds of  $\text{Mn}_{1-x}\text{V}_x\text{P}$  ( $x = 0, 0.25, 0.5, 0.75$  and  $1.0$ ) between alloying reaction type MnP and insertion reaction type VP were firstly synthesized via a high energy mechanical milling. The homogeneously substituted vanadium ions in the  $\text{Mn}_{1-x}\text{V}_x\text{P}$  compounds enable the alloying/insertion hybrid electrochemical reactions in a single phase by changing the local structure of prismatic site in  $\text{Mn}_{1-x}\text{V}_x\text{P}$  close to the that of insertion-reaction type VP. The superior electrochemical performance of  $\text{Mn}_{1-x}\text{V}_x\text{P}$  was attributed to the synergistic effect of hybrid alloying/insertion electrochemical reaction occurred close to a few-nanometer scale in a single compound  $\text{Mn}_{1-x}\text{V}_x\text{P}$  phase, which effectively relieve volume change and agglomeration of active materials and ensure fast electron and ion transport. This kind of novel approach suggests that multi-component substitution in different reaction type anode materials with considering their structural and chemical relation can substantially improve the tunable electrochemical performance and it is one of the methods for developing a new promising anode material for LIBs.

## 4.5. Bibliography

- [4.1] D. Larcher, J.-M. Tarascon, *Nature Chem.* **2015**, 7, 19-29.
- [4.2] T. M. Gur, *Energy Environ. Sci.* **2018**, 11, 2696.
- [4.3] M. A. Hannan, M. M. Hoque, A. Mohamed, A. Ayob, *Renew. Sustain. Energy Rev.* **2017**, 771-789.
- [4.4] Y. Zhao, L. P. Wang, M. T. Sougrati, Z. Feng, Y. Leconte, A. Fisher, M. Srinivasan, Z. Xu, *Adv. Energy Mater.* **2017**, 7, 1601424.
- [4.5] M. D. Bhatt, J. Y. Lee, *Inter. J. Hydro. Energy* **2019**, 44, 10852-10905.
- [4.6] N. Nitta, G. Yushin, *Part. Part. Syst. Charact.* **2014**, 31, 317-336.
- [4.7] V. Aravindan, Y.-S. Lee, S. Madhavi, *Adv. Energy Mater.* **2015**, 5, 1402225.
- [4.8] M. Ebner, F. Marone, M. Stampanoni, V. Wood, *Science* **2013**, 342, 716-720.
- [4.9] K. Feng, M. Li, W. Liu, A. G. Kashkooli, X. Xiao, M. Cai, Z. Chen, *Small* **2018**, 14, 1702737.
- [4.10] H. Ying, W.-Q. Han, *Adv. Sci.* **2017**, 4, 1700298.
- [4.11] Z. Li, X. Yu, Y. Liu, W. Zhao, H. Zhang, R. Xu, D. Wang, H. Shen, *J. Mater. Chem. A* **2016**, 4, 19123.
- [4.12] C.-M. Park, J.-H. Kim, H. Kim, H.-J. Sohn, *Chem. Soc. Rev.* **2010**, 39, 3115-3141.
- [4.13] Y. Tang, Y. Zhang, W. Li, B. Ma, X. Chen, *Chem. Soc. Rev.* **2015**, 44, 5926.
- [4.14] M. R. A. Hassan, A. Sen, T. Zaman, M. S. Mostari, *Mater. Today Chem.* **2019**, 11, 225-243.
- [4.15] Q. An, F. Lv, Q. Liu, C. Han, K. Zhao, J. Sheng, Q. Wei, M. Yan, L. Mai, *Nano Lett.* **2014**, 14, 6250-6256.

- [4.16] D. Zhao, Q. Hao, C. Xu, *Electrochim. Acta* **2016**, 211, 83-91.
- [4.17] S. Li, Y. Zhang, J. Huang, *J. Alloys and Comp.* **2019**, 783, 793-800.
- [4.18] Y. Zhong, Y. Ma, Q. Guo, J. Liu, Y. Wang, M. Yang, H. Xia, *Sci. Rep.* **2017**, 7, 40927.
- [4.19] K. Zhao, F. Liu, C. Niu, W. Xu, Y. Dong, L. Zhang, S. Xie, M. Yan, Q. Wei, D. Zhao, L. Mai, *Adv. Sci.* **2015**, 2, 1500154.
- [4.20] Y. Xu, Y. Zhu, Y. Liu, C. Wang, *Adv. Energy Mater.* **2013**, 3, 128-133.
- [4.21] D. Bresser, S. Passerini, B. Scrosati, *Energy Environ. Sci.* **2016**, 9, 3348.
- [4.22] P. F. Teh, S. S. Pramana, C. Kim, C.-M. Chen, C.-H. Chuang, Y. Sharma, J. Cabana, S. Madhavi, *J. Phys. Chem. C* **2013**, 117, 24213-24223.
- [4.23] P. F. Teh, S. S. Pramana, Y. Sharma, Y. W. Ko, S. Madhavi, *ACS Appl. Mater. Interfaces* **2013**, 5, 5461-5467.
- [4.24] X. Guo, X. Lu, X. Fang, Y. Mao, Z. Wang, L. Chen, X. Xu, H. Yang, Y. Liu, *Electrochem. Commun.* **2010**, 12, 847-850.
- [4.25] P. A. Connor, J. T. S. Irvine, *Journal of Power Sources* **2001**, 97-98, 223-225.
- [4.26] S. Lei, K. Tang, C. Chen, Y. Jin, L. Zhou, *Mater. Res. Bull.* **2009**, 44, 393-397.
- [4.27] C.-C. Chang, Y.-C. Chen, C.-W. Huang, Y. H. Su, C.-C. Hu, *Electrochim. Acta* **2013**, 99, 69-75.
- [4.28] Y.-C. Chen, T.-F. Hung, C.-W. Hu, C.-Y. Chiang, C.-W. Huang, H.-C. Su, R.-S. Liu, C.-H. Lee, C.-C. Chang, *Nanoscale* **2013**, 5, 2254-2258.
- [4.29] X. Xin, X. Zhou, T. Shen, Z. Liu, *J. Nanomat.* **2015**, 965061, 1-10.
- [4.30] S. Li, M. Ling, J. Qiu, J. Han, S. Zhang, *J. Mater. Chem. A* **2015**, 3, 9700.
- [4.31] A. Courtney, J. R. Dahn, *J. Electrochem. Soc.* **1997**, 144, 2045.

- [4.32] H. Fjellvag, A. Kjekshus, *J. Phys. Chem. Solids* **1984**, 45, 709-718.
- [4.33] H. Fjellvag, A. Kjekshus, *Acta Chemi. Scan. A* **1986**, 40, 8-16.
- [4.34] H. Fjellvag, A. Kjekshus, *Acta Chemi. Scan. A* **1984**, 38, 703-710.
- [4.35] S.-G. Woo, J.-H. Jung, H. Kim, M. G. Kim, C. K. Lee, H.-J. Sohn, B. W. Cho, *J. Electrochem. Soc.* **2006**, 153, A1979-A1983.
- [4.36] C.-M. Park, Y.-U. Kim, H.-J. Sohn, *Chem. Mater.* **2009**, 21, 5566-5568.
- [4.37] L. Li, Y. Peng, H. Yang, *Electrochim. Acta* **2013**, 95, 230-236.
- [4.38] K.-H. Kim, W.-S. Kim, S.-H. Hong, *Nanoscale* **2019**, 11, 13494-13501.
- [4.39] F. Han, C. Zhang, J. Yang, G. Ma, K. He, X. Li, *J. Mater. Chem. A* **2016**, 4, 12781-12789.
- [4.40] D. Yang, J. Zhu, X. Rui, H. Tan, R. Cai, H. E. Hoster, D. Y. W. Yu, H. H. Hng, Q. Yan, *ACS Appl. Mater. Interfaces* **2013**, 5, 1093-1099.
- [4.41] P. G. Bruce, B. Scrosati, J.-M. Tarascon, *Angew. Chem. Int. Ed.* **2008**, 47, 2930-2946.
- [4.42] M. G. Kim, J. Cho, *Adv. Funct. Mater.* **2009**, 19, 1497-1514.
- [4.43] J. W. Choi, J. McDonough, S. Jeong, J. S. Yoo, C. K. Chan, Y. Cui, *Nano Lett.* **2010**, 10, 1409-1413.
- [4.44] M. Fan, Y. Chen, Y. Xie, T. Yang, X. Shen, N. Xu, H. Yu, C. Yan, *Adv. Funct. Mater.* **2016**, 26, 5019-5027.
- [4.45] Y.-L. Bai, Y.-S. Liu, C. Ma, K.-X. Wang, J.-S. Chen, *ACS Nano* **2018**, 12, 11503-11510.
- [4.46] X. Li, J. Liang, Z. Hou, W. Zhang, Y. Wang, Y. Zhu, Y. Qian, *Adv. Funct. Mater.* **2015**, 25, 5229-5238.
- [4.47] J.-H. Chen, K. H. Whitmire, *Coordin. Chem. Rev.* **2018**, 355, 271-327.

# **Chapter 5. Solid Solution $Mn_{1-x}TM_xP_4$ (TM = V and Fe) Anode with High Performance Conversion Reaction for Sodium-Ion Batteries**

## **5.1. Introduction**

Over the past three decades, Li-ion batteries (LIBs) have attracted great attention as the common power sources in energy storage fields of consumer electronics, electrical vehicles (EVs) and grid-scale energy storage system (ESS). However, since the increase in the cost of LIBs by finite lithium resources cannot meet the ever-increasing demand for LIBs, Na-ion batteries (SIBs) can be a possible alternative to conventional LIBs owing to the natural abundance and low cost of sodium resources.[5.1-5.3] Although, the battery components and energy storage mechanism of SIBs is basically similar with those of LIBs, many challenging issues derived from thermodynamic and kinetic aspects should be overcome. The commercial graphite anode used in LIBs is electrochemically less active in Na cells, presumably due to the thermodynamic instability of Na-graphite intercalation compounds resulting from a greater degree of change of the stretched C-C bond length in the graphite layer.[5.4] In addition, another promising anode silicon, which shows the highest specific capacity among LIB anodes with alloying reaction forming lithium-rich alloy phase  $Li_{15}Si_4$  (Theoretical capacity of  $3590 \text{ mA h g}^{-1}$ ), cannot form Na-rich alloy phase. Theoretical calculation shows that silicon can react

with sodium-ion as  $\text{Na}_{0.76}\text{Si}$  phase (Theoretical capacity of  $725 \text{ mA h g}^{-1}$ ), even experimentally confirmed reversible capacity was about  $500 \text{ mA h g}^{-1}$  due to the reaction kinetic limit.[5.5-5.7] Therefore, the major scientific challenge for SIBs resides in developing new anode materials with high specific capacity and an appropriately low redox potential to enhance the energy density of SIBs.

Since the phosphorus can react with Na-ion to form sodium-rich  $\text{Na}_3\text{P}$  phase, corresponding to the specific capacity of  $2596 \text{ mA h g}^{-1}$ , it has been attracted as a great potential anode for SIBs.[5.8,5.9] Although phosphorus shows the highest theoretical capacity and moderate operating voltage ( $\sim 0.4 \text{ V vs. Na/Na}^+$ ) among other SIB anode candidates, its practical application is severely hindered by several formidable problems. The large volume expansion (300-500%) of red phosphorus during cycling can cause great stress and crack formation, which will result in electrode performance degradation, and the low electrical conductivity ( $\sim 10^{-14} \text{ S cm}^{-1}$ ) slows the reaction kinetics.[5.10-5.12] To address this issues, electrochemical conversion reaction-type metal phosphide ( $\text{MP}_x$ ) was introduced as anode for SIBs because it lessened volume variation in the electrochemical sodiation/desodiation process due to the formation of less volume-variation components, which can act as a buffer matrix to accommodate volume change of alloying reaction P. In addition, faster kinetic reaction could be obtained because of the highly conductive metal phosphide phase and the generation of conductive metallic components through conversion reaction ( $\text{MP}_x + 3x \text{ Na}^+ + 3x \text{ e}^- \rightarrow \text{M} + x\text{Na}_3\text{P}$ ).[5.13-5.20]

Various metal phosphides  $\text{MP}_x$  have been reported as anode materials for both LIBs and SIBs and their reaction mechanism are different according to the features

of the metal and the metal-phosphorus bonds stability when reacted with Li- or Na-ion. Among the various metal phosphide based anode material for LIBs, in particular, phosphorus-rich phases, have attracted considerable interest due to their outstanding properties, such as good electrical conductivity and high theoretical capacity.[5.21-5.26] The earth-abundant element containing manganese tetrphosphide ( $\text{MnP}_4$ ) was introduced as a promising anode material for LIBs by Nazar et al. showing that a high lithiation/delithiation capacity by forming the high lithium content of  $\text{Li}_7\text{MnP}_4$  crystalline phase ( $\text{MnP}_4 + 7\text{Li}^+ + 7\text{e}^- \leftrightarrow \text{Li}_7\text{MnP}_4$ , theoretical capacity of  $1050 \text{ mA h g}^{-1}$ ) within potential window 3.0-0.57 V vs.  $\text{Li/Li}^+$ .[5.25] Further study on electrochemical reaction mechanism of  $\text{MnP}_4$  for a LIB anode confirmed that it firstly transformed to crystalline  $\text{Li}_7\text{MnP}_4$  phase and undertake conversion reaction ( $\text{Li}_7\text{MnP}_4 + 5\text{Li}^+ + 5\text{e}^- \rightarrow \text{Mn} + 4 \text{Li}_3\text{P}$ , theoretical capacity of  $1800 \text{ mA h g}^{-1}$ ) with further lithiation within potential window 2.0-0.01 V vs.  $\text{Li/Li}^+$ .[5.26] Despite such a superior capacity characteristic of  $\text{MnP}_4$ , practical electrochemical performance such as cycle retention and rate capability has never been reported previously. One possible reason may be related to the conventional synthesis process of  $\text{MnP}_4$  phase, which was synthesized by high pressure or chemical transportation with iodine or bromide at high temperature for a long annealing time, making it difficult to obtain the nanoparticle nature and corresponding superior electrochemical performance of  $\text{MnP}_4$ .[5.27-5.30] For this reason, although the  $\text{MnP}_4$  phase can be a promising candidate of high capacity anode for both LIBs and SIBs, the electrochemical performance is unknown yet and study on the electrochemical reaction mechanism for SIBs is also highly required.

In this study, phosphorus-rich  $\text{MnP}_4$  phase was firstly synthesized via a facile

and mass productive high energy mechanical milling process to prepare nanoparticle nature of  $\text{MnP}_4$  for high performance anode application. In addition,  $\text{MnP}_4$  phase was introduced as an anode for SIBs and its electrochemical performance and reaction mechanism were firstly investigated. To improve its electrochemical performance,  $\text{MnP}_4/\text{graphene}$  nanocomposite was fabricated with commercial graphene nanosheets. As-fabricated  $\text{MnP}_4/\text{graphene}$  nanocomposite exhibits improved cycle retention property, which delivers reversible capacity of  $446 \text{ mA h g}^{-1}$  for 250 cycles at high current density of  $0.5 \text{ A g}^{-1}$ . Further, different cation substitution of vanadium and iron in  $\text{MnP}_4$  as forming substitutional solid solution strategy was also introduced to higher reaction kinetics of conversion reaction. Since the electronic structure calculation of  $\text{TMP}_4$  ( $\text{TM} = \text{V}, \text{Cr}, \text{Mn}, \text{and Fe}$ ) phases indicated that physicochemical and electrical properties of  $\text{TMP}_4$  structure are varied with different metal components[5.31], substitutional  $\text{Mn}_{1-x}\text{TM}_x\text{P}_4$  ( $\text{TM} = \text{V}$  and  $\text{Fe}$ ,  $x = 0.25$ ) solid solution was introduced to vary its physicochemical and electrochemical properties. Among the substitutional  $\text{Mn}_{1-x}\text{TM}_x\text{P}_4$  solid solutions,  $\text{Mn}_{1-x}\text{V}_x\text{P}_4$  ( $x=0.25$ ) electrode showed improved high rate capability, which delivers reversible capacity of  $790 \text{ mA h g}^{-1}$  for 50 cycles at high current density of  $0.5 \text{ A g}^{-1}$ .

## 5.2. Experimental Procedure

### *Synthesis of MnP<sub>4</sub> and solid solution Mn<sub>1-x</sub>TM<sub>x</sub>P<sub>4</sub> (TM = V and Fe) Nanoparticles*

MnP<sub>4</sub> and Mn<sub>1-x</sub>TM<sub>x</sub>P<sub>4</sub> (TM = V and Fe; x = 0.25 and 0.5) solid solution nanoparticles were synthesized via a facile high energy mechanical milling (HEMM) method with a planetary ball mill (Pulverisette 6, Fritsch). The starting materials used for synthesis are commercial manganese (99.95%, Alfa Aesar), vanadium (99.95%, Alfa Aesar), iron (99.5%, Alfa Aesar), and red phosphorus (98.9%, Alfa Aesar) without a further purification. Stoichiometric amount of starting materials was placed into a hardened steel vial (80 cm<sup>3</sup>) with hardened steel balls (diameter of 3/8 in.) at a ball-to-powder ratio of 40 (in weight) and sealed inside an argon-filled glove box. The HEMM was conducted at room temperature with a rotation speed of 300 rpm for 30 h.

### *Fabrication of MnP<sub>4</sub>/Graphene Nanocomposite*

As prepared MnP<sub>4</sub> nanoparticles and commercial graphene nanosheets (Angstrom Materials) were placed into a hardened steel vial (80 cm<sup>3</sup>) with hardened steel balls (diameter of 3/8 in.) at a ball-to-powder ratio of 60 (in weight) and sealed inside an argon-filled glove box. The HEMM was conducted at room temperature with a rotation speed of 150 rpm for 3 h.

### *Materials Characterization*

Synchrotron X-ray powder diffraction (SXPDP) patterns of as-prepared powders were examined at the 9B high-resolution powder X-ray diffraction (HRPD) beamline of the Pohang Accelerator Laboratory (PAL) in Korea. The incident beam was vertically collimated using a mirror and monochromatized to a wave length of 1.5167

Å using a double-crystal Si (111) monochromator. Diffraction patterns were collected in the 2 theta scan mode with a step size of 0.02°, step time of 15 s, from 10 to 130°. The lattice parameters of the as-synthesized samples were obtained with the FullProf software. The morphology of the powders and electrodes were observed by field emission scanning electron microscopy (FE-SEM, SU70, Hitachi) and transmission electron microscopy (TEM, JEM-2100F, JEOL). The *ex-situ* measurement of X-ray absorption near-edge structure (XANES) was carried out with a transmission mode at the 7D beamline of Pohang accelerator laboratory (PAL, Korea) in a storage ring of 2.5 GeV with a ring current of 330-360 mA. The cross section of electrode was examined using a cross section polisher (CP, IB-19510CP, JEOL) and FE-SEM.

#### *Electrochemical Measurements*

The electrode was prepared by mixing 70% active material, 15% Super P carbon black, and 15% carboxymethyl cellulose (CMC) binder by weight to form a slurry, which was coated on the copper foil and followed by drying in a vacuum oven at 65 °C overnight. The electrode was punched into a round disk with 1.8-2.2 mg cm<sup>-2</sup> loading of active material and then kept in the vacuum oven at 70 °C for 12 h. For electrochemical measurements, the CR2032 coin cell was assembled inside an argon-filled glove box. For Li-ion battery cell, lithium foil was used as a counter/reference electrode and a poly-propylene (Welcose, Korea) was used as a separator. The electrolyte used was 1.0 M LiPF<sub>6</sub> in a mixture of ethylene carbonate (EC) and dimethyl carbonate (DMC) (1:1 v/v) with the addition of 5 vol.% of fluoroethylene carbonate (FEC) additive. The cells for Na-ion battery were also assembled in a similar manner by employing glass micro fiber (Whatman) separator

and sodium metal foil as a counter/reference electrode. The electrolyte used was 1.0 M NaClO<sub>4</sub> in a mixture of ethylene carbonate (EC) and dimethyl carbonate (DMC) (1:1 v/v) with an addition of 5 vol.% of fluoroethylene carbonate (FEC). Galvanostatic cycling and cyclic voltammetry (CV) tests were performed with a battery testing system (Wonatech, Korea) within a voltage range of 0.01–2.0 V (vs. Na/Na<sup>+</sup>). Electrochemical impedance spectroscopy (EIS) experiment was carried out at a frequency range of 100 kHz to 0.1 Hz with an AC amplitude of 5 mV using an impedance analyzer (Zive, SP1). For the *ex-situ* SEM and TEM analyses, the electrode materials were collected by disassembling the test cells in the argon-filled glove box, rinsing with DMC several times, and drying at room temperature.

## 5.3. Results and Discussions

### 5.3.1. Synthesis and Physicochemical Characterization

Figure 5.3.1a shows the XRD pattern of as-synthesized MnP<sub>4</sub> nanoparticles obtained by synchrotron X-ray beam. The XRD pattern was well matched with a triclinic (*P-1*) structure of MnP<sub>4</sub> (ICDD # 01-072-0949) confirmed by Le Bail fitting result (Table 5.3.1). There are four different polymorphs in MnP<sub>4</sub> (2-MnP<sub>4</sub>, 6-MnP<sub>4</sub>, 8-MnP<sub>4</sub>, and  $\gamma$ -MnP<sub>4</sub>), which are classified according to the arrangement of MnP<sub>6</sub> octahedra in the crystal structure.[5.30] In as-synthesized triclinic structure of 6-MnP<sub>4</sub>, manganese atoms are octahedrally coordinated with six P atoms and the zigzag arrangement in unit of six edge-sharing MnP<sub>6</sub> octahedra is repeated along the *a*-axis (Figure 5.3.1b). This triclinic MnP<sub>4</sub> phase is different from the previously reported MnP<sub>4</sub> phase used for LIB anode whose crystal structure was monoclinic (*C/2c*) of 8-MnP<sub>4</sub> (ICDD # 01-071-0334). The calculated band gaps of 6-MnP<sub>4</sub> and 8-MnP<sub>4</sub> were 1.76 and 1.60 eV, respectively and the difference between indirect and direct band gaps at the  $\Gamma$  point was only about 0.09 eV, which is expected to show the similar electrical behavior.[5.31] The electronic structure and phonon calculation for MnP<sub>4</sub> polymorphs showed that the 6-MnP<sub>4</sub> phase is thermodynamically favorable at lower temperature and the high-temperature synthetic routes prefer to form the 8-MnP<sub>4</sub> phase.[5.30] This is consistent with our experimental result that the 6-MnP<sub>4</sub> phase was synthesized using the relatively low temperature HEMM process than the conventional synthesis processes.[5.27-5.30]

As shown in the SEM image (Figure 5.3.1c), the relatively low temperature synthesis condition of HEMM produced the nanoparticles of 6-MnP<sub>4</sub> phase. The low magnification TEM image shows that the agglomerated MnP<sub>4</sub> nanoparticles were composed of 5 to 20 nm-sized crystallites (Figure 5.3.1d). The selected-area electron diffraction (SAED) pattern was well indexed to 6-MnP<sub>4</sub> phase and the ring-like SAED pattern indicates the randomly oriented polycrystalline nature (Figure 5.3.1e). The lattice fringes were clearly observed in the high resolution TEM image and the corresponding spots in fast Fourier transform (FFT) pattern were indexed with a zone axis of [110] of triclinic (*P-1*) MnP<sub>4</sub> structure (Figure 5.3.1f). To confirm the elemental distribution throughout as-synthesized MnP<sub>4</sub> nanoparticles, the high-angle annular dark-field (HAADF) scanning transmission electron microscopy (STEM) image and elemental mapping images by energy dispersive spectroscopy (EDS) were obtained (Figure 5.3.1g-i). The EDS mapping images of Mn K and P K reveal the homogeneous distribution of Mn and P elements throughout the MnP<sub>4</sub> nanoparticles.

The MnP<sub>4</sub> electrode is expected to show the high reversible capacity in both LIBs and SIBs and the high capacity discharge/charge reactions might result in the particle cracking and loss of active material, which leads to the continuous electrolyte decomposition and increase of the cell resistance during cycling. To relieve the capacity degradation, a highly conductive graphene nanosheet was introduced to fabricate the MnP<sub>4</sub>/graphene nanocomposite. As-synthesized MnP<sub>4</sub> nanoparticles were mixed with the different content of graphene (10 and 20 wt% referred as MnP<sub>4</sub>/G10 and MnP<sub>4</sub>/G20, respectively) using the HEMM under 150 rpm for 3 h, and the graphene content was optimized to be 20 wt% based on the electrochemical performance presented later. The XRD pattern of as-fabricated

MnP<sub>4</sub>/G20 indicates that no phase change occurred during mixing with MnP<sub>4</sub> nanoparticles and graphene nanosheets under the mechanical milling condition (Figure 5.3.2). The morphology of as-fabricated MnP<sub>4</sub>/G20 shows that the agglomerated MnP<sub>4</sub> nanoparticles were wrapped with the graphene nanosheets (Figure 5.3.3a and b). The high resolution TEM image and corresponding FFT pattern (Figure 5.3.3c) indicates that the observed lattice fringes are indexed with a zone-axis [124] of MnP<sub>4</sub> structure. The HAADF STEM image and EDS mapping images for Mn K, P K, and C K indicate that the MnP<sub>4</sub> nanoparticles homogeneously distributed throughout the MnP<sub>4</sub>/G20 nanocomposite (Figure 5.3.3d-g).

**Table 5.3.1** Le Bail fitting results of as-synthesized MnP<sub>4</sub> nanoparticles.

Formula	MnP <sub>4</sub>
Crystal system	Triclinic
Space group	<i>P-1</i>
a (Å)	16.272(7)
b (Å)	5.841(8)
c (Å)	5.103(7)
$\alpha$ (°)	115.67(2)
$\beta$ (°)	95.41(6)
$\gamma$ (°)	89.12(1)
R <sub>exp</sub> (%)	1.97
R <sub>p</sub> (%)	2.59
R <sub>wp</sub> (%)	3.38

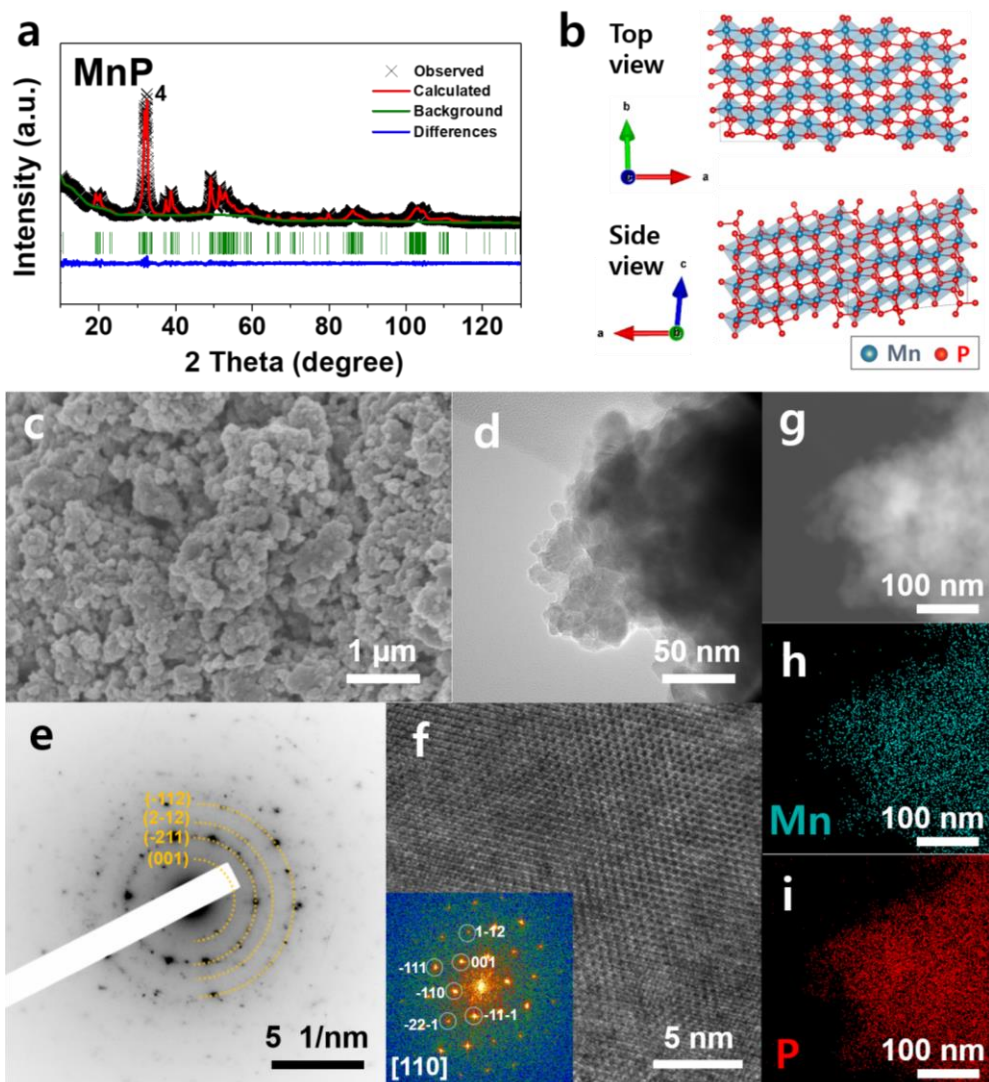


**Figure 5.3.1** (a) XRD pattern and refined results, (b) crystal structure, (c) SEM image, (d) TEM image in low magnification, (e) SAED pattern, (f) HR-TEM image, (g) HAADF STEM image, and EDS mapping images of (h) Mn K and (i) P K of as-synthesized  $\text{MnP}_4$  nanoparticles.

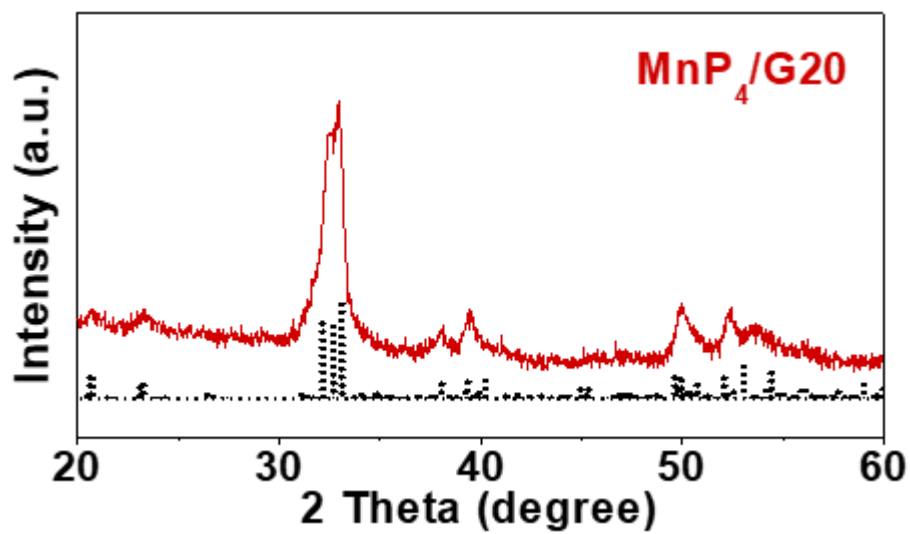


**Figure 5.3.2** XRD pattern for as-fabricated  $\text{MnP}_4/\text{G20}$  composite. The reference peaks for  $\text{MnP}_4$  (ICDD # 01-072-0949, black dash line) is included.

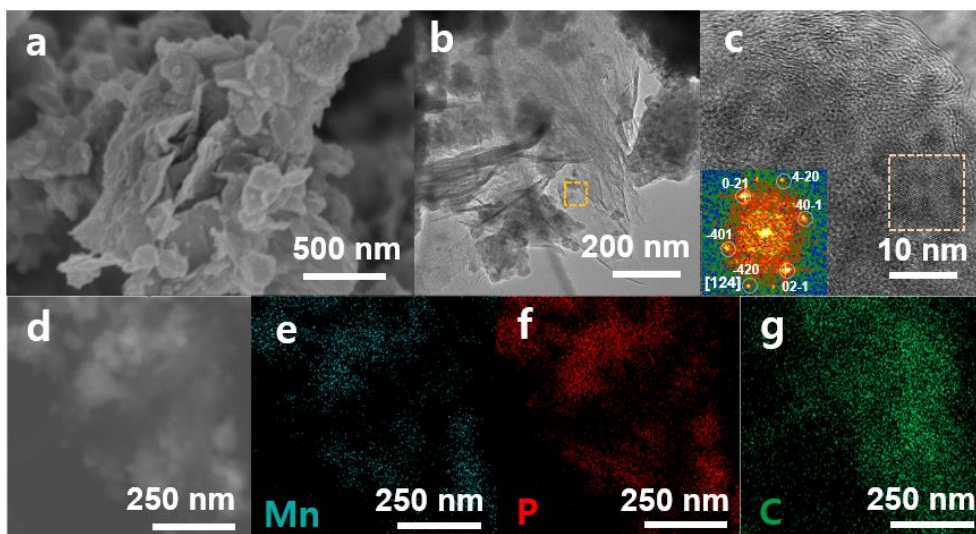


**Figure 5.3.3** (a) SEM image, TEM images in (b) low magnification and (c) high magnification, (g) HAADF STEM image, and EDS mapping images of (e) Mn K, (f) P K, and (g) C K of as-synthesized  $\text{MnP}_4/\text{G20}$  nanocomposite.

### 5.3.2. Electrochemical Reaction Mechanism and Performance

To evaluate the electrochemical performance and understand the electrochemical reaction mechanism of  $\text{MnP}_4$  electrode as an anode for LIBs, the galvanostatic discharge and charge test was performed at a current density of  $100 \text{ mA g}^{-1}$  within a potential range of 0.01-2.0 V (vs  $\text{Li/Li}^+$ ). The voltage profiles and corresponding differential capacity ( $dQ/dV$ ) plots (DCPs) indicate that the  $\text{MnP}_4$  electrode delivered the high initial discharge and charge capacities of 1876 and 1615  $\text{mA h g}^{-1}$ , respectively, with a high initial Coulombic efficiency (ICE) of 86% (Figure 5.3.4a and b). In the first lithiation process, the  $\text{MnP}_4$  electrode delivered the discharge capacity of  $\sim 1000 \text{ mA h g}^{-1}$  corresponding to  $\sim 7$  Li ion insertion per  $\text{MnP}_4$  with a voltage plateau at 0.57 vs.  $\text{Li/Li}^+$ , which is in agreement with the two-phase reaction of anti-fluorite  $\text{Li}_7\text{MnP}_4$  phase ( $\text{MnP}_4 + 7 \text{Li}^+ + 7\text{e}^- \rightarrow \text{Li}_7\text{MnP}_4$ ) observed in previously reported  $\text{MnP}_4$  electrode at 0.62-0.65 V vs.  $\text{Li/Li}^+$ . [5.25,5.26] In the *ex-situ* XRD pattern of  $\text{MnP}_4$  electrode at 0.5 V vs.  $\text{Li/Li}^+$  during lithiation process, anti-fluorite  $\text{Li}_7\text{MnP}_4$  phase (ICDD # 00-014-0045) was well identified ( $c_2$  state in Figure 5.3.4c). The *ex-situ* XRD pattern for further lithiated  $\text{MnP}_4$  electrode at 0.01 V vs.  $\text{Li/Li}^+$ , delivering the capacity of  $1876 \text{ mA h g}^{-1}$  equivalent to  $\sim 12$  Li ion insertion per  $\text{MnP}_4$ , indicates that the conversion reaction ( $\text{Li}_7\text{MnP}_4 + 5 \text{Li}^+ + 5 \text{e}^- \rightarrow \text{Mn}^0 + 4 \text{Li}_3\text{P}$ ) occurred ( $c_3$  state in Figure 5.3.4c). In addition, the noticeable change in *ex-situ* normalized Mn K-edge X-ray absorption near edge structure (XANES) spectra of fully lithiated  $\text{MnP}_4$  electrode (at 0.01 V vs.  $\text{Li/Li}^+$ ) further confirmed the metallization of  $\text{Mn}^0$  at fully discharged state (Figure 5.3.4d). During the first

delithiation process, a voltage plateau was observed at 1.13 V vs. Li/Li<sup>+</sup> (Figure 5.3.4a and b) and the full amorphization occurred (c<sub>4</sub> state in Figure 5.3.4c) after the fully delithiation (at 2.0 V vs. Li/Li<sup>+</sup>), which well agreed with the previous report.[5.26] The XANES spectrum of fully charged MnP<sub>4</sub> electrode (at 2.0 V vs. Li/Li<sup>+</sup>) indicates that manganese was oxidized close to that of pristine state indicating the reversible electrochemical reaction of MnP<sub>4</sub> electrode (Figure 5.3.4d).

The cycle performance of MnP<sub>4</sub> and MnP<sub>4</sub>/G20 electrodes was investigated by galvanostatic discharge/charge test at the current density of 100 mA g<sup>-1</sup> (Figure 5.3.5a). For the MnP<sub>4</sub> electrode, the high initial reversible capacity of 1615 mA h g<sup>-1</sup> was rapidly reduced to 515 mA h g<sup>-1</sup> after 40 cycles. On the other hand, the MnP<sub>4</sub>/G20 electrode delivered the initial discharge and charge capacities of 1728 and 1326 mA h g<sup>-1</sup>, respectively, with an ICE of 76.7%. The relatively low ICE of MnP<sub>4</sub>/G20 electrode could be derived from the high irreversible capacity by forming a solid-electrolyte interface (SEI) layer on the high surface area of graphene. The MnP<sub>4</sub>/G20 electrode showed the improved cycle retention property delivering the high reversible capacity of 1004 mA h g<sup>-1</sup> after 100 cycles, corresponding to the cycle retention of 75.7%. In addition, the MnP<sub>4</sub>/G20 electrode exhibited the improved rate capability and the reversible capacity was 1295, 1100, 1022, and 950 mA h g<sup>-1</sup> at the current density of 100, 500, 1000, and 2000 mA g<sup>-1</sup>, respectively (Figure 5.3.5b-d). The high capacity of 950 mA h g<sup>-1</sup> obtained at 2000 mA g<sup>-1</sup> was well maintained and reduced to 856 mA h g<sup>-1</sup> after 100 cycles corresponding to the high cycle retention of 90%. The obtained high rate capability of MnP<sub>4</sub>/G20 electrode was an outstanding result among other transition metal (TM)-based phosphorus-rich phosphides (TMP<sub>x</sub>, x > 2) as anodes for LIBs (Figure 5.3.6).[5.20-5.21,5.32-5.42]

Based on the reversible lithiation/delithiation reaction of  $\text{MnP}_4$  electrode, we performed the galvanostatic discharge/charge test for  $\text{MnP}_4/\text{Na}$  cell to verify the electrochemical activity of  $\text{MnP}_4$  in sodiation/desodiation. The voltage profiles and corresponding DCPs obtained at the current density of  $50 \text{ mA g}^{-1}$  within a potential range of  $0.01\text{-}2.0 \text{ V}$  (vs.  $\text{Na}/\text{Na}^+$ ) indicate that the  $\text{MnP}_4$  electrode delivered the discharge and charge capacities of  $1234$  and  $1028 \text{ mA h g}^{-1}$ , respectively, with a high ICE of  $83.3\%$  (Figure 5.3.7a and b). The  $\text{MnP}_4$  electrode showed a voltage plateau below  $0.2 \text{ V}$  vs.  $\text{Na}/\text{Na}^+$  in the first sodiation process and a voltage plateau at  $\sim 0.43 \text{ V}$  vs.  $\text{Na}/\text{Na}^+$  in the first desodiation process. Thus, the voltage profile of  $\text{MnP}_4/\text{Na}$  cell was similar to that of the high voltage region of  $\text{MnP}_4/\text{Li}$  cell resulting from the relatively high redox potential of  $\text{Na}/\text{Na}^+$  than that of  $\text{Li}/\text{Li}^+$ . The *ex-situ* XRD patterns, XANES spectra, and TEM image of  $\text{MnP}_4$  electrode during sodiation indicate that  $\text{MnP}_4$  was directly converted to  $\text{Mn}^0$  and  $\text{Na}_3\text{P}$  without the formation of Na-Mn-P ternary compound during sodiation process (Figure 5.3.7c and d, and Figure 5.3.8). This can be attributed to the rare presence of ternary Na-Mn-P compounds unlike the various ternary Li-Mn-P compounds (Table 5.3.2).

The cycle performance of  $\text{MnP}_4$  and  $\text{MnP}_4/\text{G20}$  electrodes was also examined in Na cells for SIB applications. As shown in the Figure 5.3.9a, the galvanostatic discharge/charge test of  $\text{MnP}_4$  electrode at the current density of  $50 \text{ mA g}^{-1}$  indicates that the initial reversible capacity of  $1028 \text{ mA h g}^{-1}$  was gradually decreased to  $617 \text{ mA h g}^{-1}$  during 40 cycles with a cycle retention of  $60\%$ . On the other hand, the  $\text{MnP}_4/\text{G20}$  electrode showed the low initial reversible capacity of  $718 \text{ mA h g}^{-1}$ , but exhibited much improved cycle retention maintaining the high reversible capacity of  $627 \text{ mA h g}^{-1}$  after 100 cycles with a cycle retention of  $87.3\%$ . In addition,  $\text{MnP}_4/\text{G20}$

electrode showed the better rate capability than that of  $\text{MnP}_4$  electrode delivering the reversible capacities of 724, 697, 656, 600, 478, and 385  $\text{mA h g}^{-1}$  at the tenth cycle at the current densities of 50, 100, 200, 500, 1000, and 2000  $\text{mA g}^{-1}$ , respectively (Figure 5.3.9b-d). When the current density returned to 50  $\text{mA g}^{-1}$ , the reversible capacity of 700  $\text{mA h g}^{-1}$  was recovered exhibiting a good rate capability. To compare the long-term cyclability of  $\text{MnP}_4$ ,  $\text{MnP}_4/\text{G10}$ , and  $\text{MnP}_4/\text{G20}$  electrodes, a galvanostatic discharge/charge test was conducted at high current density of 500  $\text{mA g}^{-1}$  for 250 cycles with an activation at 50  $\text{mA g}^{-1}$  for 3 cycles (Figure 5.3.10a). At the current density of 500  $\text{mA g}^{-1}$ , the  $\text{MnP}_4$  electrode delivered 695  $\text{mA h g}^{-1}$  at initial cycle and it gradually decreased during 50 cycles. Although  $\text{MnP}_4/\text{G10}$  electrode showed relieved capacity fading compared to  $\text{MnP}_4$  electrode, long-term stability could not be achieved due to continuous degradation of reversible capacity during cycling. In case of  $\text{MnP}_4/\text{G20}$  electrode, initial reversible capacity was 575  $\text{mA h g}^{-1}$  at 500  $\text{mA g}^{-1}$  and this was well retained as 446  $\text{mA h g}^{-1}$  corresponding cycle retention of 78%, exhibiting highly improved long-term cyclability. The obtained electrochemical performance of  $\text{MnP}_4/\text{G20}$  electrode was superior to those of previously reported various phosphorus-rich metal phosphide nanocomposites synthesized by a high energy milling as anodes for SIBs (Figure 5.3.10b).[5.14,5.22,5.32,5.43-5.48]

Such a good cycling performance of the  $\text{MnP}_4/\text{G20}$  electrode can be attributed to the void space between adjacent  $\text{MnP}_4$  nanoparticles enwrapped with the flexible graphene nanosheets, which effectively relieves the large volume change, hinders agglomeration of active materials during cycling, and ensures good kinetics favorable for surface charge transfer and fast ionic diffusion. This was corroborated

by comparing the electrode morphology by *ex-situ* SEM and TEM and electrochemical impedance of MnP<sub>4</sub> and MnP<sub>4</sub>/G20 electrodes before and after cycle test. To observe the degree of electrode swelling that occurs after the sodiation process, a cross-sectional polishing was performed on MnP<sub>4</sub> and MnP<sub>4</sub>/G20 electrodes before and after 1<sup>st</sup> sodiation. To prevent the swing of electrode specimens during the cross-sectional polishing, Cu tape was attached on the electrode (Figure 5.3.11a). In the pristine state, MnP<sub>4</sub> and MnP<sub>4</sub>/G20 electrodes showed the similar electrode thickness of 17-18  $\mu\text{m}$  (Figure 5.3.11b and d). The thickness of MnP<sub>4</sub> electrode drastically increased to 41  $\mu\text{m}$  after the 1<sup>st</sup> sodiation, corresponding to an expansion rate of 228% (Figure 5.3.11c). On the other hand, the thickness of the MnP<sub>4</sub>/G20 electrode increased to 26  $\mu\text{m}$  with the expansion rate of 153% (Figure 5.3.11e), relieving the volume change compared to that of MnP<sub>4</sub> electrode. Such a superior relieving volume change was also observed in silicon anode for LIBs by enwrapping with the reduced graphene oxide nanosheet.[5.49] Furthermore, the original morphology of the MnP<sub>4</sub>/G20 electrode was relatively well retained than that of MnP<sub>4</sub> electrode after 100 cycles at 500 mA g<sup>-1</sup>, inhibiting the severe agglomeration of MnP<sub>4</sub> nanoparticles during cycling (Figure 5.3.12). To determine the electrode resistances related to the morphological change, electrochemical impedance spectroscopy (EIS) measurements were conducted at 2.0 V vs. Na/Na<sup>+</sup> for MnP<sub>4</sub> and MnP<sub>4</sub>/G20 electrodes before cycle (Figure 5.3.13a) and after 100 cycles tested at 500 mA g<sup>-1</sup> (Figure 5.3.13b). At the pristine state, the MnP<sub>4</sub> and MnP<sub>4</sub>/G20 electrodes showed the comparable charge transfer resistance ( $R_{ct}$ ) at high frequency region, but the MnP<sub>4</sub>/G20 electrode exhibited the steeper straight sloping line at low frequency region implying the fast sodium ion diffusion within the bulk

electrode. After 100 cycles, the observed  $R_{ct}$  of  $MnP_4/G20$  at charged state (2.0 V vs.  $Na/Na^+$ ) was much smaller and the incline line was much steeper than those of  $MnP_4$  electrode indicating that the fast kinetics was well maintained during cycle in case of  $MnP_4/G20$  electrode. Consequently, the high performance of  $MnP_4/G20$  electrode for both LIBs and SIBs was derived from high capacity and electrochemical activity of  $MnP_4$  nanoparticles as well as structural integrity of conductive and flexible enwrapping graphene nanosheets.

**Table 5.3.2** ICDD database of Li-Mn-P and Na-Mn-P ternary compounds.

Composition	Crystal system	Space group	ICDD number
$\text{Li}_7\text{MnP}_4$	Cubic	Fm-3m	00-014-0045
$\text{Li}_{1.75}\text{Mn}_{0.25}\text{P}$	Cubic	Fm-3m	04-005-3949
$\text{Li}_{6.67}\text{Mn}_{1.33}\text{P}_4$	Cubic	-	00-014-0047
$\text{Li}_{1.5}\text{Mn}_{0.5}\text{P}$	Tetragonal	P-42m	04-009-9099
$\text{Li}_{1.5}\text{Mn}_{0.5}\text{P}$	Tetragonal	P4/nmm	04-005-3954
$\text{Li}_{1.67}\text{Mn}_{0.33}\text{P}$	Tetragonal	P4/nmm	04-005-3951
$\text{Li}_{1.37}\text{Mn}_{0.63}\text{P}$	Tetragonal	P4/nmm	04-005-3955
LiMnP	Tetragonal	P4/nmm	04-004-0359
NaMnP	Tetragonal	P4/nmm	04-004-0354

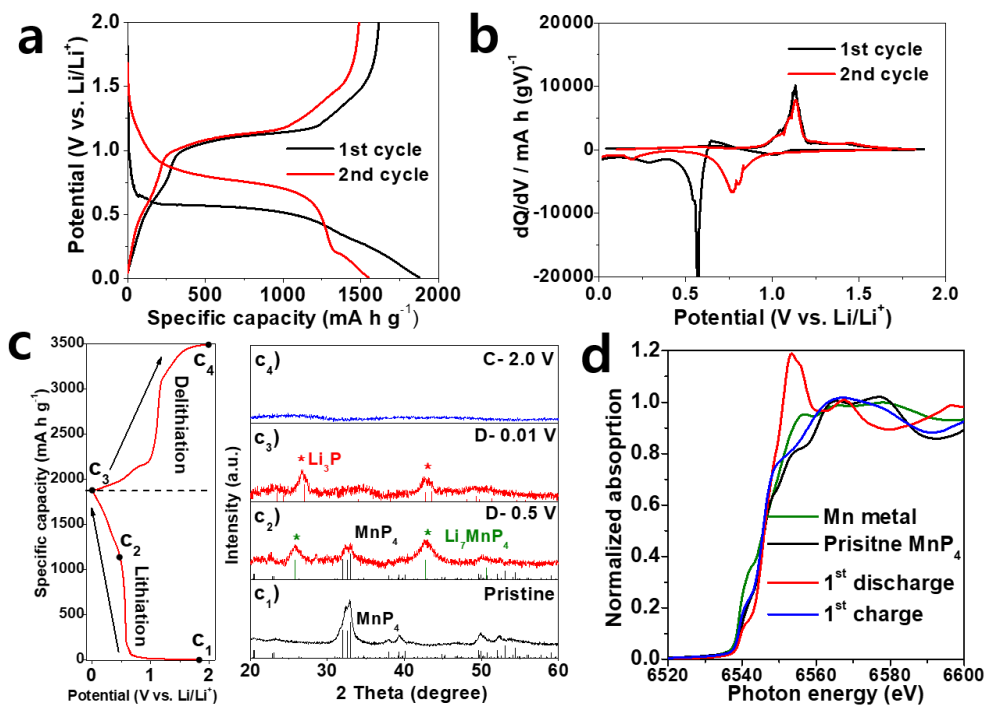


**Figure 5.3.4** (a) Galvanostatic discharge/charge voltage profiles, (b) corresponding differential capacity plots (DCPs), (c) *ex-situ* XRD patterns, and (d) X-ray absorption near-edge structure (XANES) spectra of  $\text{MnP}_4/\text{Li}$  cell for fully discharged and charged states. The reference peaks for  $\text{MnP}_4$  (ICDD # 01-072-0949, black solid line),  $\text{Li}_7\text{MnP}_4$  (ICDD # 00-014-0045, green solid line), and  $\text{Li}_3\text{P}$  (ICDD # 01-076-9759, red solid line) are included in (c).

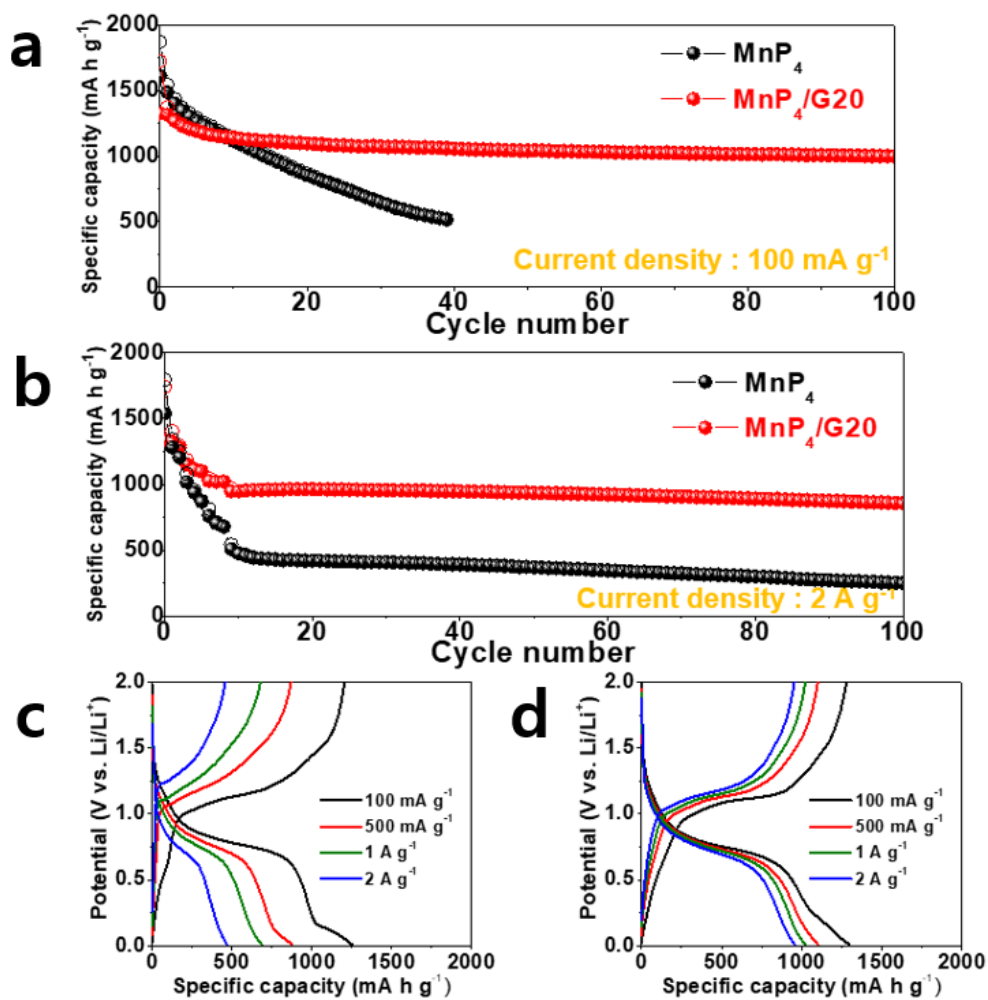


**Figure 5.3.5** Cycle performance of MnP<sub>4</sub> and MnP<sub>4</sub>/G20 electrodes for LIBs at current density of (a) 100 mA g<sup>-1</sup>, and (b) 2 A g<sup>-1</sup> with activation of each initial 3 cycles at 100 mA g<sup>-1</sup>, 500 mA g<sup>-1</sup>, and 1 A g<sup>-1</sup>. Galvanostatic discharge/charge voltage profiles of (c) MnP<sub>4</sub> and (d) MnP<sub>4</sub>/G20 electrodes for (b).

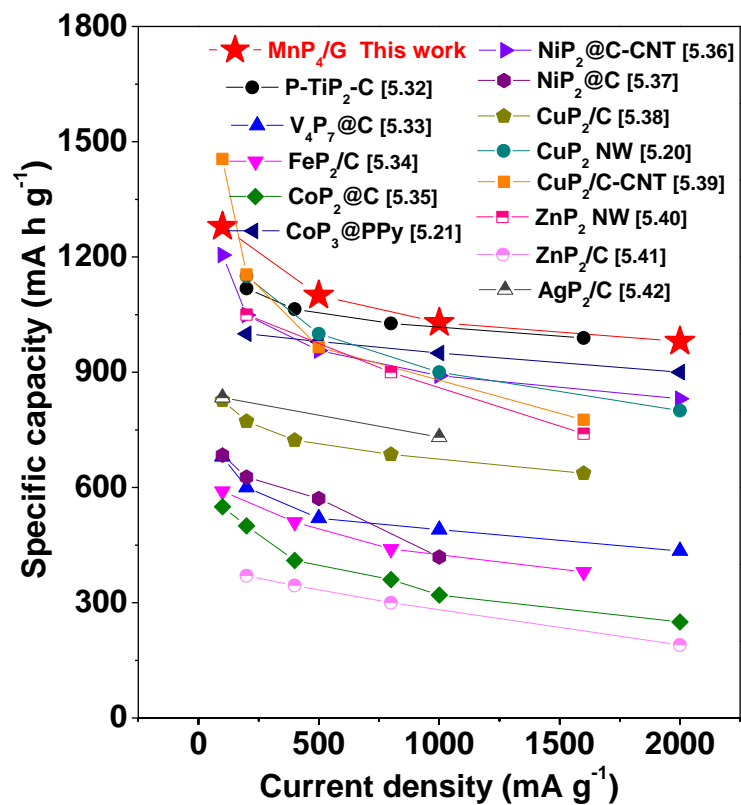


**Figure 5.3.6.** State-of-the-art high-rate capability of transition metal-based P-rich phosphides (TMP<sub>x</sub>, x > ~2) as anodes for LIBs.

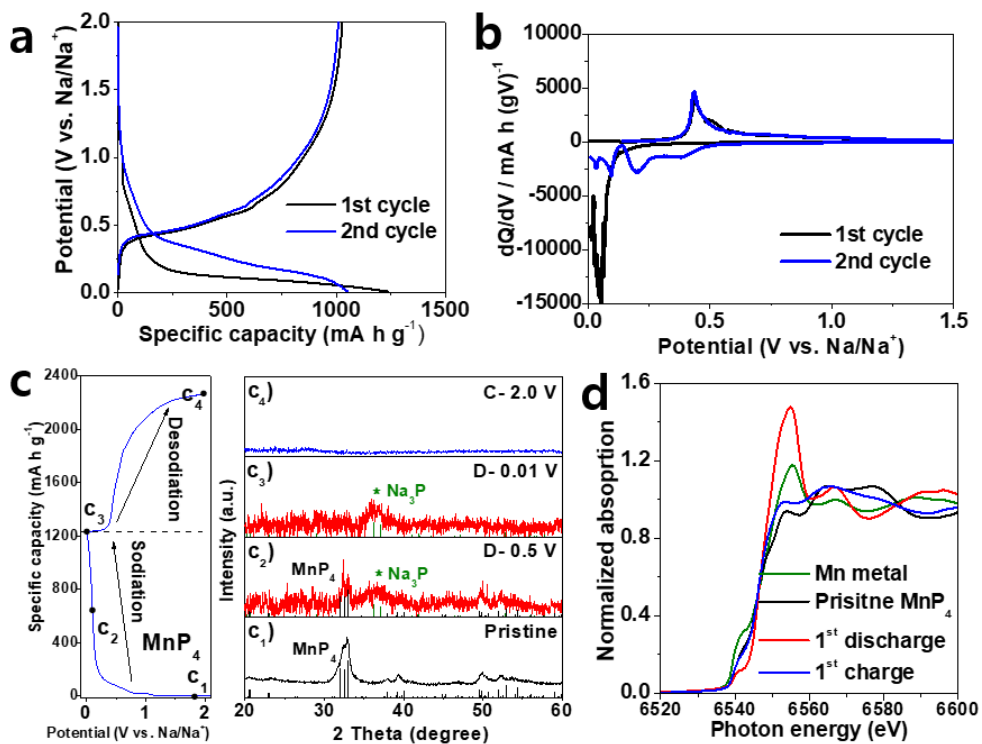


**Figure 5.3.7** (a) Galvanostatic discharge/charge voltage profiles, (b) corresponding DCPs, (c) *ex-situ* XRD patterns, and (d) XANES spectra of  $\text{MnP}_4/\text{Na}$  cell for fully discharged and charged states. The reference peaks for  $\text{MnP}_4$  (ICDD # 01-072-0949, black solid line) and  $\text{Na}_3\text{P}$  (ICDD # 01-073-3917, green solid line) are included in (c).

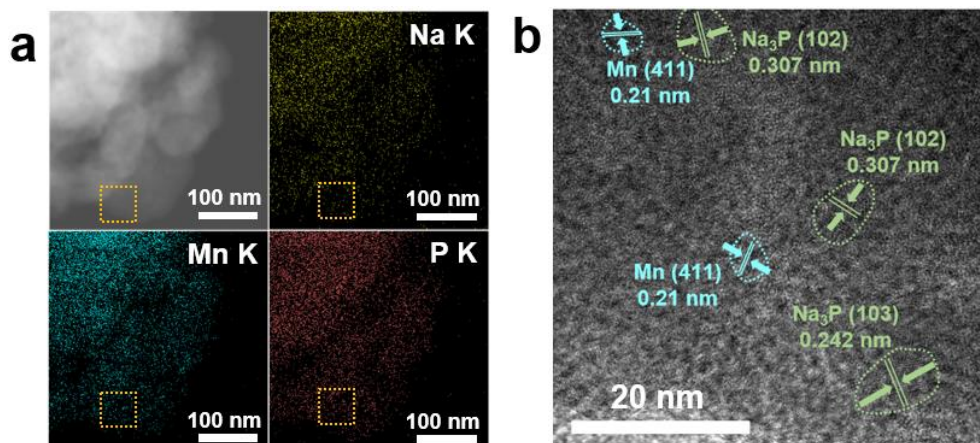


**Figure 5.3.8** (a) HAADF STEM image and EDS mapping images of Na K, Mn K, and P K, respectively, for fully sodiated  $\text{MnP}_4$  electrode (0.01 V vs.  $\text{Na}/\text{Na}^+$ ), and (b) TEM image of marked area in (a).

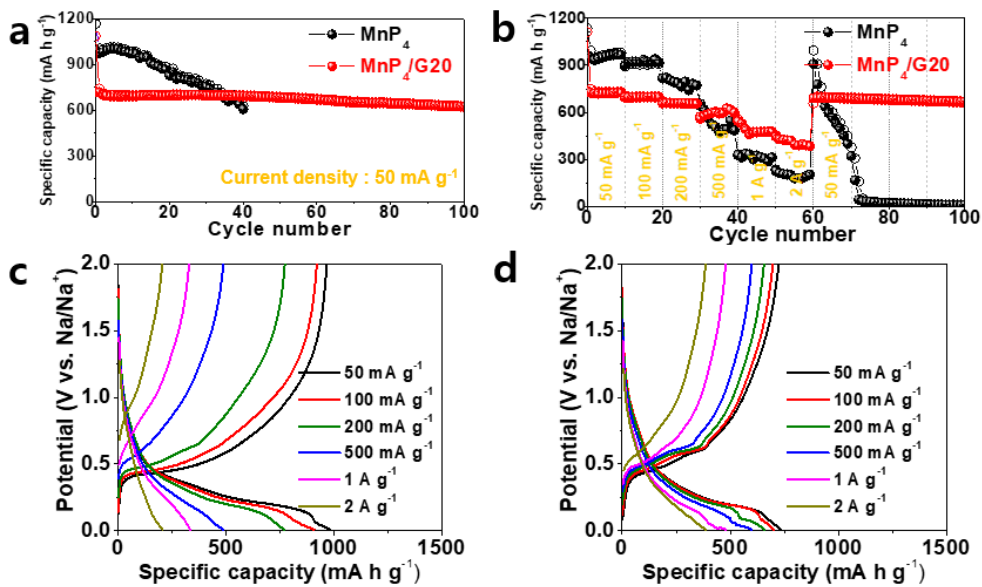


**Figure 5.3.9** (a) Cycle performance of MnP<sub>4</sub> and MnP<sub>4</sub>/G20 electrodes for SIBs at current density of 50 mA g<sup>-1</sup> and (b) rate capability. Galvanostatic discharge/charge voltage profiles of (c) MnP<sub>4</sub> and (d) MnP<sub>4</sub>/G20 electrodes for each 10<sup>th</sup> cycle at various current densities for (b).

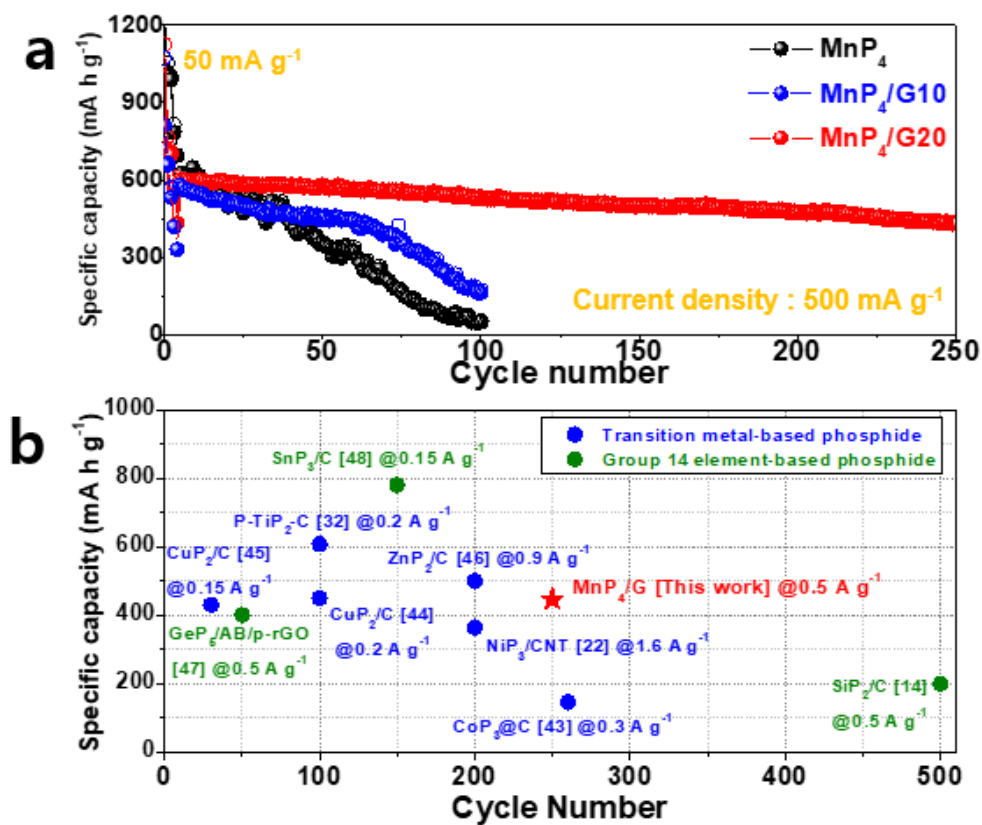


**Figure 5.3.10** (a) Cycle performance of MnP<sub>4</sub> and MnP<sub>4</sub>/G electrodes for SIBs at current density of 500 mA g<sup>-1</sup> with activation initial 3 cycles at 50 mA g<sup>-1</sup>. (b) State-of-the-art electrochemical performance of P-rich phosphides (TMP<sub>x</sub>, x > ~2) synthesized by a high energy milling as anodes for SIBs.

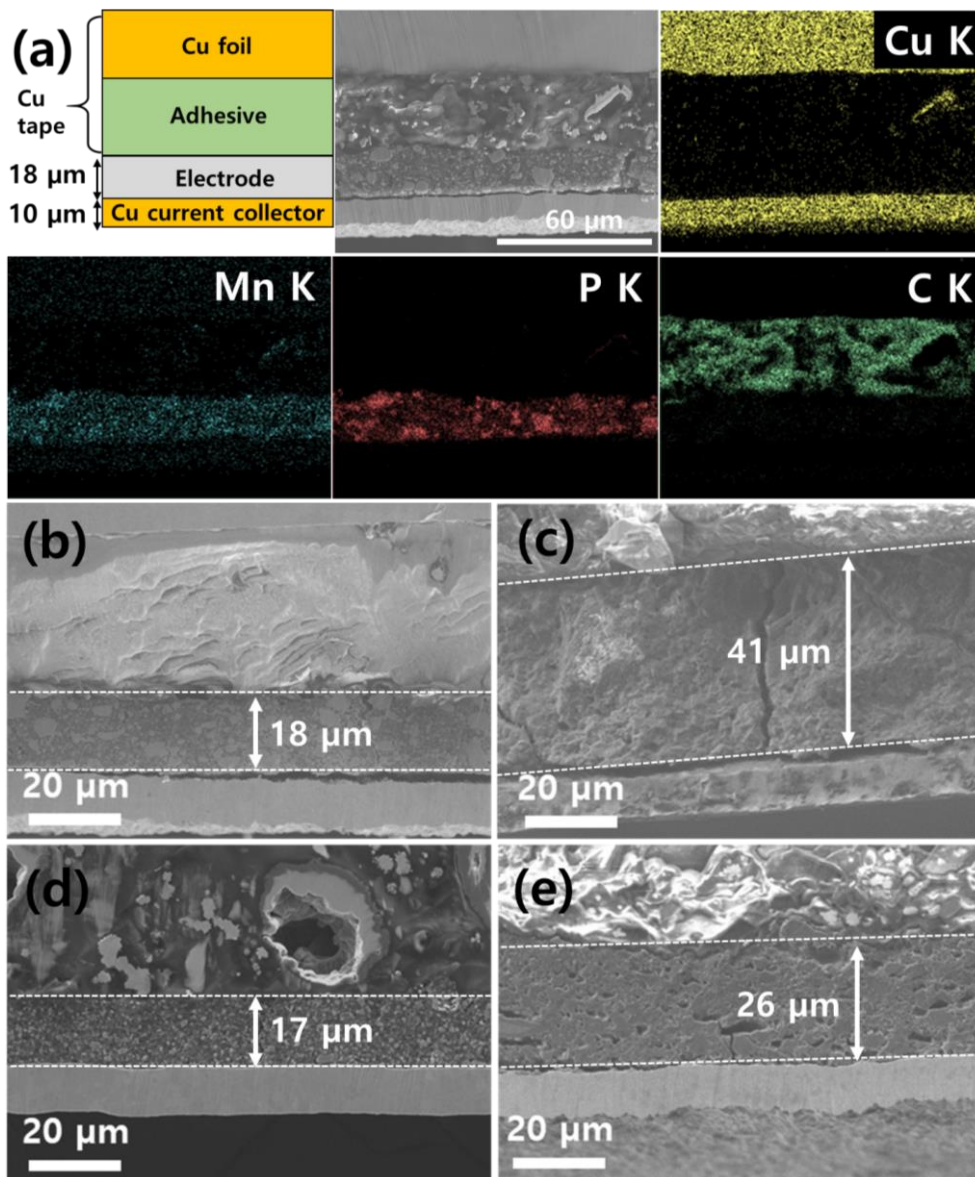


**Figure 5.3.11** (a) Schematic image, SEM image, EDS mapping images of Cu K, Mn K, P K, and C K for cross section of MnP<sub>4</sub> electrode before cycle. Cross sectional SEM image of MnP<sub>4</sub> and MnP<sub>4</sub>/G20 electrodes of (b,d) before cycle and (c,e) after fully sodiated state (0.01 vs. Na/Na<sup>+</sup>) at 50 mA g<sup>-1</sup>, respectively.

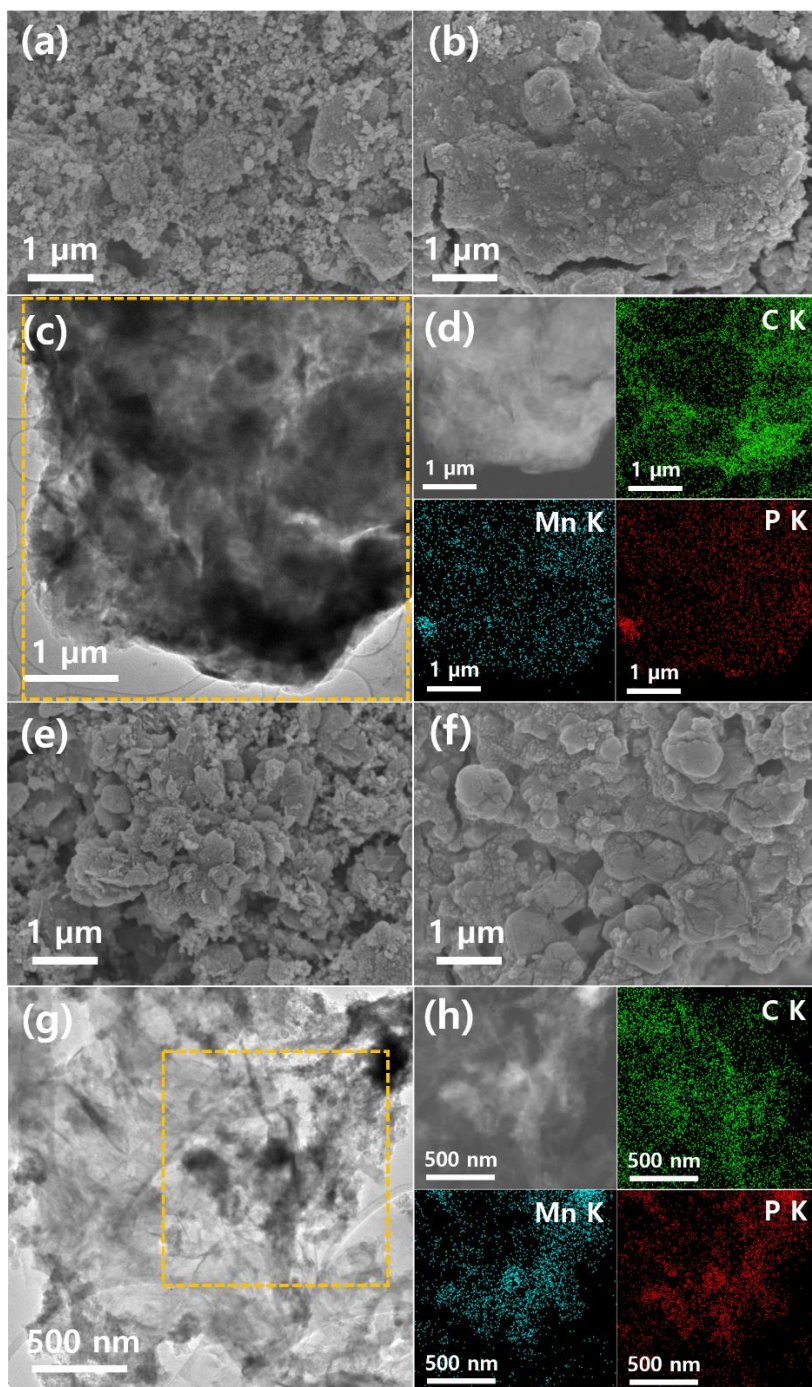


**Figure 5.3.12** (a) SEM image of before cycle, and (b,f) SEM, (c,g) TEM, (d,h) HAADF STEM, and EDS mapping images of C K, Mn K, and P K for after 100 cycles at 500 mA g<sup>-1</sup> for MnP<sub>4</sub> and MnP<sub>4</sub>/G20 electrodes, respectively.

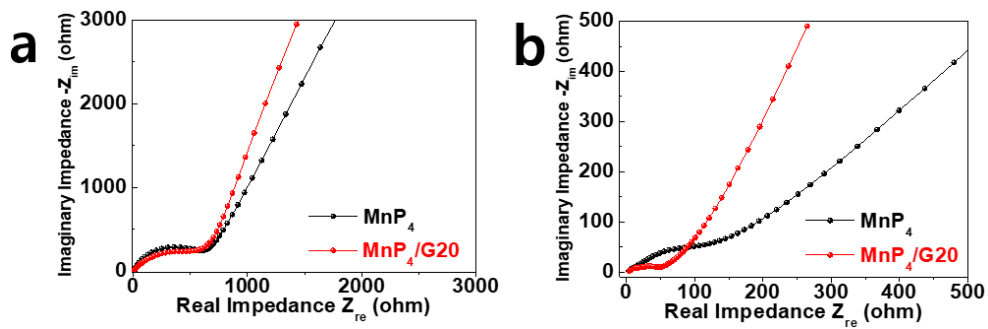


**Figure 5.3.13** Nyquist plots of MnP and MnP<sub>4</sub>/G20 electrodes (a) before cycle and (b) after 100 cycles tested at current density of 500 mA g<sup>-1</sup>.

### 5.3.3. Improvement of Rate Capability by Forming Solid Solution

In addition to fabricating MnP<sub>4</sub>/G nanocomposite with conductive carbon based material to improve the electrochemical properties of MnP<sub>4</sub> electrode, we also introduced a novel approach forming a substitutional solid solution to change physicochemical properties of the MnP<sub>4</sub> phase and corresponding electrochemical properties for SIBs anode. As discussed in the phase analysis part for 6-MnP<sub>4</sub> phase, the arrangement variation of MnP<sub>6</sub> octahedron affect the electronic structure among four different polymorphs for MnP<sub>4</sub>. This electronic structure variation was also observed in other composition materials of TMP<sub>4</sub> (TM = V, Cr, and Fe) phases, which have similar crystal structure to MnP<sub>4</sub> phase.[5.31] The electronic structure calculation for TMP<sub>4</sub> (TM = V, Cr, and Fe) phases indicated that VP<sub>4</sub> showed a continuous band energy indicating metallic behavior and CrP<sub>4</sub> showed a relatively narrow bandgap of 0.63 eV than that of MnP<sub>4</sub>. On the other hand, three different FeP<sub>4</sub> polymorphs showed relatively large band gap of 1.76, 1.83, and 2.13 eV with semiconducting behaviors. Based on their electronic structure variation and structural similarities, substitutional solid solution Mn<sub>1-x</sub>TM<sub>x</sub>P<sub>4</sub> (TM = V and Fe, x = 0.25) was synthesized using HEMM to vary its electronic structure and electrochemical properties.

Figure 5.3.14 shows the XRD patterns of as-synthesized MnP<sub>4</sub> and Mn<sub>1-x</sub>TM<sub>x</sub>P<sub>4</sub> (TM = V and Fe, x = 0.25) compounds measured by X-ray synchrotron beam. In the XRD patterns for Mn<sub>1-x</sub>TM<sub>x</sub>P<sub>4</sub> (TM = V and Fe, x = 0.25) compounds,

characteristic peaks were similar to those of  $\text{MnP}_4$  phase with no impurity phase, however, the peak shifts of 2 theta value were observed with obvious shape change of main characteristic peak region of 30-34°. For vanadium ion substitution for manganese ion as  $\text{Mn}_{1-x}\text{V}_x\text{P}_4$  ( $x = 0.25$ ), characteristic XRD peaks were shifted to lower 2 theta value compared with those of  $\text{MnP}_4$  phase due to the larger ionic radius of vanadium ion than that of manganese. In addition, main peak region of 30-34° changed similar to monoclinic structure of  $\text{VP}_4$  phase (space group of  $C/2c$ , ICDD # 01-077-0262). On the other hand, iron ion substitution for manganese ion as  $\text{Mn}_{1-x}\text{Fe}_x\text{P}_4$  ( $x = 0.25$ ) indicated that its characteristic XRD peaks were slightly shifted to higher 2 theta value compared with those of  $\text{MnP}_4$  phase due to the smaller ionic radius of iron ion than that of manganese and the main XRD peaks also changed similar to monoclinic structure of  $\text{FeP}_4$  phase (space group of  $C/2c$ , ICDD # 01-079-0486). This might be derived from the different  $\text{MP}_6$  octahedron arrangement of 6- $\text{MnP}_4$ , 2- $\text{VP}_4$ , and 4- $\text{FeP}_4$  phases (Figure 5.3.15). Since the reference ICDD database of  $\text{Mn}_{1-x}\text{TM}_x\text{P}_4$  ( $\text{TM} = \text{V}$  and  $\text{Fe}$ ,  $x = 0.25$ ) compounds does not exist, a structural identification was performed with the Fullprof Software. The structure refined results for  $\text{Mn}_{1-x}\text{TM}_x\text{P}_4$  ( $\text{TM} = \text{V}$  and  $\text{Fe}$ ,  $x = 0.25$ ) compounds indicated that those compounds, in accordance with extinction rules, were the same crystal structure with triclinic 6- $\text{MnP}_4$  phase, indicating substitutional solid solution (Figure 5.3.16a and b, and Table 5.3.3). In addition, the XRD pattern of  $\text{Mn}_{1-x}\text{V}_x\text{P}_4$  ( $x = 0.5$ ), which additional vanadium ions are substituted, shows similar characteristic peaks with  $\text{Mn}_{1-x}\text{V}_x\text{P}_4$  ( $x = 0.25$ ) and secondary phase  $\text{VP}_2$  (ICDD # 01-080-0990), indicating that solid solution limit of vanadium is close to  $\text{Mn}_{1-x}\text{V}_x\text{P}_4$  ( $x = 0.25$ ) (Figure 5.3.16c). The chemical composition and elemental distribution of  $\text{Mn}_{0.75}\text{TM}_{0.25}\text{P}_4$  ( $\text{TM} = \text{V}$

and Fe) compounds were confirmed by EDS spectrum and mapping images, which showed homogeneously distributed with the expected composition of the components throughout the solid solution nanoparticles (Figure 5.3.17a and b).

The electrochemical properties of  $\text{Mn}_{0.75}\text{TM}_{0.25}\text{P}_4$  (TM = V and Fe) electrodes were examined as anodes for both LIBs and SIBs. The galvanostatic discharge/charge voltage profiles and corresponding DCPs at  $100 \text{ mA g}^{-1}$  of  $\text{Mn}_{0.75}\text{TM}_{0.25}\text{P}_4$  (TM = V and Fe) electrodes are identical with those of  $\text{MnP}_4$  electrode for LIBs, indicating that same conversion reaction was occurred in two solid solution electrodes (Figure 5.3.18a-c). The  $\text{Mn}_{0.75}\text{TM}_{0.25}\text{P}_4$  (TM = V and Fe) electrodes showed similar cycling behavior to  $\text{MnP}_4$  electrode at a low current density of  $100 \text{ mA g}^{-1}$ , whereas different rate capabilities were observed in solid solution electrodes when the current density changed from  $100 \text{ mA g}^{-1}$  to a high current density of  $1 \text{ A g}^{-1}$  (Figure 5.3.19a). The reversible capacity reduction of  $\text{MnP}_4$  and  $\text{Mn}_{0.75}\text{TM}_{0.25}\text{P}_4$  (TM = V and Fe) electrodes with kinetic polarization at high current density was 24%, 11%, and 52%, respectively, showing reversible capacities of 943, 1285, and 592  $\text{mA h g}^{-1}$ , which indicates superior rate capability of  $\text{Mn}_{0.75}\text{V}_{0.25}\text{P}_4$  electrode (Figure 5.3.19b).

Those observed different rate capabilities of  $\text{MnP}_4$  and  $\text{Mn}_{0.75}\text{TM}_{0.25}\text{P}_4$  (TM = V and Fe) electrodes were also obvious in SIBs application (Figure 5.3.20). In addition, the high-rate cyclability of three electrodes were compared at  $500 \text{ mA g}^{-1}$  with the initial activation process of 3 cycles at  $50 \text{ mA g}^{-1}$  (Figure 5.3.21). In case of the  $\text{Mn}_{0.75}\text{V}_{0.25}\text{P}_4$  electrode, it delivers high initial capacity of  $909 \text{ mA h g}^{-1}$  at  $500 \text{ mA g}^{-1}$  and reversible capacity of  $790 \text{ mA h g}^{-1}$  was well maintained during 50 cycles

with a high capacity retention of 87%. At pristine state, the Nyquist plots of  $\text{Mn}_{0.75}\text{V}_{0.25}\text{P}_4$  electrode showed smaller semi-circle and steeper inclined line than those of  $\text{MnP}_4$  and  $\text{Mn}_{0.75}\text{Fe}_{0.25}\text{P}_4$  electrodes and this tendency was well maintained after 50 cycle test, exhibiting fast reaction kinetics of  $\text{Mn}_{0.75}\text{V}_{0.25}\text{P}_4$  electrode (Figure 5.3.22). On the other hand, the Nyquist plots for  $\text{Mn}_{0.75}\text{Fe}_{0.25}\text{P}_4$  electrode showed the largest charge transfer resistance and slowest diffusion kinetic among three electrodes. The different kinetic behavior of the two solid solution electrodes compared to  $\text{MnP}_4$  electrode could be derived from electronic structure changes close to metallic  $\text{VP}_4$  phase and semiconducting  $\text{FeP}_4$  phase, respectively, caused by their observed structural change (Figure 5.3.14). The electronic structure calculation of two solid solution phases using the density functional theory (DFT) calculation is not available at this stage because the low crystallinity, along with the low symmetry of the triclinic structure, makes it difficult to determine the physically meaningful atomic positions using the Rietveld refinements. Nevertheless, the above result suggests that formation of solid solution based on crystal structure and chemistry relation can affect the intrinsic physicochemical properties and corresponding electrochemical performance of anode materials and it can be a new opportunity for achieving better electrochemical performance for previous reported anode materials in LIBs and SIBs.

**Table 5.3.3** Le Bail fitting results of as-synthesized  $\text{Mn}_{1-x}\text{TM}_x\text{P}_4$  (TM = V and Fe, x = 0.25) nanoparticles.

Formula	$\text{Mn}_{0.75}\text{V}_{0.25}\text{P}_4$	$\text{Mn}_{0.75}\text{Fe}_{0.25}\text{P}_4$
Crystal system	Triclinic	Triclinic
Space group	<i>P-1</i>	<i>P-1</i>
a (Å)	16.52(5)	16.66(3)
b (Å)	5.806(8)	5.830(6)
c (Å)	5.076(2)	5.07(1)
$\alpha$ (°)	115.5(2)	115.62(2)
$\beta$ (°)	95.76(1)	94.96(2)
$\gamma$ (°)	88.96(1)	89.85(1)
$R_{\text{exp}}$ (%)	1.99	2.25
$R_{\text{p}}$ (%)	2.39	2.45
$R_{\text{wp}}$ (%)	3.21	3.16

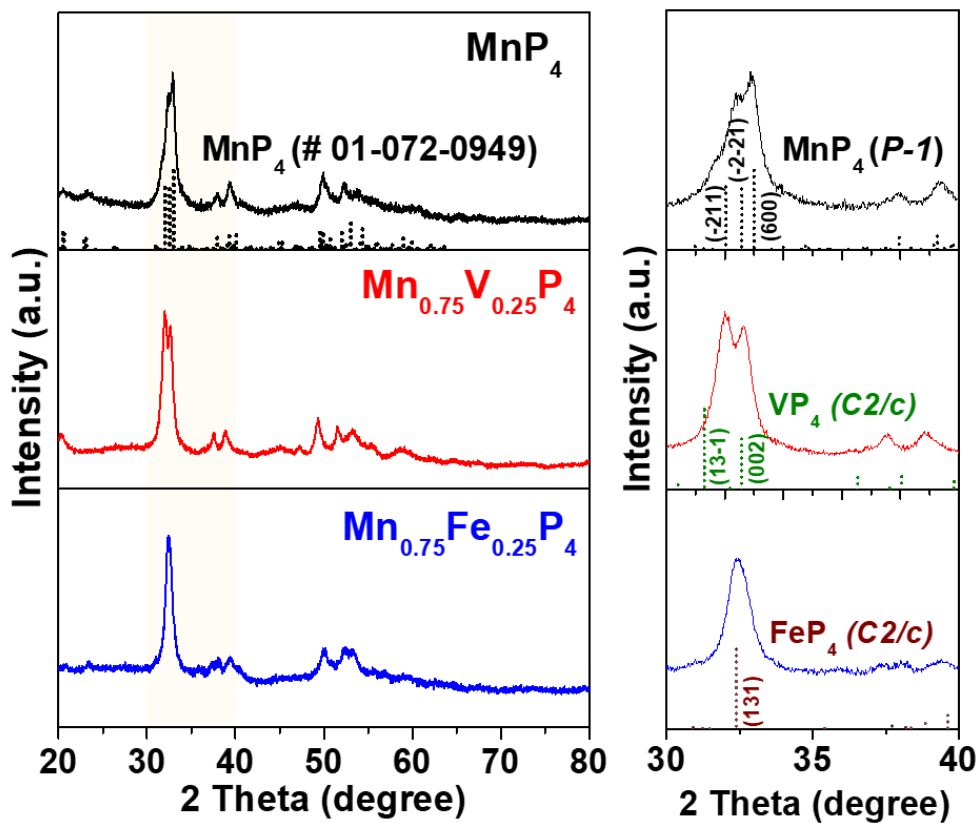


**Figure 5.3.14** XRD patterns for  $\text{MnP}_4$  and  $\text{Mn}_{1-x}\text{TM}_x\text{P}_4$  (TM = V and Fe,  $x=0.25$ ), respectively. The reference peaks for  $\text{MnP}_4$  (ICDD # 01-072-0949, black dash line),  $\text{VP}_4$  (ICDD # 01-077-0262, green dash line), and  $\text{FeP}_4$  (ICDD # 01-079-0486, brown dash line) are included.

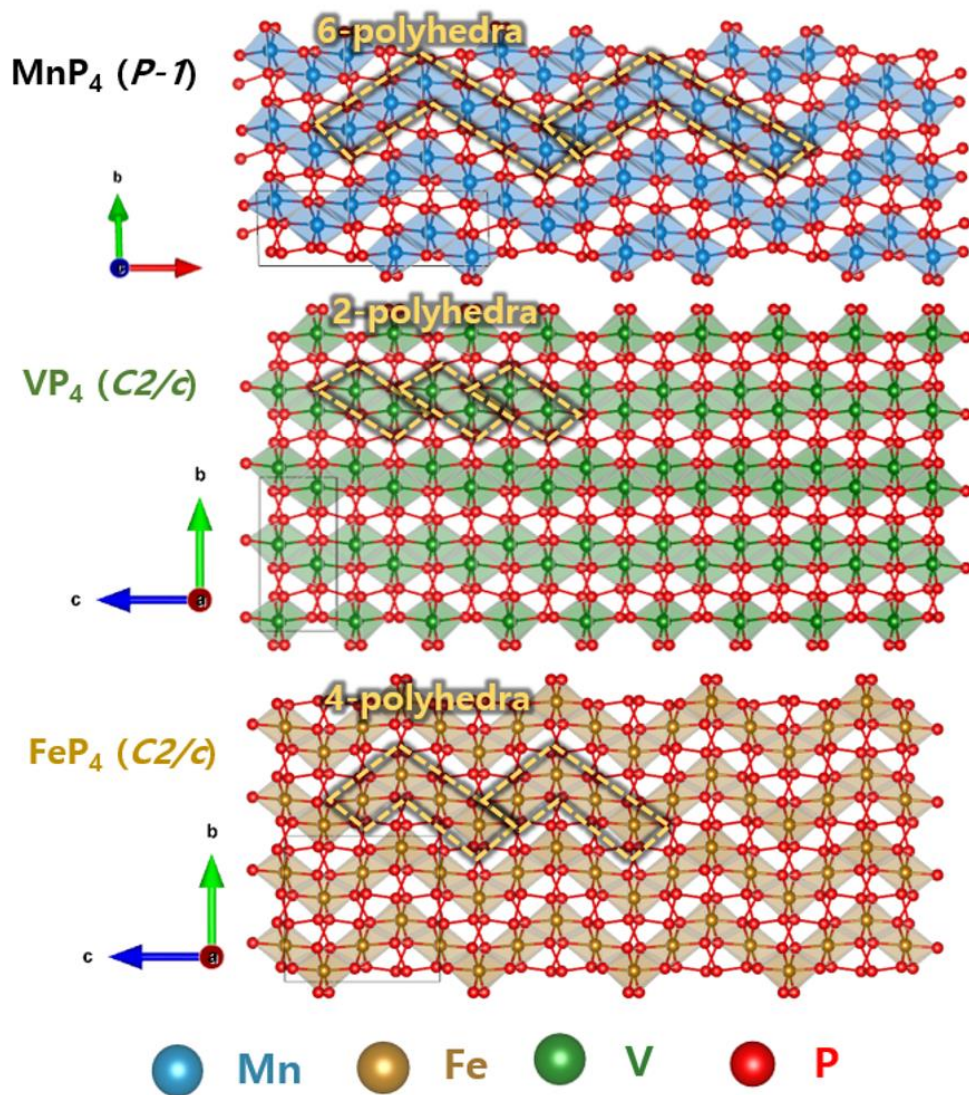


**Figure 5.3.15** Crystal structures of triclinic (*P-1*) MnP<sub>4</sub> and monoclinic (*C2/c*) of FeP<sub>4</sub> and VP<sub>4</sub> phases.

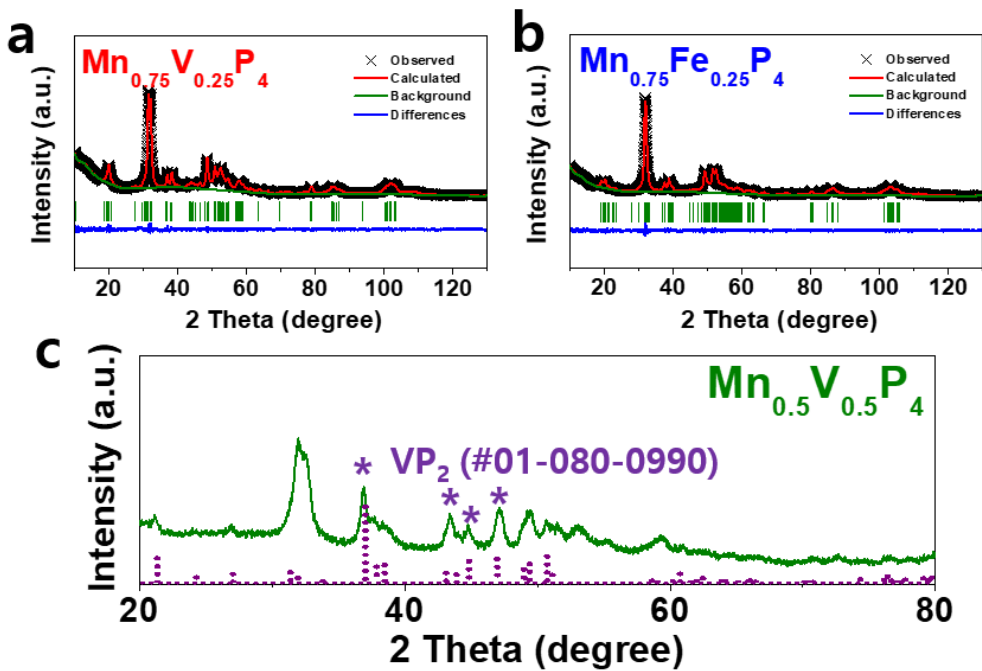


**Figure 5.3.16** XRD pattern and refined results of (a)  $\text{Mn}_{0.75}\text{V}_{0.25}\text{P}_4$  and (b)  $\text{Mn}_{0.75}\text{Fe}_{0.25}\text{P}_4$  compounds, respectively. (c) XRD pattern of  $\text{Mn}_{1-x}\text{V}_x\text{P}_4$  ( $x=0.5$ ) with the reference peak for  $\text{VP}_2$  (ICDD # 01-080.0990, purple dash line).

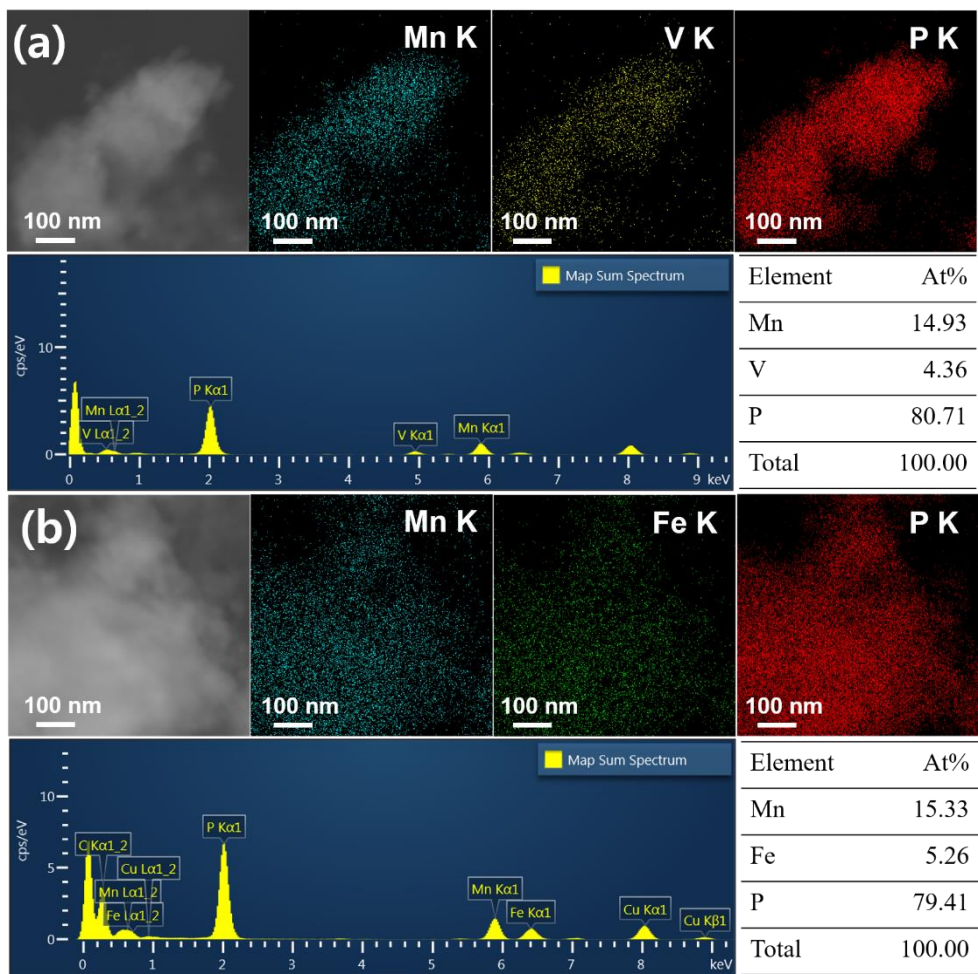


**Figure 5.3.17** HAADF STEM image, EDS mapping images for Mn K, V K, and P K, EDS spectrum and detected composition table for as-synthesized  $\text{Mn}_{0.75}\text{TM}_{0.25}\text{P}_4$  (TM = (a) V and (b) Fe) compounds, respectively.

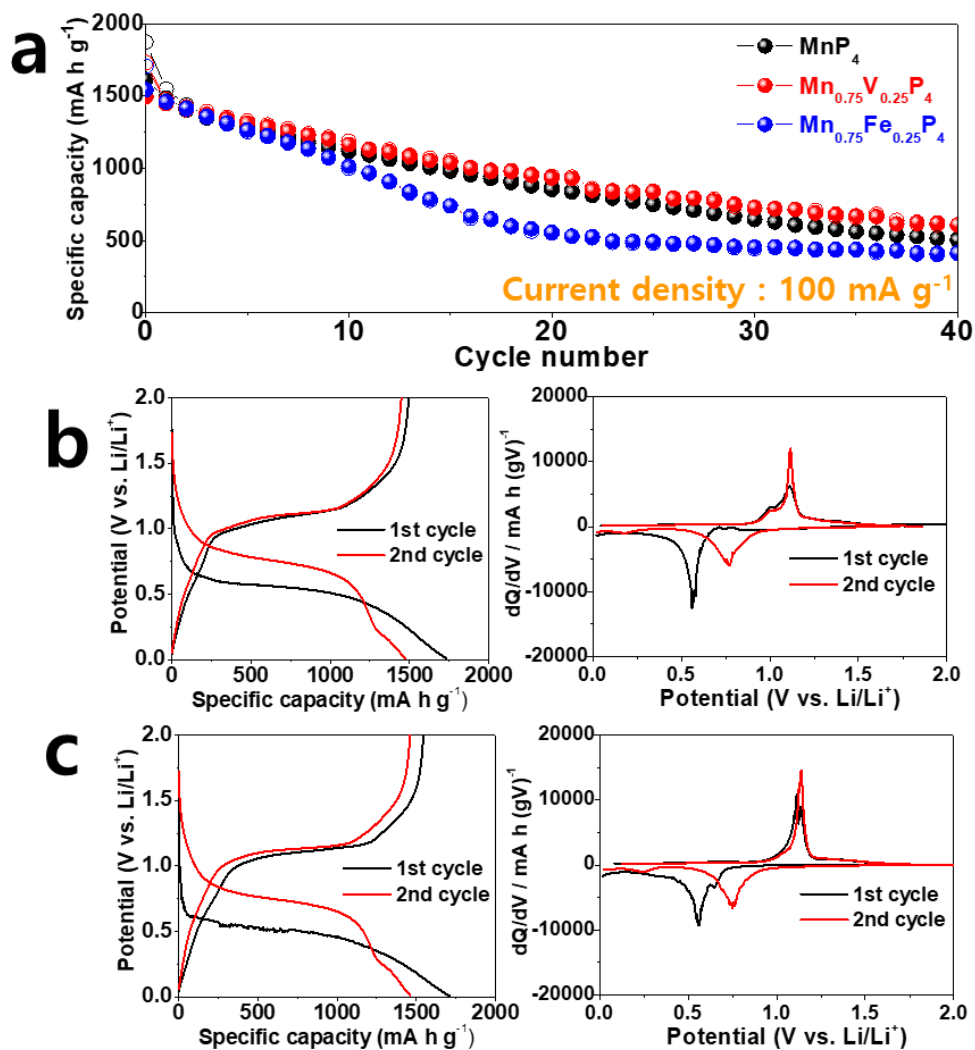


**Figure 5.3.18** (a) Cycle performances of  $\text{Mn}_{1-x}\text{TM}_x\text{P}_4$  (TM = V and Fe,  $x = 0.0$  and  $0.25$ ) electrodes as anodes for LIBs tested at current density of  $100 \text{ mA g}^{-1}$ . Galvanostatic discharge/charge voltage profiles and corresponding DCPs for 1<sup>st</sup> and 2<sup>nd</sup> cycles for  $\text{Mn}_{1-x}\text{TM}_x\text{P}_4$  (TM = (b) V and (c) Fe,  $x = 0.25$ ) electrodes.

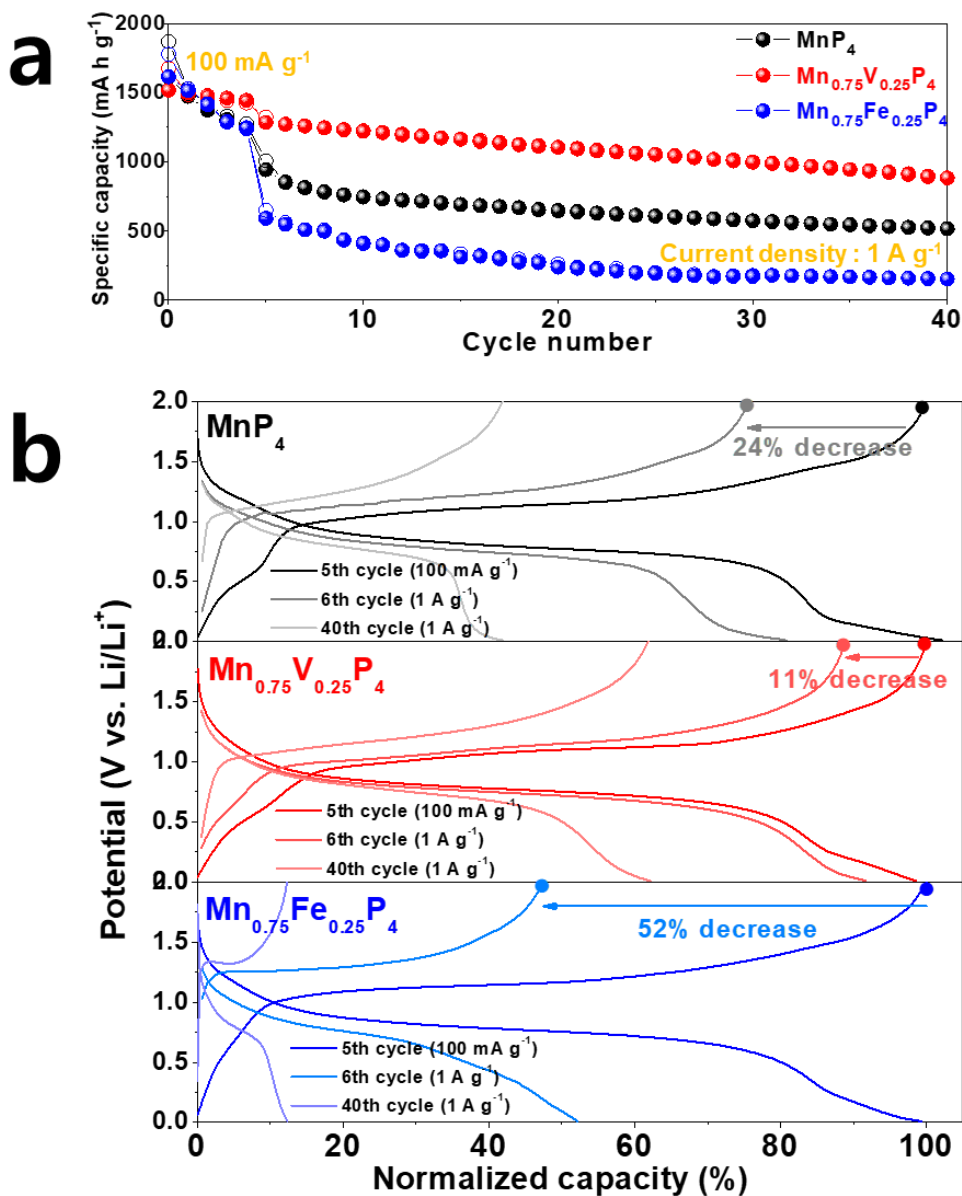


**Figure 5.3.19** (a) Cycle performances of  $\text{Mn}_{1-x}\text{TM}_x\text{P}_4$  (TM = V and Fe,  $x = 0.0$  and  $0.25$ ) electrodes as anodes for LIBs at current density of  $1 \text{ A g}^{-1}$  with initial activation 5 cycles at  $100 \text{ mA g}^{-1}$ . (b) Galvanostatic discharge/charge voltage profiles for 5<sup>th</sup>, 6<sup>th</sup>, and 40<sup>th</sup> cycles for  $\text{Mn}_{1-x}\text{TM}_x\text{P}_4$  (TM = V and Fe,  $x = 0.0$  and  $0.25$ ) electrodes.

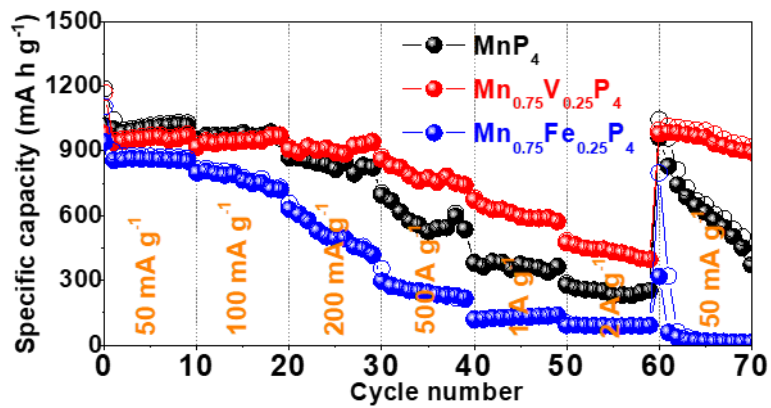


**Figure 5.3.20** Rate capability of  $\text{Mn}_{1-x}\text{TM}_x\text{P}_4$  (TM = V and Fe,  $x = 0.0$  and  $0.25$ ) electrodes as anodes for SIBs at various current densities.

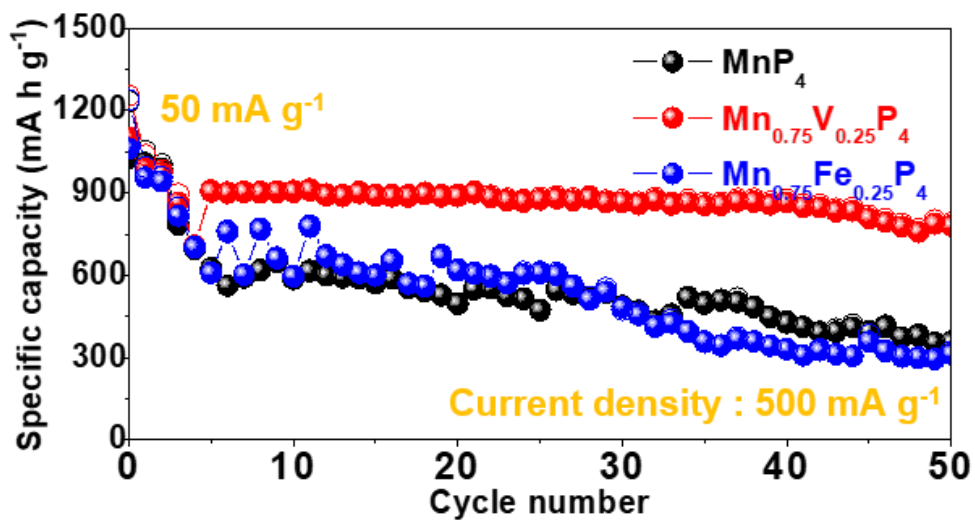


**Figure 5.3.21** High rate cyclability of  $\text{Mn}_{1-x}\text{TM}_x\text{P}_4$  (TM = V and Fe,  $x = 0.0$  and  $0.25$ ) electrodes as anodes for SIBs at current density of  $500 \text{ mA g}^{-1}$  with initial activation 3 cycles at  $50 \text{ mA g}^{-1}$ .

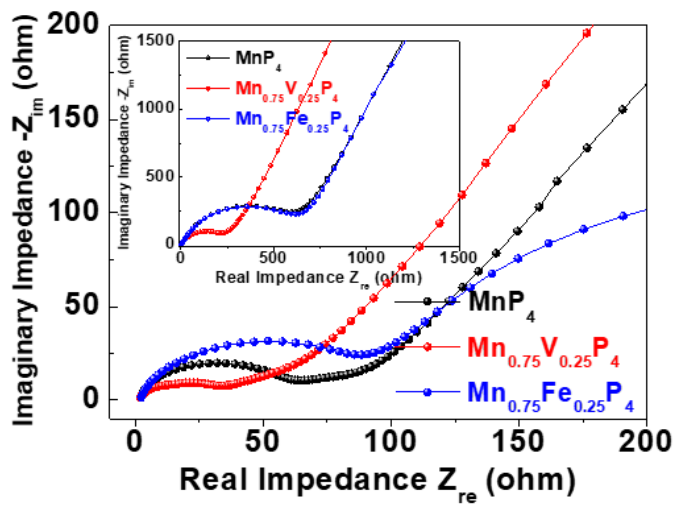


**Figure 5.3.22** Nyquist plots after 50 cycles (inset figure for pristine state) for  $\text{MnP}_4$  and  $\text{Mn}_{1-x}\text{TM}_x\text{P}_4$  (TM = V and Fe,  $x=0.25$ ) electrodes, respectively.

## 5.4. Conclusion

In summary, phosphorus-rich  $\text{MnP}_4$  phase was firstly synthesized in nanoparticle nature via a facile and mass productive high energy mechanical milling process for high performance anode application.  $\text{MnP}_4$  phase was introduced as an anode for both LIBs and SIBs, and its electrochemical performance and electrochemical reaction mechanism for SIBs were firstly investigated. Based on the *ex-situ* XRD and XAS analyses, it was revealed that conversion reaction of  $\text{MnP}_4$  was occurred in SIB application, which is same trend in LIB application. As-fabricated  $\text{MnP}_4/\text{graphene}$  nanocomposite exhibits improved cycle retention and high-rate capability with superior electrochemical performance for both LIBs and SIBs, which delivers reversible capacities of  $856 \text{ mA h g}^{-1}$  for 100 cycles at high current density of  $2000 \text{ mA g}^{-1}$  for LIBs and  $446 \text{ mA h g}^{-1}$  for 250 cycles at current density of  $0.5 \text{ A g}^{-1}$  for SIBs, respectively. Further, different cation substituted  $\text{Mn}_{1-x}\text{TM}_x\text{P}_4$  (TM = V and Fe,  $x=0.25$ ) solid solution exhibits different rate capability at high current density for both LIBs and SIBs, which might be derived from the structural and electronic structure changes. Among the substitutional  $\text{Mn}_{1-x}\text{TM}_x\text{P}_4$  solid solutions,  $\text{Mn}_{1-x}\text{V}_x\text{P}_4$  ( $x=0.25$ ) electrode showed improved high rate capability, which delivers reversible capacity of  $790 \text{ mA h g}^{-1}$  for 50 cycles at high current density of  $0.5 \text{ A g}^{-1}$ . The facile synthesis process and its excellent electrochemical performance of  $\text{MnP}_4/\text{graphene}$  nanocomposite and its substitutional solid solution make it as a promising alternative anode material for high-performance both LIBs and SIBs system.

## 5.5. Bibliography

- [5.1] M. D. Slater, D. Kim, E. Lee, C. S. Johnson, *Adv. Funct. Mater.*, **2013**, 23, 947-958.
- [5.2] J.-Y. Hwang, S.-T. Myung, Y.-K. Sun, *Chem. Soc. Rev.*, **2017**, 46, 3529-3614.
- [5.3] T. Liu, Y. Zhang, Z. Jiang, X. Zeng, J. Ji, Z. Li, X. Gao, M. Sun, Z. Lin, M. Ling, J. Zheng, C. Liang, *Energy Environ. Sci.*, **2019**, 12, 1512-1533.
- [5.4] K. Nobuhara, H. Nakayama, M. Nose, S. Nakanishi, H. Iba, *J. Power Sources*, **2013**, 243, 585-587.
- [5.5] S. C. Jung, D. S. Jung, J. W. Choi, Y. K. Han, *J. Phys. Chem. Lett.*, **2014**, 5, 1283-1288.
- [5.6] Y. Xu, E. Swaans, S. Basak, H. W. Zandergen, D. M. Borsa, F. M. Mulder, *Adv. Energy Mater.*, **2016**, 6, 1501436.
- [5.7] C. H. Lim, T. Y. Huang, P. S. Shao, J. H. Chien, Y. T. Weng, H. F. Huang, B. J. Hwang, N. L. Wu, *Electrochim. Acta*, **2016**, 211, 265-272.
- [5.8] J. Qian, X. Wu, Y. Cao, X. Ai, H. Yang, *Angew. Chem.*, **2013**, 125, 4731-4734.
- [5.9] J. Song, Z. Yu, M. L. Gordin, S. Hu, R. Yi, D. Tang, T. Walter, M. Regula, D. Choi, X. Li, A. Manivannan, D. Wang, *Nano Lett.*, **2014**, 14, 6329-6335.
- [5.10] P. Extance, S. R. Elliott, *Philos. Mag. B*, **1981**, 43, 469-483.
- [5.11] Y. Fu, Q. Wei, G. Zhang, S. Sun, *Adv. Energy Mater.*, **2018**, 8, 1703058.
- [5.12] G. Chang, Y. Zhao, L. Dong, D. P. Wilkinson, L. Zhang, Q. Shao, W. Yan, X. Sun, J. Zhang, *J. Mater. Chem. A*, **2020**, 8, 4996-5048.
- [5.13] Y. Zhang, G. Wang, L. Wang, L. Tang, M. Zhu, C. Wu, S.-X. Dou, M. Wu, *Nano Lett.*, **2019**, 19, 2575-2582.

- [5.14] J. Saddique, X. Zhang, T. Wu, X. Wang, X. Cheng, H. Su, S. Liu, L. Zhang, G. Li, Y. Zhang, H. Yu, *ACS Appl. Energy Mater.*, **2019**, 2, 2223-2229.
- [5.15] Y. Wang, Q. Fu, C. Li, H. Li, H. Tang, *ACS Sustainable Chem. Eng.*, **2018**, 6, 15083-15091.
- [5.16] Z. Li, L. Zhang, X. Ge, C. Li, S. Dong, C. Wang, L. Yin, *Nano Energy*, **2017**, 32, 494-502.
- [5.17] S. Yu, S.-O. Kim, H.-S. Kim, W. Choi, *J. Electrochem. Soc.*, **2019**, 166(10), A1915-A1919.
- [5.18] W. Liu, H. Zhi, X. Yu, *Energy Storage Materials*, **2019**, 16, 290-322.
- [5.19] Q. Xia, W. Li, Z. Miao, S. Chou, H. Liu, *Nano Research*, **2017**, 10(12), 4055-4081.
- [5.20] G.-A. Li, C.-Y. Wang, W.-C. Chang, H.-Y. Tuan, *ACS Nano*, **2016**, 10, 8632-8644.
- [5.21] Q. Liu, Y. Luo, W. Chen, Y. Yan, L. Xue, W. Zhang, *Chem. Eng. Journal*, **2018**, 347, 455-461.
- [5.22] J. Fullenwarth, A. Darwiche, A. Soares, B. Donnadieu, L. Monconduit, *J. Mater. Chem. A*, **2014**, 2, 2050.
- [5.23] M. Ihsan-Ul-Haq, H. Huang, J. Cui, S. Yao, J. Wu, W. G. Chong, B. Huang, J.-K. Kim, *J. Mater. Chem. A*, **2018**, 6, 20184.
- [5.24] J.-Y. Chen, L.-C. Chin, G.-A. Li, H.-Y. Tuan, *CrystEngComm*, **2017**, 19, 975-981.
- [5.25] D. C. S. Souza, V. Pralong, A. J. Jacobson, L. F. Nazar, *Science*, **2002**, 296, 2012-2015.
- [5.26] F. Gillot, L. Monconduit, M.-L. Doublet, *Chem. Mater.*, **2005**, 17, 5817-5823.

- [5.27] W. Jeitschko, P. C. Donohue, *Acta Cryst.*, **1975**, B31, 574.
- [5.28] W. Jeitschko, R. Ruhl, *Mat. Res. Bull.*, **1980**, 15, 1755-1762.
- [5.29] R. Ruhl, W. Jeitschko, *Acta Cryst.*, **1981**, B37, 39-44.
- [5.30] D. B. Henge, M. Hermus, C. F. Litterscheid, N. Wagner, J. Beck, B. Albert, J. Brgoch, *Inorg. Chem.*, **2015**, 54, 8761-8768.
- [5.31] N. Gong, C. Deng, L. Wu, B. Wan, Z. Wang, Z. Li, H. Gou, F. Gao, *Inorg. Chem.* **2018**, 57, 9385-9392.
- [5.32] S.-O. Kim, A. Manthiram, *Chem. Mater.*, **2016**, 28, 5935-5942.
- [5.33] K.-H. Kim, C.-H. Jung, W.-S. Kim, S.-H. Hong, *J. Power Sources*, **2018**, 400, 204-211.
- [5.34] J. Jiang, W. Wang, C. Wang, L. Zhang, K. Tang, J. Zuo, Q. Yang, *Electrochim. Acta*, **2015**, 170, 140-145.
- [5.35] J. Shen, Y. Wang, Y. Yao, L. Hou, K. Gu, Y. Zhu, C. Li, *ACS Appl. Energy Mater.*, **2018**, 1, 7253-7262.
- [5.36] P. Lou, Z. Cui, Z. Jia, J. Sun, Y. Tan, X. Guo, *ACS Nano*, **2017**, 11, 3705-3715.
- [5.37] G. Li, H. Yang, F. Li, J. Du, W. Shi, P. Cheng, *J. Mater. Chem. A*, **2016**, 4, 9593-9599.
- [5.38] S.-O. Kim, A. Manthiram, *ACS Appl. Mater. Interfaces*, **2017**, 9, 16221-16227.
- [5.39] R. Muruganatham, P.-C. Chiang, W.-R. Liu, *ACS Appl. Energy Mater.*, **2018**, 1, 3674-3683.
- [5.40] J.-Y. Chen, L.-C. Chin, G.-A. Li, H.-Y. Tuan, *CrystEngComm*, **2017**, 19, 975.
- [5.41] C.-M. Park, H.-J. Sohn, *Chem. Mater.*, **2008**, 20, 6319-6324.

- [5.42] M. Zhang, R. Hu, J. Liu, L. Ouyang, J. Liu, L. Yang, F. Fang, M. Zhu, *J. Alloys and Compounds*, **2018**, 762, 246-253.
- [5.43] W. Zhao, X. Ma, G. Wang, X. Long, Y. Li, W. Zhang, P. Zhang, *Appl. Surf. Sci.*, **2018**, 445, 167-174.
- [5.44] S.-O. Kim, A. Manthiram, *Chem. Commun.*, **2016**, 52, 4337.
- [5.45] F. Zhao, N. Han, W. Huang, J. Li, H. Ye, F. Chen, Y. Li, *J. Mater. Chem. A*, **2015**, 3, 21754.
- [5.46] K.-H. Nam, Y. Hwa, C.-M. Park, *ACS Appl. Mater. Interfaces*, **2020**, 12, 15053-15062.
- [5.47] Q.-L. Ning, B.-H. Hou, Y.-Y. Wang, D.-S. Liu, Z.-Z. Luo, W.-H. Li, Y. Yang, J.-Z. Guo, X.-L. Wu, *ACS Appl. Mater. Interfaces*, **2018**, 10, 36902-36909.
- [5.48] X. Fan, J. Mao, Y. Zhu, C. Luo, L. Suo, T. Gao, F. Han, S.-C. Liou, C. Wang, *Adv. Energy Mater.*, **2015**, 5, 1500174.
- [5.49] M. Tokur, M. Y. Jin, B. W. Sheldon, H. Akbulut, *ACS Appl. Mater. Interfaces* **2020**, 12, 33855.

## Chapter 6. Conclusions

In this study, the novel hybrid electrochemical reaction anode was introduced by forming substitutional solid solution strategy with structural and chemical relationship to obtain high performance secondary-ion battery. This new strategy is suggested to overcome intrinsic shortcomings of each electrochemical reaction mechanism (insertion, alloying, and conversion reaction) by generating hybrid electrochemical reaction of two different mechanisms in a single phase.

First of all, complete solid solution  $Mn_{1-x}Fe_xP$  ( $0 \leq x \leq 1$ ) compounds between alloying reaction-type MnP and conversion reaction type FeP were introduced as conversion/alloying hybrid electrochemical reaction anode by using their isostructural character. As-prepared  $Mn_{1-x}Fe_xP$  ( $0 \leq x \leq 1$ ) electrode showed the hybrid reaction with alloying reaction of MnP and conversion reaction of FeP electrodes, and it was investigated that the contribution rate of conversion and alloying reactions to total electrochemical reaction can be controlled by varying the composition in  $Mn_{1-x}Fe_xP$  solid solution. Through this novel strategy, the intrinsic shortcomings of fast capacity fading for MnP electrode and capacity activation behavior at high current density for FeP electrode were improved by hybrid conversion/alloying reaction of  $Mn_{1-x}Fe_xP$  ( $x=0.75$ ) electrode, which delivered a reversible capacity of  $360 \text{ mA h g}^{-1}$  after 100 cycles at high current density at  $2 \text{ A g}^{-1}$ . This improved electrochemical performance of  $Mn_{1-x}Fe_xP$  electrode can be attributed to the *in situ* generated nanocomposite nature of the Li–Mn–P alloying

element and the Fe nano-network in combination with the surrounding amorphous lithium phosphide, which effectively buffers the accompanying volume variation, hinders the aggregation of the alloying element, and ensures electron and ion transport.

Based on the feasibility of tunable conversion/alloying hybrid electrochemical reaction of complete solid solution  $\text{Mn}_{1-x}\text{Fe}_x\text{P}$ , alloying/insertion hybrid electrochemical reaction anode as  $\text{Mn}_{1-x}\text{V}_x\text{P}$  was introduced to further obtain highly stable cycle retention properties with intermediate specific capacity. The series of  $\text{Mn}_{1-x}\text{V}_x\text{P}$  compounds ( $x = 0, 0.25, 0.5, 0.75, \text{ and } 1.0$ ) between alloying reaction-type of orthorhombic MnP and insertion reaction-type of hexagonal VP are synthesized based on their similar crystal structure relation. The homogeneously substituted vanadium ions in the  $\text{Mn}_{1-x}\text{V}_x\text{P}$  compounds enable the alloying/insertion hybrid electrochemical reactions in a solid solution phase by expanding the volume of prismatic site in  $\text{Mn}_{1-x}\text{V}_x\text{P}$  close to the that of insertion-reaction type VP. The optimized  $\text{Mn}_{1-x}\text{V}_x\text{P}$  ( $x=0.25$ ) electrode showed reversible capacity of  $352 \text{ mA h g}^{-1}$  after 1500 cycles even at high current density of  $1 \text{ A g}^{-1}$ . Such a superior electrochemical performance of  $\text{Mn}_{1-x}\text{V}_x\text{P}$  was attributed to the synergistic effect of hybrid alloying/insertion electrochemical reaction occurred close to a few-nanometer scale in a single compound  $\text{Mn}_{1-x}\text{V}_x\text{P}$  phase, which effectively reduce the rate of volume change and hinder pulverization and agglomeration of alloying reaction elements and ensure fast electron and ion transport.

Finally, phosphorus-rich  $\text{MnP}_4$  phase was firstly synthesized in nanoparticle nature for high performance anode application and it was firstly introduced as an anode for SIBs. By encapsulating as-synthesized  $\text{MnP}_4$  nanoparticles with

commercial graphene nanosheets, superior electrochemical performance for both LIBs and SIBs could be achieved, which delivered reversible capacities of 856 mA h g<sup>-1</sup> after 100 cycles at 2 A g<sup>-1</sup> for LIBs and 446 mA h g<sup>-1</sup> after 250 cycles at 0.5 A g<sup>-1</sup> for SIBs, respectively. Further, different cation substituted Mn<sub>1-x</sub>V<sub>x</sub>P<sub>4</sub> (x=0.25) solid solution exhibits improved rate capabilities for both LIBs and SIBs, which could be derived from the structural and electronic structure change. The Mn<sub>1-x</sub>V<sub>x</sub>P<sub>4</sub> (x=0.25) electrode showed improved high rate capability, which delivers reversible capacity of 790 mA h g<sup>-1</sup> for 50 cycles at high current density of 0.5 A g<sup>-1</sup>.

The obtained results through this thesis show the promising potential with dramatic changes in performance of hybrid electrochemical reaction materials designed with multi-component substitution by considering chemical and structural relation and suggests that there are many other candidates in transition metal compounds to explore in high performance both lithium-ion and sodium-ion battery application.

## Abstract in Korean

### 국 문 초 록

#### 고성능 이차 전지용 하이브리드 전기화학 반응 고용체 음극 소재 연구

김 경 호

서울대학교 공과대학

재료공학부

전세계적으로 에너지 수요 및 저장에 대한 이슈들이 계속적으로 늘어나면서 친환경적인 에너지 저장 장치의 중요성이 대두되고 있다. 재충전 식 리튬 이온 전지와 소듐 이온 전지는 높은 에너지 및 전력 밀도 특성으로 인해 전기 자동차, 하이브리드 전기차 또는 그리드 규모 에너지 저장 장치 등의 대용량 에너지 저장에 적용할 수 있는 차세대 에너지 저장 시스템으로 떠오르고 있다. 현재 리튬 이차 전지에서 상용화 되어 있는 음극 소재는 흑연으로 이를 대체할 높은 에너지 밀도의 음극 소재 개발을 위해 삽입, 합금, 변환 반응을 전기화학 반응 메커니즘으로 하는 다양한 소재들에 대해서 연구 개발이 이루어지고 있다. 하지만 각 전기화학 반응 메커니즘들이 가지는 고유의 단점들이 존재하여 충-방전 시 전극의 성능을 열화시키는 요인으로 작용하고 있다.

각 반응 메커니즘들이 가지는 고유의 단점을 보완하기 위한 방안 중 안정적인 충-방전 특성을 보이는 삽입 반응 음극 소재를 상대적으로 전극 성능 저하가 빠르게 일어나는 합금 및 변환 반응 음극 소재와의 조합을 통해 이를 해결하고자하는 노력이 있다. 전극 성능 저하가 빠른 합금 및 변환 반응 음극 소재들에 대해서 전도성 탄소 계열 음극 소재나

티타늄 혹은 바나듐 산화물 계열의 삽입 반응 음극 소재를 혼합 또는 코팅하는 접근을 통하여 전극 열화를 완화하는 기존의 연구들이 많이 수행되어왔다. 충-방전 시 상대적으로 부피 변화가 작은 삽입 반응 소재들이 합금 및 변환 반응 소재의 큰 부피 팽창을 완충하는 공간을 제공할 수 있어 전극 구성 입자의 파쇄 및 응집 현상들을 완화하여 전극 구조의 안정성 향상을 통해 전극 수명 특성을 개선하였다. 하지만 이러한 접근을 통한 전극 성능의 개선에는 이종의 반응 메커니즘을 보이는 소재 간 나노 복합체를 형성하기 위한 균일한 혼합 공정의 최적화가 요구되며, 나노 복합체 내의 이종 반응 소재들은 나노 단위 영역에서 개별적으로 반응하기 때문에, 이종 소재 간 상호작용 및 시너지 효과가 제한되어 나노 영역에서 일어나는 전극 열화 인자를 효과적으로 완화하기 어렵다.

따라서 본 연구에서는 각 반응 소재의 고유 단점들을 효과적으로 보완할 수 있는 하이브리드 전기화학 반응 고용체 음극 소재 연구를 통해 고성능의 이차 이온 전지를 개발하는 것을 목표로 한다. 각 전기화학 반응 메커니즘의 단점을 완화하기 위한 이 새로운 전략은 서로 다른 반응 메커니즘을 보이는 이종의 소재 간 구조-화학적 관계를 활용하여 치환형 고용체를 형성하고 이를 통해 이종의 혼합된 전기 화학 반응을 하나의 고용체 소재에서 발현시킨다. 고용체 결정 구조 내 이종의 원소가 초기 원자 단위에 가깝게 혼합된 형태에서 기인하여 극대화된 두 이종 전기화학 반응 간 상호 작용 및 시너지 효과는 이종 소재가 물리적으로 혼합된 나노 복합체보다 뛰어난 전극 특성 향상을 가져올 것으로 기대한다. 또한, 개발된 고용체 전극 소재를 구성하는 이종 원소 간의 비율 조절을 통해 발현되는 전기화학 반응 메커니즘의 비율을 조절하여 원하는 전극 성능을 조정한다.

먼저 전기화학 합금 반응을 보이는 MnP 구조와 변환 반응을 보이는 FeP 구조 간 동형 구조 특성을 이용해 전율 고용체(전

조성범위에서 고용체를 형성)를 합성하고 그에 따른 하이브리드 합금/변환 반응을 도입하여 리튬 이온 전지 전극 특성을 확인하였다. 합성된  $Mn_{1-x}Fe_xP$  ( $0 \leq x \leq 1$ ) 고용체 전극의 화합물 조성ة 따른 전기화학 반응 메커니즘, 반응 전위, 용량 및 수명 특성의 조절 가능성을 중점적으로 연구하였으며 물리적으로 혼합된 MnP/FeP 나노 복합체 전극의 전기화학적 거동과 비교 분석하였다. 합성된  $Mn_{1-x}Fe_xP$  ( $0 \leq x \leq 1$ ) 고용체 전극들의 전기화학 반응 분석을 통해 고용체 전극의 총 전기화학 반응에 대한 합금 및 변환 반응의 기여율을 조성비로 제어할 수 있음이 확인되었다. 조성 최적화를 통해 MnP 합금 반응 전극의 빠른 용량 감소의 단점과 FeP 전극의 고 전류 밀도에서의 용량 활성화 거동 (가역 용량이 초기에 완전히 구현되지 않고 점진적으로 활성화)의 단점을  $Mn_{1-x}Fe_xP$  ( $x=0.75$ ) 조성에서 완전히 개선하여  $2 \text{ A g}^{-1}$ 의 고 전류밀도에서 약  $360 \text{ mA h g}^{-1}$ 의 가역 용량을 100 사이클 동안 유지하였다. 이러한 전극 특성 향상의 경우 하이브리드 합금/변환 반응 시 형성되는 나노 복합체 형상 (Li-Mn-P 삼성분계 합금 상과 환원된 Fe 나노 입자가 비정질  $Li_3P$  매트릭스에 둘러 쌓인 나노 네트워크)에 의해 합금 반응의 부피 팽창을 완충하는 동시에 응집 현상을 억제하여 전극 구조의 안정화를 통해 리튬 이온 및 전자의 이동을 빠르게 잘 유지하였다.

상기 연구 결과를 기반으로 후속 연구에서는 높은 용량 특성을 보이면서 수명 특성도 안정적일 수 있는 반응 소재들 간의 조합인  $Mn_{1-x}V_xP$  하이브리드 합금/삽입 반응 고용체 소재를 제안하였다. 합금 반응 소재인 orthorhombic 구조의 MnP 소재와 유사한 결정학적 관계를 가지는 hexagonal 구조의 삽입 반응 소재 VP 간의 고용체 화합물  $Mn_{1-x}V_xP$  ( $x = 0.25, 0.5, 0.75$ )를 합성하고 이차전지 전기화학 특성을 분석하였다.  $Mn_{1-x}V_xP$  고용체 화합물 내 균일하게 치환된 바나듐 이온은 리튬 이온이 삽입될 수 있는 프리즘 자리를 VP 구조에 가깝게 변화시키면서 그 부피를 팽창시켜 하이브리드 합금/삽입 반응을

가능하게 하였고 최적화된  $Mn_{1-x}V_xP$  ( $x=0.25$ ) 조성의 고용체 화합물은  $1 A g^{-1}$ 의 고 전류 밀도에서 약  $352 mA h g^{-1}$ 의 가역 용량을 1500 사이클까지 잘 유지하였다. 이러한  $Mn_{1-x}V_xP$  고용체 전극의 우수한 전기화학 성능은 몇 나노 단위 내에서 하이브리드한 형태로 일어나는 합금/삽입 반응의 시너지 효과로 인해 충-방전 시 전극 입자의 체적 변화율을 효과적으로 낮추고 합금 반응 입자의 파쇄 및 응집을 방해하여 빠른 전자와 이온의 이동을 가능하게하였기 때문이다. 또한, 이 연구를 통해 확인된 구조-화학적 관계를 이용하여 유사한 조성의 화합물( $Mn_{1-x}Ti_xP$  및  $Mn_{1-x}Mo_xP$ )에 대한 합성 및 분석을 통해 합금/삽입 하이브리드 음극 소재 개발 시 중점적으로 고려해야할 요인에 대한 고찰을 진행하였다.

마지막 파트에서는 상기 고용체 형성을 통한 이차전지 전기화학 성능의 변화 유도를  $Mn_{1-x}TM_xP_4$  ( $TM = V$  및  $Fe$ ) 조성에 적용하여 우수한 전기화학 성능을 나타내는 고용량의 소듐 이차 전지 음극 소재를 개발하였다. 리튬 이차 전지 음극 특성 평가에 대한 사전 연구를 통해 유망한 음극 소재로 판단되는  $MnP_4$  음극 소재에 대해 소듐 이차 전지로서의 가능성을 확인하고 전기화학 반응 메커니즘을 연구하였으며 이중 원소 치환을 통한 고용체 형성을 통해 전기화학 성능을 향상시켰다. 또한, 합성된  $MnP_4$  나노 입자와 상용 그래핀 나노 시트를 이용해  $MnP_4$ /그래핀 나노 복합체를 제조하여 리튬 이온 전지에서 약  $856 mA h g^{-1}$ 의 높은 가역 용량을  $2 A g^{-1}$ 의 고 전류 밀도에서 100 사이클 동안 유지시켰고, 소듐 이온 전지에서 약  $446 mA h g^{-1}$ 의 가역 용량을  $0.5 A g^{-1}$ 의 전류밀도에서 250 사이클 동안 유지시켰다. 또한, 이중의 원소 ( $V$  또는  $Fe$ )를  $MnP_4$  구조에 치환한 고용체 전극 소재의 경우 결정 구조 및 전자 구조 변화에서 기인한 고속 충-방전 특성 변화를 리튬 및 소듐 이차전지 모두에서 보였다. 최적화된  $Mn_{1-x}V_xP_4$  ( $x=0.25$ ) 고용체 전극의 경우  $0.5 A g^{-1}$ 의 고 전류 밀도에서 약  $790 mA h g^{-1}$ 의 높은 가역

용량을 50 사이클 동안 안정적으로 유지하는 향상된 고속 충-방전 특성을 나타내었다.

위와 같은 일련의 결과들을 통해 본 연구에서는 이중 반응 음극 소재들의 구조-화학적 관계를 고려하여 도입한 하이브리드 음극 반응 고용체 개발을 통해 각 반응 메커니즘이 보이는 고유의 단점들을 완화하는 시도를 수행하였다. 본 연구의 결과들은 구조적, 화학적 관계를 가지는 다성분계 치환을 통해 개발된 하이브리드 반응 고용체 전극은 기존의 각 성분 소재들이 나타내지 못하는 전기화학 특성을 보이는 우수한 잠재력을 보여주었으며, 차세대 리튬 및 소듐 이차 전지의 고성능 달성을 위해 해결해야할 각 반응 메커니즘의 한계점을 극복하는 새로운 방법을 제안한다.

**주요어:** 하이브리드 전기화학 반응, 고용체, 금속 인화물, 음극 소재, 리튬 이차 전지, 소듐 이차 전지

**학번:** 2015-20800